CORSO DI DOTTORATO DI RICERCA IN INGEGNERIA MECCANICA E INDUSTRIALE

XXXI CICLO DEL CORSO DI DOTTORATO

ACOUSTIC ANALOGY-BASED FORMULATIONS FOR AERO/HYDRO-ACOUSTIC ANALYSIS OF ROTARY WING DEVICES

CANDIDATO: FEDERICO PORCACCHIA _____

TUTOR: PROF. MASSIMO GENNARETTI _____

CO-TUTOR ESTERNO: DR. CLAUDIO TESTA _____

CO-TUTOR ESTERNO: DR. STEFANO ZAGHI _____

COORDINATORE: PROF. EDOARDO BEMPORAD _____

"*It always seems impossible until it's done.*"

Nelson Mandela

Ai miei genitori . . .

Abstract

This thesis deals with the prediction of fluid dynamic generated noise from rotary-wing devices, operating both in air and water and characterized by significant vortical and turbulent flows.

Nowadays, among the many theoretical approaches available for the aero/hydro-acoustics predictions, the Acoustic Analogy-based methodologies seem to be the most effective way to deal with the sound induced by complex shaped bodies in relative motion with respect to the medium.

As a matter of fact, among them, the Ffowcs Williams and Hawkings Equation (FWHE) represents a well known and widely used effective tool able to carry out reliable noise predictions due to fluid-fluid, fluid-body interactions.

Since when the first integral solution was proposed by Farassat in 1975, it has been fruitfully used to investigate the noise of rotary-wing devices such helicopter rotors and propeller driven aircraft, yielding results in great accordance with the experimental data.

One of the strength of such model resides in the straightforward identification of the noise generation mechanisms, that, combined to the linearity of the acoustic problem, allows to split the acoustic effect of noise sources over the moving bodies from those associated with the flow field around it. The former are due to the shape, motion and pressure over the body, whereas the latter to the turbulence and vorticity flow field as well as cavitating phenomena (for underwater applications).

Such capability undoubtedly represents a major advantage, in that, although the physics behind the sound generation of the rotary wing devices is the same (i.e. it does not matter what the field application is, marine or aeronautical) the relative weight among the volume and surface contributions differs.

Evidence of this is represented by the huge know-how gained by the aeroacoustic community in the last thirty years; it indeed proves that, for applications involving thin bodies moving through air (such as helicopter rotors or aeronautical propellers) and in absence of shock waves (i.e. subsonic applications) the noise is dominated by the surface sources.

In general, however, the volume sources of noise may play a significant role; thus, limiting the radiation domain to the blade surfaces may leads to an inadequate prediction of the acoustic signature. This is the case of many applications of engineering interest involving rotary wings such as underwater propellers and wind turbines.

The former, working underwater, have completely different geometrical features (compared to the analogues devices operating in air) which reflect in a different acoustic behavior. In addition, the operating condition behind the hull often involves the ingestion of a high turbulent inflow due to the separation phenomena in the boundary layer upon it. Besides, underwater applications are often characterized by an high vorticity and turbulent flow field generated by the propeller itself which persists both in space and time near the rotor. Such condition produces almost ever complex wake interactions and vortex coalescence that considerably affect the noise signature.

Similarly, the acoustic behavior of wind turbines is often dominated by the volume noise sources induced essentially by the operating conditions. Indeed, large changes in the wind intensity and direction produce high angles of attack reflecting in wide zones of detached flow over the blade. Besides, turbulent inflow conditions due to the atmospheric boundary layer often interact with the blades causing flow field non linear noise contributions.

Based on these findings, the inclusion of volume noise contributions became mandatory for a reliable acoustic predictions. To this aim, throughout the thesis the acoustic effects of field noise sources are accounted for by the use of the so called permeable approach. It represents a configuration of the FWHE in which the emitting body is replaced by an arbitrary shaped moving surface which embeds the body itself and all noise sources generated by its motion through the flow. It represents, de facto, a surface in the space radiating the sound induced by the sources embedded inside it.

Besides, the same permeable approach is used to achieve noise predictions on the base of a new Acoustic Analogy-based formulation. It is derived starting from the conservation laws (continuity and momentum equations) by applying the same special mathematical tools used to achieve the FWHE, namely Hybrid Lighthill-Ffowcs Williams and Hawkings Equation (H-FWHE).

Along the thesis it is shown how the permeable approach of this formulation recasts into the well known K-Equation.

Comparisons between them confirm, once more and in agreement with the literature outcomes, how the FWHE is nowadays the best Acoustic Analogy-based approach to carry out reliable aero/hydro-acoustic analysis.

Theoretical and numerical findings (available by the literature works) highlight how the surface location does not influence the acoustic predictions, provided that it contains all noise sources. In view of this, a wide part of the thesis concern with the assessment of the influence of shape and position of the porous surface through comparisons against analytic solutions of the wave equation. Such process allows to confirm the reliability in the noise prediction and get a deep awareness of its features.

Particularly, a first methodological approach based on the velocity potential flows theory along with the Bernoulli Equation allows to provide the fluid dynamic data over the permeable surface as well as the reference pressure signals for the acoustic observers. The case studies concern with moving monopoles and rototranslating vortex ring; the last, especially, allows to get a better insight into the principles behind the porous approach particularly with respect to the *End Cap* issue (i.e. the effect of eddies convected through the permeable surface).

The first application of the acoustic models to rotating wing devices is done by the means of a potential flows based aerodynamics for a slender lifting blade. Issues concerning with the potential wake convected through the porous surface soon highlight the generation of *spurious noise* contributions as the most important limitation to the applicability of such technique, confirming the outcomes of the vortex ring case study.

Thus, such unwanted effect is at first deeply investigated from a theoretical point of view, then, some possible solutions are given in view of the application to configurations of engineering interest.

Pushing through such aspect, the extension of the classic FWHE porous approach to account with the acoustic effects of thin vorticity layers (as potential wakes) crossing and going outside the permeable surface is proposed. It turn out in a novel formulation obtained by combining the H-FWHE (over the wake) and the FWHE (over a surface, either permeable or the rotor itself), namely Combined FWHE/H-FWHE which seems to provide good findings.

A significant part of the thesis is devoted to the assessment of noise sources detection capabilities for different types of fluid dynamic solutions (a suitability analysis). Such process is of crucial importance, in that, from it depend the features of the predicted acoustic signatures. Particularly, the fluid dynamic solution are carried out by the

means of a 3D full unsteady potential flows-based panel method along with the Bernoulli Equation and a in house fully validated CFD solver. Both solvers, with different strength points and weakness, are able to give an accurate prediction of the hydro/aero-dynamic loads and a consistent description of flow field velocity and pressure around and past the blades. In view of this, the capability of the CFD solver to account with the viscous effects in the resolution of the flow field give the possibility to assess the effects of both, turbulence and vorticity field, on the noise generation mechanisms.

However, it is worth to note that the currently available computational resources do not allow to carry out Direct Numerical Simulation (DNS) (able to numerically resolve the lowest time space scale of turbulence phenomena) at least for Reynolds numbers greater than 4000, that is, orders of magnitude lower than those inhere faced. Hence, models based on the functional (eddy–viscosity) such as Reynolds Averaged Navier Stokes Equation (RANSE), Large Eddy Simulation (LES) and Detached Eddy Simulation (DES) are used to model the fluid dynamic effects of turbulence yielding an insight of its role in the noise generation mechanism with respect to the other noise sources.

As a matter of fact, it turns out how the detection of fluctuating velocity and pressure flow field induced by the turbulence phenomena is one of the key point for an accurate prediction of the rotary-wing noise signature. Such condition appears to be especially true for underwater propeller applications, where the effects of nonlinearities (i.e. zones of the flow field where the behaviour of the fluid is non linear) dominate the noise generation phenomena.

From this standpoint the RANSE simulations, which inherently dissipates the fluctuation component of the flow field just outside the boundary layer, turn out to be not suited for acoustic purposes.

Differently, the use of a DES turbulence model proves to be an effective detector of noise sources due to both vorticity and turbulence phenomena.

A statistical based approach allows to separate, for the noise sources detected by the DES model, those related with the vortical flow field from those induced by fluctuating phenomena due to the turbulence; thus giving their mutual contribution to the acoustic signature.

The thesis shows how, for the kinds of rotating blade devices analyzed, the vorticity induced noise plays a secondary role with respect to the turbulence one.

The effectiveness of this decoupling procedure is also assessed through the comparisons with acoustic predictions arising by aero/hydro-dynamic data provided by a 3D panel method for lifting bodies, based on the hypothesis of potential flows and the Bernoulli Equation.

In essence, when such technique is applied to the same configuration analyzed by the CFD solver, it yields the acoustic effects due to the rotor and the vortical flow downstream it without the contribution of turbulence phenomena. Hence, it is expected to be able to detect the same tonal noise sources identified by the CFD simulation.

As a matter of fact it turn out to be true only in part, in that, noise sources arising from complex interactions between vortices (especially for underwater applications) are not well detected.

Comparison between potential flows-based hydrodynamics against DES solutions give, as well, the opportunity to understand the capability of the former approach to be able to provide a fruitful noise detection for the permeable approach at reasonable computational efforts.

Interesting outcomes on this prove how it is true only if the goal is to achieve acoustic predictions "near" the body where the noise detection is excellent.

One of the more interesting part of the thesis concerns the identification and quantification of the role played by the boundary conditions of the CFD/DES solver in the noise detection process. Surprisingly, it is shown that their contribution is potentially harmful for the acoustic prediction if not well identified. The quantification of such phenomenon in terms of acoustic effects is made through an unusual application of the permeable FWHE technique which avoids the integration of the whole computational CFD domain, giving surprising and very interesting results.

Acknowledgements

I wish to thank my Supervisor, Prof. Massimo Gennaretti for his precious help and advice during my period of research.

A special thanks goes to my Co-Supervisors, Dr. Claudio Testa for his important contribution given to this thesis and Dr. Stefano Zaghi for his human and scientific support.

I would also like to thank all the people of CNR-INM institute I worked with in these years, for their kindness, warmth and welcoming.

Last but not the least, I would like to thank my parents for supporting me spiritually throughout writing this thesis and my life in general.

The researches described in this thesis was carried on while I held a Research Studentship from the CNR-INM.

Contents

List of Figures

List of Tables

Chapter 1

Introduction

The prediction of noise generated by bodies moving throughout a fluid domain is of great interest for several engineering applications. In this framework, rotary-wing propulsor systems are largely investigated from a numerical standpoint because a driving factor in the design of modern vehicles (such as airplanes and ships) is the acoustic signature to comply with international standards related to environmental issues, comfort onboard, detectability of war units, etc...

Historically, the main efforts for the characterization of the fluid dynamic generated noise have been closely related to aeronautical applications, namely *aeroacoustics*, typically aimed at reducing the emitted noise. From the beginning, aeroacoustics has gained constantly more and more importance due to an increased consciousness of environmental issues and the strong international competition between airplane/helicopter manufacturers pushing toward the design of quieter vehicles (inside and outside the cabin).
Consequently, in the last 80 years, the scientific community has devoted considerable efforts toward the understanding of the physical mechanisms governing the noise generation in rotating propulsive systems and toward the development of computational methods able to predict the acoustic field.
Propeller and helicopter rotor noise theory has been developed starting from 1940's; the importance of the role of unsteady loading in acoustics of moving bodies was recognized in the 1960's, and this yielded a great deal of progress in the development of theoretical modeling and noise prediction codes.

In this framework the *Acoustic Analogy* represents a milestone in the theory for the prediction of fluid dynamic generated noise. Proposed by Lighthill [1] in the 1952, it was the first theoretical model able to describe the physical mechanisms behind the turbulence generated noise, i.e. the acoustic effects due to the presence of a finite region of rotational flow in an unbounded fluid. The novelty of such approach was a re-writing of the Navier-Stokes Equations in the form of a inhomogeneous wave equation in which forcing terms represent acoustic sources consisting of density, pressure and velocity fluctuation.

Since then, many efforts were done to include in this framework the acoustic effects of the interaction fluid-solid until to the 1969 when Ffowcs Williams and Hawkings proposed their well known and widely used theoretical model [2]. It extends the Lighthill's original theory for turbulence generated noise, to account for the presence of moving bodies and identifies different noise generation mechanisms consisting of a combination of *linear* and *non-linear*

contributions.

To the former are associated surface noise contributions which are related to the shape and kinematic of the body as well to the time-space pressure distribution over it, known in literature as *thickness* and *loading* noise, respectively. Differently, nonlinear noise contributions are associated to fluid dynamic phenomena occurring in a certain volume fluid *surrounding* the moving body. Among them, vorticity, turbulence, cavitation phenomena, shock waves occurring at high Mach number as well as the fluid dynamic behaviour of the boundary layer represent the most important ones.

The notable know-how gained through 30 years of research activities in Aeroacoustics prove that the Ffowcs Williams and Hawking Equation (FWHE) is the most powerful approach to tackle the aeroacoustic analysis of rotary-wing devices. Indeed, since the first solving formulations of the FWHE was developed by Farassat [3, 4] (1975,1981) the application to propeller-driven aircraft and proprotors provided excellent results compared to the experimental findings.

Even more important, since then it was clear how in air, in absence of shock wave phenomena and up to a blade tip Mach number approximately equal to 0.8, the acoustic field is dominated by noise generation mechanisms strictly related to the body surface terms, the *linear* ones. Further confirmations to these outcomes were given by the many European projects founded during the 90s aimed to fill the knowledge gap with the USA and to support the aeronautical industry. Indeed, from the 1990 to the 2001 HELINOISE [5], RHINO [6], HELISHAPE [7], SNAAP [8], EROS [9], HELIFLOW [10], ROSAA,[11] and finally APIAN [12] projects all proved the same suggestions; in air, propellers and rotors acoustic behaviour (if not operating in transonic conditions) is dominated by the thickness and loading noise whereas the *non linear contribution* play a negligible role.

Beside to these aeroacoustics outcomes, the straightforward and computational efficient calculation of the surface integral contributions in the FWHE, (i.e. thickness and loading noise), have relegated the question of noise radiation from rotating wings to a closed question for years to come.
Although that, the problems associated with environmental pollution due to the *carbondioxide* emissions and the increasing sensitivity of the community towards the production of energy from renewable sources have raised new issues related to the emission of noise due to increasing use of large horizontal axis wind turbines[1]. Indeed, literature works show how the noise spectrum of these devices is spread over a wide range of frequencies [13], from 1-4 Hz up to 1000Hz (broadband noise).

Such behaviour is mainly related to flow field phenomena induced by operating conditions often unpredictable and characterized by a wide range of variability because affected by many environmental aspects (i.e. wind direction, non homogeneous inflow conditions, atmospheric turbulence due to the ground boundary layer, etc..). In particular, the blades of wind turbines may experience large changes in angle of attack associated with sudden large gusts, changes in wind direction, or interaction with the unsteady wake shed from the tower

[1] Nowadays devices with Power rating up to 9.5MW and rotor diameter 164m are are used in the conversion (MHI Vestas V164-9.5MW)

support on downwind which may result in dynamic stall over wide portions of the rotating blade.

In addition, flow field phenomena around the blades, i.e. the boundary layer transition laminar-turbulent and its interaction with the trailing edge, are well known and effective noise emitters.

From the aeroacoustic standpoint those phenomena are accountable to be non linear noise contributions whose effects are comparable or even greater than the thickness and loading noise [13] related to the tonal (narrowband) noise component; namely, the sound pressure characterized by spectrum content only at multiple of the number of blades (BPF). As a matter of fact, the tonal noise is not usually a problem for large wind turbines that operate at high Reynolds numbers whereas it may become a significant source of acoustic annoyance for small wind turbines ($\leq$ 10kW), in spite of the low Mach numbers operating conditions (generally, up to 0.4) [13].
On the other hand, the hydroacoustics, *i.e.* the science of noise generation and propagation mechanisms through water, is relatively younger than aeroacoustics. Looking at the literature it is indeed easy to recognize a lack of both theoretical and computational models able to deal with this challenging problem. As a matter of fact the criteria adopted to satisfy the noise emission requirements have been based for many years on empirical basis and some approximated numerical procedure able to provide, to the utmost, a qualitative raw estimation of the acoustic field [14].

However, the basic understanding of hydrodynamically generated sound has increased significantly by the contamination with the developments achieved in the aeronautical context thanks to the commonalities existing among fluid-dynamics of marine propellers, helicopter rotors and aeronautical propellers. Therefore in the last years the notable know-how gained by aeroacousticians has been suitably and successfully used to study the underwater noise due to the ship and/or its structural subcomponents (by also exploiting the increased computing resources). Although the first applications of the Acoustic Analogy to the underwater propeller noise prediction was considered, based on the similarities with the aeroacoustic problems, only matter of *linear* noise contributions [14], lately things turned out to be going diversely.

Indeed, the hydroacoustics of underwater propeller seems to be inherently a non linear problem despite operating conditions characterized by the low rotational Mach number [14]. To this aim, starting from the SILENV [15] $(2009 \div 2011)$, going through STREAMLINE [16] and currently AQUO-SONIC research projects have been devoted to the analysis of the underwater noise (often more extended and general contexts) yielding the basic understanding of hydro-dynamically generated sound. The first, SILENV, soon highlighted important differences in the noise generation phenomena between air and water. It represents a sort of breakpoint for hydroacousticians respect to the analogue problems of noise generation and propagation in air, pointing out that non-cavitating propeller underwater acoustics is inherently a nonlinear problem, in that governed mainly by the hydrodynamic sources of sound in the flow field around the propeller. Specifically, sound from the FWHE surface terms (namely, thickness and loading noise) appears significant only close to the propeller,

decreasing rapidly with respect to the volume terms contribution (namely, the quadrupole noise) induced by the hydrodynamic sources of sound (i.e., vortex released at the blade tip, vorticity, turbulence, etc..) which can be very intense and persisting around/downstream the propeller disk [17].
Therefore, based on the foregoing, beside the standard thickness and loading noise terms, an acoustically-consistent prediction of the low Mach number rotating blades devices inducing considerable flow field phenomena needs the inclusion of the non-linear contributions. To this aim the use of the permeable approach of the FWHE allows to avoid the cumbersome computations of volume integral through the use of a porous surface surrounding the body and all the noise sources around it [18].
Following this approach, the evaluation of the overall noise signature is transformed into the application of boundary integral representation (on the permeable surface advancing with the body) for the solution of the FWHE. Thus, the permeable surface assumes the role of acoustic boundary, emitting the noise contributions enclosed by it. Literature works demonstrate that the Ffowcs Williams and Hawking Equation for permeable surfaces (FWH-P) is nowadays widely used whenever nonlinear noise sources have to be included into the acoustic analysis [19] [20]. This is even more important for hydroacoustic applications because, unlike the aeroacoustic ones, they are characterised by a considerable spatial distribution of noise sources whose direct inclusion (i.e. field contribution) would require considerable numerical efforts.

However, the unquestionably numerical advantage of this technique is paid in terms of critical issues concerning with the permeable surface. Although the shape is well proven not to be a matter [18], its placement with respect to the embedded noise sources, the possibility of turbulent eddies crossing the porous surface (giving rise to the well-known *spurious noise*) and the related different level of accuracy associated to the techniques able to face this issue [21] are critical aspects for which a debate is still open, thus, extensively treated throughout the thesis.
On the other hand, since flow field phenomena are at the origin of sound generation, their detection is mandatory for an accurate aero/hydro-acoustic prediction. To this aim, numerical techniques able to solve the non linear velocity and pressure flow field *around* the body represent a mandatory requirement for a successful noise sources detection.

Among them, Computational Fluid Dynamic (CFD) approach represents the most suitable technique because able to deal with massive turbulence and vorticity phenomena. Nevertheless, RANS (Reynolds Averaged Navier Stokes) simulations, widely and fruitfully used for the prediction of propeller performance, have proven to be unsuited for hydroacoustic purposes. Essentially, this is due to the relevant numerical diffusion, which inherently makes the model incapable to correctly model the vorticity and turbulence fields spreading downstream the propeller [22].

To overcome this limitation, the use of Detached Eddy Simulation (DES) technique allows to combine the advantages of RANS computations (near solid boundaries) with those of Large Eddy Simulation (LES) calculations in fluid domains where the spatial discretization is fine enough. Although well suited for aero/hydro-acoustics, the computational cost of the

combined FWHE/DES formulation is significant due to the demanding DES grid resolution. However, limiting our interest to the near-field (few diameters from the propeller hub) the narrowband noise generated by periodic passages of blades and vortical structures, namely tonal noise, may play an important role. To this aim a potential-based hydrodynamic theory for unsteady three-dimensional (3D) flows might be used, at reasonable computational costs, to detect the sources of sound inherently associated to the blades and vorticity convected downstream. Acoustic scattering problems in which hydroborne propeller sound interacts with the hull, being spread out into reflected and diffracted noise components, fall within this field of application [23], [24].

1.1 Propeller Noise

Propeller induced noise is one of the most critical aspect for applications in many different field of engineering interest both in air and underwater. In the aeronautic field the commercial usage of propeller driven aircraft is limited by high levels of cabin noise and by the stringent civil regulations in terms of noise pollution especially near the airports.

For what concerns underwater noise, propellers are the major cause of both shipboard noise and radiation to the far field representing the most important noise source for submarines which need quiet propellers to be stealthy. Although the noise generation mechanism are the same, the dominant sound components depend on the application and to the operating condition. Hereafter the main noise sources in the propeller noise generation mechanism are analyzed.

1.1.1 Propeller Noise in Aeronautical Application

The acoustic signature of propellers may be divided into two different types: the tonal noise characterized by periodic pressure fluctuations and the so-called broadband noise, which is characterized by a randomic, non-periodic behaviour. The tonal content of the acoustic signature is characterized by multiples of the *blade passing frequency* (BPF). It is essentially due to the rotation of the noise sources over the blades which is seen by an acoustic observer as a time depend pressure disturbance repeated for the number of blades belonging to the rotor. Differently, a typical broadband noise content of the pressure signature has not periodicity and its envelop varies periodically in time.

1.1.1.1 Tonal Source of Noise from Aeronautical propellers

The rotor tip speed and the flow conditions in which the propeller operates define the primary tonal sources of noise.

For low speed propeller the tonal noise is dominated by the unsteady pressure on the blade surface which may be affected by many different effects. If the propeller operates in a completely clean inflow, which is rarely the case, the aerodynamic forces are steady in a blade fixed frame of reference but the component of the lift and drag perceived by the observer (at any point fixed on the rotor disk) varies as the blade rotates [25]. Therefore, the directivity of such noise component is very high (not omnidirectional) because the amount of variation of forces seen by the observer is strongly dependent respect to its location. Such kind of sound, namely *rotational noise*, is present for all kind of propellers, however is effects on the acoustic pressure is quite weak compared to those induced by the unsteady loads over the blades.

The latter are mainly associated to:

i) periodically change of the inflow conditions seen by the blades (for abs due to the propeller pitch respect to the aircraft) thus the angle of attack varies continuously as the propeller rotates.

ii) sudden change of attack angle arising when the blades encounter a velocity deficit in the flow which may be induced by particular vortical inflow condition.

In addition to the noise generated by time depending loads over the blades, for tip Mach number higher than 0.7 an important contribution to the acoustic pressure comes from the blade motion and is referred to *thickness noise*. The noise generation mechanism related to this acoustic source is the time varying displacement of fluid generated by the blades as it rotates. Indeed, similarly to what said about the acoustic effect of the steady loading distribution over the blades, for a fixed observer the volume of fluid displaced by the blades passage change in time during the rotation, thus producing pressure disturbance.

Another important noise generation mechanism is related with the eventuality of tip blades operating in high transonic conditions. Such condition can give rise to shock discontinuities both over the blade surface and in the fluid surrounding the tips. Similarly to the rotational noise, the acoustic observer perceive the shock changing its position as the blade rotates, thus producing time depending disturbance pressure, i.e. sound. This mechanism can be as important as thickness noise in some rotor designs.

1.1.1.2 Broadband Source of Noise from Aeronautical propellers

Broadband rotor noise is produced by random variation of the inflow conditions mainly due to the turbulence which result in blade sudden load variations. Usually propellers operate in condition of high level of turbulence generated upstream the rotor. When such turbulent inflow is ingested by the propeller, unsteady non periodic loads are generated over the blade producing random fluctuating pressure. In addition, important turbulent phenomena may also arise from the propeller itself (self-induced) in the process of transition laminar-turbulent of the boundary layer. As a matter of fact it is well known in literature that the turbulence in the blade boundary layer acts like a weak emitter by itself, however when it interacts with the blade trailing edge the local boundary conditions change rapidly and significant sound generation occurs. This is called boundary layer-trailing edge interaction noise and is often considered as the most important mechanism of broadband noise generation in fans and propellers.

1.1.2 Propeller Underwater Noise

Nowadays the underwater radiated noise of ships represents one of the most critical issues for naval engineers. For naval vessels the underwater radiated noise is part of the signature requirements with respect to threats. Moreover, high underwater noise levels may also affect fish behavior, therefore noise requirements for fishery research vessels are nowadays constraints to comply with. In addition, increasing concerns regard the adverse influence of underwater noise, including shipping noise, on marine wildlife.

As a matter of fact most of the acoustic field emitted by large vessels is the result of propeller cavitation, causing ships to radiate both low-frequency tonal sounds, which can be heard over great distance, and high-frequency noise (up to 20 kHz) close to the vessel. In the absence of cavitating phenomena the propellers still remain the most important noise sources for both directly radiated sound and as impinging noise source for hull scattering phenomena.

The main features of the marine propeller noise and the relative generation phenomena are presented in the following.

1.1.2.1 Non Cavitating Propeller Noise

Although the phenomena at the base of noise generation for the propeller are the same as in air, underwater propellers works in completely different operating conditions, thus altering the relative role played by each source of noise.

A marine propeller works on a fluid having density thousand times that of air and where the speed of sound is five time greater. As result for marine propellers the rotational Mach number can at most reach values of 10^{-2}, thus one or even two orders of magnitude lower than an aeronautical propellers or a helicopter rotors. In addition, the blades have a very compact planform compared, for example, with those of a helicopter rotor. They are usually characterized by a low aspect ratio, a remarkable twist and a notable variation of chord and thickness along the span [14].

Therefore, besides the noise due by fluctuating hydrodynamic forces generated on the propellers and to the time varying displacement of fluid by the blades volume as it rotates, considerable noise contribution can be ascribed to the flow field around and downstream the blades. As in the case of aeronautical propellers, the noise can be classified as discrete frequency (tonal), and continuous spectrum (broadband).

Discrete frequency content are caused by the action of a propeller operating in the presence of upstream non-uniform wakes. Such noise component correspond to the blade passage frequencies (BPF) (i.e. the number of blades multiplied by the shaft rotation rate) and generally do not exceed 20 Hz (first 3 harmonics) [26].

Continuous spectrum content are generated as a result of upstream flow disturbances or by turbulence generated on the blade surface. Of such component, low frequency contents are induced when the hull turbulent boundary layer generated over the vessel surface is ingested by the propeller, whereas high frequency broadband contents are caused by the interaction of the boundary layer formed on the blade surface the trailing edge. In addition, continuous noise contribution are also associated with persisting, both in space and time, vortical wakes departing from the tip and hub of the propeller which develop downstream and inevitably go through a breaking phase.

1.1.2.2 Cavitating Propeller Noise

The simplest description of noise propeller cavitation mechanisms can be achieved by the Rayleigh-Plesset equation [27] which explains the dynamic behaviour of a single bubble volume acceleration.

The equation has been extended and studied in much detail (see Ref. [28]), furthermore, the noise spectrum of the collapse of a single bubble has been described by Fitzpatrick (see Ref. [29]). Up to the point of collapse, the bubble dynamics are well predicted by using potential flow assumptions.

However, the dynamic of bubble collapse is very complicated, it involves different phenomena producing energy dissipation in sound radiation, heat conduction and viscosity. In addition, rebounds of the bubble occur in the presence of non-condensable gas.

The noise spectrum from a prototypical cavitating propeller shows typically a low frequency region in which tonal contribution are present at harmonics of the blade passage frequency. A broadband hump, whose center frequency is proportional to the reciprocal of the typical duration time of the large scale cavity dynamics, is also present. The high frequency region is determined by the collapse of individual bubbles and the spectrum decreases with the reciprocal of the frequency squared. As bubble collapse is cushioned by the presence of gas, the magnitude of the spectrum level in this region also decreases with increasing gas content. Additionally, the compressibility of the fluid influences the radiated noise in this region. The high frequency slope of the power spectral density generally decreases according to f^{-2} , where f represents the frequency domain, which corresponds to a decreases of 6 dB/octave [26].

1.2 Wind Turbine Noise

Among the many noise sources involved in the conversion of the wind in mechanical/electrical energy through wind turbines, i.e. gearbox, generator, yaw drives, cooling fans, auxiliary equipment and application of parking brake, the literature opinion recognizes the fluid dynamic generated noise as the most important one [30]. Therefore, it goes without saying that a punctual characterization of the flow field features over and past their large blades represents a crucial aspect for a fruitful detection of the acoustic noise sources. To this aim the literature know-how concerning the phenomena involved in the Aeroacoustics of *large* wind generators is here briefly outlined.

- *Trailing Edge Noise*
  Due to the air viscosity the flow passing over the blades gives rise to a thick boundary layer, which depending on the operating conditions may or not remain attached to the blade itself. Although in nominal operating conditions the flow over the blades should remain laminar, a transition to the turbulent state is unavoidable. For these configurations the noise effects of the turbulence (by its own) seems to be a weak radiator; however, its interaction with the trailing edge, i.e the effect of eddies passing over the sharp edge of the blade, give rise to intense broadband noise sources [13]. This is known as the *Trailing edge-boundary layer interaction noise* and represents the most important sound source for wind turbines. Such acoustic effect shows a cardioid directivity pattern in which the most of the sound is radiated forward of the blade in the direction of rotation, while little is radiated behind. The frequency range is generally considered to be bounded between 160-1500 Hz. This phenomena explains the "swish" character of wind turbine noise due to the amplitude modulation of broadband aerodynamic noise created by the blades at the blade passing frequency, which is usually about 1 Hz.
- *Leading edge interaction noise*
  The atmospheric turbulence (i.e. the presence of turbulent eddies) due to the ground

boundary layer and the perturbed inflow conditions interacts with the blades and generates unsteady lift. Such phenomena creates a dipole-like sound source located at the blade leading edge characterized by a dipole-like directivity. The peak energy for this type of noise is contained at a frequency under $10^2 Hz$.

- *Blade tower interaction*
  It is defined as the acoustic disturbance induced by the interaction of the rotor blades with the tower. In the early development of wind power, downwind turbines were common and produced high levels of noise associated with the interaction of the tower wake with the rotor blades. However, impulsive noise may be generated also by the interaction of the blades with the perturbed flow upstream of the tower for upwind turbines. The noise generation mechanism is associated with the blade-tower interaction (BTI) due to the rotor blades passage through the perturbed flow region induced by the pillar upstream. As result the angle of attack changes on the blades, causing a fluctuation in lift force. The "thumping sound" characteristic of wind turbine is often associated to the (BTI). It represent a narrowband noise source whose the most of energy in contained under $20Hz$. It is characterized by a dipole directivity pattern.
- *Blade Tip Noise*
  This noise source is associated with the trailed vorticity past the blade tip, generating an interaction with the edge of the blade similar to that occurring in the trailing edge noise. It is characterized by a cardioid directivity pattern.
- *Airfoil tonal noise*
  Discrete vortices form either the boundary layer or the wake and create intense tonal noise, with or without a self-reinforcing feedback loop. Tonal noise occurs at low-to-moderate Reynolds numbers (approximately 50,000 to 250,000), hence is not usually a problem for large wind turbines that operate at higher Reynolds numbers. Small wind turbines (<10 kW) may operate at conditions where tonal noise constitutes a major part of the noise source energy.

1.3 Helicopter Rotor Noise

Although the helicopter is the quietest Vertical Take-Off and Landing (VTOL) aircraft, sometimes its noise can still be high enough to compromise its utility unless specific attention is given in its design. The contribution to the helicopter rotor noise can be classified as *Rotational noise*, *Blade slap* and *Broadband noise*; hereafter a briefly description of such phenomena is given.

- *Rotational Noise*
  The rotational noise is a thumping sound at the blade passage frequency; as the higher harmonic content increases, the thumps sharpen into bangs. Such sound component is a purely periodic sound pressure radiated as result of the periodic forces exerted by the blade on the air at any point fixed on the rotor disk because of the rotation of lift and

drag with the blade. Its contribution dominate the low frequencies of the noise spectrum from below audible frequencies up to $150Hz$.

- *Blade Slap*
  Blad slap is a sharp, cracking, popping or slapping sound occurring at the blade passage frequency which can be considered an extreme case of rotational noise. When occurs it is the dominant noise source. The most likely source of blade slap are vortex-blade interaction (BVI), the effect of thickness at high Mach number, local stall condition and eventually shock waves. Such phenomena produce large, localized and transient forces over the blades which turn into impulsive noise radiation.
- *Broadband noise*
  Broadband noise is high frequency swishing sound produced by the rotor and modulated in amplitude and frequency at the BPF. It is mainly generated by random fluctuation of lift and drag on the blades due to operating conditions close to the turbulent wake. Besides, forces due to the vortex shedding at the trailing edge, turbulence in the free stream and boundary layer transition laminar-turbulent and separation phenomena are effective broadband noise sources. The resulting sound energy is spread over a portion of the spectrum in the audible range, typically extending from about $150Hz$ to $1000Hz$ with peaks around 300-400 Hz

1.4 Present Research

1.4.1 Motivation

The considerable know-how gained by aeroacousticians in 30 years of researches has highlighted how the FWHE is the most effective tool to carry out reliable noise predictions. Indeed, the linear (thickness and loading noise) application of the FWHE has proven to be effective and straightforward for the acoustic prediction of aeronautical configuration as helicopter, proprotors and propeller driven aircraft up to Mach number 0.8. In spite of this, some rotary wing configurations operating at low Mach number, both in air and water, seem to be acoustically dominated by the non linear noise sources.
Nowadays, the mature level of the modern CFD fluid dynamic predictions allow to well predict the non linear behaviour of the flow field near and downstream the rotor blades. To this aim, the use of low dissipative numerical schemes and turbulence models based on the turbulent viscosity technique, such as LES and DES, allow an effective noise source detection.
The capability to take into account these acoustic effects is nowadays of major importance for the aeronautical and marine industry, since the acoustic signature has to comply with international standards related to environmental issues, comfort onboard, detectability etc..
In view of these considerations, this thesis deals with the study of the permeable Acoustic Analogy-based formulations for moving bodies, as they allow to include the nonlinear contributions in the calculations avoiding the computational burden related to the evaluation of the volume integral.

1.4.2 Objective

The goal of this thesis is to get an insight into the capabilities, reliability and limits concerning the permeable approach of the Acoustic Analogy-based formulations; the attention is limited to the prediction of noise emitted by rotary wing devices, characterized by considerable flow field noise sources.
In detail, the objectives are:

- General assessment and validation of the permeable formulation of the FWHE. Particularly, the following aspects of the permeable approach of FHWE are investigated:
  i) The location of the porous surface with respect to the noise sources, including the analysis of the effects on the predicted acoustic pressure of noise sources outside it.
  ii) The effects of the observers position with respect to the porous surface on the acoustic prediction, including the case of observers inside it.
  iii) The effect of spurious noise generation due to eddies convected through the porous surface (namely the *End Cap* issue [31]).
- Proposal of a new formulation that includes a different expression of surface and volume terms with respect to the FWH Equation, namely Hybrid Lighthill-Ffowcs Williams and Hawkings Equation for Moving Surfaces (H-FWHE).
- Proposal of a new formulation that extends the porous approach to the presence of surfaces of discontinuity external with respect to it (i.e. shock waves and thin layers of vorticity). In addition, the characterization of this model for a contact discontinuity allows to obtain a combined FWHE/H-FWHE formulation, capable of including acoustic effects of potential wakes released by lifting bodies only partially embedded by to the FWHE porous surface.
- Application of the permeable approach of FWHE and the H-FWHE to configurations of industrial interest characterized by high turbulence an vorticity phenomena (marine propellers and wind turbines) to shed light on their relative role in the sound generation mechanisms.
- Assessment of the capabilities of the potential flows theory to detect the noise sources inherently associated to blades and vorticity convected downstream of marine propellers compared to DES simulations.
- Assessment of the combined FWHE/H-FWHE capabilities to take into account the acoustic effects of a potential wake released by a slender rotating blade.

1.4.3 Overview of discussion

The dissertation is organized as follows: Chapter 2 illustrates the details of the aero/hydrodynamic approaches inhere used to detect the noise sources. Chapter 3 is focused on the theoretical aero/hydro-acoustic formulation used throughout the thesis. Chapter 4 proposes a novel approach to account with the acoustic effects of discontinuity surfaces (as shock waves, potential wakes etc...) in the framework of the rotating blade devices. Chapter 5 Numerical results of the above mentioned acoustic approaches are presented for the noise prediction of

rotary wing devices. Finally, conclusions and recommendations for future works are given in chapter 6.

Chapter 2

Approaches for Rotating Blade Noise Prediction

2.1 Introduction

This chapter presents an overview on the fluid dynamic approaches, used throughout the thesis to characterize the aero/hydro-dynamic sources of sound involved in low Mach number rotating blades devices. To this aim some recent investigations, above all [14], on the role of volume terms in the hydroacoustic behaviour of marine propellers (in open water condition or complete scaled ship model in steady course) play a crucial role. Specifically, those papers show that the acoustic contribution from the *linear* noise sources, i.e. those related to the motion, shape and pressure over the body, also known in literature as *thickness* and *loading noise*, seem to be circumscribed to a very limited spatially region. Indeed, moving far from the emitting body, pressure fluctuations rapidly reduce, appearing substantially related to *nonlinear* sources of sound, such as vorticity and turbulence, regardless of the blade rotational speed. On the other hand, the notable know-how gained through 30 years of research activities on Aeroacoustics prove that, in air, the noise of propellers and rotors up to tip Mach number approximately equal to 0.8 is dominated by the *thickness* and *loading* noise, thus restricting the effects of the *nonlinear* contributions only to local shock waves due to transonic phenomena [5]. Even though these outcomes are nowadays widely accepted, particularly operating conditions encountered by low rotational Mach number devices operating in air, as wind turbines, represent an exception. In particular, their blades can experience large changes in angle of attack associated with sudden large gusts, changes in wind direction, or interaction with the unsteady wake shed from the tower support on downwind. These blade/inflow/tower wake interactions can result in dynamic stall over wide portions of the rotating blade. In addition, their aerodynamic behaviour is strongly influenced by non homogeneous inflow conditions associated to atmospheric turbulence and to the ground boundary layer. All the above mentioned phenomena generate an high non linear flow field around the blades whose acoustic contribution may be comparable or even greater than the linear thickness and loading noise [13].

Based on spectral character, flow noise sources are grouped into one of two classes as broadband or narrowband [17]. Narrowband sources entail flow shedding excitation of a structural resonance resulting in strong tonal character which occurs at specific Strouhal

numbers. Broadband sources are ones for which there is no frequency selectivity for either the excitation (flow) or the structural response. As a matter of fact, a complete (i.e. broadband) noise characterization may be achieved only through some fluid dynamic analysis for turbulent flows based on Computational Fluid Dynamics (CFD) simulations, as Unsteady Reynolds Averaged Navier Stokes equations (URANS), Large Eddy Simulation (LES) or hybrid approaches, which are able to provide a description of the flow field, in terms of vorticity and turbulence levels. However, for noise predictions purposes, LES or hybrid RANS LES methods can capture more detailed vortex and turbulent structures than URANSE approaches, which have inherently higher dissipative effects [21, 32]. Differently, LES and hybrid methods provide reasonable results, especially in terms of broadband noise predictions [33, 34]. The tonal noise from non cavitating propellers can be predicted either by using the potential flow assumption or by solving the full set of viscous flow equations (Navier Stokes equations) by means of CFD. The lifting surface and Boundary Element Method (BEM) can be used to solve the tonal noise with the potential flow assumption, for abs [35]. In the present work the evaluation of the acoustic pressure concerns marine propellers free from cavitation and wind turbines; for both configurations a two step strategy is used to predict the radiated noise. First the sources of sound are detected by a devoted fluid dynamic analysis of the devices; then, acoustic propagation modeling, accounting for the main noise generating mechanisms, are applied to radiate the sound waves "far" from the sources.

The theoretical aspects of the aero/hydro-dynamic formulations herein used to characterize the sources of sound are briefly outlined in the following. Specifically:

- A three dimensional unsteady potential-based approach for compressible and inviscid flows combined with the Bernoulli Equation;
- A general purpose Computational Fluid Dynamic approach for incompressible flows;

Beside them, some closed-form solution of the wave equation, carried out within the contest of compressible potential flow, are derived. Their use is limited to validation purposes, only.

2.2 The Bernoulli Equation–based Approach

The prediction of the flow field features generated by moving bodies may be achieved through a potential-flow based formulation. The suitability of such model is limited to high Reynolds number flows ($Re \geq 10^6$) around thin bodies for which separation phenomena are confined over restricted areas and the influence of viscous effects is negligible. Note that, at frequencies of most practical interest, viscous effects are negligible on acoustic predictions [36]. Under the assumption of subsonic, compressible, potential flows, the aero/hydrodynamic problem around a lifting bodies, in terms of velocity potential, is solved by the formulation introduced by Morino and Gennaretti [37], whereas the further application of the Bernoulli Equation provides the pressure disturbance in the flow domain around it. Specifically the solution of a inhomogeneous wave equation for the velocity potential by the Green function technique [38] yields an integral solution that is used, first, as integral equation to evaluate the potential distribution upon the body surface and in the volume around it where

non-linear terms are not negligible, and then as integral representation to predict the potential distribution everywhere in the flow field. The main theoretical aspects are outlined in the following. Some details are found in Appendix D.2.

2.2.1 Differential Equation for Velocity Potential

The potential flow theory is based on the hypothesis that an inviscid, nonconducting, shock-free, initially isentropic and non-rotational fluid at rest, remains isentropic and non-rotational at all times (except for wake points). Under these assumptions, the flow field velocity may be expressed in terms of a scalar potential ϕ, as $\mathbf{u} = \nabla\phi$. For such kind of fluid it may be shown (see, Ref. [37]) that in a frame of reference connected to the undisturbed medium, the velocity potential is governed by the following differential equation

$$\nabla^2\phi - \frac{1}{c_0^2}\frac{\partial^2\phi}{\partial t^2} = \sigma \tag{2.1}$$

where σ accounts for all the non–linear terms (in aerodynamic applications they are important in the transonic regime) and c_0 indicates the speed of sound in the medium at rest. The differential problem is closed by suitable boundary conditions. Three surfaces are considered as boundary of the field: i) the surface at infinity, ii) the body, iii) the potential wake. In the air frame of reference, at infinite distance from the body, the perturbation velocity is zero, hence $\mathbf{u} = 0$, *i.e.*, $\phi = 0$. Assuming the body surface $\mathcal{S}$ as impermeable, it results $\partial\phi/\partial n = \mathbf{v}\cdot\mathbf{n}$ where $\mathbf{v}$ is the local velocity of a point on the body surface and $\mathbf{n}$ the local outward unit normal vector. The hypothesis of non-rotational flow fails for those points that, in their motion, have been in touch with the body surface, for which the theorem of Kelvin can not be applied. These points form a discontinuity surface $\mathcal{S}_W$ (namely potential wake) that cannot be crossed by fluid particles and across which the pressure behaves as a continuous function. The above condition can be expressed in terms of velocity potential as follows (see appendix D.2.)

$$\Delta\left(\frac{\partial\phi}{\partial n}\right) = 0 \tag{2.2}$$

$$\frac{D_W(\Delta\phi)}{Dt} = 0 \tag{2.3}$$

where $\dfrac{D_W}{Dt} = \dfrac{\partial}{\partial t} + \mathbf{u}_W\cdot\nabla$ is the substantial derivative made following a point belonging to the wake. Here, $\mathbf{u}_W$ is the wake particle velocity, defined by the average of the velocities corresponding to two particles at two sides of the wake. Equation (2.3) represents the evolution equation for $\Delta\phi$ stating that it is constant in time following a wake point. Thus, the actual value of $\Delta\phi$ following a point $\mathbf{x}_w$ remains constant and equal to that it had when it left the trailing edge. At the trailing edge the Kutta condition states that no concentrated vortices exist [39] so that $\Delta\phi$ on the wake and on the body coincides at the trailing edge.

In terms of potential jump, one obtains

$$\lim_{\mathbf{x}_W \to \mathbf{x}_{TE}} \Delta\phi(\mathbf{x}_W, t) = \phi_u(t) - \phi_l(t) \tag{2.4}$$

and

$$\Delta\phi(\mathbf{x}_W, t) = \Delta\phi(\mathbf{x}_{TE}, t - \tau_w) \tag{2.5}$$

where ϕ_u and ϕ_l are the potential at the upper and lower side of the wake respectively, $\mathbf{x}_{TE}$ denotes a wake point located at the trailing edge whereas τ_w is the convection time between $\mathbf{x}_W$ and $\mathbf{x}_{TE}$.

2.2.2 Integral Solution

In order to solve the potential problem defined by Eq. (2.1) it is convenient to recast it into the following equivalent infinite–space differential equation (see appendix D.2)

$$\begin{aligned} -\Box^2\hat{\phi} &= \sigma\, H(f) + \nabla\phi\cdot\mathbf{n}\,\delta(f) + \nabla\cdot[\phi\,\mathbf{n}\,\delta(f)] + \\ &- \frac{1}{c_0^2}\{-\dot{\phi}\,\mathbf{v}\cdot\mathbf{n}\,\delta(f) + [-\phi\,\mathbf{v}\cdot\mathbf{n}\,\delta(f)]^{\cdot}\} \quad \forall\mathbf{x}\in\Re^3 \end{aligned} \tag{2.6}$$

where $\hat{\phi}(\mathbf{x},t) = H(f)\phi(\mathbf{x},t)$, $\sigma = [(c^2 - c_0^2)\nabla^2\phi + 2\mathbf{u}\cdot\dot{\mathbf{u}} + \mathbf{u}\cdot\dfrac{\nabla u^2}{2}]/c^2$, c represents the local speed of sound in the perturbed flow, $f(\mathbf{x},t) = 0$ indicates the shape of the body and $\delta(f)$ and $H(f)$ are the Dirac and Heaviside functions, respectively. The application of the Green function method to Eq.(2.6), (see Appendix A.2) yields the following boundary field integral representation for the potential ϕ in a frame of reference fixed to the body

$$\begin{aligned} \phi(\mathbf{x},t) &= \int_V \hat{G}\,[\sigma]_\theta\,\mathrm{d}V + \int_S \left[\frac{\partial\phi}{\partial\tilde{n}}\hat{G} - \phi\frac{\partial\hat{G}}{\partial\tilde{n}}\right]_\theta \mathrm{d}S + \\ &+ \int_S \left[\hat{G}\frac{\partial\phi}{\partial t}\left(\frac{\partial\vartheta}{\partial\tilde{n}} + 2\frac{\mathbf{v}\cdot\mathbf{n}}{c_0^2}\right)\right]_\theta \mathrm{d}S \\ &+ \frac{1}{c_0^2}\int_S \left[\phi\,\hat{G}\frac{\partial}{\partial t}[\mathbf{v}\cdot\mathbf{n}\,(1-\mathbf{v}\cdot\nabla\vartheta)]\right]_\theta \mathrm{d}S \end{aligned} \tag{2.7}$$

where suffix θ indicates that all kernels have to be computed at the retarded (emission) time $\tau = t - \vartheta$, with ϑ denoting the compressibility delay, that is, the time required by the acoustic disturbance released from a source point $\mathbf{y} = \mathbf{y}(\tau)$ to reach the observer at point $\mathbf{x} = \mathbf{x}(t)$. Moreover $\hat{G} = \{-(1/4\pi\, r)\,[1/(1 - M_r)]\}_\theta$ indicates the retarded Green function, in which $\mathbf{r} = \mathbf{x}(t) - \mathbf{y}(\tau)$, $r = |\mathbf{r}|$ and $M_r = \mathbf{v}/c_0\cdot\hat{\mathbf{r}}$ with $\hat{\mathbf{r}} = \mathbf{r}/|\mathbf{r}|$. In addition $\partial/\partial\tilde{n} = \partial/\partial n - 1/c_0^2\,(\mathbf{v}\cdot\mathbf{n})\,(\mathbf{v}\cdot\nabla)$. For bodies without wake (non-lifting), Eq. (2.7) is an integral representation of ϕ anywhere in the field, in terms of the values of ϕ, $\partial\phi/\partial\tilde{n}$ and $\partial\phi/\partial t$ on $\mathcal{S}$, and of σ in $\mathcal{V}$. The extension of the formulation to lifting bodies requires to account for the presence of the potential wake surface; in the following, propellers are considered as lifting bodies. In this case, let us consider the presence of N disjoint, closed rigid surfaces S_i and S_i^W surrounding, respectively, the volume occupied by the i-th propeller

blade and the volume occupied by a thin fluid region containing the corresponding i-th wake surface. It may be shown [40] that the integral representation for the solution of Eq. (2.1), neglecting the nonlinear terms σ, has the form

$$\phi(\mathbf{x},t) = \sum_{i}^{N} \left(\mathcal{I}_i^S + \mathcal{I}_i^W \right) \tag{2.8}$$

Each integral contribution appearing in Eq. (2.8) may be evaluated in a different frame of reference. In the case of rigid surfaces, the most suitable frame of reference is attached to the surface (*i.e.,* the frame where the integration domain does not depend on time). In this frame, the most general expression for the blade surface contributions $\mathcal{I}_i^S$ is given by Eq. (2.7). Under the assumption of a prescribed, non–deforming wake shape and propellers in axial flow, it is convenient to use a propeller-fixed frame of reference to evaluate both blade and wake contributions to the velocity potential field.[1] A more reliable propeller aerodynamic modeling requires S_w to be considered as an *unknown* of the problem since its shape is related to the vorticity generated onto the propeller and shed into the field. Therefore, S_w, not-known *a priori* , makes the stated problem intrinsically nonlinear. To this aim, a free-wake algorithm is used to align wake points to the local flow, that is, moving them under the effect of the advancing speed and local fluid velocities due to propeller blades and wakes [35]. A general description of S_w is conveniently achievable in a non-rotating frame of reference centered at propeller hub and aligned with the advancing speed.[2]. The wake contribution $\mathcal{I}_W$ may be obtained by coupling Eq. (2.7) with the wake boundary conditions, yielding

$$\mathcal{I}_W(\mathbf{x},t) = -\int_{S_W} \left[\Delta\phi \, \frac{\partial \hat{G}}{\partial \tilde{n}} \right]_{\vartheta} \mathrm{d}S \tag{2.9}$$

For those problems where σ is negligible, positioning point $\mathbf{y}$ on the body surface provides a *boundary integral equation* for ϕ from Eq. (2.8). This step enables the evaluation of the velocity potential on the integration domain itself. Once ϕ is known on S, the same equation appears as an *integral representation* of the potential and can be used to determine such a variable at any point in the field. At this stage the pressure p can be determined through the Bernoulli theorem (written for compressible, isentropic flows)

$$\frac{\partial \phi}{\partial t} + \frac{1}{2}|\mathbf{u}|^2 + \frac{\kappa}{\hat{\gamma}} p^{\hat{\gamma}} = \frac{1}{\hat{\gamma}} \frac{p_0}{\rho_0} \qquad \text{where:} \qquad \hat{\gamma} = \frac{\gamma - 1}{\gamma} \quad ; \quad \kappa = \frac{p_0^{1/\gamma}}{\rho_0} \tag{2.10}$$

where γ denotes the specific heat ratio, ρ_0 and p_0 are respectively the density and pressure of the medium at rest.

[1] The same arguments are valid for a helicopter rotors in hovering. In forward flight conditions, the formulation is more complicated because in the body space the wake surface is not time independent. However, in this case, the wake may be assumed to be time independent in the air space.

[2] The same arguments are valid for a helicopter rotors in forward flight

2.2.3 Low Mach Number Applications

Under the assumption of low rotational Mach number, the d'Alembert operator (wave operator) can be approximate by the Laplacian, recasting Eq. (2.7) into

$$\phi(\mathbf{x},t) = \int_S \left(\frac{\partial \phi}{\partial n}G - \phi\frac{\partial G}{\partial n}\right)\mathrm{d}S - \int_{S_W} \Delta\phi\,\frac{\partial G}{\partial n}\mathrm{d}S \tag{2.11}$$

where $G = -1/4\pi r$, whilst the following expression of the Bernoulli equation holds

$$\frac{\partial \phi}{\partial t} + \frac{1}{2}|\mathbf{u}|^2 + \frac{p}{\rho_0} = \frac{p_0}{\rho_0} \tag{2.12}$$

Such approximation is reasonable for the evaluation of the air/hydro-loads as well as for the prediction of near flow field features. Moreover, although the incompressibility assumption does not comply with any sound definition, the pressure disturbance carry out by Eq.(2.12) yields a good approximation of the *noise* signature up to few diameter from the rotor hub [23, 41].

2.3 Computation Fluid Dynamic solutions

Nowadays the computational resources available for the High Performance Computing (HPC) applications guarantee a profitably solution of the Navier Stokes Equations through the use of numerical schemes. The high quality of the flow field predicted by Computational Fluid Dynamics (CFD) allows to *detect* the noise sources generated by vorticity and turbulence downstream the rotor as well as by the presence of large zones of detached flow. Nevertheless, the capability to solve the time-space scale of the turbulence with a Direct Numerical Simulation (DNS) is currently unapproachable for the high Reynolds number involved in problems of practical interest. This condition forces to adopt a numerical scheme to *model* turbulence phenomena under a given characteristic spatial size through the addition of a turbulent viscosity in the governing equations. The choice of the turbulence model, may be very complex because it considerably affects the resulting flow field features and then the suitability of the aero/hydro-dynamic solution for aero/hydro-acoustic purposes. In the following a brief overview on the theoretical-numerical approaches used to solve the Navier Stokes Equations is presented. An extensive description is reported in Appendix D.1.

2.3.1 Theoretical and Numerical Model

The governing equations for the unsteady motion of an incompressible viscous fluid are briefly recalled in this section. The equations are written in an inertial frame of reference; as some blocks on the total grid move to follow possible moving boundaries, the general form of the governing equations are written with respect to a moving control volume. The continuity and momentum equation in non–dimensional integral form (with respect to a reference

velocity $\mathbf{u}_\infty$ and a reference length L) are

$$\begin{aligned} \oint_{S(\mathcal{V})} \mathbf{u}\cdot\mathbf{n}\,\mathrm{d}S &= 0 \\ \frac{\partial}{\partial t}\int_{\mathcal{V}} \mathbf{u}\,\mathrm{d}v + \oint_{S(\mathcal{V})} (\mathcal{F}_c - \mathcal{F}_d)\cdot\mathbf{n}\,\mathrm{d}S &= 0 \end{aligned} \tag{2.13}$$

$\mathcal{V}$ being a control volume, $S(\mathcal{V})$ its boundary, and $\mathbf{n}$ the outward unit normal. In equation (2.13), $\mathbf{u}$ is the flow velocity vector whereas $\mathcal{F}_c$ and $\mathcal{F}_d$ represent convective (inviscid and pressure components) and diffusive fluxes, respectively:

$$\begin{aligned} \mathcal{F}_c &= p\mathbf{I} + (\mathbf{u}-\mathbf{v})\,\mathbf{u} \\ \mathcal{F}_d &= \left(\frac{1}{Re} + \nu_t\right)\left[\nabla\mathbf{u} + (\nabla\mathbf{u})^{\mathrm{T}}\right] \end{aligned} \tag{2.14}$$

where $\mathbf{v}$ is the local velocity of the control volume boundary, $Re = U_\infty L/\nu$ the Reynolds number, ν the kinematic viscosity, whereas ν_t denotes the non–dimensional turbulent viscosity. In the following equations, u_i indicates the i–th Cartesian component of the velocity vector (the Cartesian components of the velocity will be also denoted with u, v, and w); p is a variable related to the pressure P and the acceleration of gravity g (parallel to the vertical axis z, downward oriented) by $p = P + z/Fr^2$, $Fr = U_\infty/\sqrt{gL}$ being the Froude number.

The problem in Eq. (2.13) is closed by enforcing appropriate conditions at physical and computational boundaries. On solid walls, the relative velocity is set to zero (whereas no condition on the pressure is required); at the (fictitious) inflow boundary, velocity is set to the undisturbed flow value, and the pressure is extrapolated from inside; on the contrary, the pressure is set to zero at the outflow, whereas velocity is extrapolated from inner points.

At the free surface, whose location is one of the unknowns of the problem, the dynamic boundary condition requires continuity of stresses across the surface; if the presence of the air is neglected, the dynamic boundary conditions (see Appendix D.1 for theoretical details) reads:

$$\begin{aligned} p &= \tau_{ij} n_i n_j + \frac{z}{Fr^2} + \frac{\kappa}{We^2} \\ \tau_{ij} n_i t^1_j &= 0 \\ \tau_{ij} n_i t^2_j &= 0 \end{aligned} \tag{2.15}$$

where τ_{ij} is the stress tensor, κ is the average curvature, $We = \sqrt{\rho U_\infty^2 L/\sigma}$ is the Weber number (σ being the surface tension coefficient), whereas $\mathbf{n}$, $\mathbf{t^1}$ and $\mathbf{t^2}$ are the surface normal and two tangential unit vectors, respectively. The actual position of the free surface $F(x,y,z,t) = 0$ is computed by enforcing the kinematic condition

$$\frac{\mathrm{D}\,F(x,y,z,t)}{\mathrm{D}\,t} = 0\,. \tag{2.16}$$

Initial conditions have to be specified respectively for the velocity field and the free surface configuration; specifically we set

$$\begin{aligned} u_i(x,y,z,0) &= \bar{u}_i(x,y,z) \\ F(x,y,z,0) &= \bar{F}(x,y,z). \end{aligned} \tag{2.17}$$

A fully coupled implicit finite volume formulation is used to solve numerically the Navier-Stokes equations. To this aim, at each (discrete) time instant t^n the physical time derivatives are discretized by a backward second order finite difference, and the spatial operator (residual) is computed at the same time level; in semi-discrete form, the equations reads

$$\begin{aligned} &\oint_{S(\mathcal{V})} u_i^n n_i \, \mathrm{d}S = 0 \qquad (i = 1,2,3) \\ &\int_{\mathcal{V}} \frac{3u_i^n - 4u_i^{n-1} + u_i^{n-2}}{2\Delta t} \, \mathrm{d}V + \mathcal{O}(\Delta t^2) \\ &+ \oint_{S(\mathcal{V})} \left[u_i^n \left(u_j^n - v_j^n \right) n_j + p^n n_i - \tau_{ij}^n n_j \right] \mathrm{d}S = 0 \,. \end{aligned} \tag{2.18}$$

The dual time stepping approach (see, e.g., [42], that generalizes the pseudo-compressibility method [43] to unsteady problems), is used to solve the fully coupled Navier-Stokes Equations. In this technique, the numerical solution of (2.18) is computed as the asymptotic solution of an auxiliary unsteady problems in a pseudo-time τ

$$\begin{aligned} &\int_{\mathcal{V}} \frac{\partial p^n}{\partial \tau} \, \mathrm{d}V + \oint_{S(\mathcal{V})} u_i^n n_i \, \mathrm{d}S = 0 \\ &\int_{\mathcal{V}} \frac{\partial u_i^n}{\partial \tau} \, \mathrm{d}V + \int_{\mathcal{V}} \frac{3u_i^n - 4u_i^{n-1} + u_i^{n-2}}{2\Delta t} \, \mathrm{d}V + \\ &\oint_{S(\mathcal{V})} \left[u_i^n \left(u_j^n - v_j^n \right) n_j + p^n n_i - \tau_{ij}^n n_j \right] \mathrm{d}S = 0 \,. \end{aligned} \tag{2.19}$$

In the above equations, the solution at time t^{n-1} and t^{n-2} that appears in the physical time derivative acts as a known source term, whereas the solution at time t^n produces a stabilizing effects, which grows when dt decreases. This system of equations (that includes an evolution equation for the pressure) is hyperbolic in the pseudo-time τ for its Eulerian part; therefore, all the numerical methods developed for compressible flow simulation can be adapted and applied to the above system. In the numerical scheme here adopted, all the spatial operators are approximated by a finite volume technique, with pressure and velocity determined at the cell center. The computational domain is discretized by partially overlapping structured blocks. Each block is split into $N_i \times N_j \times N_k$ hexahedral cells and on each control volume

the above equation can be specialized into

$$\begin{aligned}
&\int_{\mathcal{V}_{ijk}} \frac{\partial p}{\partial \tau}\, \mathrm{d}V + \sum_{s=1}^{6} \oint_{S_s(\mathcal{V}_{ijk})} u_i^n n_i\, \mathrm{d}S = 0 \\
&\int_{\mathcal{V}_{ijk}} \frac{\partial u_i^n}{\partial \tau}\, \mathrm{d}V + \int_{\mathcal{V}_{ijk}} \frac{3u_i^n - 4u_i^{n-1} + u_i^{n-2}}{2\Delta t}\, \mathrm{d}V + \\
&\sum_{s=1}^{6} \oint_{S_s(\mathcal{V}_{ijk})} \left[u_i^n \left(u_j^n - v_j^n \right) n_j + p^n n_i - \tau_{ij}^n n_j \right] \mathrm{d}S = 0\,,
\end{aligned} \tag{2.20}$$

where $S_s(\mathcal{V}_{ijk})$, $s = 1, ..., 6.$ are the six faces of the hexahedron $\mathcal{V}_{ijk}$. Both the volume and the surface integrals are evaluated in Eqs. (2.20) by means of a second order Gauss formula (i.e., as the product of the function in the center times the measure of the integration domain). For any further detail concerning the computation of the different fluxes see [44, 45]. Finally, the system (2.20) is discretized with an implicit Euler scheme with respect to τ and it is solved by the approximate factorization technique introduced by Beam and Warming [46]. Convergence is accelerated by local time stepping and a full-multigrid technique [47].

Although the above equations are able, in principle, to carry out a Direct Numerical Simulation (DNS), applications of engineering interest are computationally too demanding for presently available resources. Therefore, the effect of turbulence phenomena are *modeled* through numerical techniques based on the turbulent viscosity. Specifically, to evaluate it different approaches are available: i) Reynolds Averaged Navier Stokes Equations (RANSE) with one-equation Spalart and Alamaras [48] closure model ii) Large Eddy Simulation (LES) with Smagorisky [49] closure model iii) a suitable combination of both model (RANS/LES) namely Detached Eddy Simulation (DES) which allows, through a transition criteria, to swap between the Spalart-Alamaras (RANSE) in the boundary layer and the Smagorisky (LES) in the flow field [50].

2.3.2 Dynamic Overset Grid

In order to handle complex geometries and bodies in relative motion, the discretization of the computational domain is performed by a *chimera-type* approach, i.e., by a set of structured blocks with partial overlap. The details of the numerical algorithm are given in [51, 52], and only the main characteristics are briefly recalled here. In this technique, the computational domain is split into $l = 1, N_{blocks}$ subdomains, each being handled as a structured domain consisting of $N_i \times N_j \times N_k$ cells. In some regions of the computational domain these blocks are allowed to overlap partially. The motivation for using this type of discretization lies in the ease of use when handling bodies with a complex boundary, because each piece of the body can be discretized on its own right. Moreover, the temporal change of the computational domain, that takes place as a consequence of a variation of the frontier (for a rotating propeller or a moving rudder, for instance), can be dealt with very easily by enforcing a rigid motion of each group of structured blocks that are attached to a particular piece of the boundary itself. Consequently, the lack of strict constraints when generating the mesh (because of the allowed overlapping) and the lack of grid deformation during the motion (rigid

motion) enable to control grid quality very easily. Of course, the connection between blocks at each simple connection like in standard multi-block approach where the block faces are all abutting. Moreover, the overlapping regions must be located, so that the solution can be transferred between blocks as explained in the following. The technique used in the code to compute grid topology can be summarized as follows:

1. For each cell center of the ghost cells on any block boundary, on which no simple (wall, inflow, outflow, etc.) boundary condition is specified, all possible donor cells from other blocks are sought. Then, of all possible donors, the centroid of the smaller cell is chosen as the basic point of a convex set, consisting of eight points and containing the cell center under analysis, used for tri-linear interpolation.
2. For each inner cell, a global check is done to find all the possible cells, belonging to other blocks, within which it lies. Of all the possible cells containing the point under inspection, the smaller one is picked out as donor only if it is smaller than the current cell. By doing so, only the smallest cell of all the possible overlapping grid remains active. Once the donor is selected, a convex set of eight points for tri-linear interpolation is chosen as done for boundary points.

In order to speed up topology computation, a nested search that exploits the multigrid structure of each block is used. With this method, for each cell center the search for a possible donor starts on the coarsest possible grid that can be extracted from the global grid; on this very coarse level (and only for it) all the points are checked, in order to prevent the algorithm from stagnating for nonconvex block shapes; among all points, the closest one is then chosen. Then, when passing to the next finer grid level, the previously identified point is chosen as a first approximation for a search of the closest point along each coordinate line. The process is repeated on each finer grid level, up to the actual grid. This algorithm is very fast and convenient, especially when dealing with unsteady problems, where the grid topology has to be recomputed at each time step; of course, in this case, the donors are sought only for those cells whose donors come from a block in relative motion. Nevertheless, the overlapping test for internal point must be executed for all grid points. A particular care must be devoted to donor search in the boundary layer, where the aspect ratio of the cells can be extremely high. For this cell, the search must be made in a transformed computational space, where one of the coordinate planes coincides with the wall itself. Once the donors are known, the solution between blocks is transferred with an interpolation at block boundaries. On the contrary, a nonstandard procedure is used for internal points. In fact, for the cells marked as *holes* by the donor search algorithm, the solution of the RANS equations is performed anyhow, through the summation of a forcing term in the form

$$\begin{aligned} &RSH_{u_i}(2.20) + \frac{k}{\delta}\,(u_i - \bar{u}_i) = 0 \qquad (i = 1,2,3) \\ &RSH_{p}(2.20) + \frac{k}{\delta}\,(p - \bar{p}) = 0\,, \end{aligned} \tag{2.21}$$

where RHS is the right-hand side of Eqs.(2.20), k is a constant parameter of $\mathcal{O}(10)$, δ is the minimum among grid size along the coordinate lines and the time step, i.e., $\delta\, min(d_\xi, d_\eta, d_\zeta)$; $\bar{u}_i$ and $\bar{p}$ are the values of velocity and pressure interpolated from the donor cells. The effect of the forcing term is to drive the solution toward the interpolated value with an exponential decay in the pseudo-time. The advantage in using formulation Eqs. (2.21) is twofold. First, it allows maintaining the structured organization of data on each block, and therefore the multigrid algorithm for convergence acceleration can be used in its standard formulation. Second, by enforcing a value of the solution also on the overlapped regions, the solution is made available at each time step also for the points that became *active* in consequence of the block motion: for these points, the solution at previous time steps must be known for the computation of the physical time derivative (that, otherwise, should be evaluated with some different procedure).

2.4 Analytical Singular Solutions

In this subsection the flow field features derived by some singular solutions of the wave equation are outlined by the application of the velocity potential theory for compressible flows. Specifically, the potential flow-based solutions induced by monopoles and potential vortices is presented and used throughout the thesis to address case-studies and validation results. Details on the mathematical aspects are found in Appendix B.1.

2.4.1 Monopole

The physical interpretation of a *monopole* may be that of a small sphere, pulsating at a given frequency, having a radius smaller than the characteristic wave-length of the induced pressure field. Under this assumption, let the sphere be a source of mass, pulsating at an angular frequency ω_p in a fluid at rest, moving, throughout it, at velocity $\mathbf{v}$ in arbitrary steady motion with respect to a frame of reference fixed to the undisturbed fluid. Within the framework of potential compressible flows the disturbance velocity potential generated by the monopole is governed by

$$-\Box^2\phi \quad = \quad \sin(\omega_p\tau)\delta(\mathbf{x}-\mathbf{x}^*,\tau-t) \tag{2.22}$$

where $\Box^2$ is the D'Alambertian operator, $\mathbf{x}$ and $\mathbf{x}^*$ identify source and receiver positions in a frame of reference connected with the undisturbed fluid, respectively, whilst t denotes the *current* time at which the disturbance generated in $\mathbf{x}$ at time τ is received. Following Appendix B.1, the application of the Green function technique yields

$$\phi(\mathbf{x}^*,t) = \hat{G}\sin\left[k\left(c_0 t-\hat{\vartheta}\right)\right] \tag{2.23}$$

where $k=\omega_p/c_0$ is the wave number and

$$\hat{G} = -\frac{1}{4\pi r\mid(1+M_r)\mid}\bigg|_\theta \tag{2.24}$$

is the (retarded) Green function with $\mathbf{r} = \mathbf{x}(\tau) - \mathbf{x}^*(t)$, $r = |\mathbf{r}|$ and $M_r = (\mathbf{v}/c_0) \cdot \hat{\mathbf{r}}$ where $\hat{\mathbf{r}} = \mathbf{r}/|\mathbf{r}|$. The linearized Bernoulli equation for compressible unsteady isentropic flows yields the acoustic pressure everywhere in the field; by assuming the observer undergoing an arbitrary steady motion with velocity $\mathbf{v}_{obs}$ it reads

$$\frac{p'}{\rho_0} = -\left.\frac{\partial \phi}{\partial t}\right|_b + \mathbf{v}_{obs} \cdot \nabla_* \phi - \frac{\nabla_* \phi \cdot \nabla_* \phi}{2} \tag{2.25}$$

where the subscript $*$ indicates that the gradient operator is calculated with respect to the observer position and $|_b$ states that the time derivative is computed following it. In Appendix B.1 Eq. (2.25) is detailed for translating and rototranslating observers. The above formulation is general, in that it holds for any steady motion of the source and observer; nevertheless, an equivalent approach yielding the pressure disturbance from translating monopoles is also shown in Appendix B.2.

2.4.2 Potential Vortices

The flow field velocity and pressure disturbances generated by a potential vortex translating along a given direction, while spinning about it, are predicted under the assumption of incompressible, inviscid, non-rotational flows. Within this framework, the velocity induced at a point $\mathbf{x}^*$ by a curved vortex filament $\mathbf{dl}$ of strength Γ (taken about any path enclosing the filament), is given by the Biot-Savart law

$$\mathbf{u}(\mathbf{x}^*) = \frac{\Gamma}{4\pi} \int_l \frac{\mathbf{dl} \times \mathbf{r}}{|\mathbf{r}|^3} \tag{2.26}$$

where $\mathbf{r} = \mathbf{x} - \mathbf{x}^*$ identifies the radius vector from $\mathbf{dl}$ to $\mathbf{x}^*$. Akin to section 2.4.1, the pressure disturbance is evaluated by the Bernoulli Equation. Referring to Eq. (2.25), the first term at the right-hand-side is zero for observers rigidly connected to the rototranslating vortex. Thus, the application of Eq. (2.25) is straightforward. Differently, for observers translating with the vortex ring at the same velocity, Eq. (2.25) is not more suited because of the incapability of getting the potential field from Eq. (2.26). In this case, the time-varying pressure field at $\mathbf{x}^*$ may be numerically carried out by facing the problem in a frame of reference rigidly connected to the vortex, that is, by applying Eq. (2.25) (with the first term at RHS equal to zero) to geometric points identified by the contra-rotation of the observer with respect to the vortex. Note that, to prevent unrealistically large pressure and velocity distributions when $\mathbf{x}^*$ approaches to $\mathbf{x}$, a suitable vortex core has to be used. In this thesis, a Rankine-type modeling is adopted [53].

Chapter 3

Theoretical Models for Aeroacoustics

3.1 Introduction

In this chapter the time-domain hydro/aero-acoustic formulations used for the prediction of the *fluid dynamic generated noise* by rotating blade devices are shown. To this aim, it is worthy note the fundamental papers *On Sound Generated Aerodynamically. I. General Theory* [1] and *On Sound Generated Aerodynamically. II. Turbulence as a Source of Sound* [54] by M. J. Lighthill who, in 1952, published the results of his research in response to emerging need to control the noise of jet propelled aircraft. By a re-arranging of the fundamental conservation laws of mass and momentum into the form of an inhomogeneous wave equation, turbulence generated noise propagation phenomena were properly separated by sound generation mechanisms. The accounting for moving bodies as sources of sound is due to Ffowcs Williams and Hawkings who, in 1969, in the paper *Sound Generation by Turbulence and Surfaces in Arbitrary Motion* extended the Lighthill's theory by using the generalized functions theory [55] and the embedding procedure technique [56]. In the following, the derivation of the Ffowcs Williams and Hawkings Equation is firstly outlined and its solution, by the Green function method, is addressed. Secondly, it is shown how the application of the same mathematical manipulations and rigor as used in the derivation of the Ffowcs Williams and Hawkings equation leads to a hybrid Lighthill-Ffowcs Williams and Hawkings formulation well suited for comparisons in terms of theoretical acoustics. Details are found in Appendix A.1.

3.2 The Ffowcs Williams and Hawkings Equation

The Ffowcs Williams and Hawkings equation (FWHE) is the most general form of the Lighthill theory able to take into account the presence of moving bodies throughout the fluid. Under the assumption of thermodynamic transformations with negligible entropy changes, the continuity and momentum conservation laws can be rearranged into the Lighthill's equation

$$\Box^2 p' = \frac{1}{c_0^2}\frac{\partial^2 p'}{\partial t^2} - \nabla^2 p' = \nabla \cdot \nabla \cdot \mathbf{T} \tag{3.1}$$

where $\Box^2$ represents the wave operator, $p' = c_0^2\ (\rho - \rho_0)$ denotes the acoustic pressure whereas p, ρ, c and $\mathbf{u}$ are pressure, density, sound speed and fluid velocity, respectively. The suffix 0 indicates flow properties referred to the undisturbed medium. The right-hand-side (RHS) of (Eq. 3.1) represents the forcing term of the wave equation, that is, the double divergence of the Lighthill stress tensor $\mathbf{T} = \left[(p - p_0)\mathbf{I} - c_0^2\ (\rho - \rho_0)\mathbf{I} + \rho(\mathbf{u} \otimes \mathbf{u}) + \mathbf{V}\right]$ where $\mathbf{V}$ is the viscous stress tensor; the double divergence operator highlights the quadrupole nature of the turbulence generated noise in the unbounded flow [1, 54].

The introduction of solid boundaries, arbitrarily moving in a fluid at rest, is obtained by

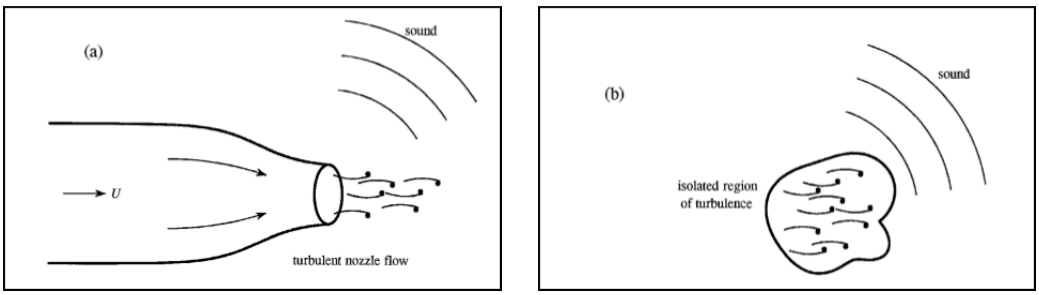

FIGURE 3.1: (a) Sketch of the sound produced by a turbulent nozzle flow jet. (b) Sketch the sound generated by a finite region of rotational flow in an unbounded fluid (as in the Lighthill's original theory). Images from [57]

embedding the exterior flow problem (in unbounded space) inside the moving body; this is accomplished by extending the definition of the fluid properties (pressure, velocity, density, etc.) inside the body surface, so that flow parameters have the same fluid state as the undisturbed medium [3]. The unavoidable fictitious flows discontinuities giving rise at the boundaries of the body surfaces are mathematically treated by the use of generalized functions [55]. The final result is a re-writing of the Navier-Stokes Equations into a inhomogeneous wave equation valid everywhere in the field, whose forcing terms are *intimately* correlated to the main physics phenomena inducing fluid dynamically generated noise. Specifically, denoting with $f(\mathbf{x}, t) = 0$ an arbitrary permeable surface $\mathcal{S}$, moving with velocity $\mathbf{v}$, such that $\nabla f = \mathbf{n}$ is the unit outwards normal, the general form of the Ffowcs Williams and Hawkings Equation (FWHE) reads [2, 18] (see also Appendix A.1 for details)

$$\begin{aligned} \Box^2 p' = & \frac{\overline{\partial}}{\partial t}\left[\rho_0\, \mathbf{v} \cdot \nabla f\ \delta\left(f\right)\right] + \frac{\overline{\partial}}{\partial t}\left[\rho\ \left(\mathbf{u} - \mathbf{v}\right) \cdot \nabla f\ \delta\left(f\right)\right] \\ & - \overline{\nabla} \cdot \left[\mathbf{P}\ \nabla f\ \delta\left(f\right)\right] - \overline{\nabla} \cdot \left[\rho\, \mathbf{u} \otimes \left(\mathbf{u} - \mathbf{v}\right)\ \nabla f\ \delta\left(f\right)\right] \\ & + \overline{\nabla} \cdot \overline{\nabla} \cdot \left[\mathbf{T}\ H(f)\right] \qquad\qquad \forall \mathbf{x} \in \Re^3 \end{aligned} \tag{3.2}$$

where overlines denote generalized differential operators, $\overline{\Box}^2$ the D'Alembert operator, $\delta(f)$ the Dirac delta function, $H(f)$ a domain function (namely Heaviside) such that

$$H[f(\mathbf{x}, t)] = \begin{cases} 1 & \text{if} \quad \mathbf{x} \in \Re^3 \setminus \mathcal{V} \\ 0 & \text{if} \quad \mathbf{x} \in \mathcal{V} \end{cases} \tag{3.3}$$

being $\mathcal{V}$ the volume enclosed by $\mathcal{S}$, whilst $\mathbf{P} = [\mathbf{V} + p\mathbf{I}]$ indicates the compressive stress tensor. For clarity, Fig. 3.2 depicts a moving body inside a permeable surface co-moving with it and embedding some of the most relevant volume sources of noise associated to turbulence, vortical and cavitating flows. If $f(\mathbf{x},t) = 0$ coincides with the body, the surface

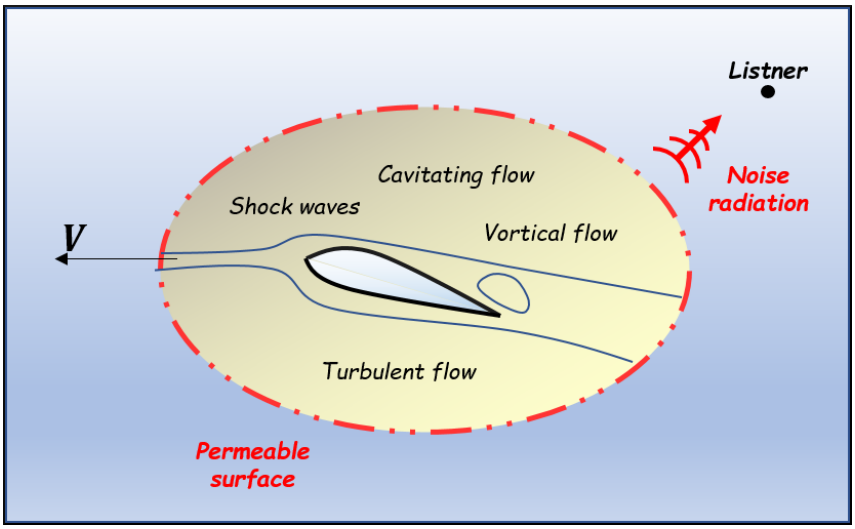

FIGURE 3.2: Sketch of the acoustic configuration for permeable surface applications.

$\mathcal{S}$ is impermeable, $(\mathbf{u} - \mathbf{v}) \cdot \mathbf{n} = 0$ thus Eq. (3.2) reduces to

$$\Box^2 p' = \frac{\overline{\partial}}{\partial t}\left[\rho_0 \, \mathbf{v} \cdot \nabla f \, \delta(f)\right] - \overline{\nabla} \cdot \left[\mathbf{P} \, \nabla f \, \delta(f)\right] + \overline{\nabla} \cdot \overline{\nabla} \cdot \left[\mathbf{T} \, H(f)\right] \qquad \forall \mathbf{x} \in \Re^3 \quad (3.4)$$

Equation (3.4) offers a great insight into noise generation mechanisms and their correlation with the mathematical operator of the related forcing terms. In details, at RHS of Eq. (3.2), the first term has a monopole structure, it defines the noise contribution due to body shape and motion (namely, *thickness noise*). The second one exhibits a dipole-like structure; it defines the noise contribution due to the pressure distribution upon the body surface (namely, *loading noise*), whereas, the third term has a quadrupole-like structure and is associated to the noise contribution coming from the acoustic sources placed in the flow field (namely, *quadrupole noise*).

Similarly, at the RHS of Eq. (3.2), the first two terms represent the *pseudo-thickness* noise contribution due to the mass-flux through $\mathcal{S}$ whereas the third and fourth terms provide the *pseudo-loading* noise contribution due to the momentum-flux through the acoustic surface $\mathcal{S}$. The last term, indeed, is responsible of the quadrupole-like noise effects induced by all the sources outside $\mathcal{S}$.

The notable know-how gained by 30 years of aeroacoustic investigations within the framework of several European Projects (since 90s) (*i.e.* HELINOISE [5], RHINO [6], HELISHAPE [7], SNAAP [8], EROS [9], HELIFLOW [10], ROSAA,[11] and finally APIAN [12]) proves that, as long as transonic effects (i.e. shock waves) do not occur in propeller and rotor aerodynamics equipping vehicles of aeronautical interests (proprotors and helicopter, for instance) the first two terms exhaustively predict the radiated noise field. In spite of

the low Mach number at the blade tip, wind turbines and marine propellers do not obey to these general outcomes. It is well known in literature that the acoustics of wind turbines is deeply influenced by aerodynamic phenomena due to large changes in angle of attack associated with sudden large gusts, changes in wind direction or interaction with the unsteady wake shed from the tower support on downwind, in addition to the effects of the turbulent boundary layer which represent well known quadrupole noise sources.

Differently, only recently the investigations carried out in the context of the European Project *SILENV* [15], *STREAMLINE* [16] and, currently, *AQUO and SONIC* [58] have demonstrated how propeller hydroacoustics is strongly dominated by the hydrodynamic sources due to vortices released at the blade tip, vorticity and turbulence phenomena which can be very intense and persisting (both in space and time) around/downstream the propeller disk. As a matter of fact, thickness and loading noise contributions are limited to a fluid region extending few blade-diameters around the propeller, depending on the operating conditions [22]. Such a behaviour is due to the destructive interference which, at very low rotational Mach numbers, makes the noise decay much more pronounced and faster [14].

3.2.1 Integral Solution

For numerical purposes, the Green function technique [38] is applied to turn the solution of Eq. (3.2) into an integral form. Specifically, following the approach proposed by [38] and summarized in appendix A.2, in a reference system rigidly connected with the moving domain $\mathcal{V}$ (SRC) the boundary-field integral representation for Eq. (3.2) reads

$$\begin{aligned} \bar{p}'(\mathbf{x},t) &= -\rho_0 \int_{\mathcal{S}} \left\{ \mathbf{v}\cdot\mathbf{n}\,\mathbf{v}\cdot\nabla\hat{G} + \left[\mathbf{v}\cdot\mathbf{n}\,(1-\mathbf{v}\cdot\nabla\vartheta)\right]^{\cdot}\hat{G} \right\}_\theta \mathrm{d}S \\ &- \int_{\mathcal{S}} \left\{ (\mathbf{P}\mathbf{n})\cdot\nabla\hat{G} - (\dot{\mathbf{P}}\mathbf{n})\cdot\nabla\vartheta\,\hat{G} \right\}_\theta \mathrm{d}S \\ &- \int_{\mathcal{S}} \left\{ \rho\,\mathbf{u}^-\cdot\mathbf{n}\,\mathbf{u}^+\cdot\nabla\hat{G} + \left[\rho\,\mathbf{u}^-\cdot\mathbf{n}\,(1-\mathbf{u}^+\cdot\nabla\vartheta)\right]^{\cdot}\hat{G} \right\}_\theta \mathrm{d}S \\ &- \int_{\Re^3} \left[\hat{G}\,\nabla\cdot\nabla\cdot(\mathbf{T}\,H)\right]_\theta \mathrm{d}V \end{aligned} \tag{3.5}$$

where $\mathbf{n}$ is the unit outward normal vector on $\mathcal{S}$ and the suffix θ indicates that all kernels have to be computed at the retarded emission time $\tau = t - \vartheta$. As said the compressibility delay ϑ denotes the time required by the acoustic disturbance released from a source point $\mathbf{y} = \mathbf{y}(\tau)$ to reach the observer at point $\mathbf{x} = \mathbf{x}(t)$, whereas $\hat{G}$ indicates the retarded Green function given by

$$\hat{G} = \left[-\frac{1}{4\pi\, r}\left(\frac{1}{1-M_r}\right) \right]_\theta \tag{3.6}$$

being $\mathbf{r} = \mathbf{x}(t) - \mathbf{y}(\tau)$, $r = |\mathbf{r}|$ and $M_r = \dfrac{\mathbf{v}}{c_0}\cdot\hat{\mathbf{r}}$ the surface Mach number in the direction of radiation. In addition the symbol $(\dot{})$ denotes time derivation performed in the body-space, whilst $\mathbf{u}^- = (\mathbf{u}-\mathbf{v})$ and $\mathbf{u}^+ = (\mathbf{u}+\mathbf{v})$. As shown in [41], by neglecting the volume integral and assuming $\mathcal{S}$ to be the (impermeable) body surface, Eq. (3.5) becomes

fully-equivalent to the well-known Farassat 1A formulation [59]. Similar argumentations prove that for permeable surfaces, Eq. (3.5) is fully-equivalent to the formulation proposed in 1997 by di Francescantonio [18]. Equation (3.5) clearly states that the sources of sound enclosed by $\mathcal{S}$ affect the noise field outside it through surface integral terms, whereas the acoustic effects due to the sources outside $\mathcal{S}$ are described by the volume integral contribution. Therefore, if the noise sources were *all* inside $\mathcal{S}$, the surface terms of the FWHE would include the noise from the sources and propagation effects inside the permeable data surface, thus removing the need for a volume integration and significantly decreasing the computation burden. For the sake of clarity, Fig. 3.3 shows a translating porous surface (in red) enclosing different acoustic point sources (in blue), in the presence of external sources of sound (in green) whose strength vanishes outside the shaded region. According to Eq. (3.5), the noise signal received by the observer outside $\mathcal{S}$ is given by the p'_s coming from the surface contributions ($\mathcal{I}_s$) and p'_v associated to the volume integration over the shaded zone ($\mathcal{I}_v$). However, by enlarging the acoustic surface up to embed the shaded region (see the black line), the volume contribution ($\mathcal{I}_v$) is inherently captured by ($\mathcal{I}_s$) once it is computed on the larger surface. In Fig. 3.4 the acoustic surface (in red) does not embed any source of noise; assuming the presence of external sources localized inside the shaded region, the noise signal at the observer is only due to $(\mathcal{I}_v)$, being zero the contribution from $(\mathcal{I}_s)$. If the term $(\mathcal{I}_v)$ is neglected *a priori* , albeit in the presence of external sources of sound, the predicted (approximated) acoustic pressure comes only from $(\mathcal{I}_s)$ (see Fig. 3.5). Last, but not least, Fig. 3.6 shows the same acoustic configuration depicted in Fig. 3.3 with the observer located inside the permeable surface (in red). Since the pressure inside $\mathcal{S}$ is null by definition, $(\mathcal{I}_s)$ and $(\mathcal{I}_v)$ perfectly balance. From a general standpoint, neglecting the quadrupole term in the permeable surface method is only valid if the quadrupole flow features are completely encapsulated inside the permeable surface. Ignoring them leads to approximated noise predictions as long as the quadrupole sources do not cross the boundaries of the acoustic surface (see Fig. 3.5). On the contrary, the convection of eddies through the porous surface may generate relevant errors, known in literature as *spurious signals* . Figure 3.7 depicts a source geometry placed in uniform flow generating a wake and acoustic sources; theoretically, the noise signature at the observer is the combination of the acoustic pressure from the permeable surface, p'_s and from the quadrupole noise p'_v generated outside the surface, calculated by a volume integration of the entire region outside $\mathcal{S}$ (see Fig. 3.8). Neglecting the computationally expensive volume integral, the noise predicted from the surface terms includes contributions p'_a from acoustic sources inside the permeable surface, shown as small circles in Fig. 3.7, and sound from flow crossing the surface that would have been canceled by the quadrupole term if it had been included. The contributions from the surface that should have been canceled by the quadrupole term are identified as spurious signals, namely p'_{ss}. Since spurious signals should have been canceled out by the volume term, they are equal to the negative of the quadrupole noise. This error occurs both inside and outside the permeable surface. As a matter of fact, without predicting the quadrupole noise, sound outside the permeable surface contains acoustic pressure from the sources inside the surface as well as spurious signals. This is depicted in Figure 3.9 for clarity. Note that it is impossible to determine if the

acoustic pressure predicted outside the surface contains spurious signals without knowledge of the flow field inside because the noise generation inside the surface is unknown; i.e., it is unclear whether flow phenomena on the surface are acoustic or hydrodynamic in nature. The numerical treatment of this issue is beyond the scope of this thesis; an exhaustive discussion is found in sections 5.3.3, 5.4.1.

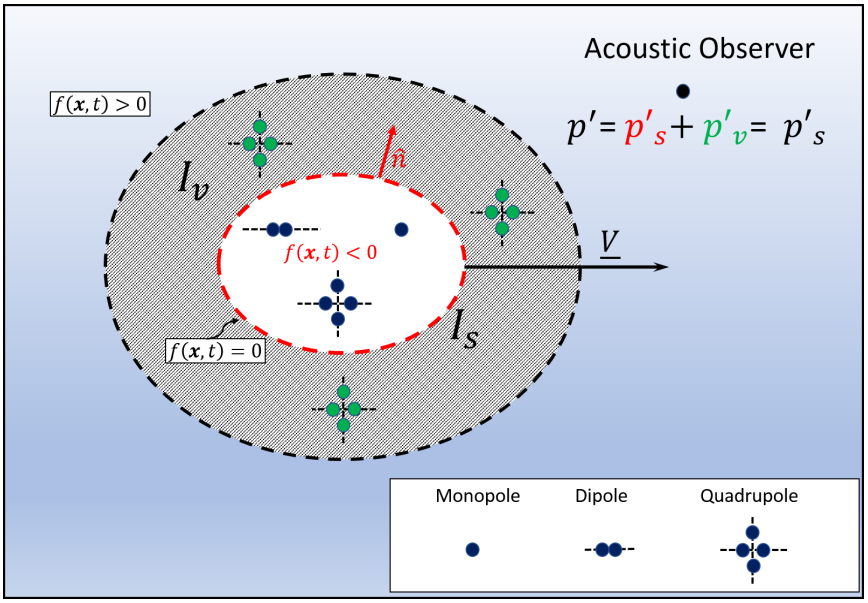

FIGURE 3.3: Sketch of the FWHE application: surface and field contributions

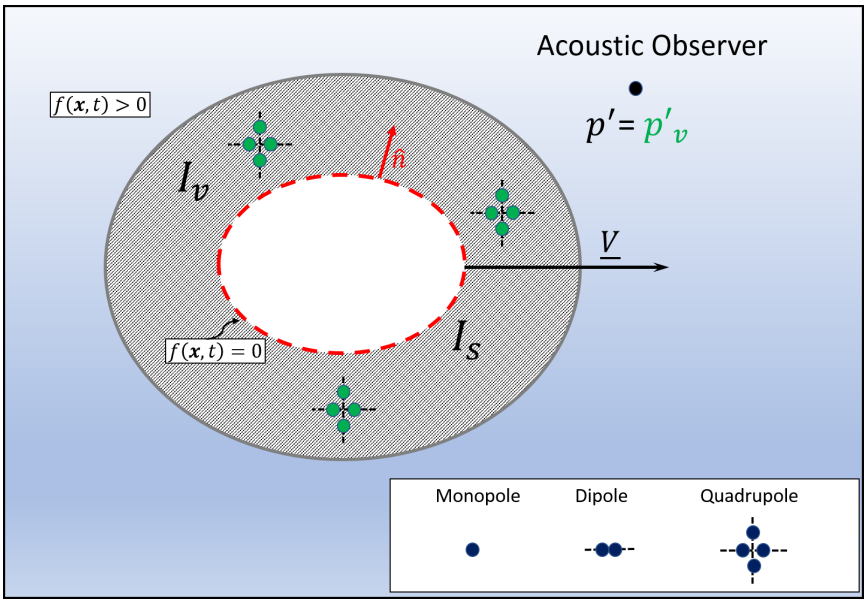

FIGURE 3.4: Sketch of the FWHE application: field contributions

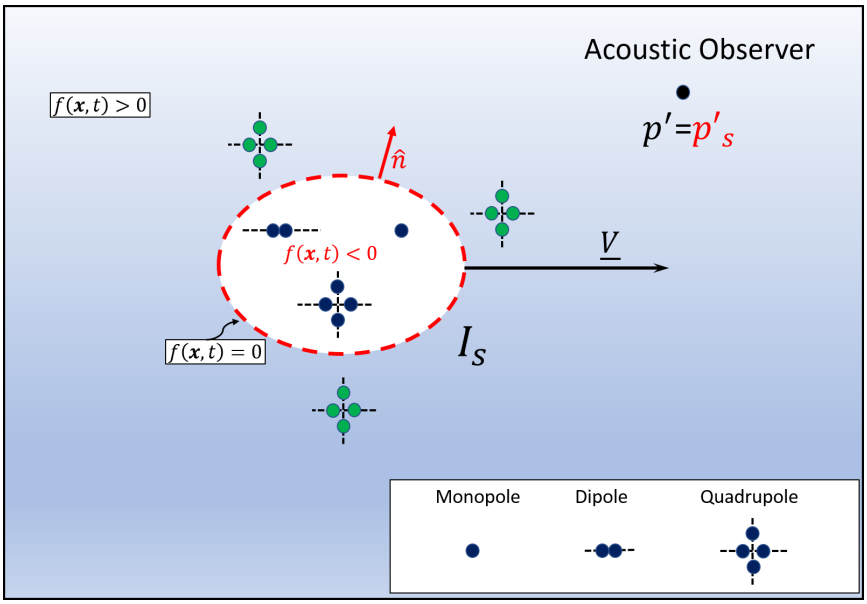

FIGURE 3.5: Sketch of the FWHE application: surface contributions

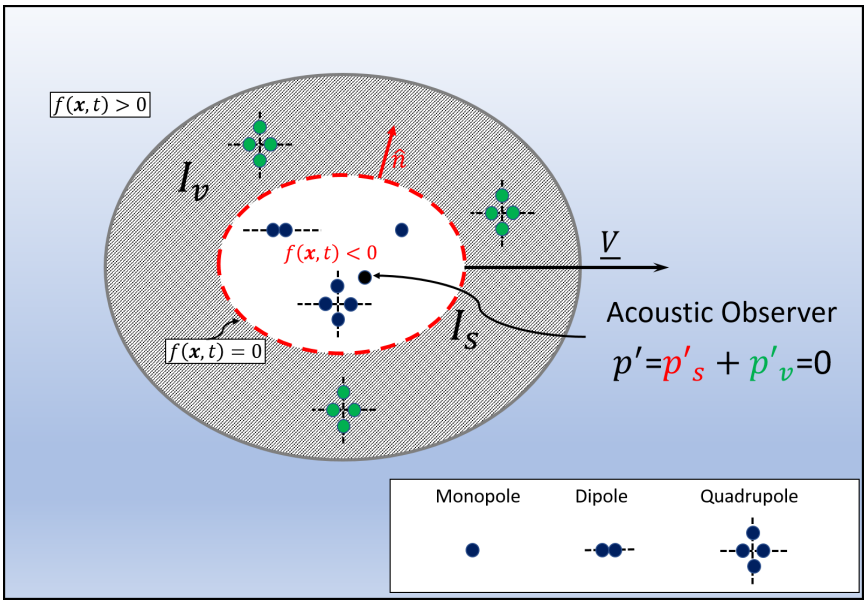

FIGURE 3.6: Sketch of the FWHE application: observer inside the porous surface

The application of Eq. (3.5) to rotary-wing devices is intrinsically prone to the issue of the spurious signals in that, the freely evolving wake convected by blades interacts with the downstream boundaries of $(\mathcal{S})$. The use of suitable numerical strategies may mitigate these undesirable effects: i) the numerical viscosity in CFD-based sources of noise detection; ii) the tailored splitting of the potential wake close to the downstream boundaries of $\mathcal{S}$ for sources of noise detection by BEM-based aero/hydro-dynamics. Beside them, a widely-used approach to face applications characterized by high vorticity and turbulence downstream is to close the porous surface far enough that fluctuations have been decayed or to leave the surface open

downstream. The last approach do not comply with the theory underlying the permeable FWHE but, as shown in Chapter 5, may provide reliable acoustic outcome depending on the observer location.

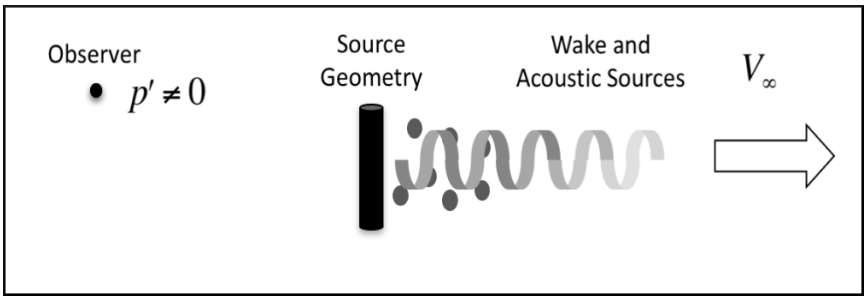

FIGURE 3.7: Diagram of source geometry placed in uniform flow generating a wake and acoustic sources. Observer is also shown. Image from [60]

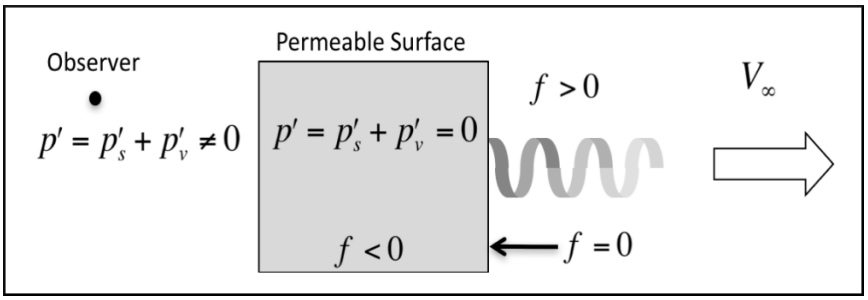

FIGURE 3.8: Genesis of the spurious noise. Diagram of permeable surface placed around source geometry and part of the wake and acoustic sources. Image from [60]

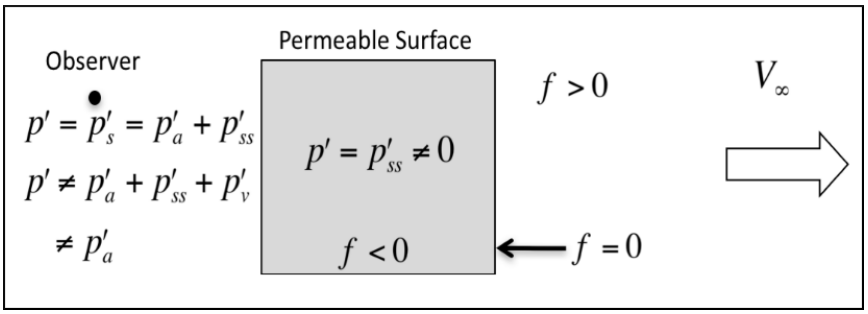

FIGURE 3.9: Diagram of spurious signals caused by not including the quadrupole term. These occur inside and outside the permeable surface. Image from [60]

3.3 Hybrid Lighthill-Ffowcs Williams and Hawkings Equation for Moving Surfaces

As shown in Appendix A.1, the application of the embedding procedure to Eq. (3.1) yields an inhomogeneous wave equation for the pressure disturbance where the structure of the acoustic forcing terms differs somehow from those appearing at the RHS of Eq. (3.4) (or Eq. (3.2)). In detail, assuming $f(\mathbf{x},t)=0$ to be an arbitrary surface $\mathcal{S}$ (permeable or not), moving in the fluid medium at velocity $\mathbf{v}$, such that$\nabla f=\mathbf{n}$, the manipulations addressed in Appendix A.1.2 lead to the following hybrid formula, namely (H-FWHE)

$$\begin{aligned}\Box^2 p' = &- \left(\frac{\overline{\partial} p'}{\partial n}+\frac{1}{c_0}\frac{\overline{\partial} p'}{\partial t}M_n\right)\delta(f)-\overline{\nabla}\cdot[p'\mathbf{n}\delta(f)]+ \\ &- \frac{1}{c_0}\frac{\overline{\partial}}{\partial t}\left[p' M_n \delta(f)\right]+H\,\overline{\nabla}\cdot\overline{\nabla}\cdot\mathbf{T} \qquad\qquad \forall \mathbf{x}\in\Re^3\end{aligned} \tag{3.7}$$

where $M_n=(\mathbf{v}/c_0)\cdot\mathbf{n}$ represents the local Mach number in the normal direction.[1] By neglecting the last term at RHS, Eq. (3.7) recasts into the *Kirchhoff formula for moving surfaces*, known in literature also as *K-equation* [61], that has been proposed by Hawkings for predicting the noise of high-speed propellers and helicopter rotors. For simplicity let us assume $\mathcal{S}$ to be impermeable; the comparison between Eqs. (3.7) and (3.4) first highlights a different structure of the volume terms due to the role of the Heaviside $H(f)$ respect to the double divergence operator, that, in turns, gives rise to different capabilities of the surface terms in describing noise radiation mechanism from $\mathcal{S}$. Observe that a drawback in using Eq. (3.7) is the need to compute $\partial p'/\partial n$ on $(\mathcal{S})$ with respect to the use of Eq. (3.4) that requires the *only* knowledge of p' (and viscous stresses if considered).

3.3.1 Integral Solution

Equation (3.7) is suited for the application of the Green function technique in the unbounded space. This is shown in Appendix (A.34) that, in a reference system rigidly connected with $\mathcal{S}$, yields the following integral solution

$$\begin{aligned}p'(\mathbf{x},t) = &\int_{\mathcal{S}}\left[\frac{\partial p'}{\partial\tilde{n}}\hat{G}-p'\frac{\partial\hat{G}}{\partial\tilde{n}}\right]_\theta \mathrm{d}S+\int_{\mathcal{S}}\left[\hat{G}\frac{\partial p'}{\partial t}\left(\frac{\partial\vartheta}{\partial\tilde{n}}+2\frac{\mathbf{v}\cdot\mathbf{n}}{c_0^2}\right)\right]_\theta \\ &+\frac{1}{c_0^2}\int_{\mathcal{S}}\left[p'\,\hat{G}\frac{\partial}{\partial t}[\mathbf{v}\cdot\mathbf{n}(1-\mathbf{v}\cdot\nabla\vartheta)]\right]_\theta \mathrm{d}S-\int_{\mathcal{V}}\hat{G}\,[H\,\nabla\cdot\nabla\cdot\mathbf{T}]_\theta\,\mathrm{d}V\end{aligned} \tag{3.8}$$

in which $\partial(\cdot)/\partial\tilde{n}=\partial(\cdot)/(\partial n)-\mathbf{M}\cdot\mathbf{n}\mathbf{M}\cdot\nabla(\cdot)$ and $\mathbf{M}=\mathbf{v}/c_0$.

The permeable surface approach discussed in section 3.2 may be conveniently applied to Eq. (3.7). Hence, by assuming $\mathcal{S}$ such to embed *all* the volume source of sound, Eq. (3.7)

[1] For the meaning of the other symbols, the reader is referred to 3.2.

reduces to the K-equation and, in turns, Eq. (3.8) becomes a boundary integral representation in terms of p', $\partial p'/\partial n$, $\partial p'/\partial t$ upon $\mathcal{S}$. Numerical troubles may be encountered in the evaluation of $\partial p'/\partial n$ because it is not a standard output of any aero/hydro-dynamic solver, yielding velocity, pressure and density flow fields. At this stage it is worth noting that the acoustic pressure p', governed by the K-equation, must satisfy the linear wave equation, everywhere [61]; thus, Eq. (3.8) (without the volume integral) may provide reliable predictions only for porous surfaces located in the linear region of propagation. From this standpoint, the FWHE is more general in that it utilizes the conservation laws. This explains the differences shown in literature [62], in the behaviour of the solutions of these equations in the near field.

Chapter 4

A Permeable Boundary Approach for Aeroacoustics of Lifting Bodies

4.1 Introduction

This chapter proposes a novel approach to rearrange the quadrupole source term of the Ffowcs Williams and Hawkings Equation (see Eq. (3.2)) in a form that noise generated by flow regions of high gradients, such as shock surfaces or vorticity layers, may be distinguished from those of other regions [63].
The reasons which lead to this further expression of the quadrupole source term are here briefly summarized.

Ideally the application of the FWHE porous approach (see Eq. (3.5)), as widely discussed in Chapter 3, would require that all the quadrupole noise contributions were embedded inside the permeable surface. Such condition assures that the predicted acoustic pressure is effectively that induced by *all* the source in the field, either the surface and volume contributions. Although theoretically valid, the use of such technique for the analysis of realistic configurations often rises issues related to the encapsulation of field noise sources. Indeed, in many applications the axial extension of the wake and the clustering grid features of the fluid dynamic solver far from the rotor, to name just a few of the known factors, de facto prevent the arbitrary extension and location of the permeable surface. This is, for abs, the case in which some shock waves are generated around an high speed helicopter blade, whose acoustic characterization would lead to the extension of the porous surface where the clustering grid is coarser, or, to the introduction of complex shape of the permeable surface to encompass the zones of the shock.

On the other hand, let us consider a underwater propeller whose hydrodynamic data are provided by a velocity potential-based fluid dynamic solver. In such cases, the wake downstream of the propeller rotor usually entails axial extension more than one order of magnitude greater with respect to the propeller diameter (in order to obtain convergent results). Thus, embeds the all wake would waste the computational advantages of the permeable technique.

In view of this, limiting our interest to cases where a discontinuity surface can be identified as source of noise, the presented technique suggests to exploit the porous surface approach (see Eq. (3.5)) to embed as much as possible non linear contributions, (i.e. as long as it does not implies to include zone of coarse grid (CFD) or it became computationally

inefficient because too long as in the case of potential hydrodynamics).
In addition, a further surface outside the porous one is introduced to account *directly* with the acoustic effects of the quadrupoles jump across it.

In the following, it will be shown how the aforementioned contribution can be deduced starting from both differential [63] and integral formulation governing the acoustic problem. In addition two integral formulations are derived: i) a first, more general approach is aimed to extent the FWHE to surfaces side of Lighthill stress tensor jump (i.e. it can be either a shock surface or a contact discontinuity) ;

ii) a second approach proposes to account with the acoustic effects of surfaces side of tangential velocity jump, as potential wakes (see Appendix C.1). In this framework the difference between the linear surface contributions of the FWHE and the Hybrid Lighthill-Ffowcs Williams and Hawkings Equations of Eq. (3.5) and Eq. (3.8), respectively, allows to recast the FWHE into a novel Combined FWHE/H-FWHE form.

4.2 Quadrupole Noise: A New Source Description

In this section the theoretical model able to characterize the acoustic pressure induced by a discontinuity surface in the flow field is shown. Akin to Chapter 3 let, $f(\mathbf{x},t)=0$ describe the motion of a surface $\mathcal{S}$, at velocity $\mathbf{v}$, in a fluid at rest. Without loss of generality, the general aspects of the problem are introduced by assuming $\mathcal{S}$ to be the impermeable body surface moving rigidly in connection to an other surface, namely $k(\mathbf{x},t)$, that represents a discontinuity surface for the Lighthill stress tensor .[1] Making reference to Eq. (3.4) forced by only the quadrupole term, the radiated noise field is solution of

$$\overline{\Box}^2 p'_\chi = \overline{\nabla}\cdot\overline{\nabla}\cdot[H(f)\mathbf{T}] \qquad \forall \mathbf{x}\in\Re^3 \tag{4.1}$$

Using the relation

$$\overline{\nabla}\cdot(\mathbf{T}\,H) = \overline{\nabla}\cdot\mathbf{T}H + \mathbf{T}\overline{\nabla}H \tag{4.2}$$

and observing that $\mathbf{T}$ has a discontinuity across $k(\mathbf{x},t)$, the application of the generalized functions differentiation rules yields

$$\overline{\Box}^2 p'_\chi = \overline{\nabla}\cdot[\nabla\cdot(H(f)\mathbf{T}) + \Delta\,(H(f)\mathbf{T})\,\nabla k\delta(k)] \tag{4.3}$$

that recasts into

$$\overline{\Box}^2 p'_\chi = \nabla\cdot\nabla\cdot[H(f)\mathbf{T}] + \nabla\cdot[H(f)\Delta\mathbf{T}\nabla k\delta(k)] + \Delta[\nabla\cdot(H(f)\mathbf{T})]\cdot\nabla k\delta(k) \tag{4.4}$$

where $\Delta = [.]_u - [.]_l$ and subscripts refer to the two sides of the discontinuity surface. Without ambiguity, the upper side of $k(\mathbf{x},t)$ is associated to the direction of the normal $\mathbf{n}'' = \nabla k$. Equation (4.4) is a re-writing of Eq. (4.1) in the presence of a generic surface of discontinuity for $\mathbf{T}$, where the quadrupole sources are expressed by the double (ordinary)

[1] Shock waves, potential wakes and boundary layer regions fall within this categories.

divergence of $(\mathbf{T}\,H)$ outside $f(\mathbf{x},t)=0$ and two contributions concerning the discontinuity surface.

Although the above differential approach allows to get awareness on the acoustic phenomenon under consideration, it is convenient to reformulate the problem into a more general form starting from Eq. (4.1) (from here on $f(\mathbf{x},t)=0$ denotes a permeable moving surface $\mathcal{S}$) and assuming the quadrupole sources decomposed into

$$\overline{\nabla}\cdot\overline{\nabla}\cdot(H\mathbf{T})=H\overline{\nabla}\cdot\overline{\nabla}(\mathbf{T})+\overline{\nabla}\cdot\left(\mathbf{T}\overline{\nabla}H\right)+\overline{\nabla}H\cdot\left(\overline{\nabla}\cdot\mathbf{T}\right)\qquad\forall\mathbf{x}\in\Re^3 \tag{4.5}$$

Then, by combining Eq. (4.5) with Eq. (4.1), in a frame of reference rigidly connected with $\mathcal{S}$ the application of the standard Green function technique yields

$$\begin{aligned}p'_\chi(\mathbf{x},t)=&-\int_{\Re^3}\int_0^\infty H\,\nabla\cdot\nabla\cdot\mathbf{T}\,\check{G}\,dt\,\mathrm{d}V-\int_{\Re^3}\int_0^\infty\check{G}\,\nabla\cdot(\mathbf{T}\nabla H)\;dt\,\mathrm{d}V\\&-\int_{\Re^3}\int_0^\infty\check{G}\,\nabla H\cdot(\nabla\cdot\mathbf{T})\;dt\,\mathrm{d}V\end{aligned} \tag{4.6}$$

where, referring to Appendix A.2, $\check{G}(\mathbf{y}-\mathbf{y}^*,\bar{t}-\bar{t}^*)=\hat{G}\,\delta(\bar{t}-\bar{t}^*+\vartheta)$. Equation 4.6 may be managed to provide two linear formulations able to describe the noise radiated by a lifting body in the presence of a discontinuity surface for $\mathbf{T}$, co-moving with it. Hereafter, such a discontinuity surface is assumed to be the potential wake generated by the particles that have been in contact with the body surfaces, released from the trailing edge. The main aspects of these acoustic modeling are outlined in the following; details are shown in Appendix C.1 and C.4.

4.2.1 Approach 1

By performing a by-part integration on the second integral term of Eq. (4.6) and using Eq. (A.39), one obtains

$$\begin{aligned}p'_\chi(\mathbf{x},t)=&-\int_{\Re^3}\int_0^\infty H\,\nabla\cdot\nabla\cdot\mathbf{T}\,\check{G}\,dt\,\mathrm{d}V+\int_{\mathcal{S}}\left\{(\mathbf{T}\mathbf{n})\cdot\nabla\hat{G}\right\}_\theta\mathrm{d}S\\&-\int_{\mathcal{S}}\left\{(\mathbf{T}\mathbf{n})\cdot\nabla\vartheta\,\hat{G}\right\}_\theta\mathrm{d}S-\int_{\mathcal{S}}\left\{(\nabla\cdot\mathbf{T})\cdot\mathbf{n}\,\hat{G}\right\}_\theta\;\mathrm{d}S\end{aligned} \tag{4.7}$$

where all integrals have to be computed at the retarded emission time. Equation (4.7) states that the solution of the FWHE forced by quadrupole sources can be interpreted as a sum of Lighthill-like jet noise term (first integral) outside $\mathcal{S}$ and a distribution of sources and doublets over it. In order to turn Eq. (4.7) in a suitable form for capturing the sound emitted by lifting body/wake configuration, let us introduce two surfaces, $\mathcal{S}_k$ and $\mathcal{S}_l$, co-moving in rigid motion with $\mathcal{S}$, whose motion is described by $k(\mathbf{x},t)=0$ and $l(\mathbf{x},t)=0$ respectively. Such surfaces are assumed to be enclosed within $\mathcal{S}$ at any time; specifically $\mathcal{S}_k$ denotes the potential wake surface ($\mathbf{n}''=\nabla k$) whereas $\mathcal{S}_l$ the lifting body ($\mathbf{n}'=\nabla l$). In the framework of potential flows theory around lifting surfaces, Fig. 4.1 depicts an example of porous surface $\mathcal{S}$ embedding a lifting airfoil and the potential wake departing from the trailing edge.

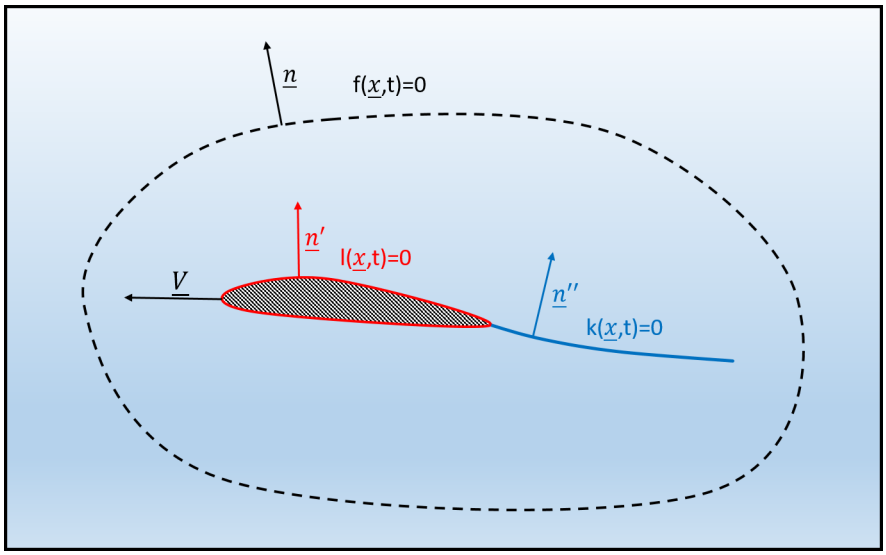

FIGURE 4.1: Sketch of the permeable FWHE surface embedding body and wake.

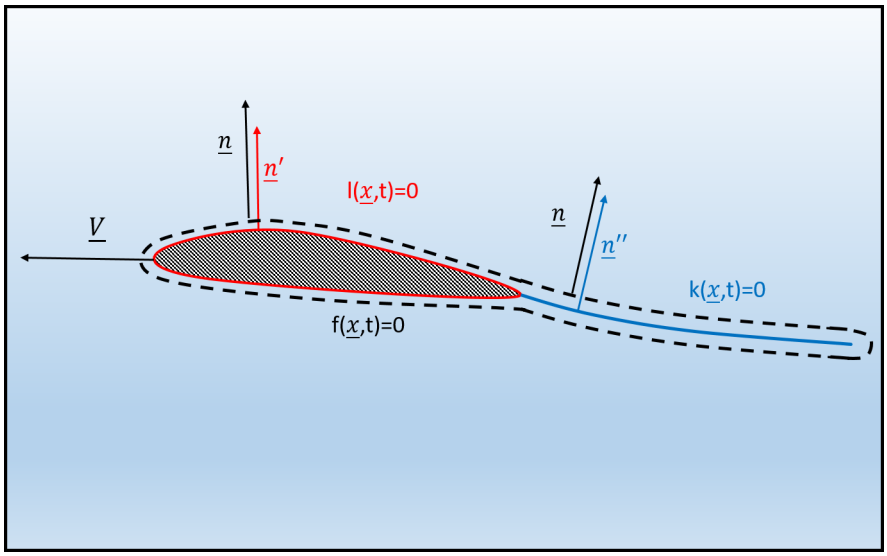

FIGURE 4.2: Sketch of the permeable FWHE surface approaching body and wake.

$$
\begin{aligned}
p'_\chi(\mathbf{x},t) = &\int_{\mathcal{S}_l} \left\{ (\mathbf{T}\mathbf{n}') \cdot \nabla \hat{G} \right\}_\theta \mathrm{d}S - \int_{\mathcal{S}_l} \left\{ (\mathbf{T}\mathbf{n}')^{\cdot} \cdot \nabla \vartheta \hat{G} \right\}_\theta \mathrm{d}S \\
&- \int_{\mathcal{S}_l} \left\{ (\nabla \cdot \mathbf{T}) \cdot \mathbf{n}' \hat{G} \right\}_\theta \mathrm{d}S + \int_{\mathcal{S}_k} \left\{ (\Delta \mathbf{T}\mathbf{n}'') \cdot \nabla \hat{G} \right\}_\theta \mathrm{d}S \\
&- \int_{\mathcal{S}_k} \left\{ (\Delta \mathbf{T}\mathbf{n}'')^{\cdot} \cdot \nabla \vartheta \hat{G} \right\}_\theta \mathrm{d}S - \int_{\mathcal{S}_k} \left\{ \Delta \left[(\nabla \cdot \mathbf{T}) \right] \cdot \mathbf{n}'' \hat{G} \right\}_\theta \mathrm{d}S \\
&- \int_{\Re^3} \int_0^\infty H \nabla \cdot \nabla \cdot \mathbf{T} \check{G} \, dt \, \mathrm{d}V
\end{aligned} \tag{4.8}
$$

Further, by letting the two side of $\mathcal{S}$ approaching $\mathcal{S}_l$ and $\mathcal{S}_k$, respectively, Eq. (4.7) recasts into Eq. (4.8) (see Fig.4.2 for clarity) where the first three integrals over $\mathcal{S}_l$ describe the

noise due to the quadrupole sources written in the form of surface contributions, the integrals over $\mathcal{S}_k$ account for the wake surface-induced sound, whilst the last integral provides the noise field associated to Lighthill-like jet noise term (pure volume integral). To compute the overall noise generated by $\mathcal{S}_l \bigcup \mathcal{S}_k$, thickness and loading noise terms have to be added to the solution given by Eq. (4.8). For a wake structure fixed in a frame of reference connected to the body[2], Appendix C.2 shows that both thickness and loading contributions are zero. Thus, accounting for thickness and loading noise by $\mathcal{S}_l$, the overall sound may be expressed as

$$\begin{aligned} p'(\mathbf{x},t) = & -\rho_0 \int_{\mathcal{S}_l} \left\{ \mathbf{v}\cdot\mathbf{n}'\, \mathbf{v}\cdot\nabla\hat{G} + \left[\mathbf{v}\cdot\mathbf{n}'\,(1-\mathbf{v}\cdot\nabla\vartheta)\right]^{\cdot}\hat{G} \right\}_\theta \mathrm{d}S \\ & - \int_{\mathcal{S}_l} \left\{ (\mathbf{P}\mathbf{n}')\cdot\nabla\hat{G} - (\mathbf{P}\mathbf{n}')^{\cdot}\cdot\nabla\vartheta\,\hat{G} \right\}_\theta \mathrm{d}S \\ & + \int_{\mathcal{S}_l} \left\{ (\mathbf{T}\mathbf{n}')\cdot\nabla\hat{G} \right\}_\theta \mathrm{d}S - \int_{\mathcal{S}_l} \left\{ (\mathbf{T}\mathbf{n}')^{\cdot}\cdot\nabla\vartheta\,\hat{G} \right\}_\theta \mathrm{d}S \\ & - \int_{\mathcal{S}_l} \left\{ (\nabla\cdot\mathbf{T})\cdot\mathbf{n}'\,\hat{G} \right\}_\theta \mathrm{d}S + \int_{\mathcal{S}_k} \left\{ (\Delta\mathbf{T}\mathbf{n}'')\cdot\nabla\hat{G} \right\}_\theta \mathrm{d}S \\ & - \int_{\mathcal{S}_k} \left\{ (\Delta\mathbf{T}\mathbf{n}'')^{\cdot}\cdot\nabla\vartheta\,\hat{G} \right\}_\theta \mathrm{d}S - \int_{\mathcal{S}_k} \left\{ \Delta\left[(\nabla\cdot\mathbf{T})\right]\cdot\mathbf{n}''\,\hat{G} \right\}_\theta \mathrm{d}S \\ & - \int_{\Re^3} \int_0^\infty H\,\nabla\cdot\nabla\cdot\mathbf{T}\,\check{G}\,dt\,\mathrm{d}V \end{aligned} \tag{4.9}$$

Theoretically, the volume domain surrounding $\mathcal{S}_l \bigcup \mathcal{S}_k$ may be thought as decomposed into $Re_l^3 \bigcup Re_k^3$, where Re_l^3 and Re_k^3 represent adjacent volume regions around $\mathcal{S}_l$ and $\mathcal{S}_k$, respectively. This *fictitious* domain decomposition allows to recognize that the first five integrals over $\mathcal{S}_l$ as well as the noise contribution from the last integral limited to Re_l^3, that is $\int_{\Re_l^3}\int_0^\infty -\left[\check{G}\,\nabla\cdot\nabla\cdot(\mathbf{T}\,H)\right]\,dt\,\mathrm{d}V$, yield the integral solution of the FWHE shown in Eq. (3.5) for the noise generated by the moving body. Moreover, observing that the sum among the third, fourth and fifth integral of Eq. (4.9) with $\int_{\Re_l^3}\int_0^\infty -\left[\check{G}\,\nabla\cdot\nabla\cdot(\mathbf{T}\,H)\right]\,dt\,\mathrm{d}V$ yields $\int_{\Re_l^3}\int_0^\infty -\left[\check{G}\,\nabla\cdot\nabla\cdot(H\mathbf{T})\right]\,dt\,\mathrm{d}V$, the following relation is derived

$$\begin{aligned} p'(\mathbf{x},t) = & -\rho_0 \int_{\mathcal{S}_l} \left\{ \mathbf{v}\cdot\mathbf{n}'\, \mathbf{v}\cdot\nabla\hat{G} + \left[\mathbf{v}\cdot\mathbf{n}'\,(1-\mathbf{v}\cdot\nabla\vartheta)\right]^{\cdot}\hat{G} \right\}_\theta \mathrm{d}S \\ & - \int_{\mathcal{S}_l} \left\{ (\mathbf{P}\mathbf{n}')\cdot\nabla\hat{G} - (\mathbf{P}\mathbf{n}')^{\cdot}\cdot\nabla\vartheta\,\hat{G} \right\}_\theta \mathrm{d}S - \int_{\Re_l^3} \left[\hat{G}\,\nabla\cdot\nabla\cdot(\mathbf{T}\,H)\right]_\theta \mathrm{d}V \\ & + \int_{\mathcal{S}_k} \left\{ (\Delta\mathbf{T}\mathbf{n}'')\cdot\nabla\hat{G} \right\}_\theta \mathrm{d}S - \int_{\mathcal{S}_k} \left\{ (\Delta\mathbf{T}\mathbf{n}'')^{\cdot}\cdot\nabla\vartheta\,\hat{G} \right\}_\theta \mathrm{d}S \\ & - \int_{\mathcal{S}_k} \left\{ \Delta\left[(\nabla\cdot\mathbf{T})\right]\cdot\mathbf{n}''\,\hat{G} \right\}_\theta \mathrm{d}S - \int_{\Re_k^3} \left[H\,\nabla\cdot\nabla\cdot\mathbf{T}\,\hat{G}\right]_\theta \mathrm{d}V \end{aligned} \tag{4.10}$$

Limiting our interest to the assessment of an acoustic linear formulation, the volume integrals over Re_l^3 and Re_k^3 are neglected *a priori* . In this way, Eq. (4.10) provides the noise signal everywhere in the fluid domain as a combination of thickness and loading noise related to the body and surface quadrupole induced effects from the convected wake. Obviously, the use of

[2]The following discussion is strictly valid for translating wings in uniform translation, propellers in axial motion and helicopter blades in hovering

the permeable FWHE where the porous surface embeds both body and *all* the potential wake would be easier and would include the neglected volume contributions. However, in several acoustic applications concerning propellers, rotors or wings, the extension of the potential wake assuring converged data set upon the acoustic surface (computed by BEM aero/hydro-dynamics and the Bernoulli equation) would require the use of a permeable surface whose sizes may represent a practical computational burden. A straightforward extension of Eq. (4.10) is achievable by the domain decomposition depicted in Figs. 4.3, 4.4 where a tailored porous surface $\mathcal{S}_p$ encapsulates the body and only *portion* of the wake. Following this idea, the solution of the permeable FWHE upon $\mathcal{S}_p$ yields the noise field in terms of thickness, loading and volume contributions radiated by the sources inside it, whereas the sound emitted by the outer portion of the wake may be captured by the quadrupole surface terms above described. In details, the general form of Eq. (4.10) reads

$$
\begin{aligned}
p'(\mathbf{x},t) = \; & - \rho_0 \int_{\mathcal{S}_p} \left\{ \mathbf{v}\cdot\mathbf{n}'\, \mathbf{v}\cdot\nabla\hat{G} + \left[\mathbf{v}\cdot\mathbf{n}'\,(1-\mathbf{v}\cdot\nabla\vartheta)\right]^{\cdot}\hat{G} \right\}_\theta \mathrm{d}S \\
& - \int_{\mathcal{S}_p} \left\{ (\mathbf{P}\mathbf{n}')\cdot\nabla\hat{G} - (\mathbf{P}\mathbf{n}')^{\cdot}\cdot\nabla\vartheta\,\hat{G} \right\}_\theta \mathrm{d}S \\
& - \int_{\mathcal{S}_p} \left\{ \rho\,\mathbf{u}^-\cdot\mathbf{n}'\,\mathbf{u}^+\cdot\nabla\hat{G} + \left[\rho\,\mathbf{u}^-\cdot\mathbf{n}'\,(1-\mathbf{u}^+\cdot\nabla\vartheta)\right]^{\cdot}\hat{G} \right\}_\theta \mathrm{d}S \\
& + \int_{\mathcal{S}_k} \left\{ (\Delta\mathbf{T}\mathbf{n}'')\cdot\nabla\hat{G} \right\}_\theta \mathrm{d}S - \int_{\mathcal{S}_k} \left\{ (\Delta\mathbf{T}\mathbf{n}'')^{\cdot}\cdot\nabla\vartheta\,\hat{G} \right\}_\theta \mathrm{d}S \\
& - \int_{\mathcal{S}_k} \left\{ \Delta\left[(\nabla\cdot\mathbf{T})\right]\cdot\mathbf{n}''\,\hat{G} \right\}_\theta \mathrm{d}S
\end{aligned}
\tag{4.11}
$$

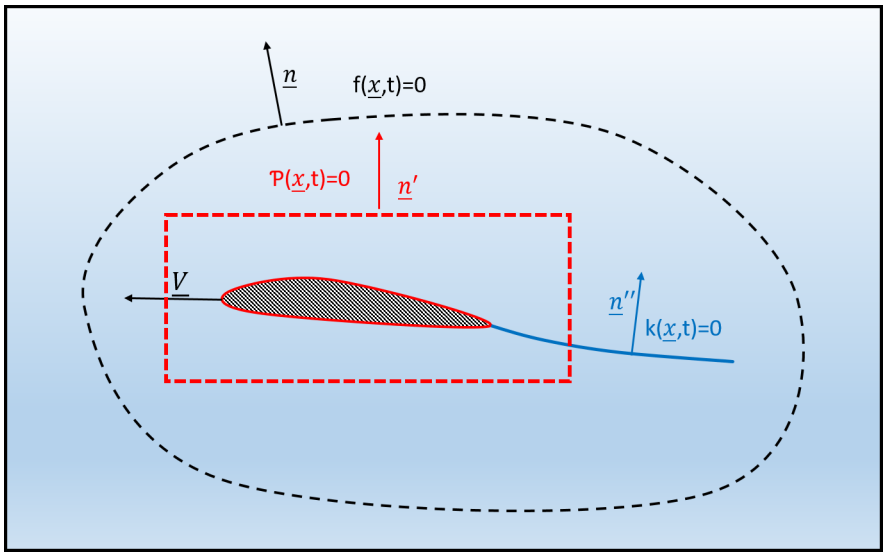

FIGURE 4.3: Sketch of the control surface $f(\mathbf{x},t)=0$, the FWHE permeable surface $\mathcal{P}(\mathbf{x},t)$ and the wake $k(\mathbf{x},t)$.

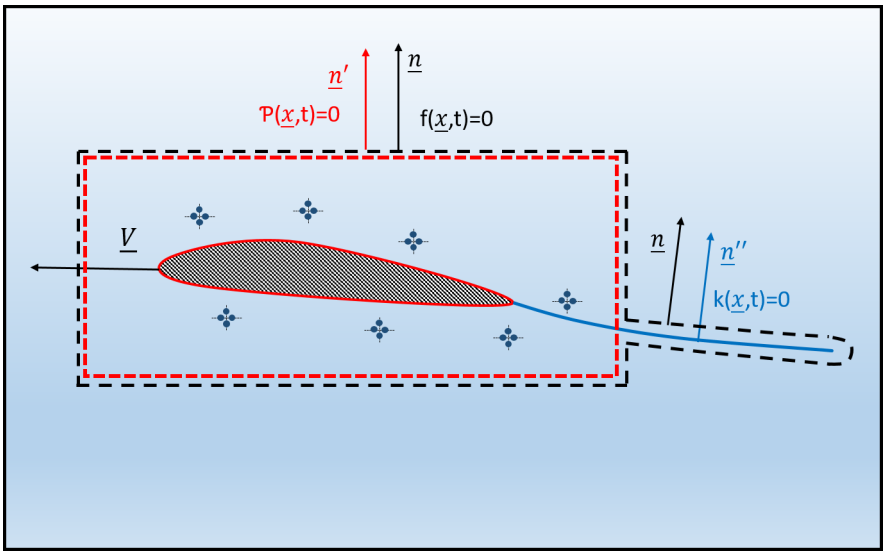

FIGURE 4.4: Sketch of the control surface approaching the FWHE permeable surface $\mathcal{P}(\mathbf{x}, t)$ and the wake $k(\mathbf{x}, t)$.

4.2.2 Approach 2

A boundary integral representation alternative to that proposed in the previous approach is shown hereafter. It allows to express wake acoustic effects through the jump of the pressure normal derivative across the wake surface, whose computation comes from the Euler equation. For this purpose, the starting point is the evaluation of the difference between the boundary integral representations referred to the K-equation ${p'}_K$ and the FWHE ${p'}_{FWHE}$, respectively; following Appendix C.4, one obtains

$$ {p'}_K - {p'}_{FWHE} = -\int_{\Re^3}\int_0^\infty \check{G}\,\nabla\cdot(\mathbf{T}\nabla H)\;dt\,\mathrm{d}V - \int_{\Re^3}\int_0^\infty \check{G}\,\nabla H\cdot(\nabla\cdot\mathbf{T})\;dt\,\mathrm{d}V \tag{4.12} $$

that combined with Eq. (4.6) provides the following relation for the quadrupole noise contribution

$$ p'_\chi(\mathbf{x},t) = {p'}_K(\mathbf{x},t) - {p'}_{FWHE}(\mathbf{x},t) - \int_{\Re^3}\int_0^\infty H\,\nabla\cdot\nabla\cdot\mathbf{T}\,\check{G}\,dt\,\mathrm{d}V \tag{4.13} $$

Akin to approach 1, the introduction of the surface $\mathcal{S}$ approaching $\mathcal{S}_l$ and $\mathcal{S}_k$ recasts Eq. 4.13 into

$$ \begin{aligned}
p'_\chi(\mathbf{x},t) \;=\;& \int_{\mathcal{S}_l}\left[\frac{\partial p'}{\partial\tilde{n}'}\hat{G} - \frac{\partial\hat{G}}{\partial\tilde{n}'}p'\right]_\theta \mathrm{d}S + \int_{\mathcal{S}_l}\left[\hat{G}\frac{\partial p}{\partial t}\left(\frac{\partial\vartheta}{\partial\tilde{n}'} + 2\frac{\mathbf{v}\cdot\mathbf{n}'}{{c_0}^2}\right)\right]_\theta \mathrm{d}S \\
&+ \frac{1}{{c_0}^2}\int_{\mathcal{S}_l}\left[p'\hat{G}\frac{\partial}{\partial t}[\mathbf{v}\cdot\mathbf{n}'(1-\mathbf{v}\cdot\nabla\vartheta)]\right]_\theta \mathrm{d}S \\
&+ \rho_0\int_{\mathcal{S}_l}\left\{\mathbf{v}\cdot\mathbf{n}'\;\mathbf{v}\cdot\nabla\hat{G} + \left[\mathbf{v}\cdot\mathbf{n}'\;(1-\mathbf{v}\cdot\nabla\vartheta)\right]\dot{\hat{G}}\right\}_\theta \mathrm{d}S \\
&+ \int_{\mathcal{S}_l}\left\{(\mathbf{P}\mathbf{n}')\cdot\nabla\hat{G} - (\mathbf{P}\mathbf{n}')\dot{}\cdot\nabla\vartheta\;\hat{G}\right\}_\theta \mathrm{d}S - \int_{\Re^3_l}\int_0^\infty H\,\nabla\cdot\nabla\cdot\mathbf{T}\,\check{G}\,dt\,\mathrm{d}V \\
&+ \int_{\mathcal{S}_k}\Delta\left[\frac{\partial p'}{\partial\tilde{n}''}\hat{G} - \frac{\partial\hat{G}}{\partial\tilde{n}''}p'\right]_\theta \mathrm{d}S + \int_{\mathcal{S}_k}\Delta\left[\hat{G}\frac{\partial p}{\partial t}\left(\frac{\partial\vartheta}{\partial\tilde{n}''} + 2\frac{\mathbf{v}\cdot\mathbf{n}''}{{c_0}^2}\right)\right]_\theta \mathrm{d}S \\
&+ \frac{1}{{c_0}^2}\int_{\mathcal{S}_k}\Delta\left[p'\hat{G}\frac{\partial}{\partial t}[\mathbf{v}\cdot\mathbf{n}''(1-\mathbf{v}\cdot\nabla\vartheta)]\right]_\theta \mathrm{d}S \\
&+ \rho_0\int_{\mathcal{S}_k}\Delta\left\{\mathbf{v}\cdot\mathbf{n}''\;\mathbf{v}\cdot\nabla\hat{G} + \left[\mathbf{v}\cdot\mathbf{n}''\;(1-\mathbf{v}\cdot\nabla\vartheta)\right]\dot{\hat{G}}\right\}_\theta \mathrm{d}S \\
&+ \int_{\mathcal{S}_k}\Delta\left\{(\mathbf{P}\mathbf{n}''\cdot\nabla\hat{G} - (\mathbf{P}\mathbf{n}'')\dot{}\cdot\nabla\vartheta\;\hat{G}\right\}_\theta \mathrm{d}S - \int_{\Re^3_k}\int_0^\infty H\,\nabla\cdot\nabla\cdot\mathbf{T}\,\check{G}\,dt\,\mathrm{d}V
\end{aligned} \tag{4.14} $$

that is equivalent to the quadrupole noise contribution given by Eq. (4.8)[3]. In addition, noting that:

- thickness and loading contributions from the wake are zero (see Appendix C.2);
- the sum of surface and volume integral contributions over $\mathcal{S}_l$ and Re_l^3, respectively, recast as $\int_{\Re^3_l}\int_0^\infty -\left[\check{G}\,\nabla\cdot\nabla\cdot(H\mathbf{T})\right]\;dt\,\mathrm{d}V$;

[3] $Re^3 = Re_l^3 \bigcup Re_k^3$

- for a wake structure fixed in a frame of reference connected to the body (see footnote 2), Appendix C.3 shows that the quadrupole noise induced by the wake surface is due to the jump of the pressure normal derivative across it;

the following final expression is achieved

$$\begin{aligned} p'(\mathbf{x},t) &= -\rho_0 \int_{\mathcal{S}_l} \left[\mathbf{v}\cdot\mathbf{n}\,\mathbf{v}\cdot\nabla\hat{G} + \left(\mathbf{v}\cdot\mathbf{n}\,(1-\mathbf{v}\cdot\nabla\vartheta)\right)^{\cdot}\hat{G} \right]_\theta \mathrm{d}S \\ &- \int_{\mathcal{S}_l} \left[(\mathbf{Pn})\cdot\nabla\hat{G} - (\mathbf{Pn})^{\cdot}\cdot\nabla\vartheta\,\hat{G} \right]_\theta \mathrm{d}S \\ &+ \int_{\mathcal{S}_k} \left[\Delta\left(\frac{\partial p'}{\partial\tilde{n}}\right)\hat{G} \right]_\theta \mathrm{d}S \\ &- \int_{\Re^3_b}\int_0^\infty \nabla\cdot\nabla\cdot(H\mathbf{T})\,\check{G}\,dt\,\mathrm{d}V(\mathbf{y}) - \int_{\Re^3_k}\int_0^\infty H\,\nabla\cdot\nabla\cdot\mathbf{T}\,\check{G}\,dt\,\mathrm{d}V \end{aligned} \tag{4.15}$$

where the source term $\Delta\left(\partial p'/\partial\tilde{n}\right)$ is derived in Appendix C.1.

Although equivalent to Eq. (4.11), Eq. (4.15) namely (Combined FWHE/H-FWHE), is more appealing for numerical purposes; hence, within linear acoustics, it is used to investigate the acoustic effects of a wake convected by a propeller in axial motion (see Chapter 5.5). Akin to approach 1, a more general form of Eq. (4.15), reads

$$\begin{aligned} p'(\mathbf{x},t) &= -\rho_0 \int_{\mathcal{S}_p} \left[\mathbf{v}\cdot\mathbf{n}\,\mathbf{v}\cdot\nabla\hat{G} + \left(\mathbf{v}\cdot\mathbf{n}\,(1-\mathbf{v}\cdot\nabla\vartheta)\right)^{\cdot}\hat{G} \right]_\theta \mathrm{d}S \\ &- \int_{\mathcal{S}_p} \left[(\mathbf{Pn})\cdot\nabla\hat{G} - (\mathbf{Pn})^{\cdot}\cdot\nabla\vartheta\,\hat{G} \right]_\theta \mathrm{d}S \\ &- \int_{\mathcal{S}_p} \left[\rho\mathbf{u}^-\cdot\mathbf{n}\,\mathbf{u}^+\cdot\nabla\hat{G} + \left(\rho\mathbf{u}^-\cdot\mathbf{n}\,(1-\mathbf{u}^+\cdot\nabla\vartheta)\right)^{\cdot}\hat{G} \right]_\theta \mathrm{d}S \\ &+ \int_{\mathcal{S}_k} \left[\Delta\left(\frac{\partial p'}{\partial\tilde{n}}\right)\hat{G} \right]_\theta \mathrm{d}S \end{aligned} \tag{4.16}$$

Chapter 5

Numerical Results

5.1 Introduction

In this section numerical results based on the acoustic formulations presented in Chapters 3 and 4 are shown.

Particular emphasis is given to the assessment of the permeable Ffowcs Williams and Hawkings Equation (FWH-P) capabilities to account with the flow field nonlinearities [1] in the noise prediction. Besides, comparisons with the permeable Hybrid Lighthill-Ffowcs Williams and Hawkings Equation (K-Equation) are shown.

The chapter starts with a brief section in which the numerical scheme adopted to solve both, the FWH-P and the K-Equation, is reported.

A first group of numerical results is aimed to assess the reliability of the acoustic models through comparisons against analytic solutions of the wave equation.

The goal is achieved through moving monopoles; the fluid dynamic data over the porous surface as well as the reference pressure signature, used as baseline for comparisons, are provided by the potential flows theory along with the Bernoulli Equation. The acoustic effects of the noise source motion act is assessed, in this context, using different kinematics of the monopoles (from the simple translation to helicoidal motion).

Besides, interesting outcome on the effects of the incomplete inclusion (inside the porous surface) of non linear flow features, give an insight into the sensibility of the acoustic models with respect to the partial inclusion of quadrupole source noise.

Remaining in the framework of potential flows, the generation of *spurious noise* contributions due to eddies convected through the boundary of the permeable surface (also known in literature as *End Cap* issue [21]) is analyzed using a rototranslating potential vortex ring partially enclosed inside it.

The physic mechanisms behind the spurious noise generation are highlighted; it is also shown where (with respect to the permeable surface) the unwanted effects are negligible and where, instead, are of major importance. Besides, possible numerical techniques for the attenuation of the *End Cap* issue are suggested.

The following of the chapter is devoted to the assessment of the permeable technique, for both the FWH-P and K-Equation, in case of application to rotary wing devices. In this

[1] With the term nonlinearities are indicated the flow field features in a data portion of volume $\mathcal{V}$ such that $\int_{\mathcal{V}} \left[\hat{G}\,\nabla\cdot\nabla\cdot(\mathbf{T}\,H)\right]_{\theta}\,\mathrm{d}V \neq 0$

context, a wide range of fluid dynamic solutions is used to detect the noise sources as well as to provide the baseline disturbance pressure for comparisons.

A Simplified model of a slender rotating blade, whose fluid dynamic data are given by the application of potential flows theory along with the Bernoulli Equation (see section 2.2), allows to draw interesting considerations, confirming de facto, the outcomes given by the application of the aforementioned singular solutions.

For what concerns the *end cap* issue, the acoustic effects of a sheet vorticity layer shed downstream the lifting blade are assessed. The outcomes well match with the considerations drawn in the case of the rototranslating vortex ring either in terms of spurious noise features and with respect to the effectiveness of the procedures suggested to mitigate it.

An interesting part of the chapter regards the noise characterization of industrial interest devices whose fluid dynamic flow field is predicted through the application of the Computational Fluid Dynamic (CFD) technique (see section 2.3). In this view, a wide discussion is carried out in order to identify the best turbulence model able to describe the energy cascade inside the fluid in a suitable way for acoustic purposes. At first glance, the Reynolds Averaged Navier Stokes (RANS) turbulence model is used to address the aeroacoustics of a Horizontal Axis Wind Turbine model scale; the outcomes suggest, in accordance with the scientific literature, how such technique, although largely used to evaluate airloads is unsuited for acoustic purposes.

The alternative approach based on the combination of RANS and Large Eddy Simulation (LES), namely Detached Eddy Simulation (DES) model, is used to detect the noise sources of the INSEAN E779A marine propeller.

This last is deeply investigated, both axial and inclined (drifted) conditions are assessed. The outcomes highlight very interesting and almost unknown aspects. The most important is the effectiveness of the DES simulation in terms of noise sources detection; indeed, it is able to detect and propagate pressure and velocity fluctuations induced by the turbulence, which revels themselves as a major noise source. However, effects of reflective CFD boundary conditions turn out to be critic, affecting the fluid dynamic solution in the mid field far from the blades and wake. A wide discussion concerning this phenomenon is included in the dissertation; besides, an uncommon application of the FWH-P is used to characterize acoustically the CFD/DES reflective behaviour avoiding the evaluation of field contribution.

The DES hydrodynamics of the INSEAN E779A propeller is also used, in this context, as base of comparison to assess the noise source detection capabilities (concerning the same device) of a 3D panel method solver, based on the potential flows hypothesis along with the Bernoulli Equation. Interesting results confirm that such hydrodynamic solution is suited only for the near field noise detection, in that, just a diameter away from the body the effects of turbulent flow (not modeled by the potential based code) are of major importance in the noise generation mechanisms. In conclusion, a test case concerning with a simplified model of rotating slender blade is used in order to assess the approach proposed in Chapter 4 (i.e. to directly account with sheet vorticity layers).

Particularly the combined FWHE/FWHE-H formulation, proposed in section 5.5 and theoretically applicable to face the "end cap" issue, at least in case of potential wakes partially

embedded inside the permeable surface, is used to extend the FWHE model to the *direct* inclusion of the acoustic effect due to a potential wake.

5.2 Discretization Strategy

A zero-th order boundary element method (BEM) is inhere used to discretize the integral boundary representation of the FWH-P and the K-Equation reported in Eq. (3.5) and Eq. (3.8), respectively. The numerical solution is obtained, for both, by dividing the moving body surface S into quadrilateral panels and assuming p' to be piecewise constant. To this aim let us at first consider the FWH-P Equation. Specifically, dividing S into M panels S_j, for an acoustic observer located outside the data surface in a point indicated by $\mathbf{x}_k$, Eq. (3.5) reads

$$p'(\mathbf{x}_k,t) = \sum_{j=1}^{M} T_{kj} + \sum_{j=1}^{M} R_{kj} + \sum_{j=1}^{M} C_{kj}\; p'_j(t-\vartheta_{kj}) + \sum_{j=1}^{M} D_{kj}\; \dot{p}'_j(t-\vartheta_{kj}) + \sum_{j=1}^{M} U_{kj} + \sum_{j=1}^{M} V_{kj} \tag{5.1}$$

The function $f(t-\vartheta_{kj})$ indicates that f must be evaluated at the emission time $(t-\vartheta)$ whereas the coefficients are defined in the following way

$$\begin{aligned}
C_{kj} &= -\int_{S_j} \left\{\nabla \hat{G}_{kj}\cdot\mathbf{n}\right\}_{\vartheta_{kj}} \mathrm{d}S \\
D_{kj} &= \int_{S_j} \left\{\nabla\hat{\vartheta}\cdot\mathbf{n}\;\hat{G}_{kj}\right\}_{\vartheta_{kj}} \mathrm{d}S \\
T_{kj} &= -\rho_0 \int_{S_j} \left\{\mathbf{v}\cdot\;\mathbf{n}\mathbf{v}\cdot\nabla\hat{G}_{kj}\right\}_{\vartheta_{kj}} \mathrm{d}S \qquad (5.2)\\
R_{kj} &= -\rho_0 \int_{S_j} \left\{\left[\mathbf{v}\cdot\mathbf{n}(1-\mathbf{v}\cdot\nabla\theta)\right]^{\cdot}\hat{G}_{kj}\right\}_{\vartheta_{kj}} \mathrm{d}S \\
U_{kj} &= -\int_{S_j} \left\{\rho\;\mathbf{u}^{-}\cdot\mathbf{n}\;\mathbf{u}^{+}\cdot\nabla\hat{G}\right\}_{\vartheta_{kj}} \mathrm{d}S \\
V_{kj} &= -\int_{S_j} \left\{\left[\rho\;\mathbf{u}^{-}\cdot\mathbf{n}\;(1-\mathbf{u}^{+}\cdot\nabla\vartheta)\right]^{\cdot}\hat{G}\right\}_{\vartheta_{kj}} \mathrm{d}S \qquad (5.3)
\end{aligned}$$

where $\hat{G}_{kj} = \hat{G}(\mathbf{x}_k,\mathbf{x})$.

The evaluation of the retarded coefficients in Eq. (5.2) requires the knowledge of the compressibility delay which is achieved by solving the following equation

$$\frac{|\mathbf{x}(t)-\mathbf{y}(t-\vartheta)|}{c_0} - \vartheta = 0 \tag{5.4}$$

The solution of Eq. (5.4) represents a typical root-finding problem which in case of rotational surfaces are find out through an iterative procedure, such as Newton Raphson and bisection methods. On the contrary, the time delay for translating surfaces is achieved by the solution of a second order algebraic equation in ϑ.

Similarly, the discretization of the K-Equation, (see Eq. (3.8)), yields

$$\begin{aligned}
p'(\mathbf{x}_k,t) &= \sum_{j=1}^{M} B_{kj}\;\psi_j(t-\vartheta_{kj}) + \sum_{j=1}^{M} C_{kj}\;p'_j(t-\vartheta_{kj}) \\
&+ \sum_{j=1}^{M} D_{kj}\;\dot{p}'_j(t-\vartheta_{kj}) \qquad (5.5)
\end{aligned}$$

where ψ_j denotes $\left.\frac{\partial p'}{\partial \tilde{n}}\right|_{\mathbf{y}_j}$ whereas the coefficients are defined as follows

$$\begin{aligned} B_{kj} &= \int_{S_j} \left\{\hat{G}_{kj}\right\}_{\vartheta_{kj}} \mathrm{d}S \\ C_{kj} &= \int_{S_j} \left\{ -\frac{\partial \hat{G}_{kj}}{\partial \tilde{n}} + \frac{1}{c_0^2}\, \hat{G}_{kj}\, \frac{\partial}{\partial t}[\mathbf{v}\cdot\mathbf{n}(1-\mathbf{v}\cdot\nabla\vartheta)] \right\}_{\vartheta_{kj}} \mathrm{d}S \\ D_{kj} &= \int_{S_j} \left\{ \hat{G}_{kj}\, \left(\frac{\partial \vartheta}{\partial \tilde{n}} + 2\frac{\mathbf{v}\cdot\mathbf{n}}{c_0^2} \right) \right\}_{\vartheta_{kj}} \mathrm{d}S \end{aligned} \tag{5.6}$$

5.3 Analytical Acoustic Singular Solutions for Validation Purposes

This section proposes a methodological approach aimed to assess the reliability of the FWH-P and the K-Equation.

Such goal is achieved through the use of singular solutions of the wave equation, particularly monopoles and vortex ring, i.e. a closed series of vortex line.

Particular emphasis is given to the understanding of mechanisms behind the *spurious noise* generation (i.e. the acoustic effect of eddies convected through the porous surface, known as *End Cap* issue) using the rototranslating vortex ring as noise source.

Besides, the analysis of the porous surface location with respect to the nonlinearities (particularly through the use of monopoles), allows to draw interesting conclusions about the effects of their partial inclusion as well as to achieve comparisons between the FWH-P and K-Equation.

5.3.1 Translating Monopole

The cases study inhere analyzed concern the acoustic pressure comparison between a single translating monopole, (see Chapter 2.4 for theoretical details), embedded by a permeable surface.

As specified in Appendix A.3.1 and A.3.2, the Eqs. (3.5) and (3.8), i.e. the FWH-P and K-Equation respectively, may be tailored for both a translating or rototranslating permeable surface; thus, both configurations are here assessed in order to prove the consistency of the results. To this aim two spherical porous surfaces moving rigidly and rotating around a translating monopole are used to reproduce the induced acoustic pressure of the noise source through the use of the FWH-P solver.

The simple mathematical form of the considered noise source allows to achieve the analytic expression of the disturbance pressure gradient upon the spherical porous surface , (for theoretical details see Appendix B.2). Therefore, beside to the outcomes of the FWH-P numerical model, the K-Equation is used to carry out acoustic predictions used as further base of comparison.

The results concern the acoustic pressure signature in the time domain for observers which are translating rigidly with the monopole and comparisons based on the directivity pattern.

5.3.1.1 Analysis of Surface Kinematics

The following results highlight the capability of the FWH-P to reproduce the acoustic pressure induced by the monopole independently on the kinematics of the porous surface.

The investigated layout is shown in Fig. 5.1; it depicts a translating monopole embedded by a rototranslating spherical porous surface. Besides, the position of microphones is listed in tables 5.1 and 5.2 . The noise source is located in the origin of the axis and characterized by a pulsating frequency ω_p= 340 rad/s. The thermodynamic conditions of the fluid at rest are

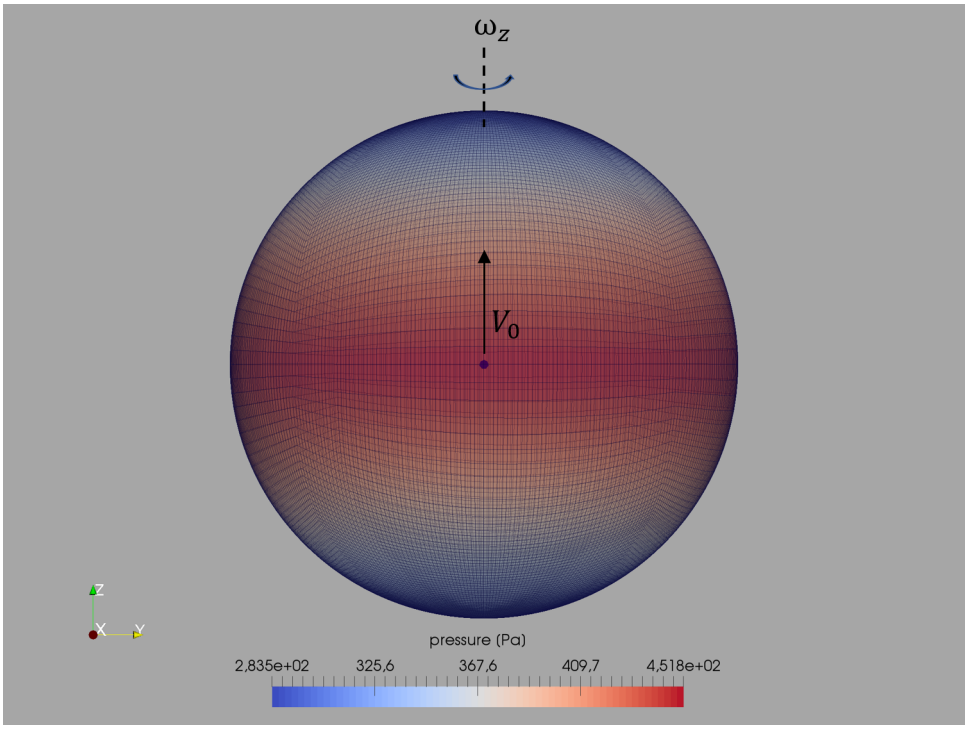

FIGURE 5.1: Spherical porous surface embedding a monopole; contours of instantaneous disturbance pressure

those identified by the air temperature $T = 15$ C° to which correspond a density $\rho = 1.225$ kg/m^3 and a sound speed $c_0 = 340$ m/s, thus resulting in a wave number $k = \omega_p / c_0 = 1$.

Near Field Microphones			
Name	$x[m]$	$y[m]$	$z[m]$
Obs 1	0.0	2.0	0.0
Obs 2	0.0	0.0	2.0
Obs 3	0.0	-2.0	0.0
Obs 4	0.0	0.0	-2.0

TABLE 5.1

Far Field Microphones			
Name	$x[m]$	$y[m]$	$z[m]$
Obs 5	0.0	200.0	0.0
Obs 6	0.0	0.0	200.0
Obs 7	0.0	-200.0	0.0
Obs 8	0.0	0.0	-200.0

TABLE 5.2

Moreover, the velocity translation is set to $v_0 = 170$ m/s which corresponds to an advancing Mach number equal to 0.5 whereas the angular velocity of the rototranslating permeable surface is chosen equal to the pulsation ω_p of the monopole.

It is worth to note that in order to keep the subsonic condition, the radius of the porous surface is limited to be less then one meter, and is set to 0.45 m. On the contrary the translating porous surface does not require any kinematic condition on the radius; however in order to be consistent with the rototranslating solution, it is set to 0.45 m. Figures 5.2 to 5.5 show the comparison between the solutions carried out through the application of potential compressible flows theory along with the Bernoulli Equation and the acoustic pressure provided by the FWH-P as function of non dimensional time $\bar{t} = (t/2\pi)\omega_p$. Particularly, the FWH-P outcomes refer to rototranslating and translating porous surface, here indicated by FWH-P-R

and FWH-P-T, respectively, for the near-field microphones listed in tab 5.1. Similarly, Figs. 5.6, to 5.9 show the same comparison for the far-field microphones listen in tab 5.2.

For the sake of conciseness, from here on the acoustic solution obtained by applying the potential flows theory combined with the Bernoulli equation will be referred as Bernoulli solution and used as baseline for the comparisons.

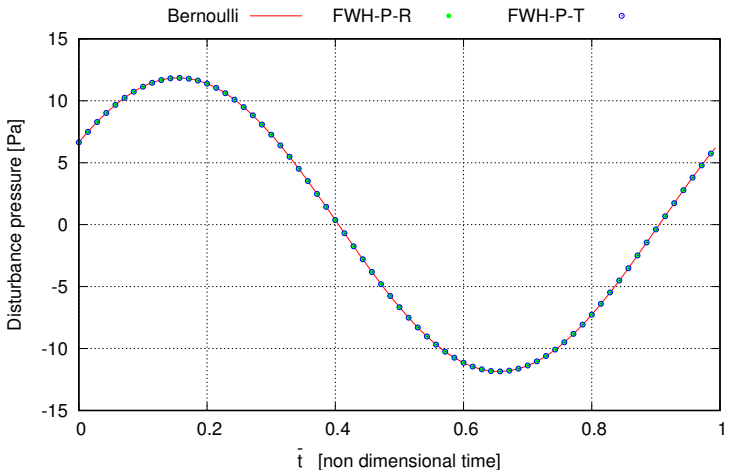

FIGURE 5.2: Translating monopole, kinematics of the permeable surface analysis. Acoustic pressure at Obs 1

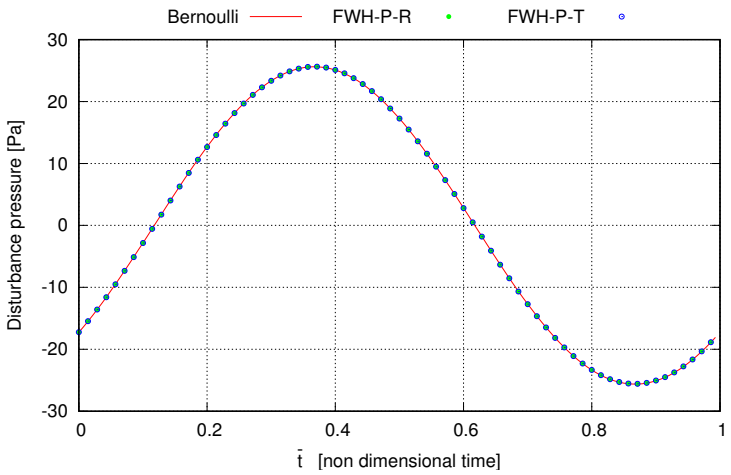

FIGURE 5.3: Translating monopole, kinematics of the permeable surface analysis. Acoustic pressure at Obs 2

The agreement between the Bernoulli solutions and the outcomes of the FWH-P model, both for translating and rototranslating permeable surfaces are in excellent agreement. This confirms that, when the *all* noise sources are embedded inside the porous surface, i.e. the monopole and the nonlinear induced flow field, the predicted acoustic pressure by the FWH-P approach is in excellent agreement with the Bernoulli solution.

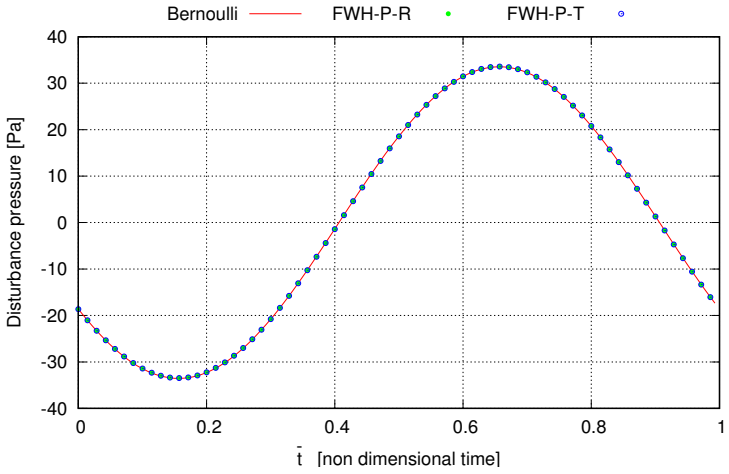

FIGURE 5.4: Translating monopole, kinematics of the permeable surface analysis. Acoustic pressure at Obs 3

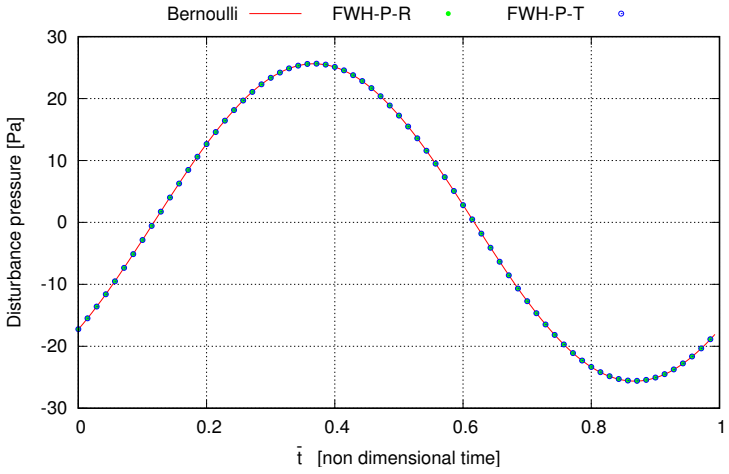

FIGURE 5.5: Translating monopole, kinematics of the permeable surface analysis. Acoustic pressure at Obs 4

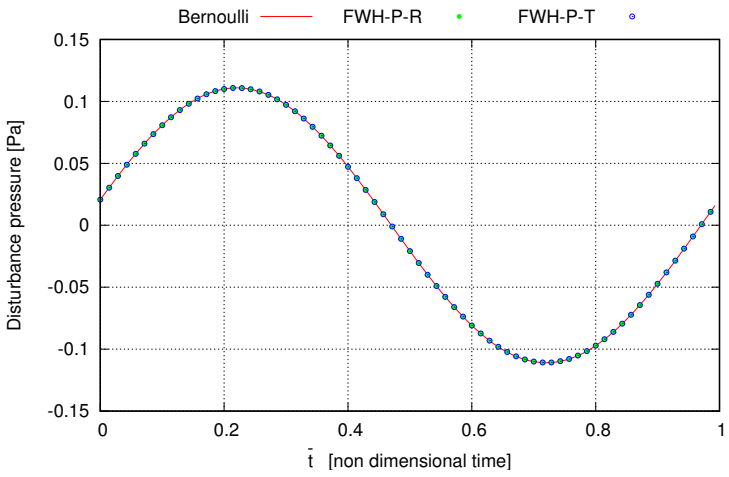

FIGURE 5.6: Translating monopole, kinematics of the permeable surface analysis. Acoustic pressure at Obs 5

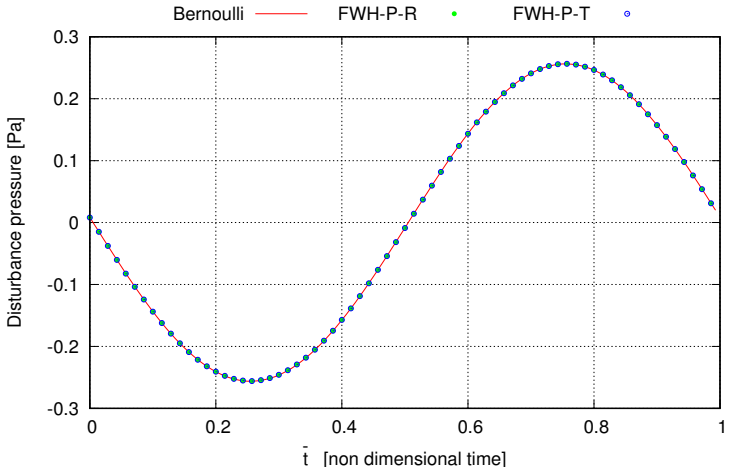

FIGURE 5.7: Translating monopole, kinematics of the permeable surface analysis. Acoustic pressure at Obs 6

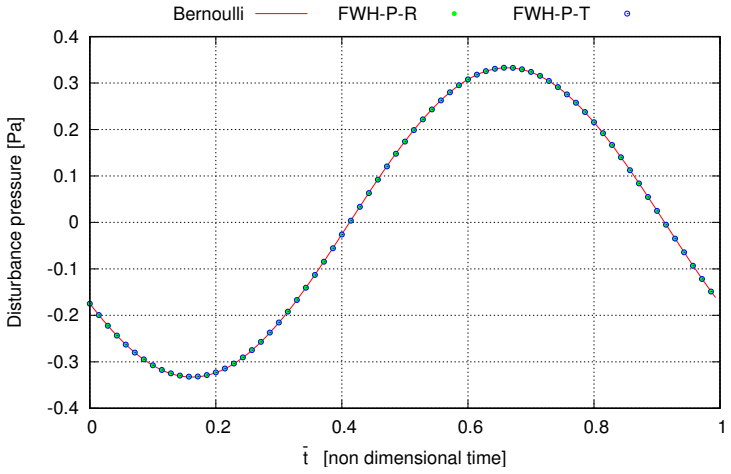

FIGURE 5.8: Translating monopole, kinematics of the permeable surface analysis. Acoustic pressure at Obs 7

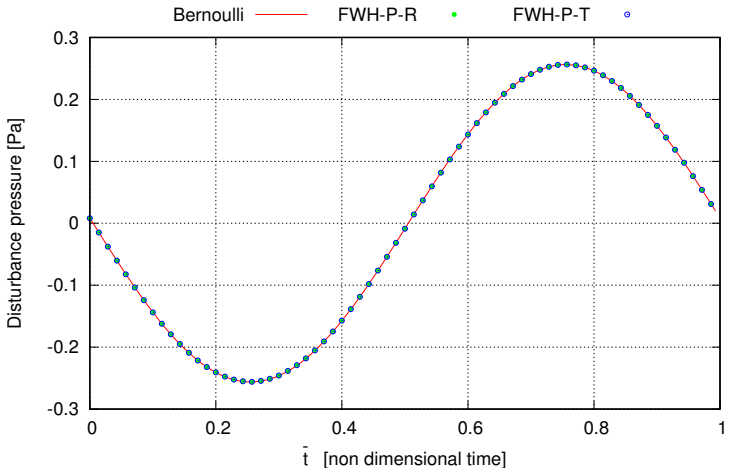

FIGURE 5.9: Translating monopole, kinematic of the FWH-P analysis. Acoustic pressure at Obs 8

5.3.1.2 Comparison Between FWH-P and the K-Equation

The purpose of this section is twofold: i) to validate the K-Equation ii) to assess the differences with the FWH-P approach on the same case study.

Particularly the effect of the permeable surface location is assessed in order to understand the behaviour of two solvers when the radius of the spherical surfaces shrinks toward the acoustic emitter (i.e. the monopole). To this aim the radius of the permeable surface ranges between 0.45 m to 0.112 m going trough 0.225 m.

5.3.1.2.1 The FWH-P Solution

Figs. 5.10 to 5.13 show the comparison between the Bernoulli reference solution and the acoustic pressure obtained for the near field observers listed in Tab. 5.1 by the FWH-P solver, as function of the radius of the porous surface.

Since the solution is not dependent on kinematics of the porous surface, the choice, arbitrary in principle, is on the rototranslating configuration. It goes without saying that the FWH-P solver provides excellent results for all the near field microphones, independently on the radius of the porous spherical surface, as shown in Figs. 5.10 to 5.13.

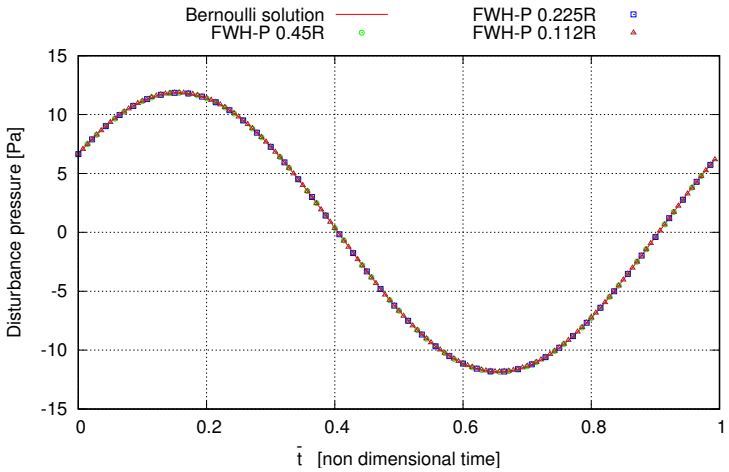

FIGURE 5.10: Translating monopole, effect of the FWH-P surface radial dimension. Acoustic pressure at Obs 1

Akin to the near field microphones, Figs. 5.14 to 5.17 show the comparison for the far field microphones listed in Tab. 5.2. Also for these microphones the agreement between the Bernoulli and FWH-P solutions is excellent and practically independent on the radius of the spherical porous surface.

In order to obtain information on frequency content of the predicted acoustic signature, the directivity pattern of the monopole is reported in Figs.5.18 and 5.19 for observers located 2 m away in radial direction from the monopole in the plane yz. Fig 5.18 depicts the directivity pattern at the frequency ω_p which shows an excellent agreement with the Bernoulli reference solution. On the contrary, Fig. 5.19 shows the directivity pattern at frequency $2\omega_p$ (incidentally, it is only due to the non linear flow field induced by the monopole) which is not well reproduced. As a matter of fact, Fig. 5.19 shows an overestimation of the directivity

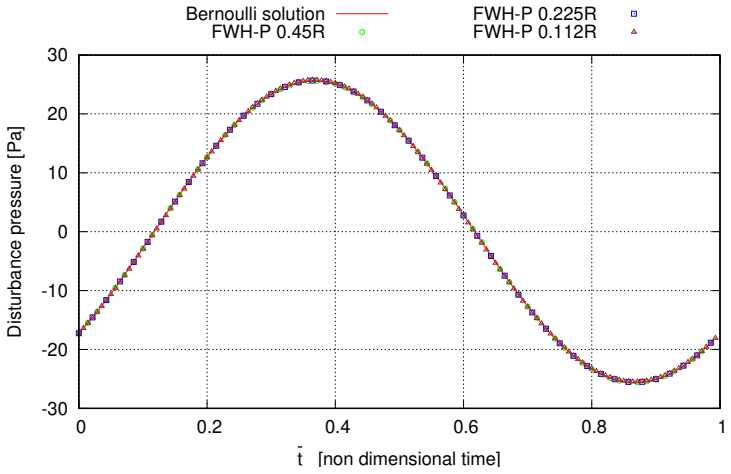

FIGURE 5.11: Translating monopole, effect of the FWH-P surface radial dimension. Acoustic pressure at Obs 2

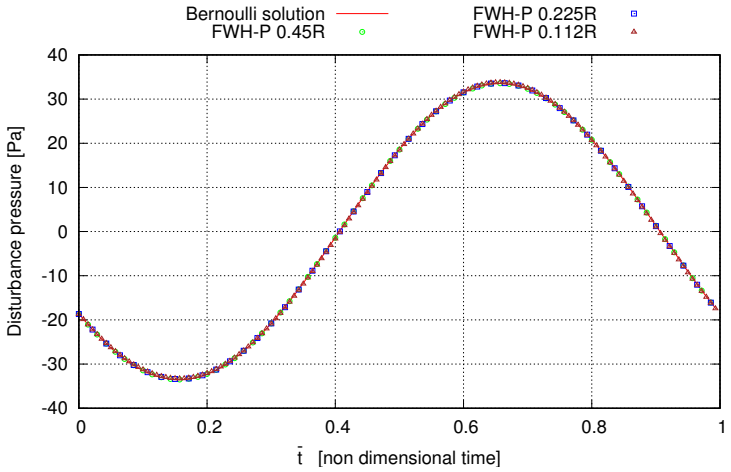

FIGURE 5.12: Translating monopole, effect of the FWH-P surface radial dimension. Acoustic pressure at Obs 3

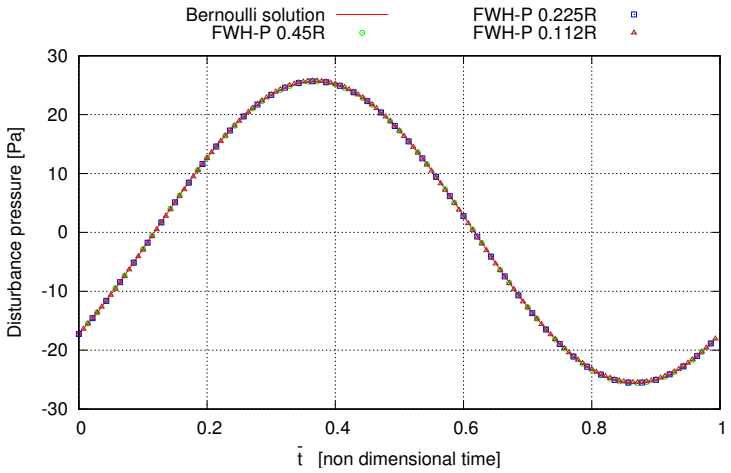

FIGURE 5.13: Translating monopole, effect of the FWH-P surface radial dimension. Acoustic pressure at Obs 4

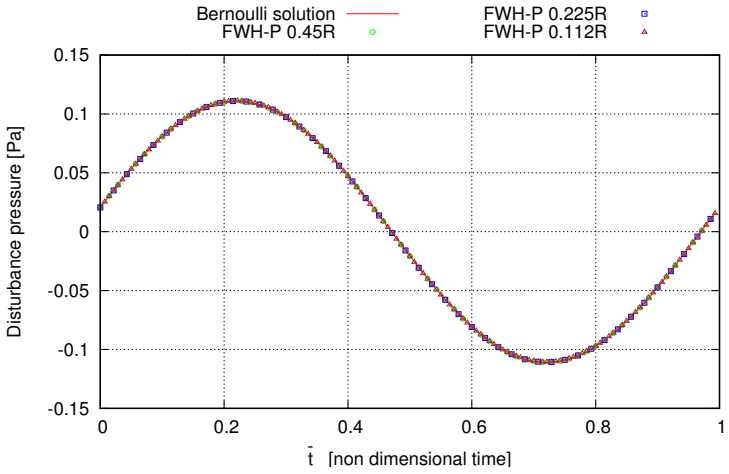

FIGURE 5.14: Translating monopole, effect of the FWH-P surface radial dimension. Acoustic pressure at Obs 5

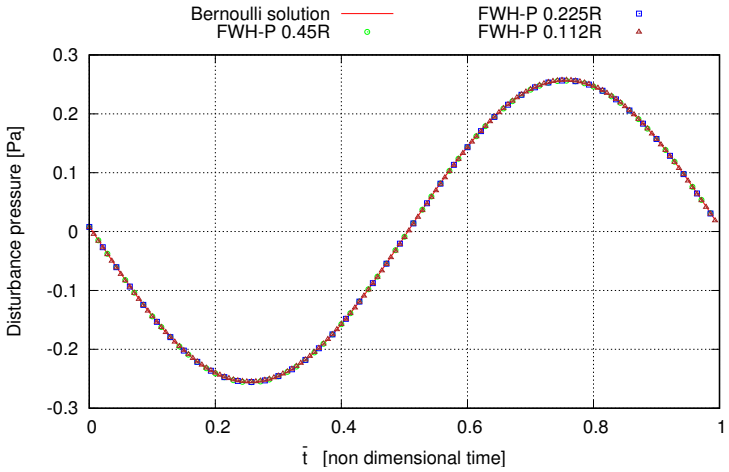

FIGURE 5.15: Translating monopole, effect of the FWH-P surface radial dimension. Acoustic pressure at Obs 6

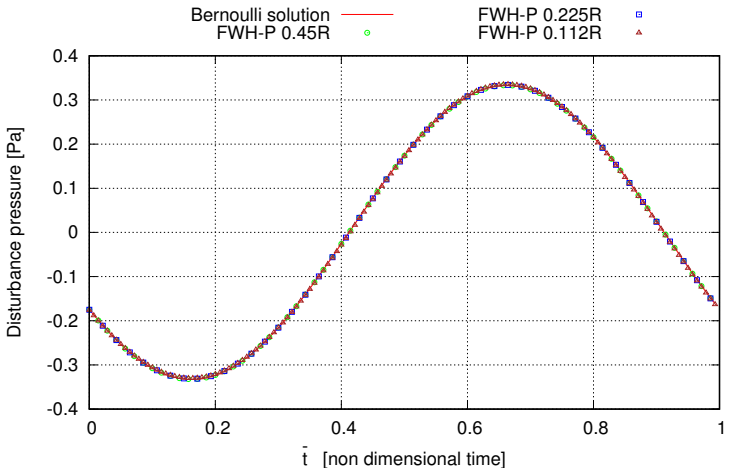

FIGURE 5.16: Translating monopole, effect of the FWH-P surface radial dimension. Acoustic pressure at Obs 7

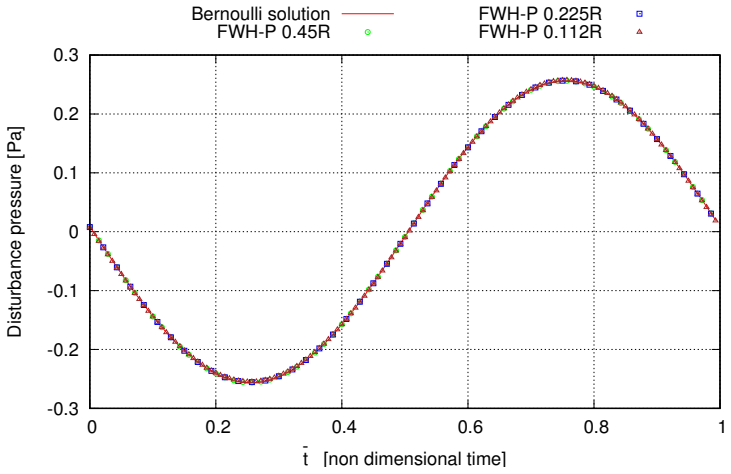

FIGURE 5.17: Translating monopole, effect of the FWH-P surface radial dimension. Acoustic pressure at Obs 8

pattern at that frequency, that, even in the better case (i.e. the largest surface) is an order of magnitude greater than the Bernoulli prediction.

This behaviour get worst as the permeable surface goes near to the monopole. Such results suggest that quadrupole contributions neglected outside the porous surface, also in the case of the largest one, are not negligible [2].

The effect is an overestimation of the FWH-P outcomes at frequency $2\omega_p$ which would be balanced by the inclusion of the quadrupole source term around the porous surface in a way to embed all the nonlinear flow field. This statement is very similar to the definition of *spurious noise* although it is usually associated to the acoustic effects of eddies convected through the permeable surface.

5.3.1.2.2 The K-Equation Solution

The same analysis described in section 5.3.1.2.1 is hereafter carried out through the use of the K-equation, (see section 3.3 for theoretical details). Akin to the FWH-P solution, the kinematic of the porous surface is rototranslating.

Figs. 5.20 to 5.23 and Figs. 5.24 to 5.27 show the acoustic pressure comparisons for the near and far field microphones listed in Tabs. 5.1 and 5.2, respectively, when the acoustic surface approaches the monopole source. For all observers, it is clear that the solution related to the larger porous surface is in excellent agreement with the reference signal provided by the Bernoulli Equation, whereas (differently to the FWH-P solution), approaching the monopole, the acoustic surface is no longer able to correctly reproduce the acoustic signal of the acoustic emitter.

Such results are not surprising, in that, the K-Equation only gives physical consistent predictions when the permeable surface is placed in a linear zone of flow field, i.e. where

[2]The FWHE recasts the continuity and momentum equations in terms of monopoles and dipoles over the permeable surface and qudrupoles into the field outside it. Hence, it provides a reinterpretation of the fluid dynamic flow field (for example that induced by the monopole) in terms of these sources. From this standpoint talking about quadrupole contributions when a monopole is the source of noise makes sense.

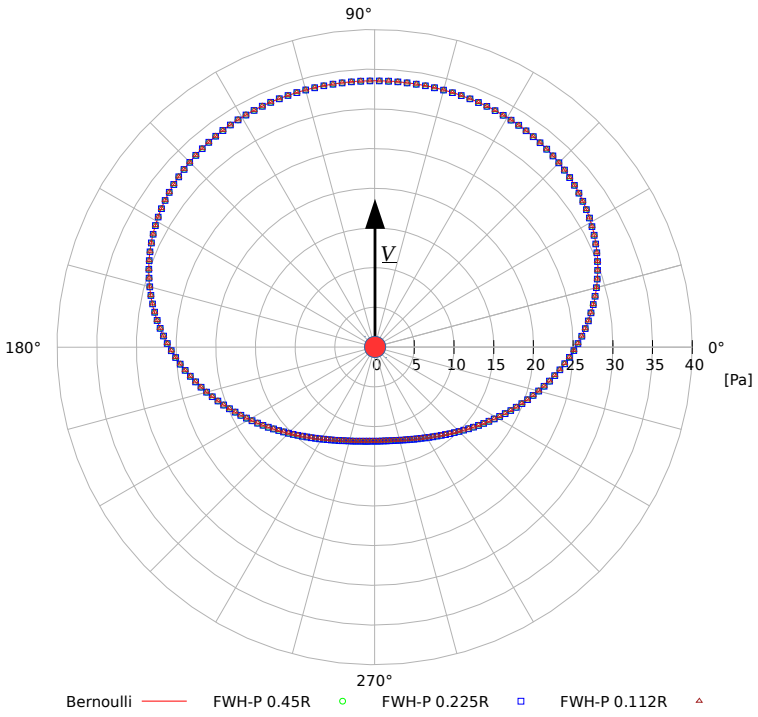

FIGURE 5.18: Comparison between FWH-P and Bernoulli solution directivity pattern at the nondimensional frequency $\frac{\omega}{\omega_p} = 1$

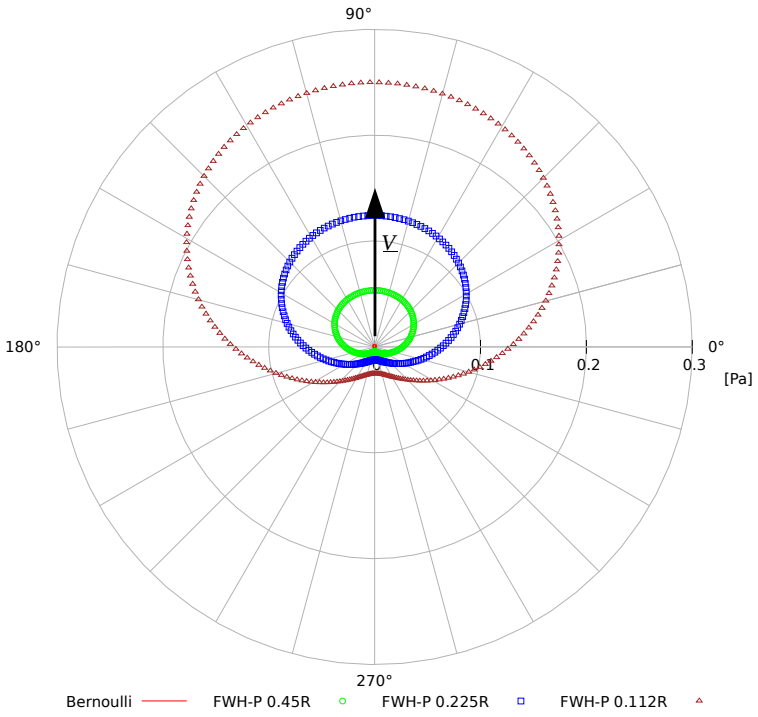

FIGURE 5.19: Comparison between FWH-P and Bernoulli solution directivity pattern at the nondimensional frequency $\frac{\omega}{\omega_p} = 2$

p', $\partial p'/\partial n$ and $\partial p'/\partial t$ satisfy the wave equation. It proof, in accordance with the literature

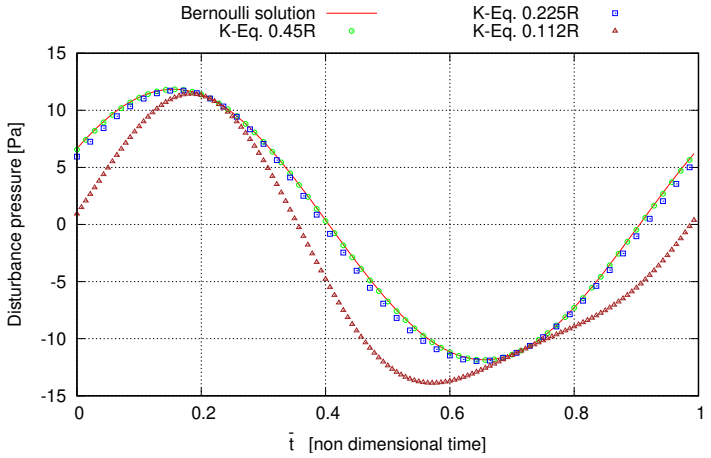

FIGURE 5.20: Translating monopole, effect of the K-Equation surface radial dimension. Acoustic pressure at Obs 1

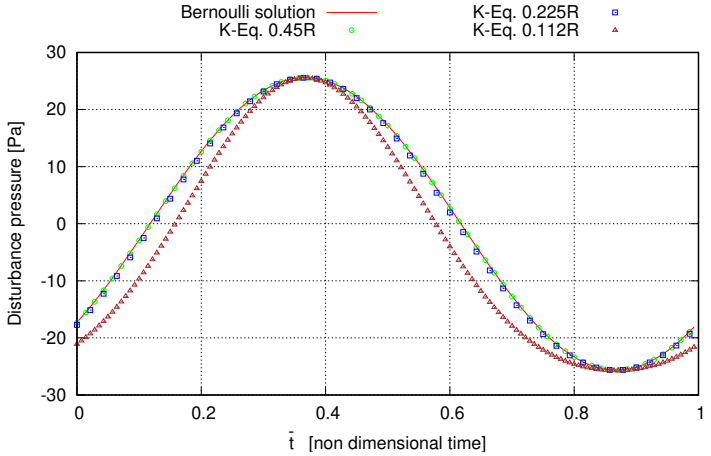

FIGURE 5.21: Translating monopole, effect of the K-Equation surface radial dimension. Acoustic pressure at Obs 2

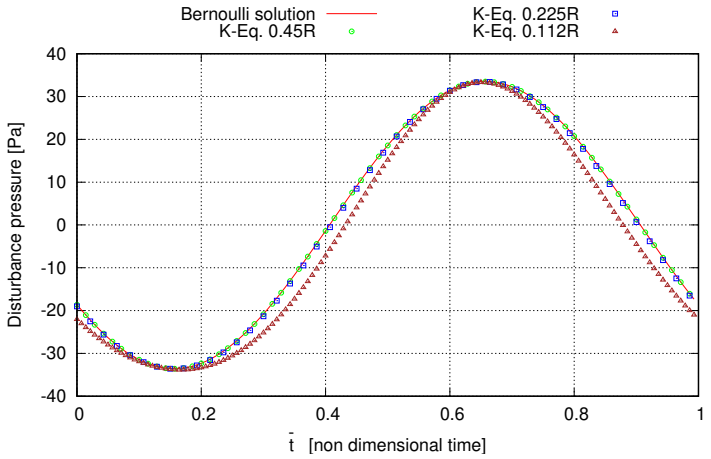

FIGURE 5.22: Translating monopole, effect of the K-Equation surface radial dimension. Acoustic pressure at Obs 3

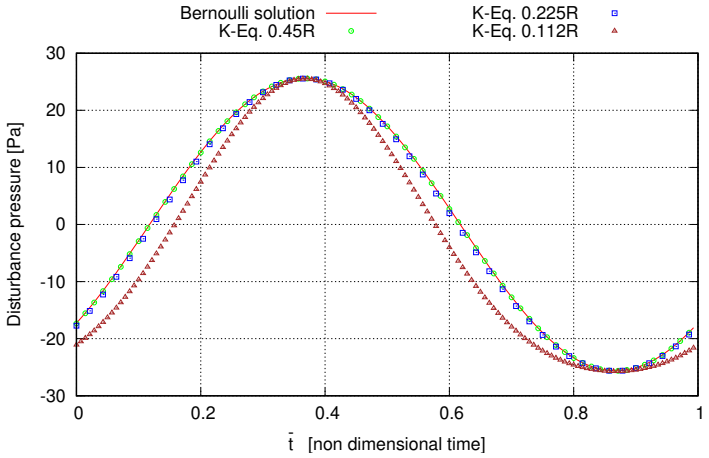

FIGURE 5.23: Translating monopole, effect of the K-Equation surface radial dimension. Acoustic pressure at Obs 4

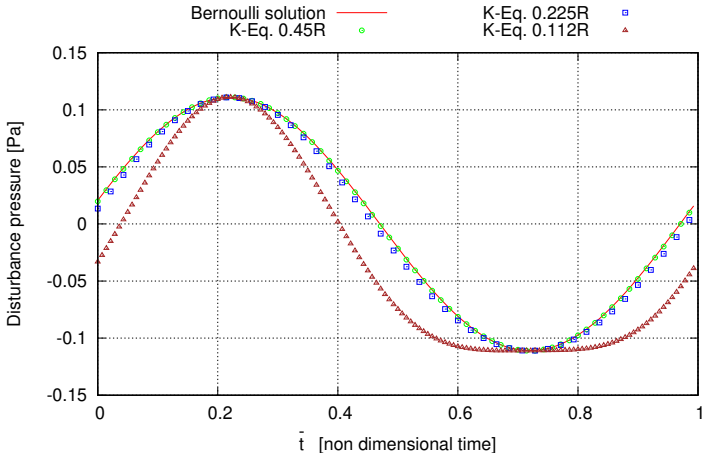

FIGURE 5.24: Translating monopole, effect of the K-Equation surface radial dimension. Acoustic pressure at Obs 5

outcomes, the better capability of the FWH-P approach to include non linear noise contributions when the permeable surface is located where flow nonlinearities are present (i.e. the quadrupole contribution are not fully embedded inside the permeable surface).

This feature will turn out to be of major importance when the noise source detection is made through a Finite Volume Code; in that case, as we will see later on, to be able to locate the porous surface as close as possible to the noise sources represents a considerable numerical advantage.

Let us now consider the directivity pattern. Akin to the FWH-P solution Fig. 5.28 shows at frequency ω_p an excellent agreement with the Bernoulli solution even in case of the tightest porous surface. On the contrary, the K-Equation predicts a directivity pattern at frequency $2\omega_p$ which magnitude increases when the permeable surface approaches to the monopole, yielding an important overestimation of the Bernoulli solution. Although similar to the outcomes of the FWH-P, such behaviour, in case of the K-Equation, is more pronounced (see Figs. 5.19 and 5.29).

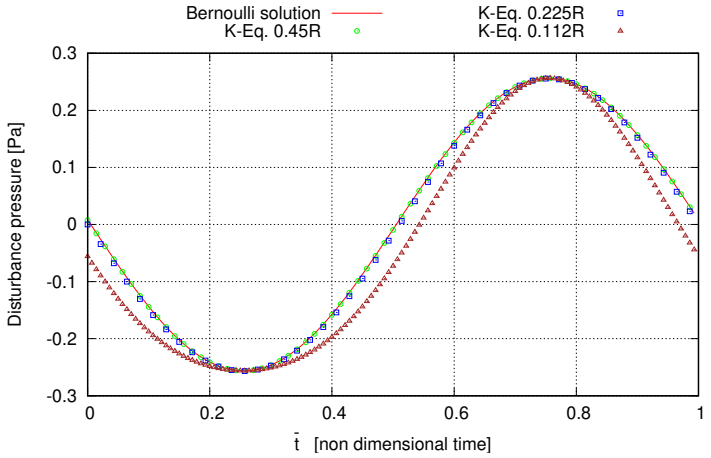

FIGURE 5.25: Translating monopole, effect of the K-Equation surface radial dimension. Acoustic pressure at Obs 6

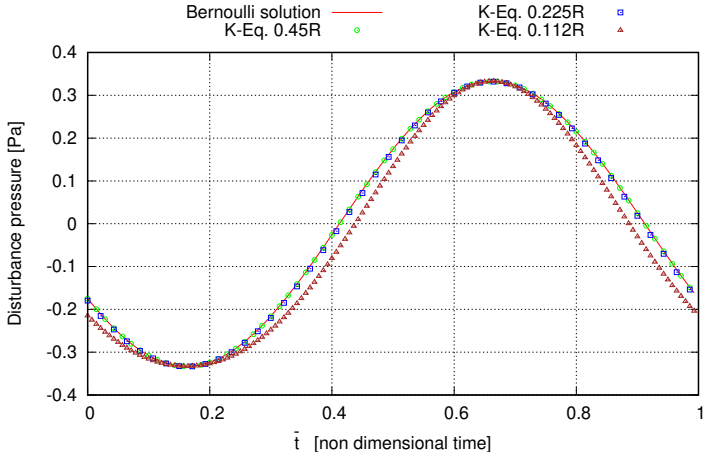

FIGURE 5.26: Translating monopole, effect of the K-Equation surface radial dimension. Acoustic pressure at Obs 7

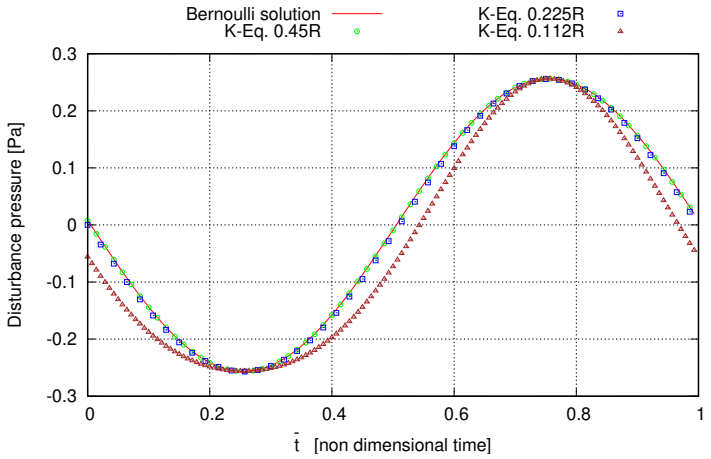

FIGURE 5.27: Translating monopole, effect of the K-Equation surface radial dimension. Acoustic pressure at Obs 8

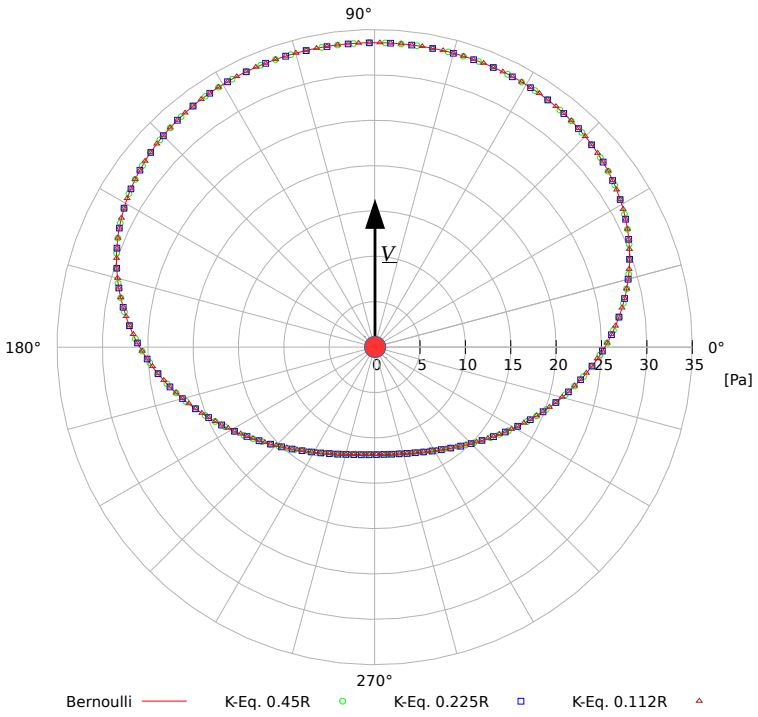

FIGURE 5.28: Comparison between K-Equation and Bernoulli directivity pattern at the nondimensional frequency $\frac{\omega}{\omega_p} = 1$

The genesis, as in the case of the FWH-P, is due to the incomplete inclusion of the nonlinear flow field features induced by the monopole, as widely discussed in section 5.3.1.2.1.

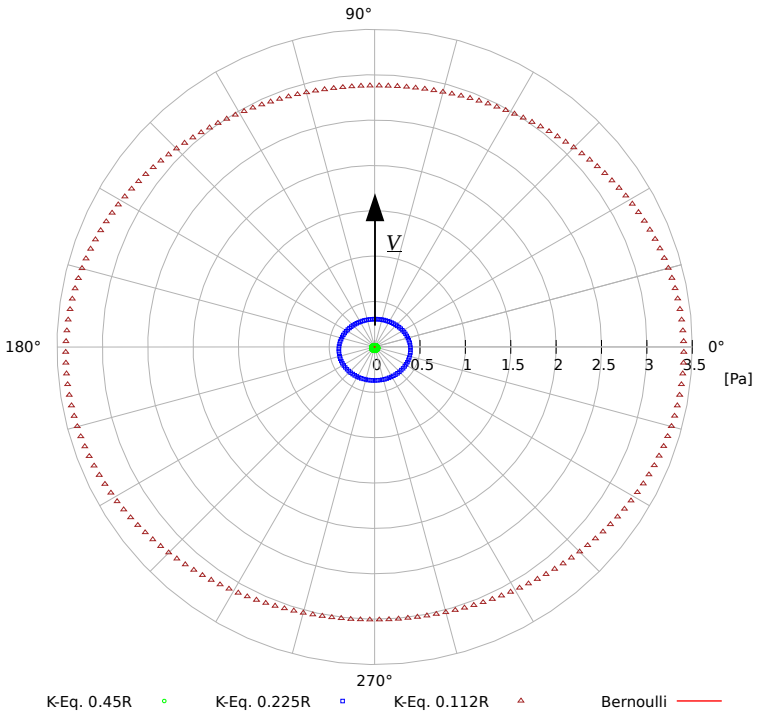

FIGURE 5.29: Comparison between K-Equation and Bernoulli directivity pattern at the nondimensional frequency $\frac{\omega}{\omega_p} = 2$

Differences in the magnitude between the FWH-P and the K-Equation predictions, at frequency $2\omega_p$, are instead explained following the dissertation in Appendix A.1.1; in that appendix, the theoretical interpretation of the difference between them, in terms of neglected the quadrupoles, is given. Essentially, it comes out that the K-Equation neglects a larger amount of noise sources respect to the FWH-P whenever the permeable surface is located where flow nonlinearities are present. Such difference, thus, explains the different predictions between the two acoustic models (i.e. FWH-P and the K-Equation) when the permeable surfaces approach to the monopole.

5.3.1.3 Effect of External Noise Sources on the FWH-P Solution

Let us now consider the layout depicted in Fig. 5.30 where a monopole placed outside the acoustic surface, at a point of coordinates $x = 0.0$ m, $y = 0.0$ m, $z = -2.0$ m, is moving with the same velocity and flow condition of the previous one. The acoustic pressure predictions for an observer located in the origin of axis (i.e. inside the porous surface) and for the *obs*1 listed in tab. 5.1 is carried out with the FWH-P solver and compared with the Bernoulli reference solution.

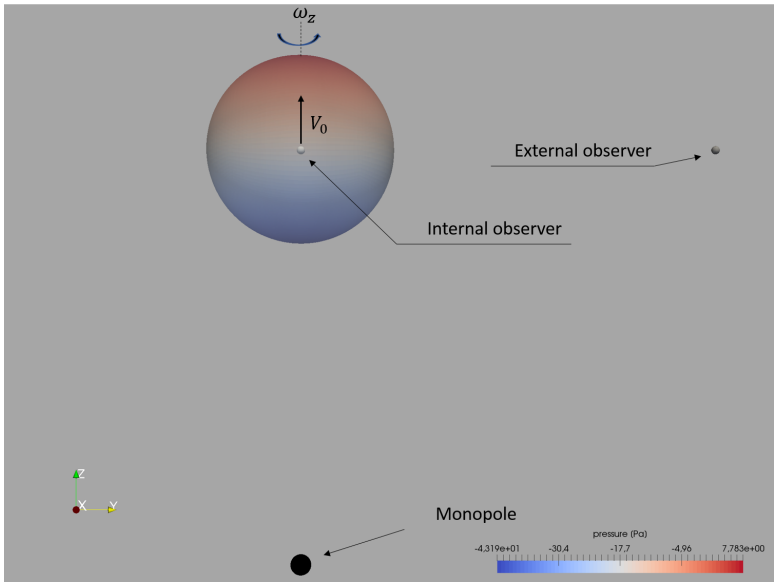

FIGURE 5.30: Monopole out of the porous surface; contours of instantaneous disturbance pressure

Fig. 5.31 depicts the acoustic pressure comparison in case of the microphone inside the porous surface; according with the findings of Chapter 3, the surface contributions due to an external noise source give rise, for an internal observer, to a pressure signature which has the opposite value of that induced by the field contribution. Therefore, the acoustic pressure

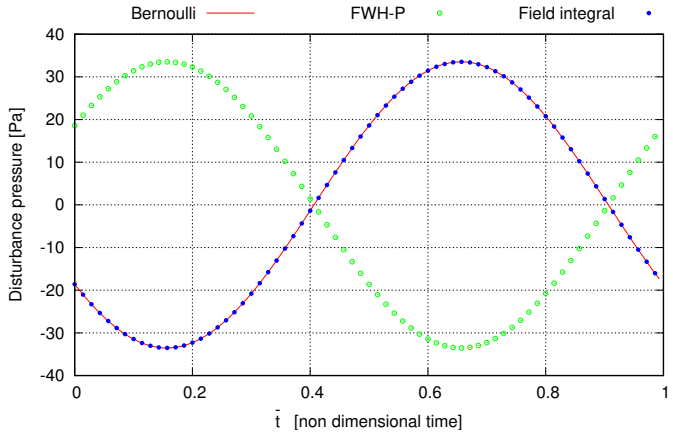

FIGURE 5.31: Acoustic pressure for an internal observer due to the external monopole

(for any observer) inside the porous surface is exactly that which would be balanced by the quadrupole field contribution.

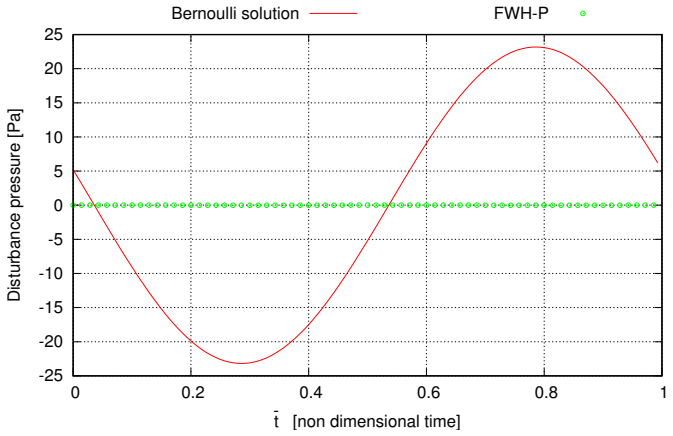

FIGURE 5.32: Acoustic pressure for an external observer due to the external monopole

Such property is useful to verify that the porous surface is located in a manner to include all the flow field noise sources in those application involving complex flow body interactions. Another important property of the porous approach is shown in Fig. 5.32 which depicts the acoustic pressure induced by external noise source on external observer. The acoustic pressure, for this observer is null. This condition is verified for any observers outside the porous surface, for which, noise sources outside the permeable surface would give their contribution, if were included, **only** through the quadrupole source term.

This also implies that in case of external noise sources the combination of monopole and dipole distributions upon the porous surface balance, giving rise to a zero contribution to the external acoustic pressure.

5.3.2 Rototranslating Monopole

Hereafter the capabilities of the FWH-P approach to replicate signals from rototranslating sources of noise is assessed through the use of a spinning monopole. To this aim the acoustic reference signal and the input data over the porous surface are provided by the theoretical model described in section 2.4, based on the potential flow theory for compressible flow and the Bernoulli Equation. The test case is characterized by a monopole rotating around the z axis and translating with three different velocity directions. The monopole is located at $x = 0.0$ m, $y = 0.2$ m, $z = 0$ m and is spinning around the z axis with an angular velocity $\omega_z = 340$ rad/s whereas the translating velocity has a magnitude equal to $|\mathbf{V}_0| = 170$ m/s and is directed in a such way to form an angle with the z axis of 0°, 30° and 60° in the zy plane.

The flow condition are characterized by air at rest at the temperature of 15 C° with a density $\rho = 1.225$ kg/m^3 and a sound speed $c_0 = 340$ m/s.

Akin to subsection 5.3.1, the pulsating frequency is set equal to $\omega_p = \omega_z$ to which corresponds a characteristic wave number $k = 1$ whereas a cylindrical porous surface is used to reproduce the acoustic pressure induced by the rototranslating monopole through the FWH-P solver.

The cylinder is centered at the origin of the reference system; it has a radius of 0.45 m and a length of 2 m. The acoustic porous surface may be either translating and rototranslating, therefore input data over the surface must be compliant with its kinematics.

Figure, 5.33 depicts a sketch of the monopole, whereas Fig. 5.34 shows the configuration under analysis in which it is embedded inside the cylindrical porous surface.

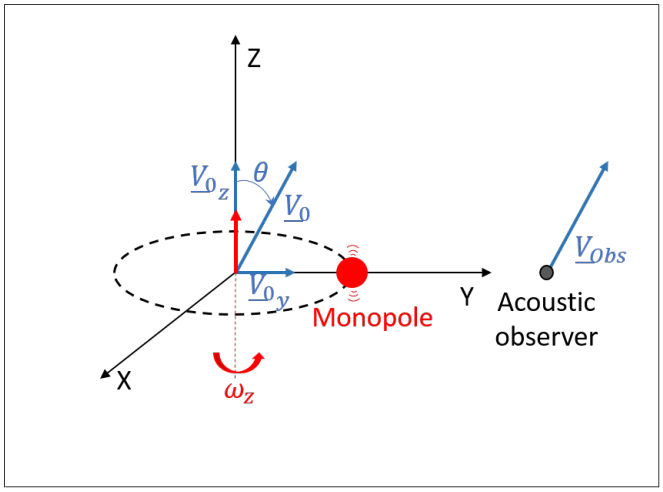

FIGURE 5.33: Sketch of the rotating monopole

Figures 5.35 to 5.38 depict the acoustic pressure comparison between the Bernoulli solution and that provided by the FWH-P solver for both kinematics of the acoustic surface, translating and rototranslating. The former is referred as FWH-P-T whereas the latter by FWH-P-R; besides, the solutions concern the near field observers listed in Tab. 5.1. Similarly, Figs. 5.39 to 5.42 show the same comparison for the acoustic observers located in the far field and listed in Tab. 5.2.

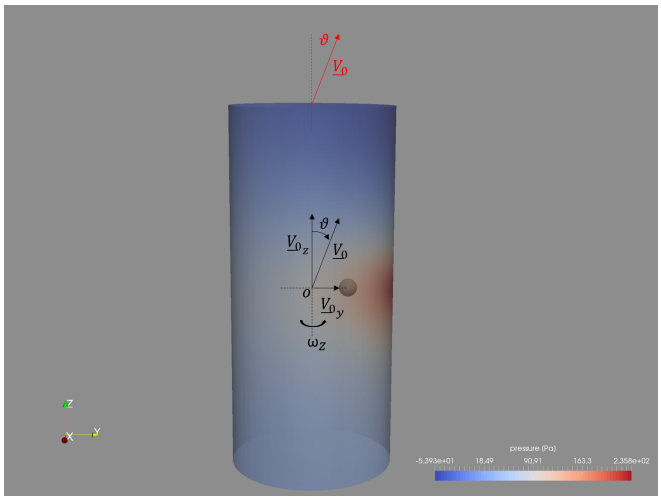

FIGURE 5.34: Cylindrical porous surface embedding a rotating monopole, contours of pressure

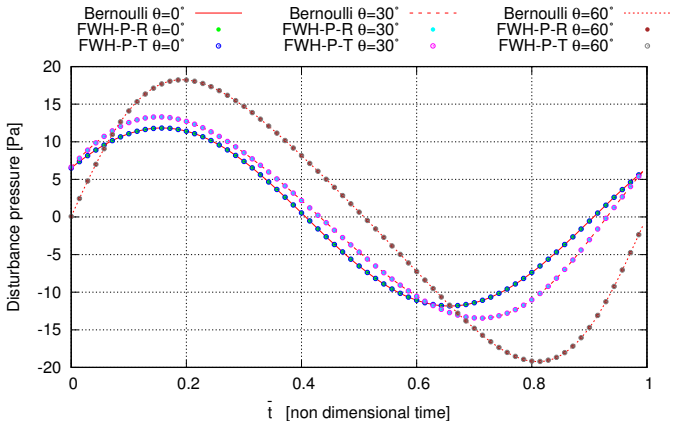

FIGURE 5.35: Rototranslating monopole, acoustic pressure comparison at Obs 1

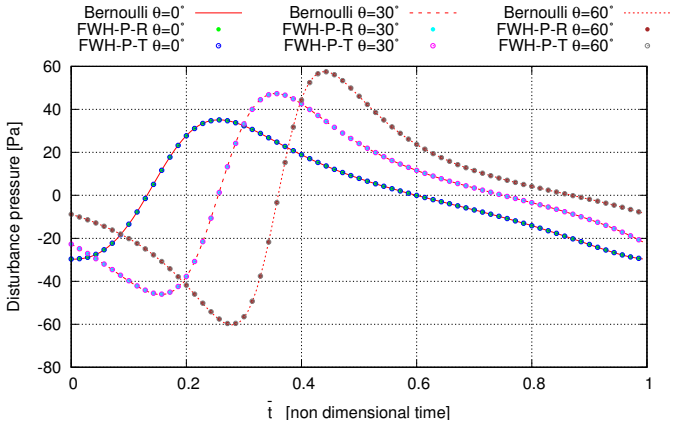

FIGURE 5.36: Rototranslating monopole, acoustic pressure comparison at Obs 2

The agreement between the Bernoulli reference solution and the acoustic pressure provided by the FWH-P in both configuration, translating and rototranslating is excellent for all

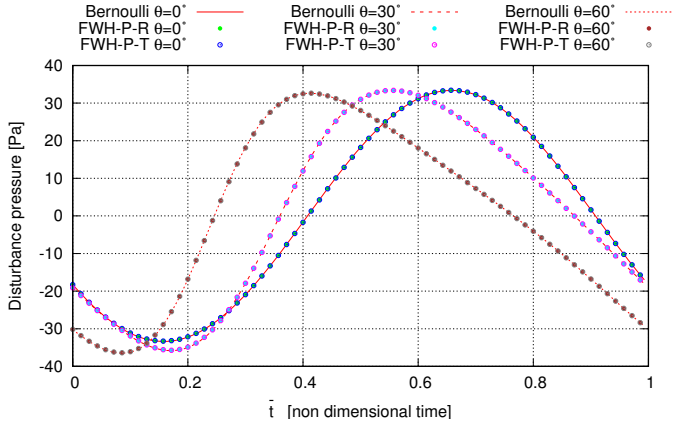

FIGURE 5.37: Rototranslating monopole, acoustic pressure comparison at Obs 3

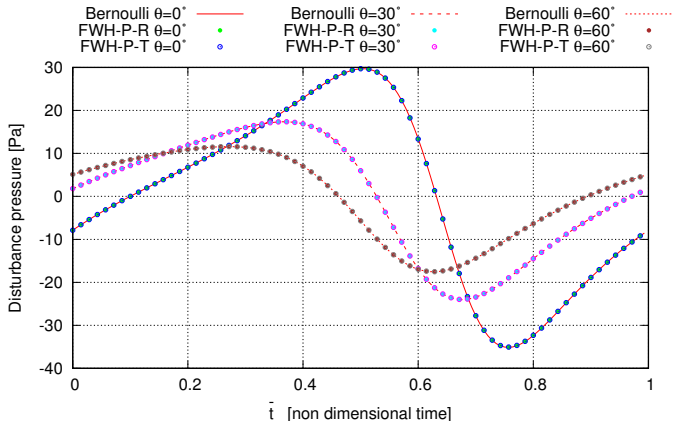

FIGURE 5.38: Rototranslating monopole, acoustic pressure comparison at Obs 4

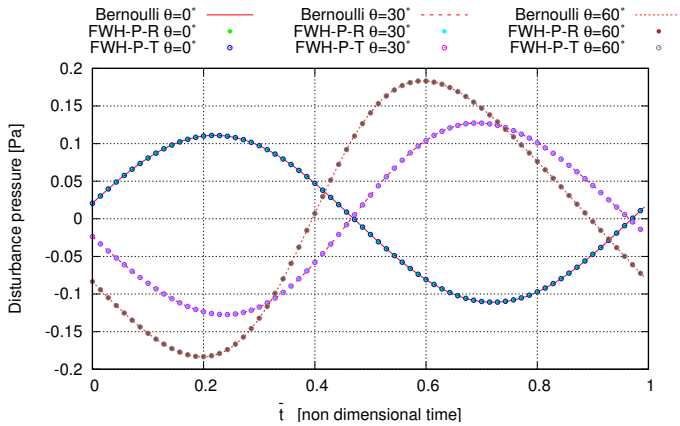

FIGURE 5.39: Rototranslating monopole, acoustic pressure comparison at Obs 5

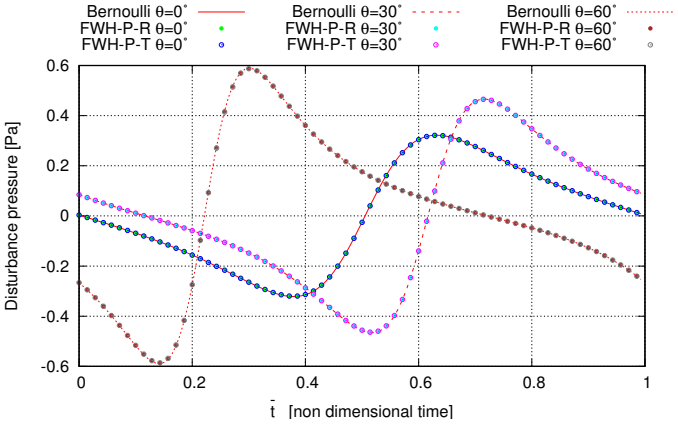

FIGURE 5.40: Rototranslating monopole, acoustic pressure at Obs 6

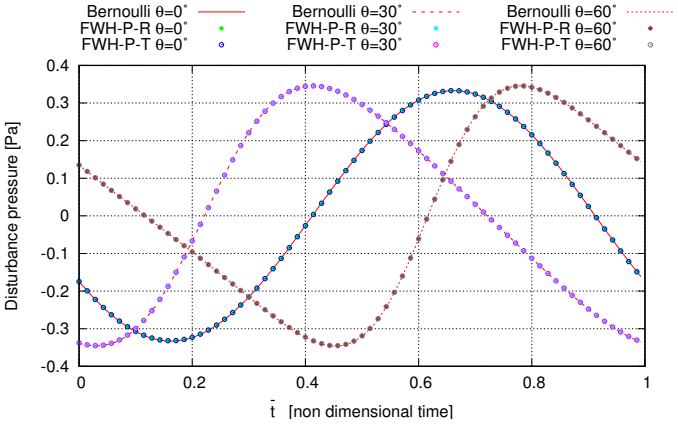

FIGURE 5.41: Rototranslating monopole, acoustic pressure comparison at Obs 7

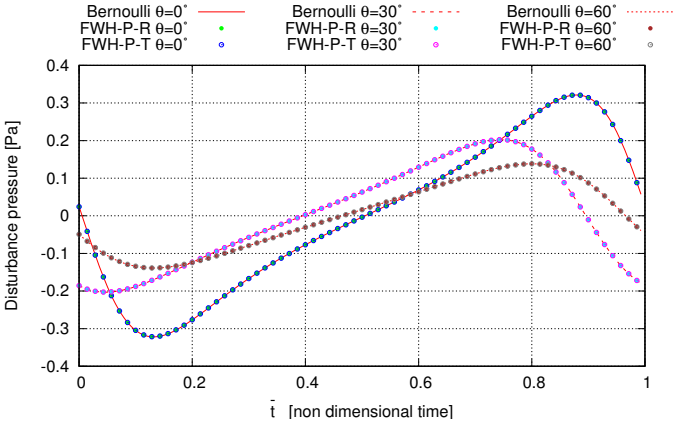

FIGURE 5.42: Rototranslating monopole, acoustic pressure comparison at Obs 8

conditions of translation velocity. However, for the rototranslating configuration the FWH-P formulation is much less computationally efficient, especially at a high Mach number [3]. This condition is essentially due to the compressibility time delay evaluation which in case of rotating surfaces is more computational expensive. Therefore, whether the data input on the acoustic surface are suitable for both configuration, the solution for translating acoustic surface represents the best choice.

[3]The comment about the computational effectiveness concerns essentially the evaluation of the source-observer time delay. The rototranslating kinematic of the porous surface entails an iterative backwards roots finding procedure. On the contrary the case of translating permeable surface allows the analytic evaluation of the time delay. Hence, the quantification of the effectiveness in terms of computational time cannot be done since it depends (strongly) on the position of the acoustic observer (the consideration of the computational effectiveness is qualitative)

5.3.2.1 Multi Monopoles at High Advancing Speed

In this subsection the behaviour of the FWH-P solver for application involving rotating noise sources moving with an high advancing ratio, as helicopter rotor configurations is addressed.

To this aim let us consider five pulsating monopoles, translating at velocity $v_0 = 180$ m/s along a direction inclined of 10° respect to the ground and spinning at angular velocity $\Omega = 6$ Hz with respect to the vertical direction, describing circles of radius 0.2 m.

Referring to the monopole M1 (see Fig. 5.43), each monopole Mk $(k = 2,3,4,5)$ is placed on a horizontal plane 0.2 m away from to the previous one and is shifted 72° around the vertical axis (counterclockwise) respect to the azimuthal position of preceding point-source (coordinates of the sources are listed in Tab.5.3). Density and sound speed of the fluid medium are $\rho_0 = 1.225$ kg/m^3 and $c_0 = 340$ m/s respectively, whereas the pulsating frequency is equal to Ω. Following the velocity-potential theory for compressible flows, the pressure disturbance and the surface data for the FWH-P formulation, are evaluated by the Bernoulli Equation at given observer positions. To this aim, a cylindrical surface 5.67 m long, co-axial with the direction defined by $\mathbf{v}_0$, having radius 1 m with end-caps placed in the horizontal plane, is taken as permeable surface S. Such a surface is assumed to translate rigidly at velocity $\mathbf{v}_0$. Figure 5.44 depicts the contour-plot of the monopoles induced-pressure pulses upon S at $t = 0$, whilst Figs. 5.45, 5.46, 5.47 propose the comparison between the Bernoulli-based signals and those predicted by the FWH-P solver at observers (co-translating at velocity $\mathbf{v}_0$) whose coordinates are summarized in Table 5.4. As shown, the agreement between pressure predictions is excellent. In addition, for a single pulsating monopole that moves as described above, Fig. 5.48 shows the directivity pattern, in the YZ plane on a circle of radius 2 m, for the first harmonic of the radiated noise spectrum. As expected, the agreement is excellent also in this case.

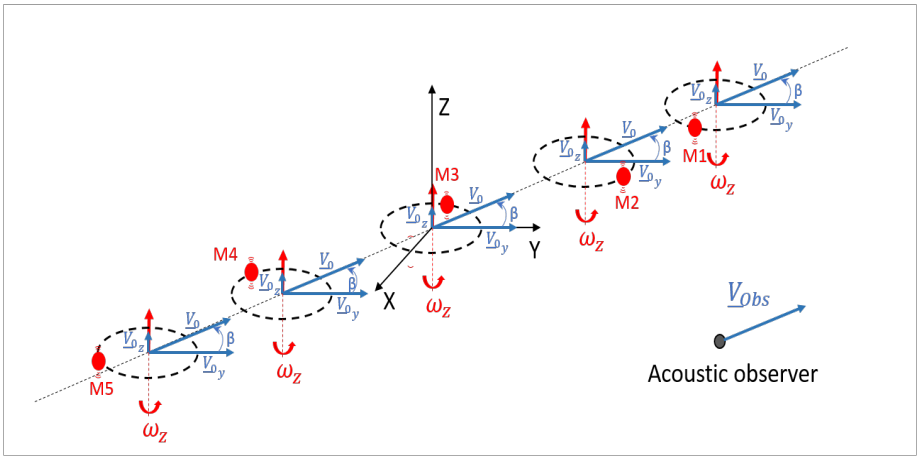

FIGURE 5.43: Sketch of the set monopoles layout.

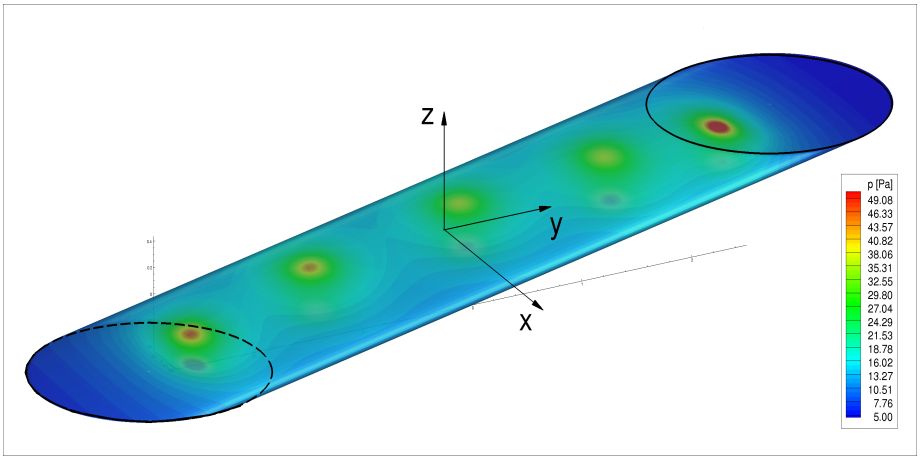

FIGURE 5.44: Acoustic porous surface and instantaneous contour of the induced pressure.

	x[m]	y[m]	z[m]
M1	0.2	2.27	0.4
M2	0.06	1.32	0.2
M3	-0.16	0.12	0.0
M4	-0.16	-1.25	-0.2
M5	0.06	-2.46	-0.4

TABLE 5.3: Sources position.

	x[m]	y[m]	z[m]
Obs1	0.0	4.76	0.84
Obs2	0.0	-476.22	-83.97
Obs3	1.20	0.0	0.0

TABLE 5.4: Microphones position.

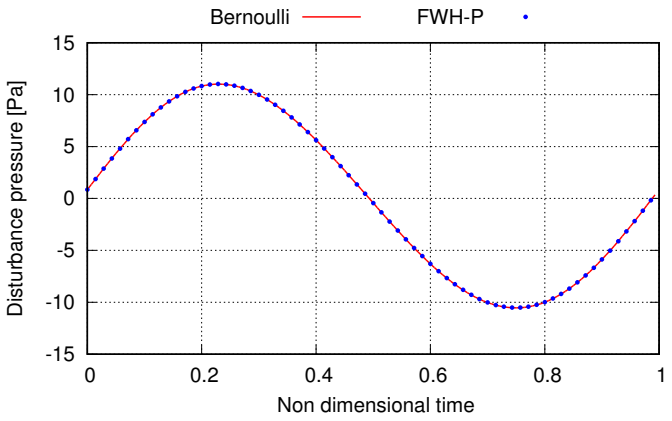

FIGURE 5.45: Comparison between FWH-P and Bernoulli results at Obs1.

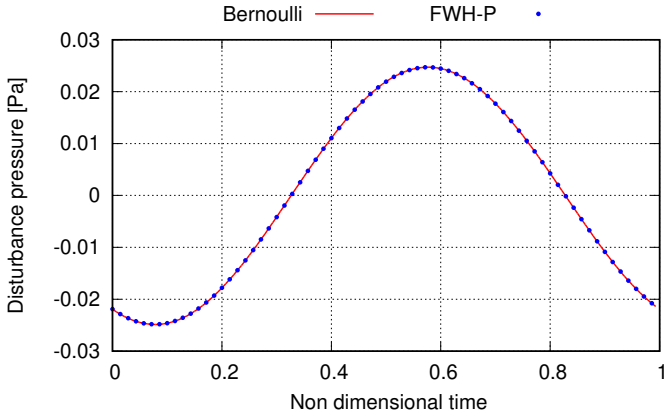

FIGURE 5.46: Comparison between FWH-P and Bernoulli results at Obs2.

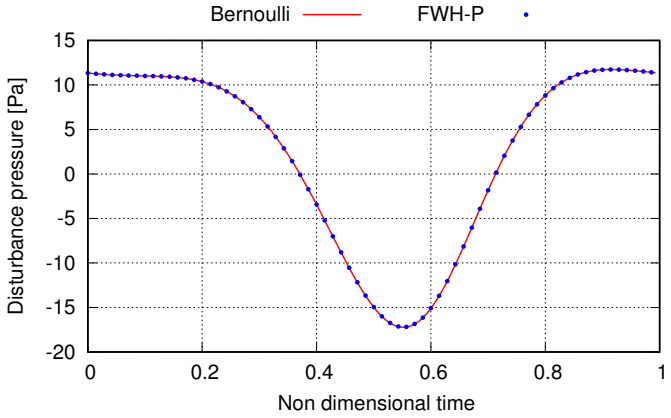

FIGURE 5.47: Comparison between FWH-P and Bernoulli results at Obs3.

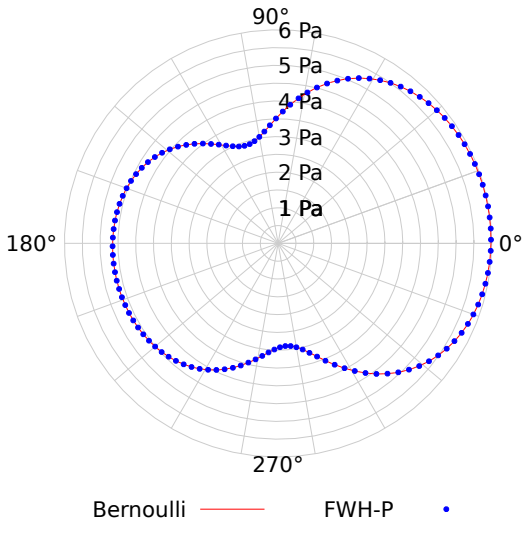

FIGURE 5.48: Comparison between noise directivity patterns.

5.3.3 Vortex Ring, the *End Cap* Phenomenon

Inside a permeable cylindrical surface S, 1.82 m long with diameter $D = 0.75$ m, let us consider a rectangular vortex-ring lying on a horizontal meridian plane, moving with axial velocity of 100 m/s and spinning around the cylinder axis at an angular velocity of 37.5 rad/s. The surface S is assumed to be rigidly connected to the vortex-ring whose internal length is 1.57 m. A sketch of this configuration is depicted in Fig.5.49: the observers $Obs1$, $Obs2$ and $Obs3$, whose coordinate are listed in Tab 5.5 are co-translating with S and placed in a plane normal to the cylinder axis, at a radial distance D from it. The pressure disturbance induced by the vortex-ring, as long as the input data on the FWH-P surface, are computed by the Bernoulli Equation combined to the Biot-Savart law.

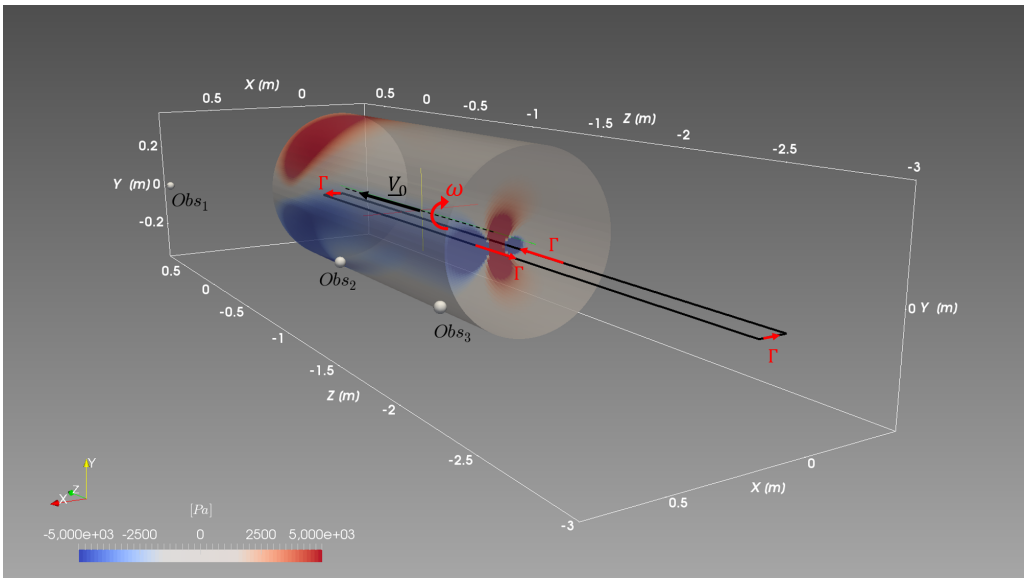

FIGURE 5.49: Sketch of the porous surface crossed by a potential vortex and the acoustic observers layout .

	x/D	y/D	z/D
Obs1	1.0	0.0	1.0
Obs2	1.0	0.0	-2.0
Obs3	1.0	0.0	-3.0

TABLE 5.5: Microphones non dimensional position with respect to the porous surface diameter, vortex ring analysis.

In view of application to rotary-wing devices (propellers or rotors) for which, unavoidably, the downstream closure intersects the wake vortices, it is useful to investigate what happens in terms of noise prediction when the acoustic surface encloses only a portion of the vortex-ring. To this aim, Fig. 5.49 shows the contour plot of the pressure upon S induced by a vortex-ring $\mathcal{C}$, 3 m long, whose filaments parallel to the cylinder axis intersect the closure section (outflow disk). To prevent unrealistically large pressure and velocity distributions over the outflow disk, a suitable vortex core is used; here, a Rankine-type modeling is adopted. At a first glance, the pressure disturbance at observers located outside S is caused by

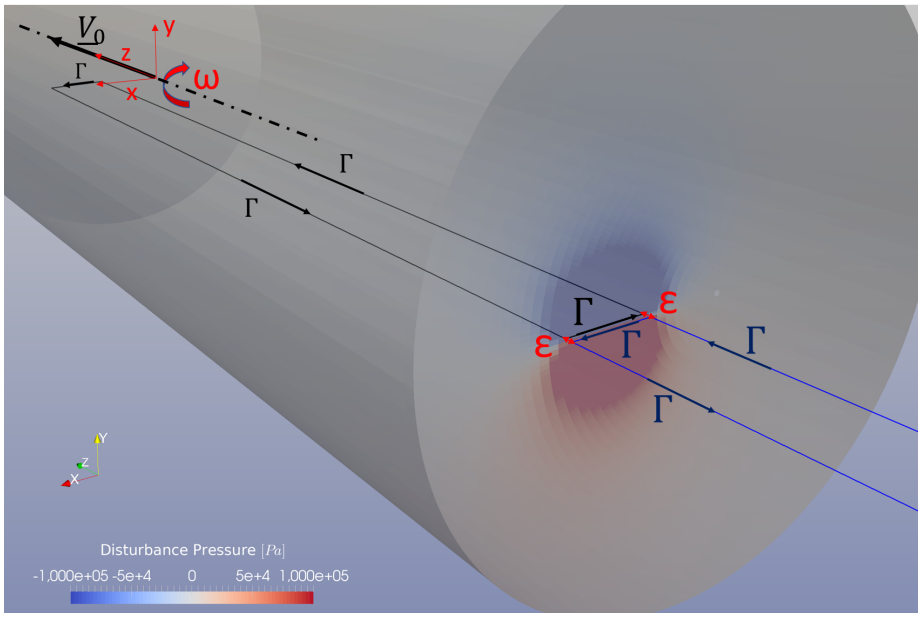

FIGURE 5.50: Sketch of the vortex cut across the outflow disk.

only the three vortex filaments inside the cylinder, whereas, those outside it, do not provide any acoustic contribution *via* the permeable surface integration in that they act as quadrupole sources of sound. This statement does obey the rules outlined by the used of generalized functions in the derivation of the FWH-P equation but, theoretically, is valid as long as the external sources of noise do not lay on the permeable surface (differently, note that the presence of sources of sound placed on the interior side of the acoustic surface is acoustically admissible). The problem herein examined is inherently out of this assumption because of the penetration between vortex and acoustic surface. To this aim figs 5.51, 5.52 and 5.53 show the comparison between the Bernoulli-based and the FWH-P acoustic pressure with and without the inclusion of the outflow disk at obs1, obs2 and obs3, respectively. The removal of the effect of the outflow disk is one of the most adopted practice shown in literature to face the highlighted *End Cap* issue. Albeit physically inconsistent the solution at obs1 provide a good estimation of the Bernoulli solution in both configuration with and without the inclusion of the outflow disk. The good quality of predictions at upstream observers is only due to the weak effect of downstream sources on upstream pressure field. Indeed, the FWH-P acoustic pressure for the acoustic observers obs2 and obs3 depicted respectively in figs. 5.52 and 5.53 badly reproduce the Bernoulli solution in both open or closed configuration when the observers are located near to the outflow disk. The issue may be overcome by splitting $\mathcal{C}$ into two closed contributions of the same intensity, $\mathcal{C}_i$ inside and $\mathcal{C}_o$ outside the acoustic surface, respectively, separated by an *infinitesimal* axial distance ϵ (see Fig. 5.50 for clarity). The comparison between the FWH-P and Bernoulli pressure signals for $\epsilon = 6.2510^{-3}[m]$ and only relative to $\mathcal{C}_i$ are shown in Figs. 5.54 and 5.55. Akin to the monopole case-studies the agreement is excellent, thus confirming the capability of the FWH-P approach to well capture the pressure disturbance due to the sources of noise enclosed by the acoustic surface, for listeners located outside S.

Moreover, Figs. 5.56, 5.57 and 5.58 show a very good agreement between FWH-P added to the pressure induced by $\mathcal{C}_o$ and Bernoulli reference signals (namely outer contribution in the figures) [4], for the obs1 , obs2 and obs3 respectively. By letting ϵ go to zero, the use of a vortex core modeling is needed and converged results are expected. However, it is found that, for values less than a threshold $\hat{\epsilon}$ (here equal to $6.2510^{-3}[m]$), the closer $\mathcal{C}_i$ and $\mathcal{C}_o$ are to the outflow disk, the higher the discrepancies of FWH-P acoustic predictions. Such a behaviour is due to the physically inconsistent fact that any vortex core modeling does not comply with the wave equation (or the Laplace equation for the incompressible case as herein).

It is also worth to note that the FWH-P solutions without the outflow disk (either in case of the vortex split into $\mathcal{C}_i$ and $\mathcal{C}_o$ or in the original configuration) coincide, proving once again, the effectiveness of the splitting procedure (see the green line in Figs. 5.52,5.57 and 5.53,5.58 relative to the Obs 2 and Obs 3, respectively). This is reasonable, in that, the union of $\mathcal{C}_i$ and $\mathcal{C}_o$, being them very close ($\epsilon = 6.2510^{-3}[m]$), is "seen" by the other two remaining portion of the porous surface (i.e. the inflow disk and the mantle of cylinder) as the original vortex. On the contrary, in case the outflow disk is included, the outcomes of the acoustic model arising from the split vortex (into the $\mathcal{C}_i$ and $\mathcal{C}_o$ parts around the outflow), or in the original configuration going trough the outflow, are very different (see the blue line in Figs. 5.52, 5.57 and 5.53,5.58 for the Obs 2 and Obs 3, respectively).

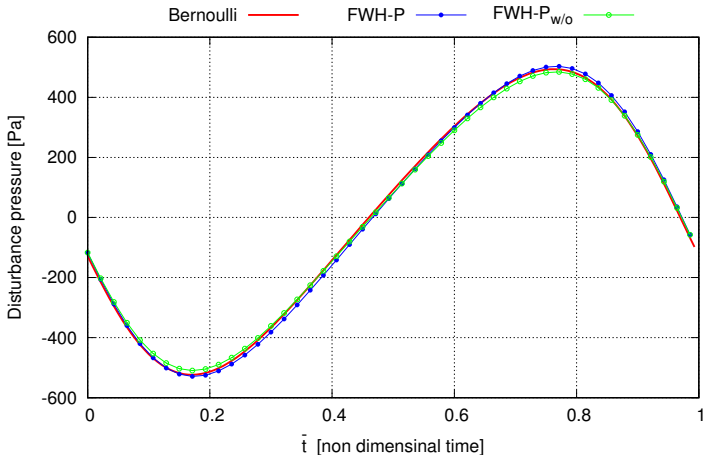

FIGURE 5.51: Vortex crossing the outflow disk, comparison between FWH-P and Bernoulli solutions at Obs1.

Such behaviour highlight the generation of spurious noise, in that, in principle, the inclusion of the outflow disk implies that only the acoustic effect of the inner vortex portion is taken into account (the influence of the external portion via the porous surface is null). Hence, if none spurious noise generation mechanism were present, both FWH-P outcomes (relative to the vortex split or not), would have been the same also in the presence of the outflow.

[4] The so called "outer" contribution represents the induced pressure evaluated at the considered observer through the potential flow theory along with the Bernoulli Equation. It concerns with the closed (in order to be compliant with the Helmholtz's theorems) vortex outside the porous surface.

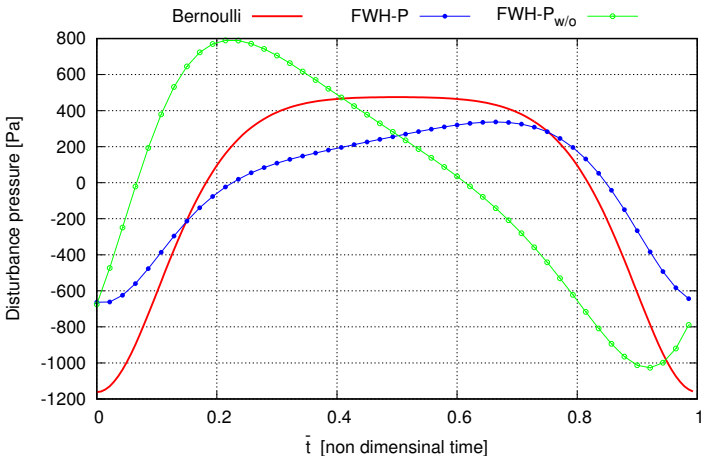

FIGURE 5.52: Vortex crossing the outflow disk, comparison between FWH-P and Bernoulli solutions at Obs2.

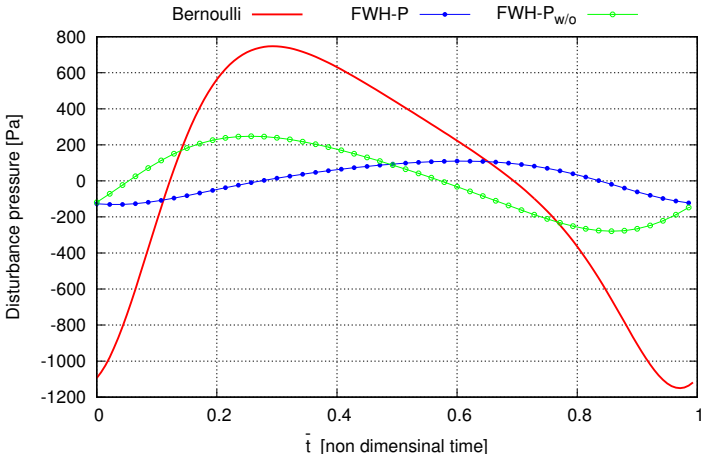

FIGURE 5.53: Vortex crossing the outflow disk, comparison between FWH-P and Bernoulli solutions at Obs3.

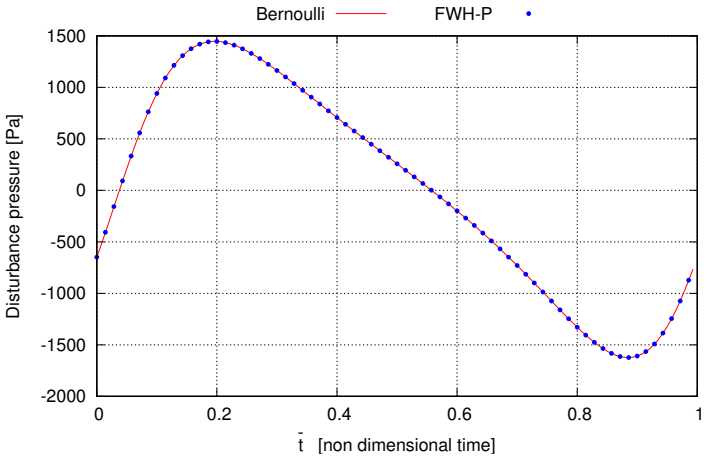

FIGURE 5.54: Comparison between FWH-P and Bernoulli solutions at Obs2 relative to the $\mathcal{C}_i$ vortex.

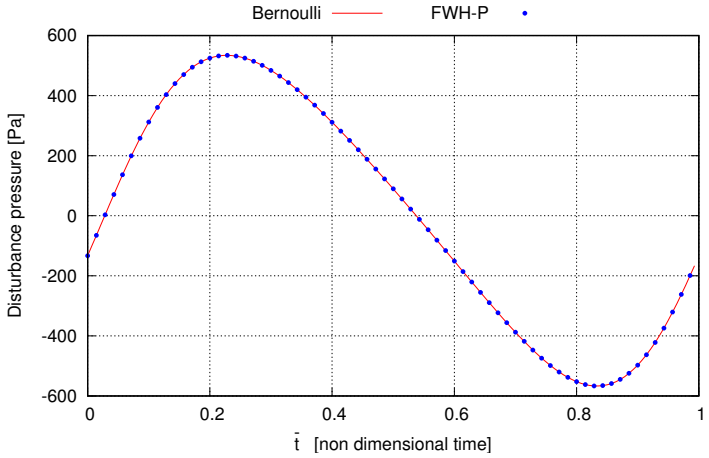

FIGURE 5.55: Comparison between FWH-P and Bernoulli solutions at Obs3 relative to the $\mathcal{C}_i$ vortex.

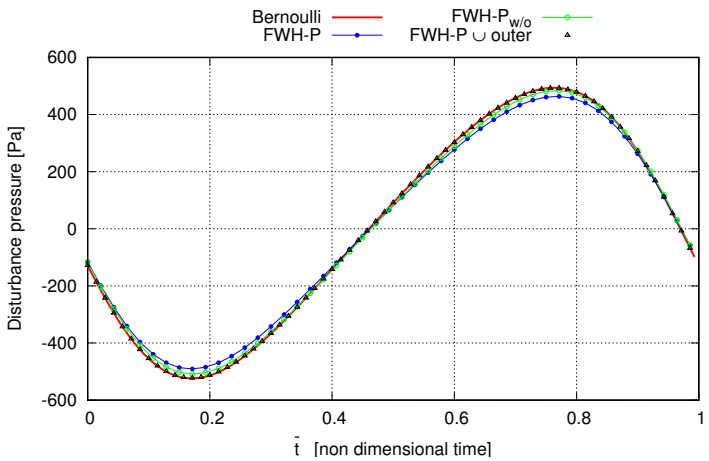

FIGURE 5.56: Vortex split around to the end cap. Comparison between FWH-P and Bernoulli solutions at Obs1.

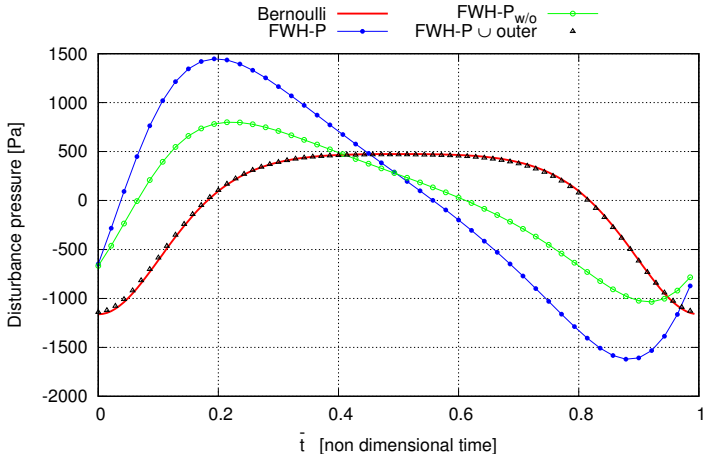

FIGURE 5.57: Vortex split around to the end cap. Comparison between FWH-P and Bernoulli solutions at Obs2.

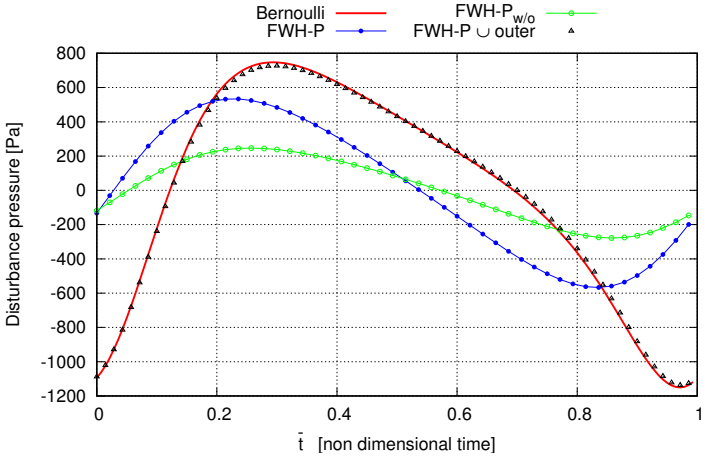

FIGURE 5.58: Vortex split around to the end cap. Comparison between FWH-P and Bernoulli solutions at Obs3.

5.4 Assessment of the Permeable FWHE

In the following the effectiveness of the Permeable FWHE (namely FWH-P) to account with the noise prediction of rotary wing configurations is assessed; both simplified test cases and devices of industrial interest are investigated. Specifically, different aero/hydrodynamic solvers are used either to provide the velocity and pressure upon the porous surface and to carry out the disturbance pressure used as baseline for comparison with the FWH-P acoustic solutions.

5.4.1 Slender Blade Propeller by 3D Panel Method Aerodynamics

The purpose of this subsection is the assessment of the FWH-P equation in case of noise generated by rotating bodies moving through the flow. Besides, the acoustic effects of the *End Cap* on realistic configurations are investigated in order to extend the suggestion obtained in the case of a single free-divergence vortex ring (see section 5.3.3). Specifically, the aeroacoustic behaviour of a simplified propeller model, composed of a single rectangular blade 1 m long, with a linear twist distribution ranging from 55° (at the root) to 19° (at the tip), constant chord $c = 0.1$ m, root cut-off of 0.2 m and NACA 0012 airfoil sections, is investigated.

The operating conditions are defined by the horizontal advance ratio $J = U/nD$ equal to 0.75 and three different angles of inclination (in the vertical plane) of the translating velocity, $(0°, 15°, 30°)$. Symbol $n = 4.77$ Hz denotes the blade angular velocity, $D = 2$ m indicates the blade diameter, whereas U represents the magnitude of the advancing velocity.

The simulation is carried out with air at rest, at a temperature of $T = 15$ C°, which corresponds a density $\rho = 1.225$ kg/m^3 and a speed of sound $C_0 = 340$ m/sec.

The permeable surfaces used for aeroacoustic computations are cylinders with generatrix line parallel to the direction of the advancing speed, rigidly translating with the propeller hub. The pressure disturbances at observers co-moving with the propeller hub, as well as pressure and velocity field distributions upon the permeable surfaces, are evaluated by combining a fully-validated panel method solver with the Bernoulli Equation. Such solution is valid under the assumptions of unsteady, incompressible, inviscid and irrotational flows around three-dimensional lifting bodies, herein extended to the analysis of propellers in arbitrary motion (see section 2.2).

5.4.1.1 Axial Motion

The condition of axial motion (i.e. characterized by a rotational and advancing velocity laying on the same direction) of the above described single blade configuration is hereafter investigated.

Particularly, the following two acoustic analysis are carried out:

i) a case in which the blade and wake are fully embedded inside the porous surface depicted in Fig. 5.59

ii) a condition in which the potential wake downstream of the rotor crosses the outflow disk (shown in Fig. 5.60) giving rise to the so called *End Cap* issue. In the following, such

aspect is deeply investigated because it represents one of the most concerning aspect in the application of the permeable configuration for which a debate is still open.

5.4.1.1.1 Fully Embedded Condition

The layout is characterized by a cylindrical porous surface able to completely embed the blade and five turns of prescribed wake; the axial position of the inflow disk upstream the rotor is $x = -1.5$ m, $y = 0$ m, $z = 0$ m whereas it has axial and radial dimension of 10 m and 2 m, respectively. The location of the acoustic observer is listed in Tab. 5.6.

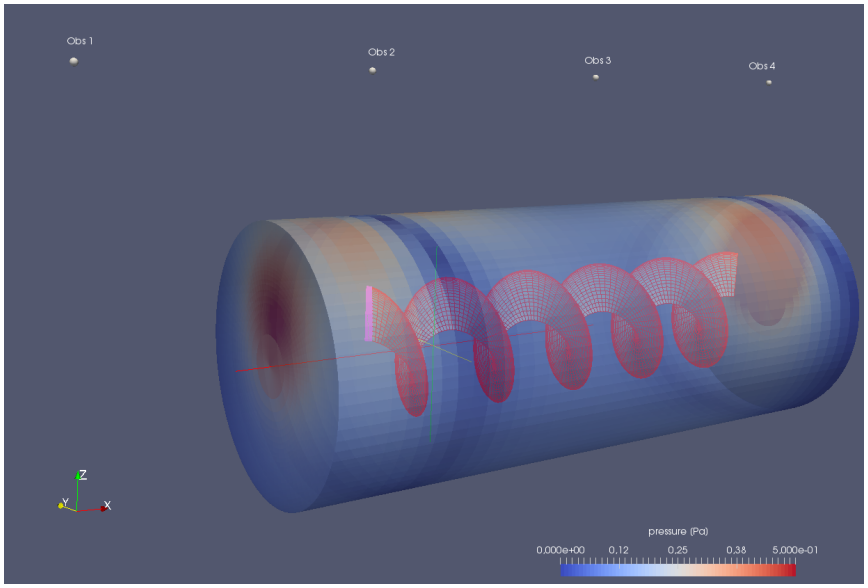

FIGURE 5.59: Blade and wake embedded inside the porous surface.

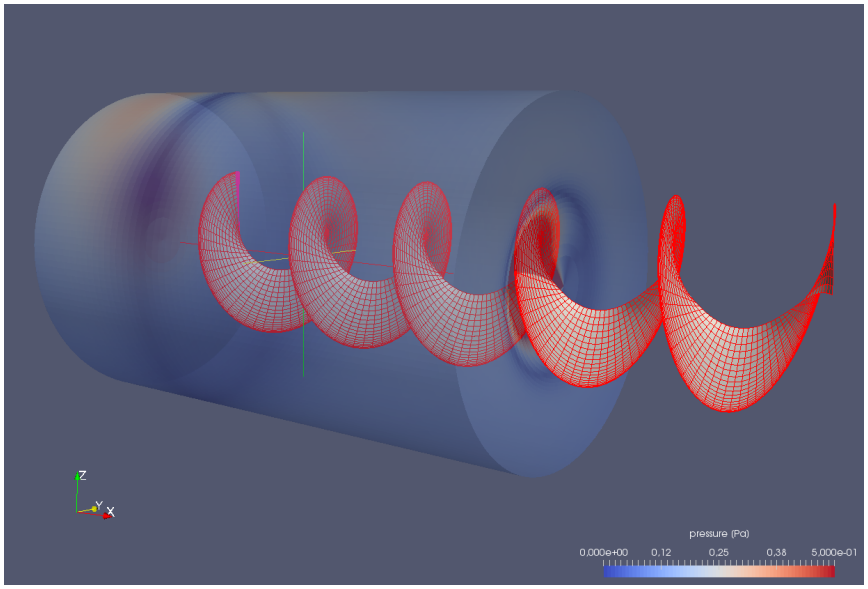

FIGURE 5.60: Potential wake interacting with the porous surface, highlight of the *End Cap* issue.

Figures 5.61, 5.62, 5.63 and 5.64 concern the comparison between the FWH-P approach and the Bernoulli reference signals.

	x[m]	y[m]	z[m]
Obs1	-4.0	0.0	4.0
Obs2	0.0	0.0	4.0
Obs3	4.0	0.0	4.0
Obs4	8.0	0.0	4.0

TABLE 5.6: Microphones position for the mono blade case.

The agreement is excellent for all observers, thus demonstrating, once again, the capability of the porous approach to replicate acoustic signals generated by moving sources of sound along with the non-linear induced flow field.

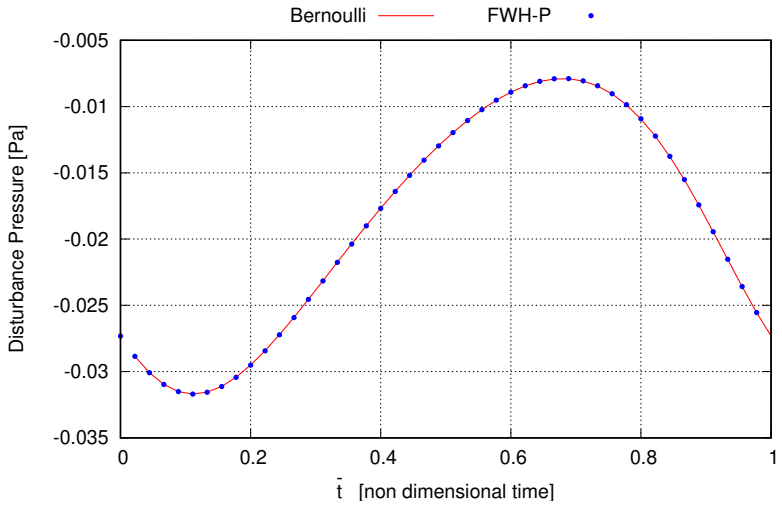

FIGURE 5.61: Fully embedded slender blade and wake, acoustic pressure comparison between FWH-P and Bernoulli at Obs1.

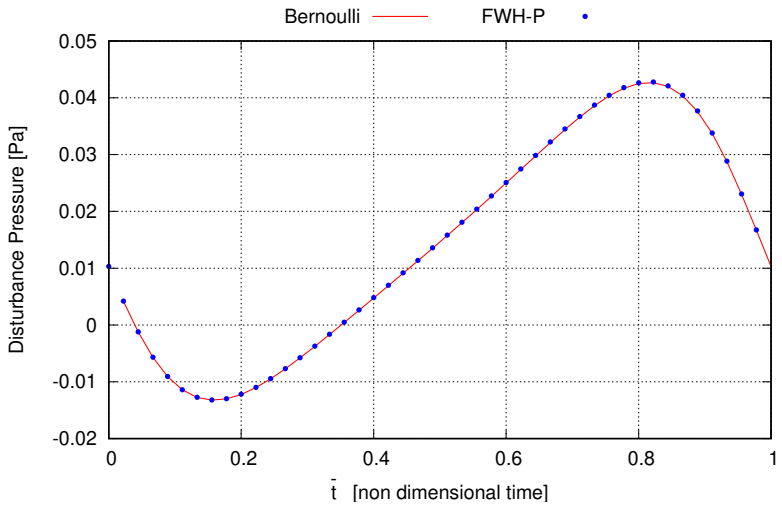

FIGURE 5.62: Fully embedded slender blade and wake, acoustic pressure comparison between FWH-P and Bernoulli at Obs2.

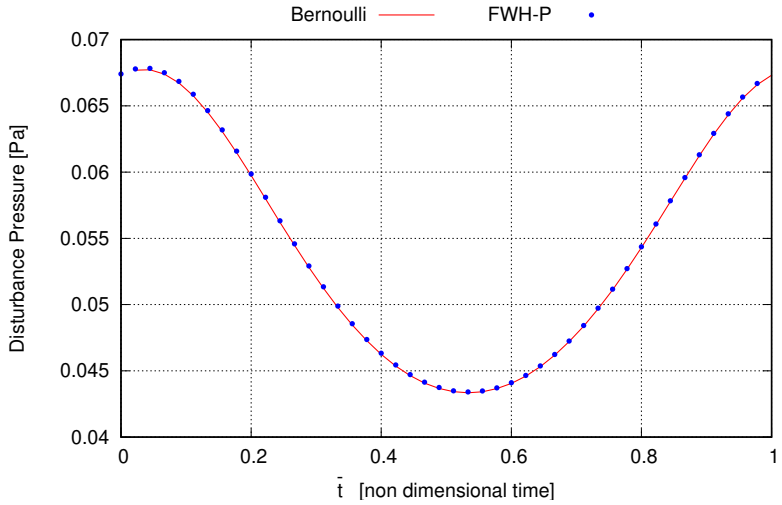

FIGURE 5.63: Fully embedded slender blade and wake, acoustic pressure comparison between FWH-P and Bernoulli at Obs3.

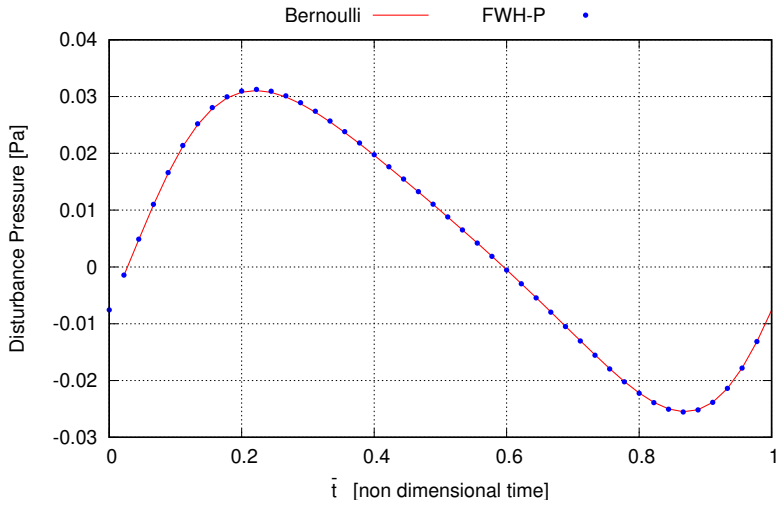

FIGURE 5.64: Fully embedded slender blade and wake, acoustic pressure comparison between FWH-P and Bernoulli at Obs4.

5.4.1.1.2 End Cap Condition

The analyzed configuration is characterized by a cylindrical porous surface embedding the blade and only a portion of the wake; the axial position of the inflow disk upstream the rotor is $x = -1.5$ m, $y = 0$ m, $z = 0$ m whereas it has axial and radial dimension of 6.5 m and 2 m, respectively.

The intersection of the wake with the outflow disk give rise to the *End Cap* condition depicted in Fig. 5.60. Acoustic spurious effects due to such phenomenon are related, as already said in Chapter 3, to the effects induced by the omission of the field contribution of the FWHE. Essentially, when eddies are convected through the outflow disk of the porous surface, the acoustic model give rise to spurious noise contribution; such effect would be canceled out by the volume integral of the FWHE if it were extended over the vortexes

portion outside the permeable surface. Thus, once the field contribution is neglected, the balancing effect is not longer present.

Hereafter, the main phenomena arising by the occurrence of the *end cap* are highlighted.

The interaction of the potential wake, which is a thin vorticity layer released from the trailing edge of a lifting body, (numerically described by a finite distribution of doublets layers) produces the following two phenomena when intercepts the closure section of the porous surface:

- the flow field induced on the porous surface by the thin vorticity layer, partially embed inside it, is not physical consistent with the wave operator (it acts as an open vortex, violating the Helmholtz's second theorem). Therefore, the resulting acoustic pressure carried out by the FWH-P approach is related with a fictitious noise sources distribution over the permeable surface which in turns produces *spurious noise*.
- aerodynamics based on the velocity potential inherently rises numerical issues when the source of noise (the potential wake) and the data surface (the closure disk) get too closer. Such phenomenon does not allow to resolve correctly the aerodynamic over the outflow disk (it would require a very fine discretization). Usually, for aero/hydrodynamic applications, the Rankine-type vortex-core is used to avoid spikes of the induced velocity; however, acoustically it does not comply with wave equation.

Keeping in mind these issues, our purpose is thus to evaluate some possible solutions of the problem in the framework of potential vortex. The above considerations, in addition to the findings of section 5.3.3, suggest as possible way to face the *End Cap* issue the cutting of the wake (composed by an unsteady discrete space distribution of vorticity layer numerically described by doublets panels) over the intersection with the outflow disk (it results in splitting the panels in two different around the outflow). The two resulting parts of the divided panels keep the same $\Delta\phi$ (i.e. the intensity of the doublets) they had before the split at the considered time. In the following it will be shown how such cut does not affects the aerodynamic solution if the gap between the two resultant panels is negligible with respect to the wake dimension.

Such procedure avoids the problem related with the violation of the Helmholtz's theorem (all noise sources inside the porous surface are acoustically physically consistent). The effect of proximity source-observer, i.e wake panels-outflow disk is also avoided, at least beyond a certain gap ϵ. Figures 5.65 and 5.66 show the result of the proposed procedure. The distance between the internal and external wake panels has here the analogous meaning of the ϵ distance considered in the section 5.3.3 such that when $\epsilon \to 0$ the original wake configuration is obtained. Although this, the wake cutting procedure turn out to be trickier than the simple vortex ring due to its helicoidal shape. A possible solution to achieve the goal, avoiding any geometrical modification of the original wake, is to remove a row of panels where the intersection wake-outflow disk occurs.

In the following, in order to assess the capability of the proposed technique two ϵ distances are analyzed, the larger is obtained cutting out two rows of panels whereas the shorter removing only one row.

Let us at first consider the shorter ϵ, Fig. 5.67 shows the comparison between the Bernoulli and the FWH-P acoustic signature relative to the blade and the inner part of the wake. The signals are in good agreement even if it is not as good as that obtained with the fully embedded configuration. This is probably due to the fact that such ϵ is not wide enough to avoid the aforementioned interaction phenomena.

In order to confirm such suggestion Figs. 5.68 and 5.69 show the acoustic pressure comparison between the Bernoulli signal relative to the external portion of wake and that arising by the FWH-P (obviously also in this case considering as noise source only the external wake) for the two different distances ϵ.

Particularly Fig. 5.68 shows the comparison of the acoustic pressure provided by the FWH-P solver and by the Bernoulli Equation for the Obs2. Such comparison concerns the closest ϵ and two different discretization strategies of the outflow disk.

The finest discretization provide better results with respect to the coarser, (the physical result should be a null acoustic pressure for the FWH-P approach since the noise sources are outside the porous surface). However, although quite low with respect to that predicted by the Bernoulli outcome, both the FWH-P solutions are unacceptable.

Differently, the results shown in Fig. 5.69, referring to the larger gap, depict an acoustic pressure which is an order or magnitude lower with respect to that obtained with the closest gap.

In view of this, the shorter ϵ turn out to be not suited, essentially because not able to avoid numerical uncertainties in the fluid dynamic data over the permeable surface (due to the inaccurate resolution of the singularities at the outflow disk).

Based on the foregoing, the following results refer to the configuration having the larger ϵ.

Figure 5.70 shows, for the Obs 2, the comparison between the Bernoulli solution relative to blade and wake (the original configuration without any cut), the solution with the gap ϵ and the FWH-P outcome summed with the outer contribution (i.e. the acoustic pressure induced by the external part of the wake at the considered acoustic observer, evaluated through the Bernoulli Equation).

The agreement between all the three solutions is excellent, thus proving that such procedure represents a viable approach to avoid the *End Cap* issue.

Furthermore, Fig. 5.71 shows for the same observer the pressure signals comparison predicted by the FWH-P with and without the inclusion of the outflow disk, indicated by FWH-P w/o and FWH-P, respectively, against the Bernoulli reference solution. In the same figure is also shown the comparison with respect to the solution obtained by summing the FWH-P closed configuration and the outer contribution (obviously predicted through the Bernoulli Equation).

The open configuration (i.e. that without the outflow disk), at least for this observer seems to provide better results in terms of wave shape. However, the mean value of the acoustic signature is not correctly reproduced. Similar considerations may be drawn for the Obs1, reported in Fig. 5.72; both the open and closed solution well reproduce the wave shape of the reference signal. Also for this observer differences in the mean value are present.

On the contrary, very different consideration may be drawn for the observers Obs3 and Obs4 reported respectively in Figs. 5.73 and 5.74.

In this case, both the open and closed configuration provide a bad estimation of the acoustic pressure.

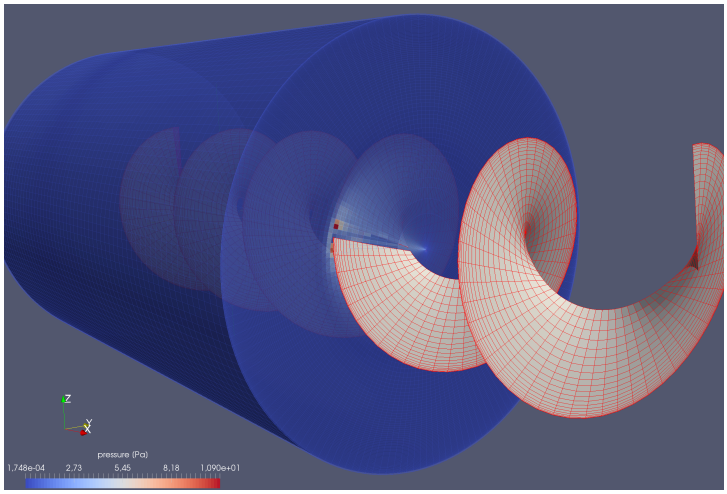

FIGURE 5.65: Segmentation of the wake crossing the outflow disk, the *End Cap* issue.

As in the case study of the vortex ring (see section 5.3.3), the spurious noise contributions due to the end cap are strongly related with the position of the observers with respect either to the noise sources and the porous surface. Particularly, such effects are negligible for observers upstream the rotor (where the intensity of the singularities over the closure disk vanish) whereas are maximum near and going behind the outflow disk for both, open and closed configurations of the porous surface. It means that, for these observers, leave noise sources outside the acoustic surface or leave it open, thus neglecting the effect of hypothetical surface S^+, such that $S \bigcup S^+$ would enclose all noise sources, produces badly estimation of the acoustic pressure.

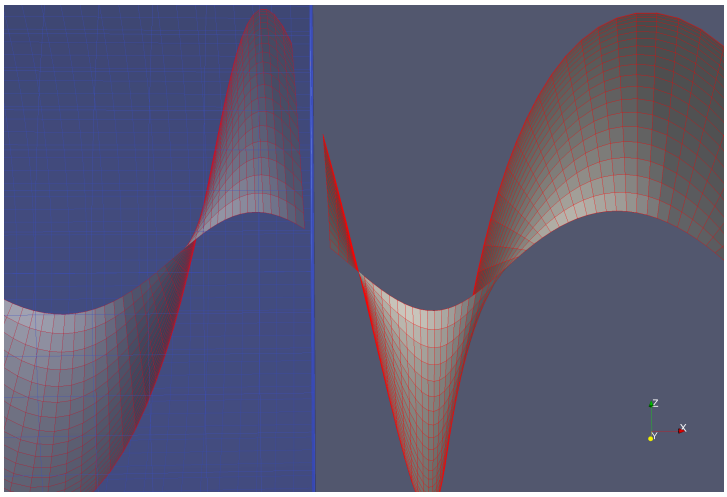

FIGURE 5.66: Enlargement of the wake interruption across the outflow disk.

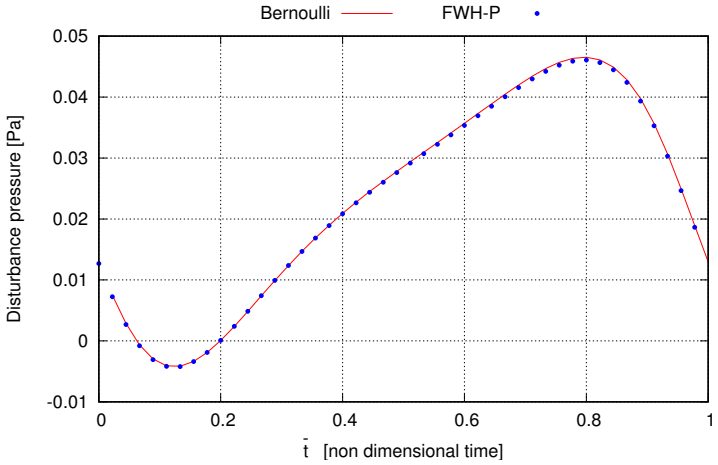

FIGURE 5.67: Comparison between FWH-P and Bernoulli solutions relative to the inner contribution at Obs2.

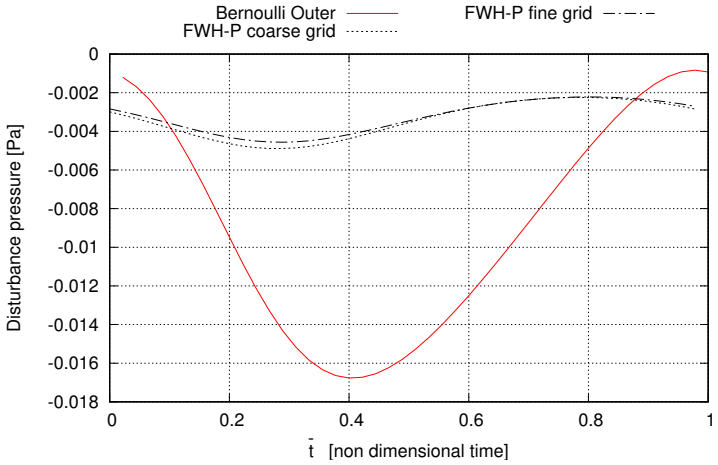

FIGURE 5.68: FWH-P vs. Bernoulli solution (only external wake); case of the closest wake cut (ϵ) across the outflow disk.

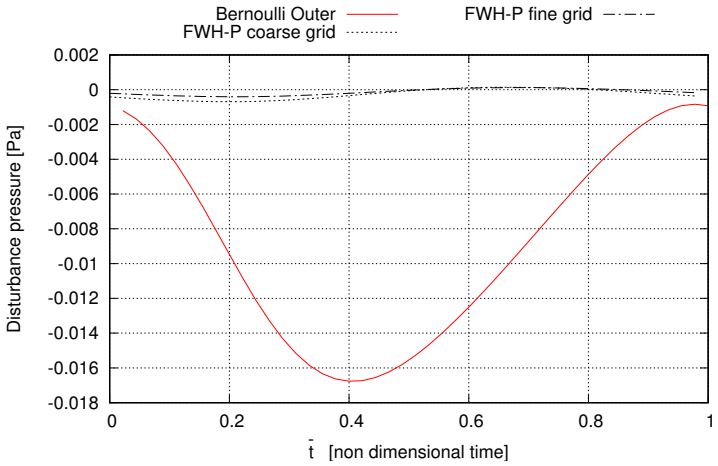

FIGURE 5.69: FWH-P vs. Bernoulli solution (only external wake); case of the largest wake cut (ϵ) across the outflow disk.

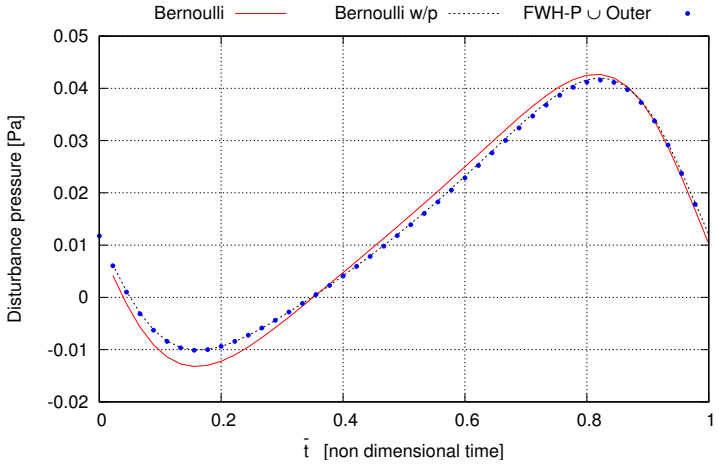

FIGURE 5.70: FWH-P summed to the outer contribution vs. Bernoulli solution relative to the whole and cut wake at Obs2.

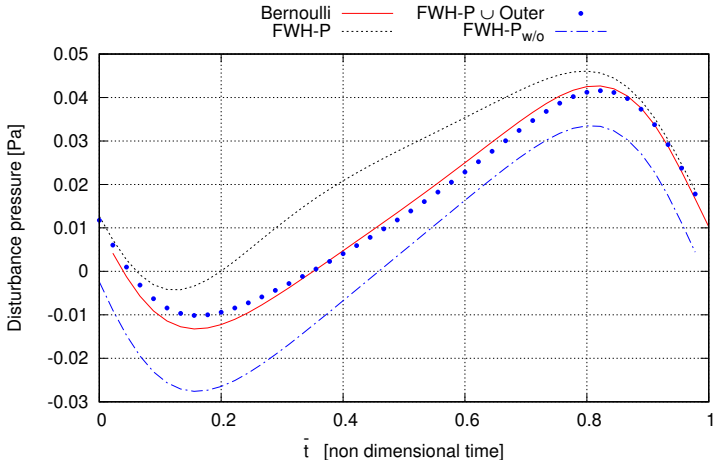

FIGURE 5.71: Comparison between FWH-P, FWH-P without the outflow disk and the Bernoulli solution at Obs2.

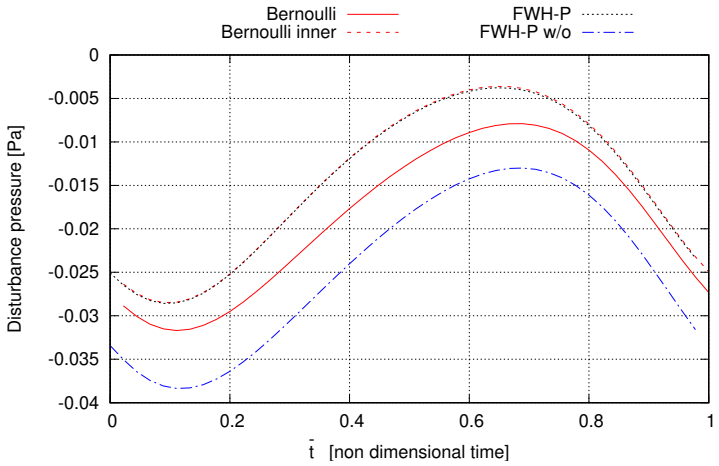

FIGURE 5.72: Comparison between FWH-P, FWH-P without the outflow disk and the Bernoulli solution at Obs1.

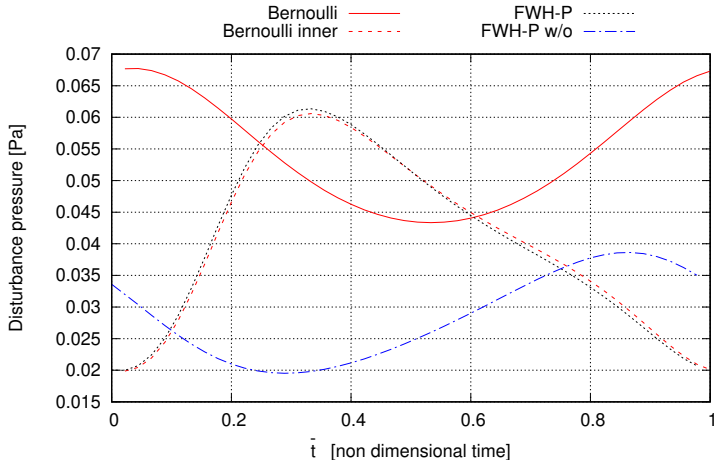

FIGURE 5.73: Comparison between FWH-P, FWH-P without the outflow disk and the Bernoulli solution at Obs3.

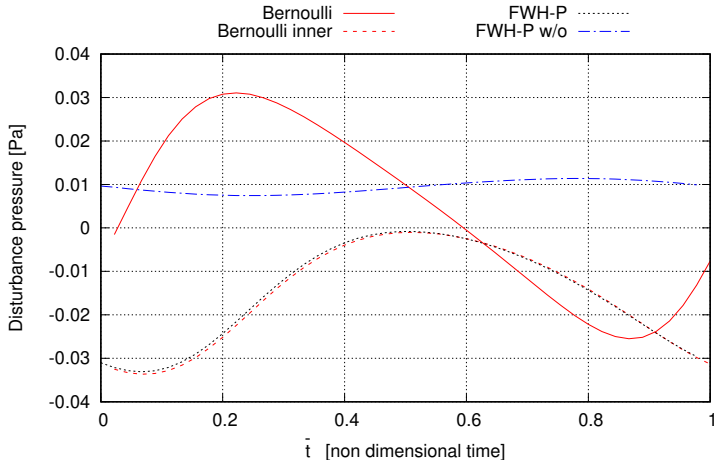

FIGURE 5.74: Comparison between FWH-P, FWH-P without the outflow disk and the Bernoulli solution at Obs4.

5.4.1.2 Inclined Inflow Condition

The inclined condition is inhere addressed (blade and wake in case of $\theta = 30^\circ$ are depicted in Fig 5.75). For an advancing speed inclined of $\theta = 15^\circ$ downward, Figure 5.76 depicts the lateral view of the pressure map upon S enclosing the blade and the potential wake convected downstream, here limited to three revolutions. Making reference to observers position shown in Fig. 5.76, whose coordinates in a frame of reference centered at the hub are given in Table 5.7, Figs. 5.77, 5.78 and 5.79 compare the Bernoulli-based converged predictions with those carried out by the FWH-P for the inclined advanced speed condition of $\theta = 30^\circ$, from the Obs1 to Obs3 respectively. As expected, the agreement is very good. Similarly, Figs. 5.80, 5.81 and 5.82 show a very good agreement for the case of inclined advanced speed condition $\theta = 30^\circ$.

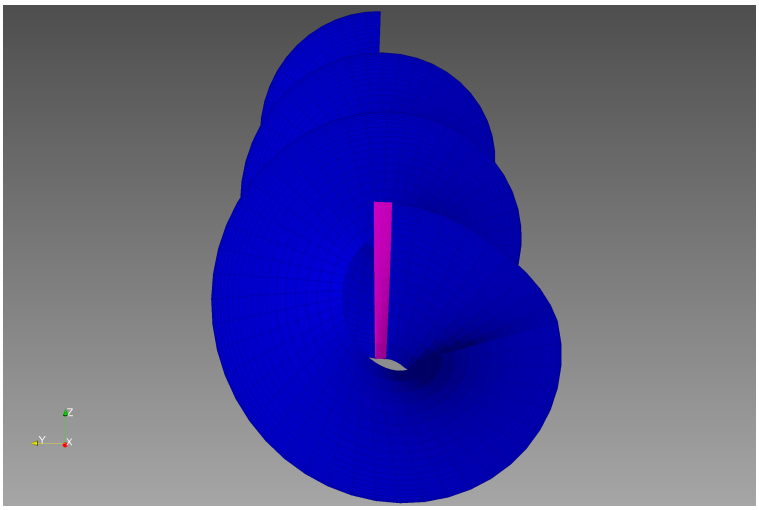

FIGURE 5.75: Front view of the blade operating in inclined inflow condition - $\vartheta = 30°$.

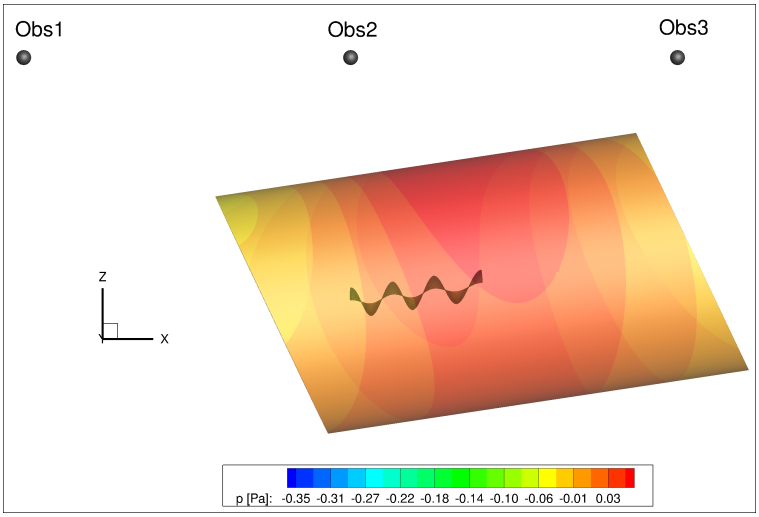

FIGURE 5.76: Side view of the blade, wake, acoustic surface and observers.

	x/D	y/D	z/D
Obs1	-3.0	0.0	4.0
Obs2	0.0	0.0	4.0
Obs3	3.0	0.0	4.0

TABLE 5.7: Nondimensional microphones position.

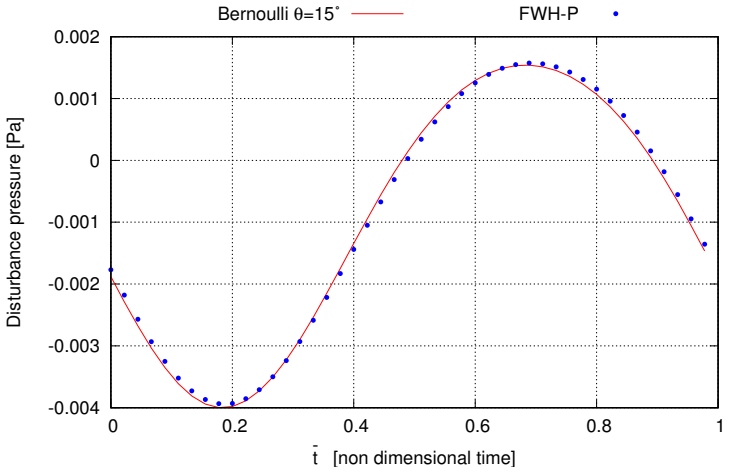

FIGURE 5.77: Comparison between FWH-P and Bernoulli results in oblique-flow at Obs1 - 15°.

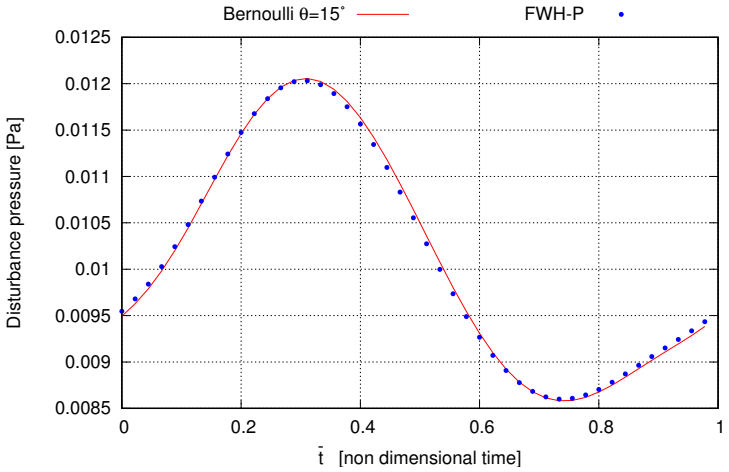

FIGURE 5.78: Comparison between FWH-P and Bernoulli results in oblique-flow at Obs2 - 15°

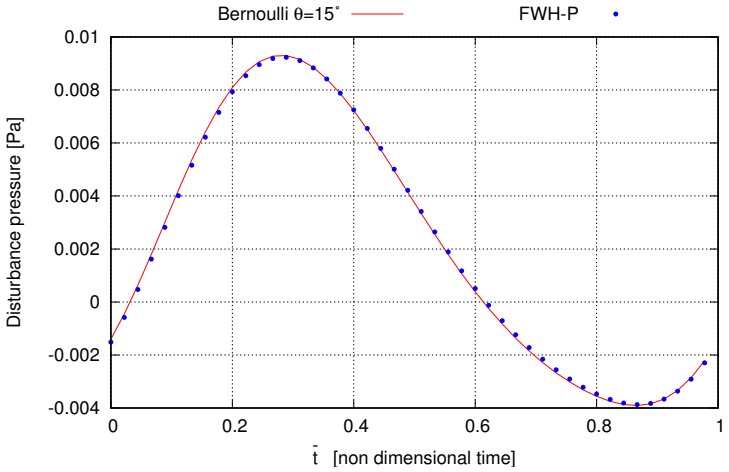

FIGURE 5.79: Comparison between FWH-P and Bernoulli results in oblique-flow at Obs3 - 15°.

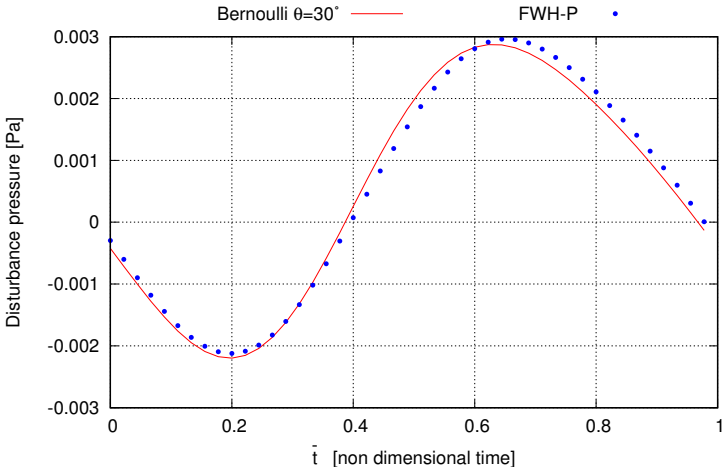

FIGURE 5.80: Comparison between FWH-P and Bernoulli results in oblique-flow at Obs1- 30°

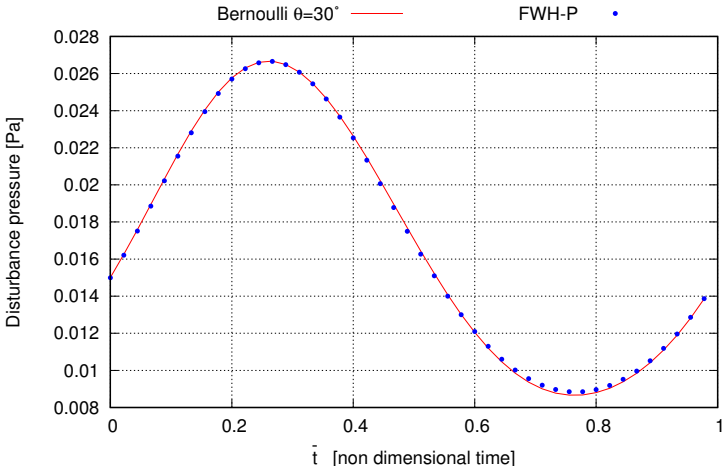

FIGURE 5.81: Comparison between FWH-P and Bernoulli results in oblique-flow at Obs2- 30°.

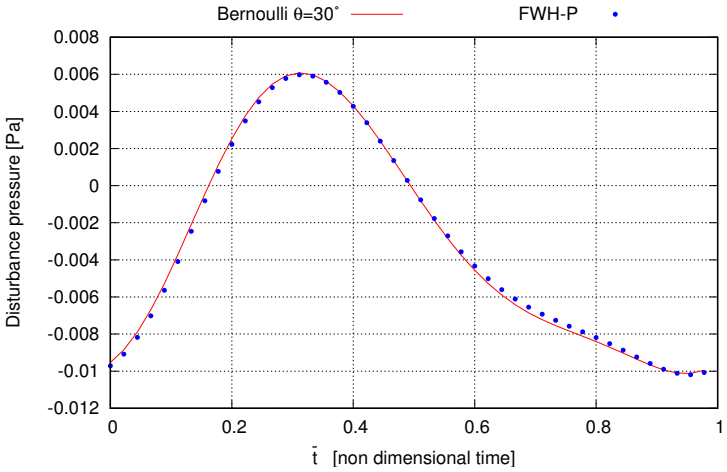

FIGURE 5.82: Comparison between FWH-P and Bernoulli results in oblique-flow at Obs3- 30°

5.4.2 Horizontal Axis Wind Turbine by RANS Aerodynamics

This section shows the application of the FWH-P technique to rotary wing devices whose fluid dynamic data over the porous surface are given by a Computational Fluid Dynamic (CFD) solver.

Specifically it concerns the aeroacoustic predictions of a three bladed Horizontal Axis Wind Turbine model scale, operating in axial onset uniform flow condition. Aerodynamic input data upon the porous surface, as well as the disturbance pressure reference used as baseline for comparisons are provided by a RANS simulation using the Spalart and Allamaras one equation closure model.

The accuracy of CFD aerodynamic results has been proven in [64] through comparisons with experimental data that include blade airloads and downstream velocity field within a 5-diameter length domain behind the rotor disk.

Geometrical and operating conditions are here briefly given.

The rotor diameter is $D = 0.9$m whereas the tip-speed ratio $\lambda = \omega D/2\, U_\infty = 6$ in which $\omega = 133.33$ rad/s and $U_\infty = 10$ m/s indicate the angular velocity of the rotor and the freestream velocity, respectively. The Reynolds number based on the tip chord length is $Re = 1.036\ 10^5$.

Aerodynamic data are carried out from a computational grid composed of many patched and partially overlapped structured blocks, with those closer to the blades assuring fine resolution of the wake portion closer to the tip and root, (see Fig 5.83). More details may be found in [64].

As widely discussed in Chapter 3 to obtain a completely equivalence between the FWH-P based acoustic solution and the field disturbance pressure provided by the fluid dynamic solver all the quadrupole source term must be embedded inside the porous surface. In order to locate the quadrupole noise sources Fig. 5.84 depicts the field distribution of the $L2$ norm of the Lighthill stress tensor for a section of field orthogonal to the $y = 0$ axis. As may be observed in Fig. 5.84 the Lighthill stress tensor cannot be fully embed inside the porous surface unless to extend it until to the boundary of the CFD computational domain. In principle, such procedure would be not correct from an acoustic standpoint because of the proximity with the computational fictitious boundary conditions (i.e. a zone where the flow field feature, pressure or velocity, are imposed). The effects induced by such part of the field are, form the fluid dynamic point of view, handled through the use of suited clustering grid strategies. To this purpose a stretching in the calculus grid is (always) introduced with essentially two intents: i) to limit the number of the grid elements in order to be compatible with the available computational resources, i.e. limit the computational time and the usage of memory ii) to introduce a numerical dissipation in order to "insulate" the zones of fluid dynamic interest (i.e. near rotor and wake) from the numerical effects of the fictitious boundary conditions.

Thus, in this and following cases, the common practice adopted is to limit the axial and radial extension of the porous surface about to the most resolved zone of the computational grid (i.e. where the CFD code is able to detect the physical consistent noise sources) [65]. The advantage of using porous surface tight to the resolved computational grid is twofold. It allows to limit the cut-off of high frequency acoustic phenomena as well as to keep out, with

respect to the porous surface, the effect of the boundary conditions. This is simply explained by the fact that pressure waves cannot cross cells with a characteristic length greater than their wave length; thus, de facto, coarse grid cells act as a low pass filter.

Based on these findings, in this and following applications the location of the permeable surface is obtained as a trade-off between the inclusion, inside it, of the L2 norm of the Lighthill stress tensor (which will be almost ever partially cut out) and the relative position with respect to the CFD grid features.

As widely discussed in chapter 3, such practice is acoustically safe, i.e. is not associated with a lost of acoustic noise features or affected by numerical issues as long as interactions between eddies convected downstream of the rotor and the permeable surface are avoided (namely, *End Cap* issue).

To this aim the Jeong's criterion [66], known as the σ_2 parameter, is here used to detect the most important vortical structures in the field. Such criterion is based on the central eigenvalue of the symmetric part of the velocity gradient; its isosurfaces of a certain negative value are associated to the vortical structures and used to detect the core of vortices convected downstream of the rotor.

Fig. 5.85 depicts the isosurfaces $\sigma_2 = 10^-3$ (the value is non dimensional); the main vortical structures predicted by the RANS simulations ends approximately after a couple of diameter downstream the rotor. Thus, it is fair to expect that vortices do not cross the porous surface if the end cap is located beyond this distance.

Such diffusive behaviour of the RANS simulation, although useful from a numerical point of view (i.e. the permeable surface may be located quite close to the body regardless to the *End Cap* issue), is not compliant with the physic of the problem; it is essentially due to the excessive turbulent viscosity predicted by the turbulence model.

Besides, although the RANS model well detect the dynamic inside the boundary layer, the numerical dissipation outside it prevents the transmission of the high frequency phenomena from the boundary layer to the porous surface (which is usually located away from the rotor in order to include as much as possible field contributions).

This makes the acoustic prediction insensitive with respect to the velocity and pressure fluctuation related with the turbulence phenomena inside the boundary layer (notably, the interaction with the trailing edge represents for the wind turbines a major noise source, see chapter 1).

Therefore, these CFD data are essentially unsuited for an accurate evaluation of the aeroacoustic field having the purposes to assess the effect of the flow field noise sources.

Nevertheless, a comparison between the pressure signals predicted by the porous formulation and those directly obtained by the CFD solver is presented. Three closed porous cylindrical surfaces depicted in fig 5.86 having diameter equal to $1.25D$ and lengths $2D$, $3D$, $4D$, respectively, fixed with the turbine blades are considered.

The comparison is shown for three acoustic observers, $Obs1$, $Obs2$, $Obs3$ located at radial position $0.75D$ from the cylinder axis, and at axial positions $x = -0.259D$, $x = 0$ and $x = 0.75D$, for $x = 0$ denoting the rotor disk plane. The location of microphones is chosen in a manner to be as close as possible to the most resolved grid in order to avoid

fictitious numerical contributions in the reference disturbance pressure directly carried out by the CFD solver.

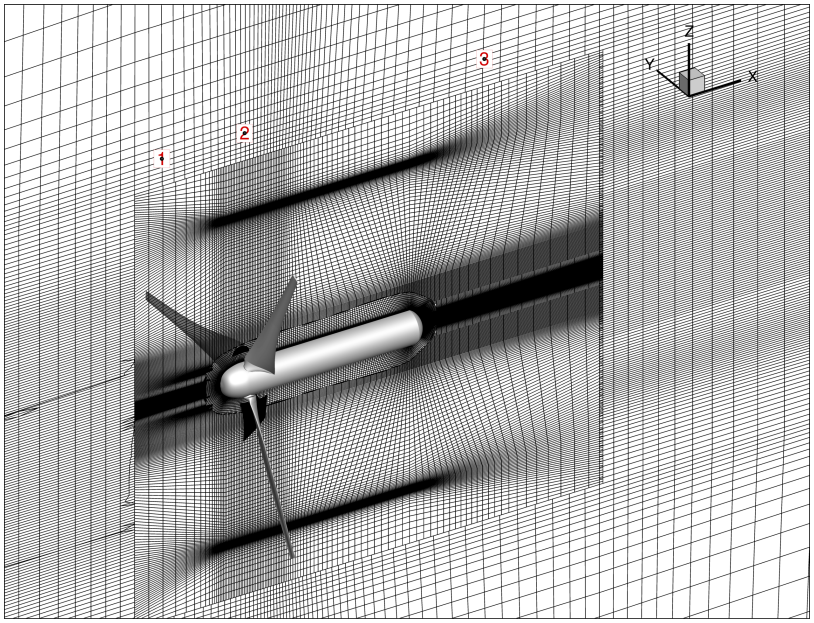

FIGURE 5.83: CFD Computational calculus grid and topology.

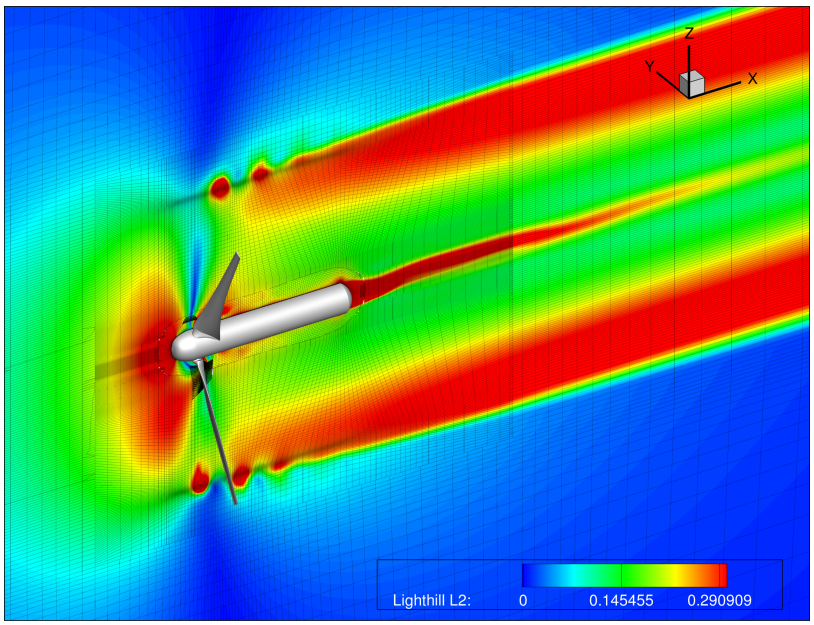

FIGURE 5.84: Contours of non dimensional norm of the Lighthill stress tensor

As depicted in Figs. 5.87, 5.88 and 5.89 for all of the observers considered, and for all of the surface lengths the agreement between CFD and FWH-P results is very good: indeed, even the 2D-length surface is capable of accurately capture the signals, in that enclosing the noise sources generated by the CFD solver.

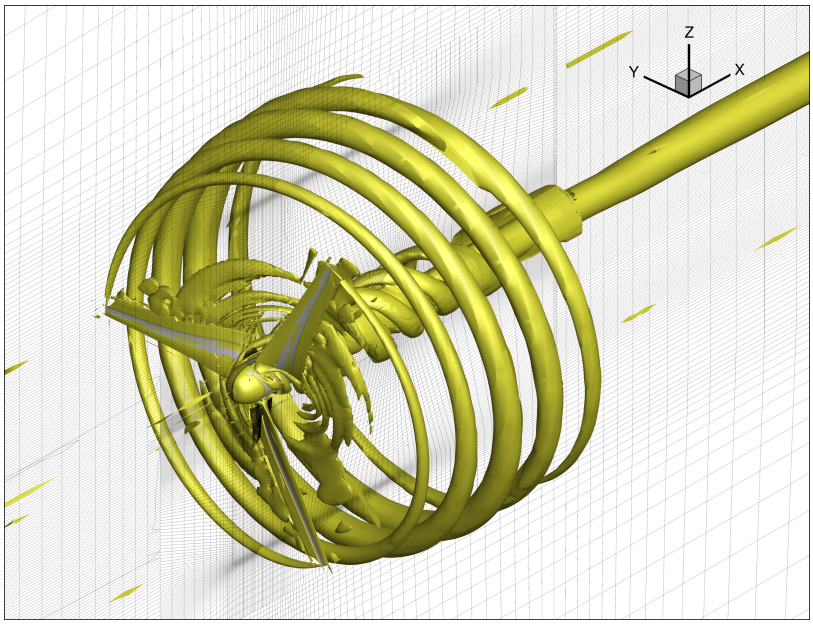

FIGURE 5.85: Jeong's criterion for the vortex core detection, $\sigma 2 = -10^{-3}$.

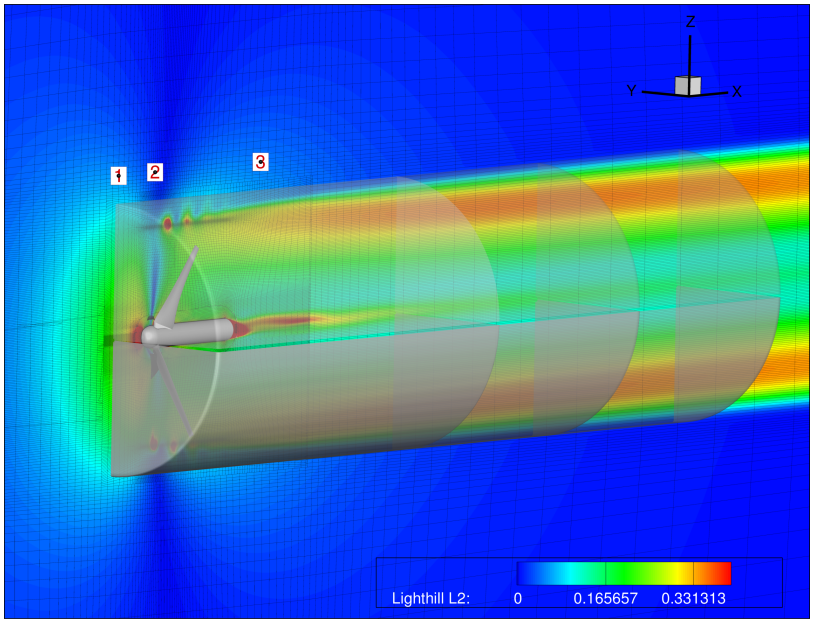

FIGURE 5.86: Porous surfaces embedding the CFD/RANS predicted Lighthill stress tensor norm.

Very similar results may be seen in Figs. 5.90, 5.91 and 5.92 [5] which show the same comparison between the CFD solution and that provided by the FWH-P solver without the closure disk.

Also in this case the agreement between two solutions is excellent, proving that all noise sources affecting the acoustic pressure at the considered observers are embed inside the acoustic surface. As evident, the character of the predicted noise signature is periodic and it

[5] The subscripts w/o in Figs.5.90,5.91 and 5.92 indicate that the acoustic effects induced by the outflow disk of the porous surface are not included in the computation of the acoustic pressure predicted by FWH-P approach.

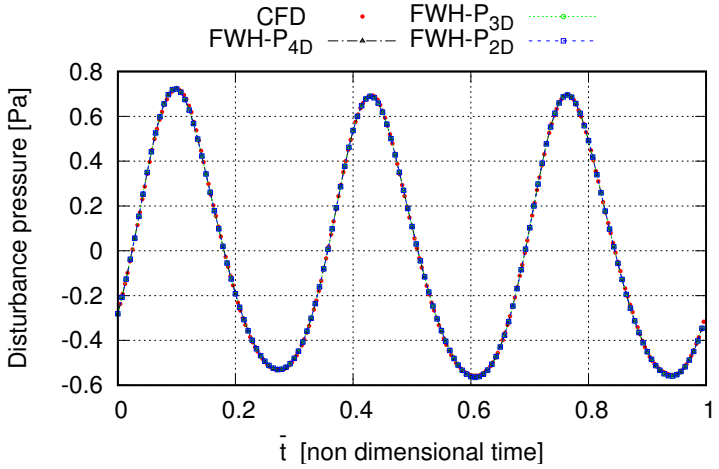

FIGURE 5.87: Comparison between the FWH-P and CFD outcomes at Obs1.

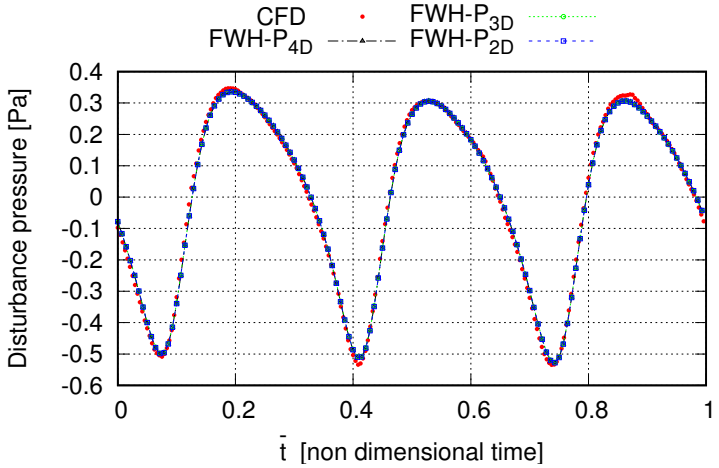

FIGURE 5.88: Comparison between the FWH-P and CFD outcomes at Obs2.

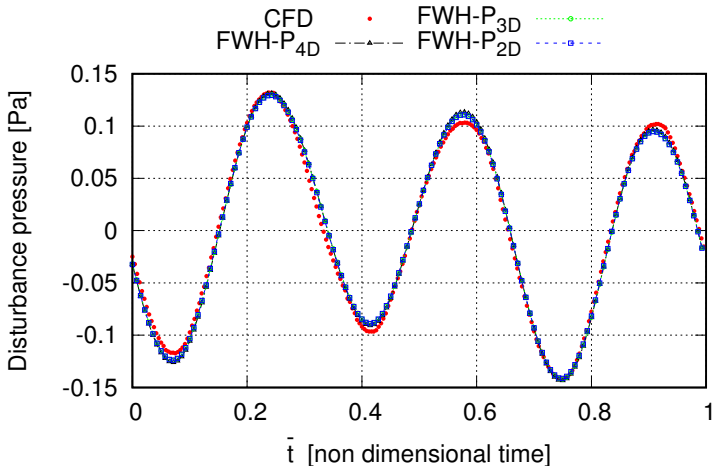

FIGURE 5.89: Comparison between the FWH-P and CFD outcomes at Obs3.

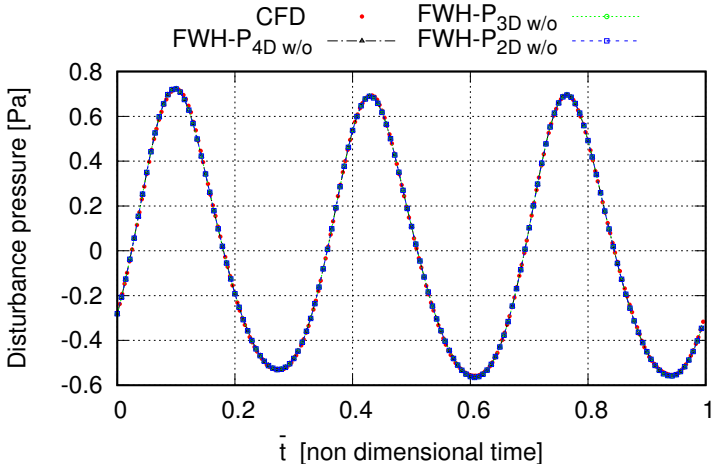

FIGURE 5.90: Comparison between the FWH-P and CFD outcomes at Obs1, porous surface without the closure disk.

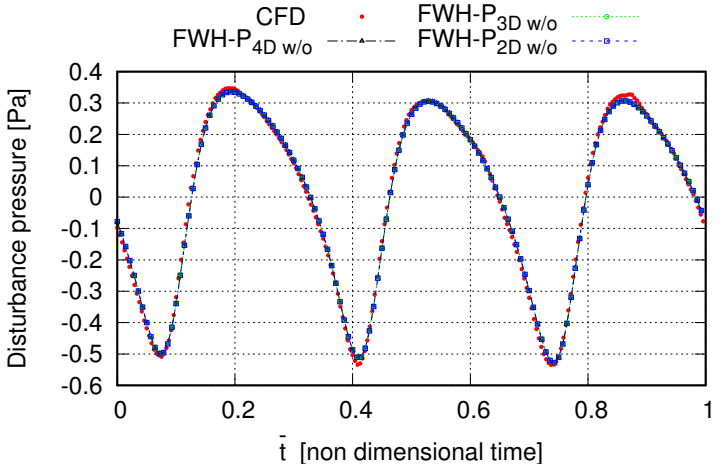

FIGURE 5.91: Comparison between the FWH-P and CFD outcomes at Obs2, porous surface without the closure disk.

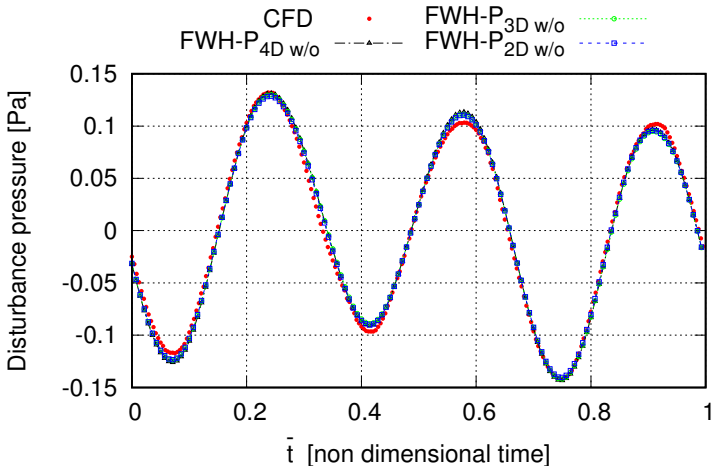

FIGURE 5.92: Comparison between the FWH-P and CFD outcomes at Obs3, porous surface without the closure disk.

does not highlight any presence of broadband noise component. Thus, although the FWH-P outcomes are in agreement with the CFD solution, the noise prediction turn out to be unable to describe the acoustic effects due to the turbulence. In fact, the high frequencies content expected in the acoustic pressure (due to the well known "swishing" acoustic character of the wind turbines noise) is not present.

Essentially, this is due to the noise detection features of the RANS model, in that able to account only for those sources related with the vorticity field convected (and quite soon damped) downstream of the rotor.

5.4.3 Four Bladed E779A Propeller by DES Hydrodynamics

The hydroacoustics of INSEAN E779A four-bladed marine propeller in open water is inhere investigated.

Operating conditions are defined by homogeneous onset flow relative to an advance ratio $J = U_\infty/(n\,D) = 0.88$ where $U_\infty = 5$ m/s is the freestream velocity, $n = 25$ rps the number of rotation per second and $D = 0.22$ m the propeller diameter.

Hydrodynamic data input over the permeable surface, as well as those of reference for the comparisons with the FWH-P solutions, are provided by a Detached Eddy Simulation whose details are found in [67].

Such numerical technique is able to combine the RANS model in the boundary layer and the LES model in the field away from the body. The RANS model being designed through a time averaging process of the Navier Stokes Equations only allows to accurately model the effect of the turbulence inside the boundary layer. However, as seen in the case of the wind turbine it is absolutely not appropriate to detect the vorticity and turbulence in the flow field, especially for hydroacoustic purposes (see also [32]). On the contrary the LES solution provides good results because based on a space filtering technique which allows to solve the Navier Stokes Equations above a characteristic parameter depending on the dimension of the computational cells.

As consequence the energy cascade is better reproduced by the closure model, thus allowing to detect the time space dependence of velocity and pressure on turbulence phenomena.

From an acoustic standpoint this represents an undoubted advantage; indeed, the DES model allows to detect the unsteady distribution of velocity and pressure due to high frequency phenomena over a porous surface located away enough from the body to include "all" the quadrupole source terms.

Therefore, the acoustic model once "coupled" with the CDF/DES simulation is able to propagate their acoustic effect in the (mid) far field.

The hydroacoustic analysis shown in the following concerns with seven hydrophones whose coordinate are listed in tab. 5.8.

5.4.3.1 DES Running Average Based Hydrodynamics

The flow field features predicted through the DES solution allow to separate the acoustic effect due to the turbulence from those related with vortical structures downstream of the rotor.

Such decomposition is allowed by the CFD solution performed on the rotating reference system moving rigidly with the body, namely (SRC). If the turbulence were not present the flow field solution relative to the homogeneous onset inflow would give rise to a constant flow field pressure and velocity with respect to the (SRC).

Therefore, the unsteadiness of the field, with respect to that frame of reference, are due to the effect of the turbulence phenomena only. From this standpoint, a time averaging process performed over the unsteady hydrodynamic flow field data, yields, (provided that the number of collected samples have a significant statistical meaning) a time independent value of flow

field pressure and velocity with respect to the (SRC). Such averaging process may be used to achieve the following time decomposition of the signals, which for the sake of conciseness is here reported only for the velocity (the same is for the pressure):

$$\begin{aligned} \mathbf{u}(\mathbf{x},t) &= \overline{\mathbf{u}}(\mathbf{x}) + \mathbf{u}'(\mathbf{x},t) \\ \overline{\mathbf{u}}(\mathbf{x}) &= \frac{1}{t}\int_0^t \mathbf{u}(\mathbf{x},\tau)\,d\tau \\ \mathbf{u}'(\mathbf{x},t) &= \mathbf{u}(\mathbf{x},t) - \overline{\mathbf{u}}(\mathbf{x}). \end{aligned} \tag{5.7}$$

Here $\overline{\mathbf{u}}(\mathbf{x})$ is the mean time independent flow field velocity, $\mathbf{u}'(\mathbf{x},t)$ is the fluctuating part around the mean value, whereas $\mathbf{u}(\mathbf{x},t)$ is the total velocity predicted by the DES solution. This procedure is statistically known as *running average*, and is oriented to verify the achieved asymptotic convergence of the wake downstream the rotor.

It is worth to note that, even though the same decomposition of Eq.(5.7) is used to derive the RANS model from the Navier Stokes Equations, the running average solution is conceptually different.

It is derived afterwards on the base of the flow field solved by the DES technique with the Smagorisky closure model. Thus, this procedure only represents a data decomposition that is just a post processing keeping all the features of DES data.

Acoustically speaking, it allows to characterize the noise sources related with a *mean vortical* flow field excluding, de facto, the effect of the turbulence. As we will see later, the proposed decomposition represents a considerable advantage and provides an insight in the noise generation phenomena.

For the sake of completeness, the following acoustic results are based on the quantities $\bar{\mathbf{u}}$ and $\bar{p}$, having the meaning of Eq. (5.7); the comparison with the CFD/DES data are as well based on the time evolution of $\bar{p}$.

Samples for the average solution have been collected from the 6-th to the 16-th revolution, which represent a statistical significant time window.

From the acoustic standpoint two different porous surfaces, open and closed, are used (both fixed in the rotating blade space). The radial dimension is chosen equal to $0.57D$ for both, whereas the axial length of the shorter is $2.75D$, located close to the finest grid zone; the other has a length $4.72D$ and encloses the zone where spatial variations of the Lighthill stress tensor are present.

The location of seven hydrophones used in the hydroacoustic analysis is listed in tab 5.8.

Since the baseline for the reliability/comparison purposes of the FWH-P solution is the CFD disturbance pressure, the microphones are located in the very near field in order to limit the effects of numerical disturbing phenomena occurring in the computation of the CFD solution.

Figure 5.93 depict the local position of the observers with respect to the topology of the computational grid and the propeller. Moreover, Figs. 5.94 and 5.95 depict the porous surfaces with respect to the flow field Lighthill stress tensor $L2$ norm and the iso-surface of the

Name	$x[m]$	$y[m]$	$z[m]$
Obs 1	-1.0D	0.0	0.75D
Obs 2	-0.5D	0.0	0.75D
Obs 3	0.0	0.0	0.75D
Obs 4	0.5D	0.0	0.75D
Obs 5	1.0D	0.0	0.75D
Obs 6	1.5D	0.0	0.75D
Obs 7	2.0D	0.0	0.75D

TABLE 5.8: Acoustic observers location

Jeong's criteria $\sigma_2 = -10^-3$ which are used to detect the core of the vortices downstream of the rotor.

Figures 5.96, 5.97, 5.98, 5.99 and 5.100 concern the acoustic signals comparison between CFD and FWH-P approach over a non dimensional period of rotation for the first five hydrophones.

The results are in very good agreement, independently on the kind of porous surface considered (note that $FWH-P_{long}$ and the $FWH-P_{short}$ indicate the axial extension of the porous surfaces, whereas subscripts w/o indicates the absence of the outflow disk).

For these observers, the contribution from the downstream end-cap is negligible and, also in the absence of it, the open cylinders well capture the acoustic contribution.

The acoustic predictions at *Obs*6 and *Obs*7 are in very good agreement with the CFD data only when the longer porous surface is used to evaluate the acoustic pressure, both with or without the end-cup. On the contrary, for these observers the shorter permeable surface is unsuited, in fact neither closed nor open configuration provide good results, as depicted in figs. 5.101 and 5.102.

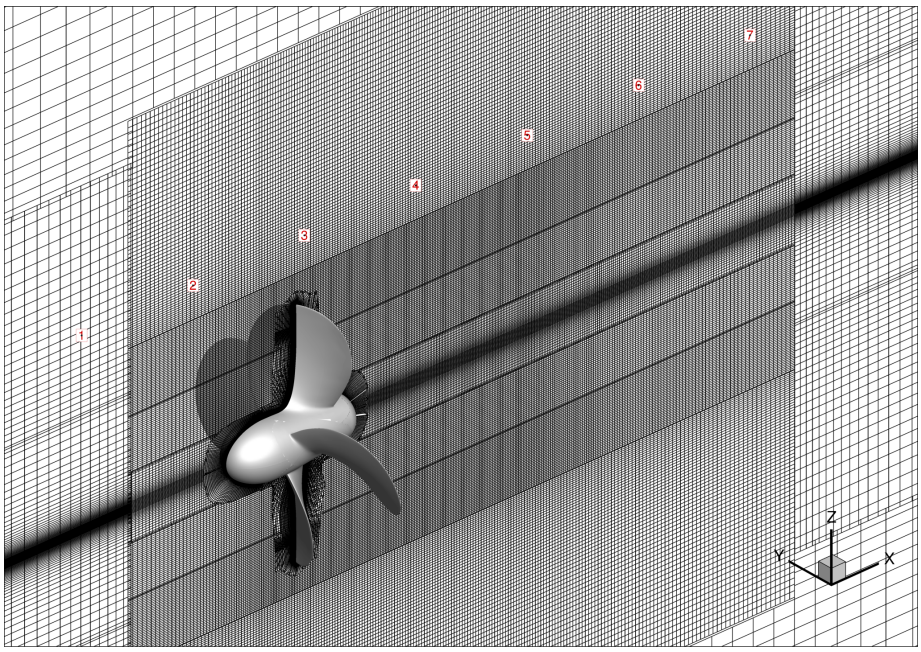

FIGURE 5.93: E779A propeller, CFD grid topology and acoustic observers position.

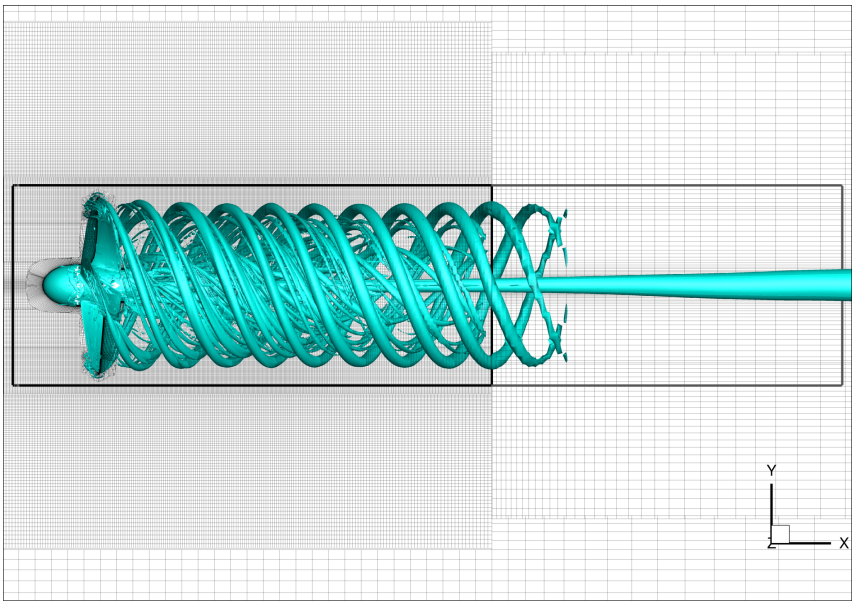

FIGURE 5.94: Vortices core detection through the Jeong's $\sigma_2 = 0.01$ method and acoustic porous surfaces

Hence, considering the observers *Obs*6, *Obs*7 and referring to the shorter porous surface S; leaving not-negligible downstream sources of noise outside S (i.e the case with the end-cap), or leave it open (i.e. without the end-cup), thus ignoring the contribution of a virtual closing surface S^+, such that $S \cup S^+$ would surround the whole set of sound sources, produces similar drawbacks in the predicted acoustic signature.

In conclusion the acoustic predictions based on the averaged CFD solution shown a complete agreement between the two solvers provided that the noise sources are embedded inside the acoustic surface. Therefore, the effects of the vortical field on the acoustic pressure are well captured by the FWH-P outcomes, thus proving it is able to radiate them in the mid and far field correctly.

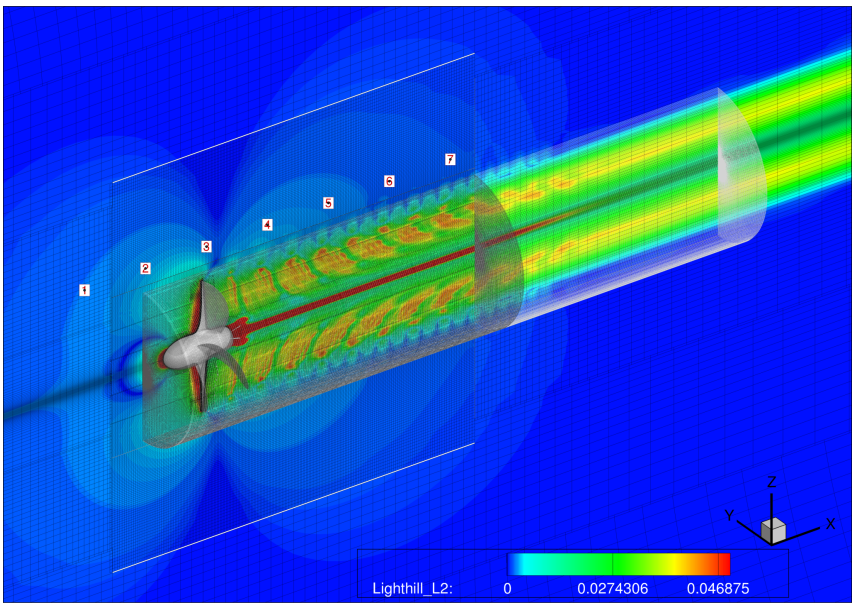

FIGURE 5.95: Frobenius norm of non dimensional Lighthill stress tensor

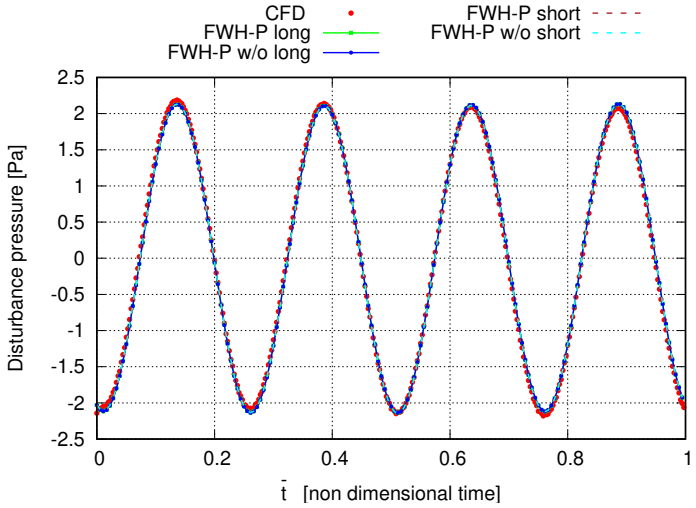

FIGURE 5.96: Observer 1, running average based predictions, comparison between FWH-P and CFD.

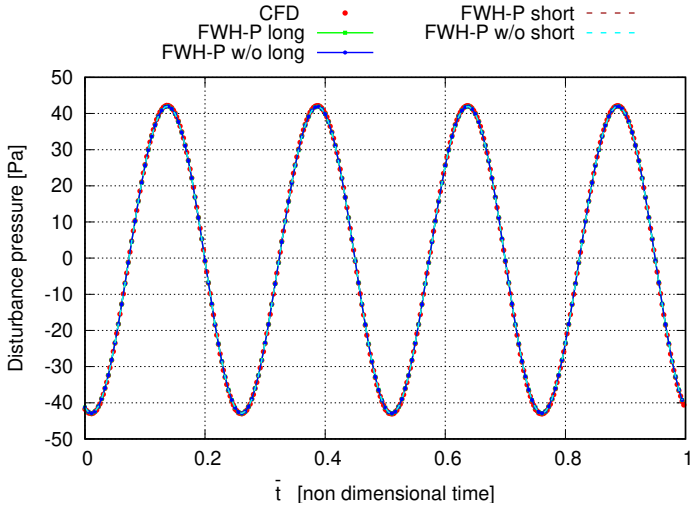

FIGURE 5.97: Observer 2, running average based predictions, comparison between FWH-P and CFD.

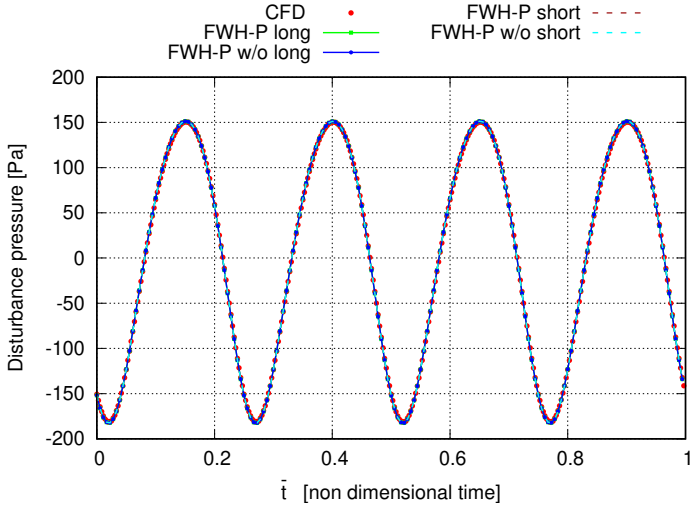

FIGURE 5.98: Observer 3, running average based predictions, comparison between FWH-P and CFD.

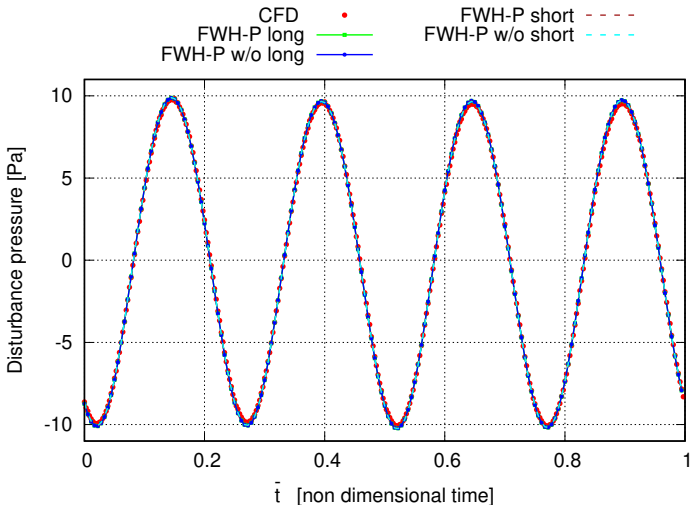

FIGURE 5.99: Observer 4, running average based predictions, comparison between FWH-P and CFD.

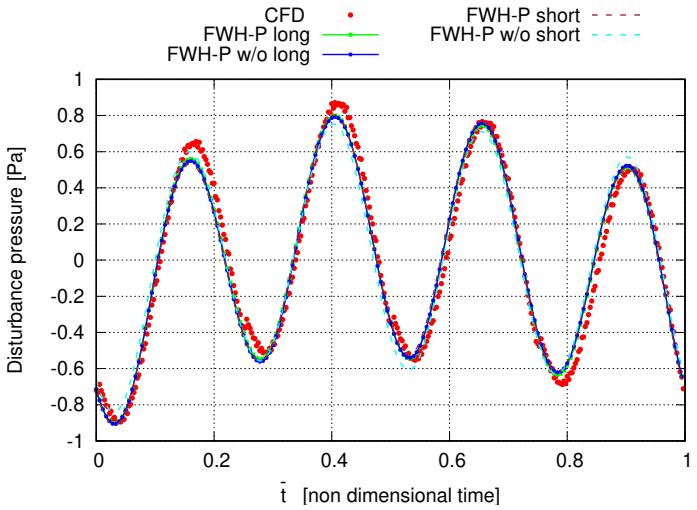

FIGURE 5.100: Observer 5, running average based predictions, comparison between FWH-P and CFD.

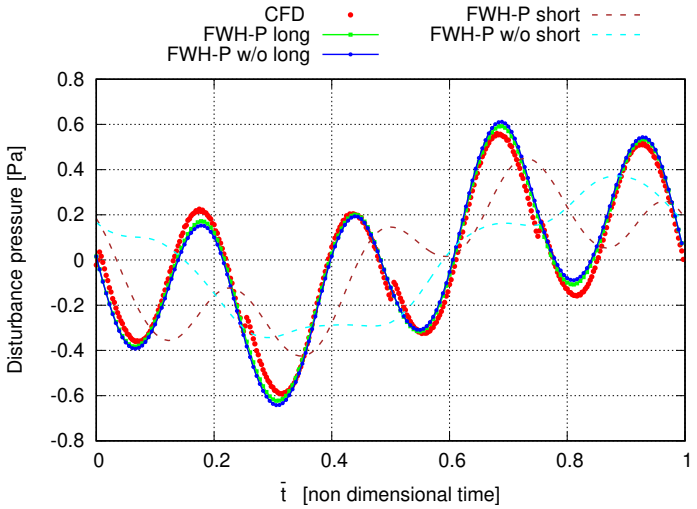

FIGURE 5.101: Observer 6, running average based predictions, comparison between FWH-P and CFD.

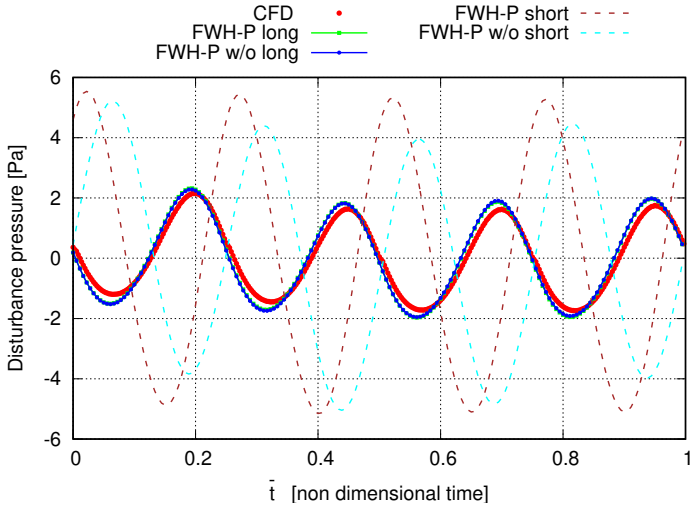

FIGURE 5.102: Observer 7, running average based predictions, comparison between FWH-P and CFD.

5.4.3.2 Unsteady DES Hydrodynamics

In this subsection the unsteady DES field solution is used to evaluate the contribution of the turbulence to the acoustic pressure signature generated by the INSEAN E779A propeller. The operating condition, as well the observers, are the same of the section 5.4.3.1.

The acoustic analysis has been made over a period after the 16 th revolution which corresponds to an averaged solution having a complete envelop of the flux tube downstream of the rotor. Therefore, the eventual presence of unsteady phenomena is related only with the turbulence phenomena and not to transient dynamics of the wake.

In this case two porous surface depicted in Fig. 5.103 having length equal to $5.1375D$ and $3.1864D$ have been used in the acoustic analysis. The enhanced extension, compared to the averaged solution is due to the increased strength of noise sources, related with the spatial and time derivative of the Lighthill stress tensor involved in the unsteady simulation.

For the sake of clarity, the legend "CFD" refers (in the following figures) to the disturbance pressure predicted by the unsteady DES simulation over a non dimensional period of revolution, whereas "FWH-P" indicates the outcomes of the acoustic model using unsteady CFD/DES data over the porous surface.

Figures 5.105, 5.106, 5.107 show a good agreement between the CFD and FWH-P solutions; the suffix s and l in these figures stand for the short and long porous surface, respectively, whereas w/o indicates the acoustic solution without the end cap.

It is also worth to note that the impermeable solution of the FWHE in which only the linear noise contributions are accounted for, namely $(FWH-L)$ provides good results for the same hydroacoustic observers.

Figures 5.104, 5.108, 5.109 and 5.110 relative to the observers Obs1, Obs5, Obs6, Obs7, respectively, show instead comparisons DES vs. FWH-P which are not as good as expected regardless to the axial dimension of the porous surface and to the presence of the outflow disk.

An interpretation of such discrepancies between DES and FWH-P results will be given later .

Beside to the aforementioned differences between signals, what catch the eyes is that acoustic signatures predicted by the FWH-P technique based on the CFD/DES unsteady hydrodynamic data are very different form those based on the running average, both in wave shape and amplitude.

This result suggests that the turbulent phenomena have a crucial role in the noise generation phenomena. In fact, looking at Obs6 and Obs7 depicted in Figs. 5.109 and 5.110, respectively, the acoustic pressure predicted by the solution accounting for the effects of the turbulence is about an order of magnitude higher with respect to the result provided by the average solution.

These results highlight how the acoustic role played by the large vortical structures seem to be of second importance respect to that induced by the turbulence.

Similar consideration can be drawn by considering acoustic signals related to the shorter and longer porous surfaces, which are very similar both in the waveform and amplitude, either in closed and open configuration.

Such a behaviour may be also ascribed to the turbulence effects.

Indeed, the most intense quadrupole noise sources are located inside the shorter acoustic surface containing the finest CFD grid, in that fine clustering features allow to the DES technique a better modeling of the fluctuating flow field induced by the turbulence (the DES model numerically solves the scale of eddies above a parameter based on the cell dimensions and models those below it). In this manner, the additional noise contributions introduced in the acoustic signal by the longer acoustic surface are de facto irrelevant (i.e. the CFD field zone included in the longer porous surface contains, with respect to the shorter, coarser grid cells which prevent to the DES model a profitable detection and propagation of noise phenomena having shorter characteristic waves length).
It is also worth to note that the pressure at Obs1, which is located upstream (thus theoretically less prone to the effects of flow field fluctuations) shows a considerably modified waveform and amplitude respect to the average solution.

In addition to that, it is also interesting to note that the linear solution of the FWHE yields a negligible acoustic pressure after a diameter downstream the rotor. Similar results were as well obtained by Ianniello in [22].

Some interesting considerations may also be carried out observing that the FWH-P solutions based on the running averaged data are very close to that provided by the impermeable configuration ($FWH-L$). Figures 5.104 to 5.108 show that at least for the first five microphones the two solution are very similar. Then, we can conclude, once again, that the difference in the acoustic prediction is given by the direct inclusion of the volume contributions accounting for the turbulence phenomena.

A further insight in the noise generating mechanism can be obtained looking at observers very near the rotor, i.e. Obs1, Obs2 and Obs3 shown in Figs.5.105, 5.106 and 5.107, respectively.

For these acoustic observers the linear contributions seem to play the major role in the noise generation, according to the fact that there, the energy is introduced by rotor in the flow and the cascade is just at the begin (up to a diameter).

Once again this shed light on the effect of the turbulence: when the energy is transferred by the cascade to the turbulent eddies, i.e. going downstream of the rotor, these eddies start to play the dominant role in noise generation, whereas the linear one soon decay.

Besides, since in radial direction the CFD grid remains fine enough to describe the fluctuating phenomena, a convergence analysis on the radius of the cylinder is carried out in order to verify that all the quadrupole sources terms are accounted for.

To this aim, a couple of porous surface (see, Fig.5.111) with length equal to the shorter one (i.e. $3.1864D$) and radial dimension equal to $0.65D$ and $0.74D$, are assessed.

The largest porous surface is intentionally located close to the microphones having radial position equal to $0.75D$; this condition is still suitable from a numerical standpoint and offers some interesting suggestion on the noise detection capability of the CFD code.

Figures 5.112 to 5.118 show that the acoustic signature is practically independent from the radius of the porous surface in terms of the wave shape. There are slight differences in the

sparks which may be expected from the different location of the porous surface with respect to the noise sources and to the CFD grid.

However, one question is not yet solved.

Why does the CFD based prediction are slightly different with respect to the FWH-P outcomes at observers located away from the rotor disk?

The answer to this question may be find out considering the different purposes of the two solvers. Indeed the CFD finite volume solvers are usual oriented to the prediction of aerodynamic loads whereas an effective evaluation of the mid field pressure would require some additional numerical technique that represent useless additional effort. The disturbance pressure in the mid field may be indeed affected by reflecting waves at the boundaries, especially when low dissipative convective schemes are used to reduce the numerical dissipations associated with the finite volume technique. Such numerical issues are well known and may be solved by the introduction of suited boundary conditions based on the characteristics method of the Navier-Stokes Equation [68] . Although this would represent the solution of the problem, it goes beyond the purpose of this work; however, an interpretation of such phenomena is inhere reported because useful to better understand the numerical results.

To this aim, the time evolution of the Lighthill stress tensor Frobenius norm well address the encountered issue. Particularly, some frames are collected over a period of time between the 16th and 17th revolutions, which also correspond to the windowing time of the acoustic simulation. Figure 5.119 show the mentioned behaviour for six angular position of the propeller, the images are relative to the non dimensional time 0.136 to 0.275, corresponding to angular positions from 49° to 99°, with increment of 10°. For the sake of conciseness only this angular range is inhere reported because sufficient to understand the phenomena. The Lighthill stress tensor norm is representative of the quadrupole field noise sources distribution.

The images clearly depict the effect of the CFD boundary condition which behave as a sort of pulsating noise source, whose contribution grows and diminishes, as depicted in figures, about five times in a complete revolution of the propeller.

The intensity of such noise sources have quite low magnitude so that the bouncing depicted in the figures weakly (or not at all) affect the fluid dynamic solution in the very near field. This is accomplished by using the stretch in the computational CFD grid which filters the low frequencies spurious contributions coming from the fictitious boundary condition in a way to *insulate* the very near field of the hydrodynamic solution.

Thus, although the aforementioned effects, the noise detection may be considered reliable and the fluid dynamic data may be profitably used to perform acoustic analysis whenever the porous surface is located tightly to the blades and wake structure (in that effects of CFD boundaries are confined only out with respect to the permeable surface and therefore not accounted by it). Proof of this statement may be find out in the outcomes of the FWH-P solution based on the larger acoustic surface. Indeed, as may be seen in Figs. 5.112 to 5.118 results coming from that permeable surface are practically identical to those provided by the tightest porous surface. Such result gives us the information that noise sources contained between the acoustic surfaces (those which would differentiate the solution between the three

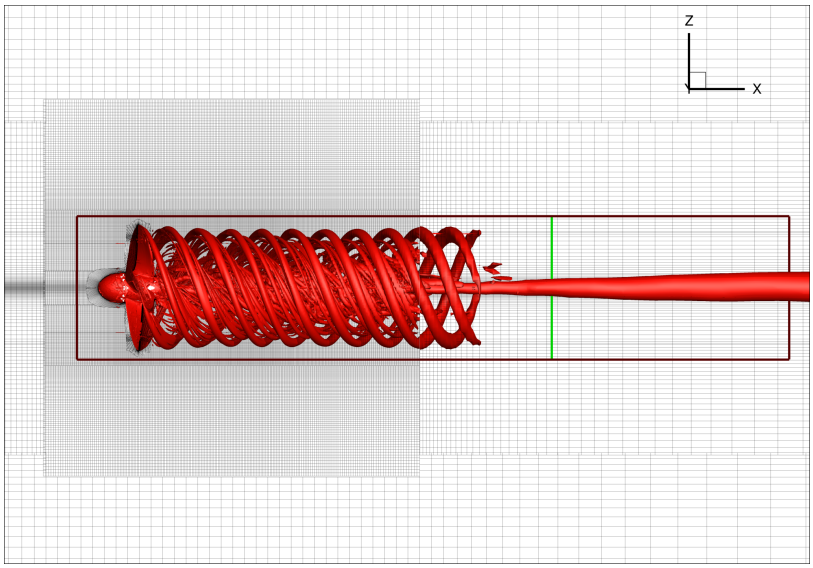

FIGURE 5.103: Vortex core detection through the Jeong's criterion $\sigma_2 = -0.03$, acoustic surfaces and observers.

porous surface) are practically null. This let us conclude that the contained noise sources (by all the three porous surface) are those that play the dominant role in the noise generated by the propeller and the wake. On the contrary, as widely discussed in Chapter 3, external noise sources (respect to the porous surface) do not give any contribution to the acoustic pressure predicted by the FWH-P (they would be accounted by the field contribution). Hence, if the aerodynamic data are trustable near the rotor and wake structure, as they are, also the acoustic effects propagated by the permeable surface are reliable. Differently, the CFD disturbance pressure accounts for the whole field features, i.e. it is not possible to distinguish the disturbance pressure due to the boundary conditions from the total one. This explains the different prediction between the two solvers away from the rotor.

In conclusion the problem may be summarized as follows; the discretization strategy of the CFD domain produces a zone near the rotor and wake *protected* by the undesired effects of the fictitious boundary conditions. Thus, a physical consistent flow field solution near the rotor and wake is carried out by the CFD-DES solution. Acoustically speaking the noise detection in these zones is still physically consistent.

On the other hand, the FWH-P formulation does not account for the external noise sources (with respect to the porous surface) because it would be accounted by the field contribution if it were evaluated (see 3.2.1 for details); thus, yielding an acoustic prediction accounting only with those physical consistent noise sources inside it.

On the contrary, the disturbance pressure predicted by the CFD at the considered observer is instead affected by the boundary conditions effects (it accounts for all field contributions).

This explains the difference between the CFD based and the FWH-P solution. It also gives an indication about the effect of the CFD boundaries and provides the cue to understand the limits in the extension of the acoustic computational domain in order to avoid the radiation of numerical not physical consistent noise sources.

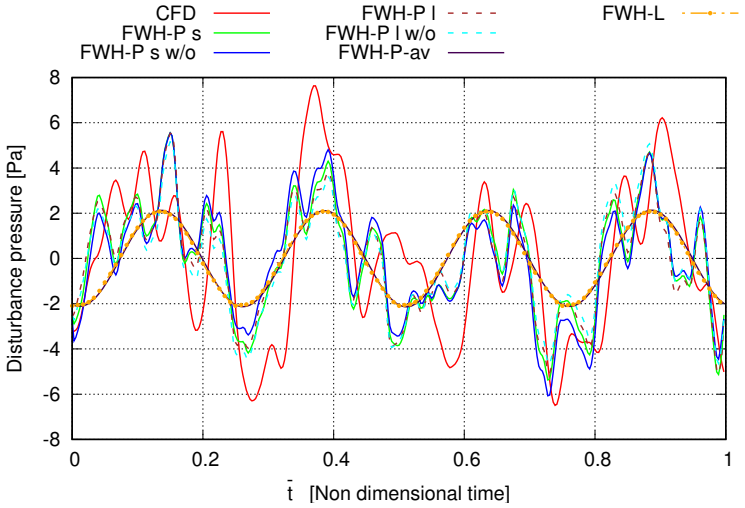

FIGURE 5.104: Observer 1, FWH-P/DES comparison of the unsteady solutions.

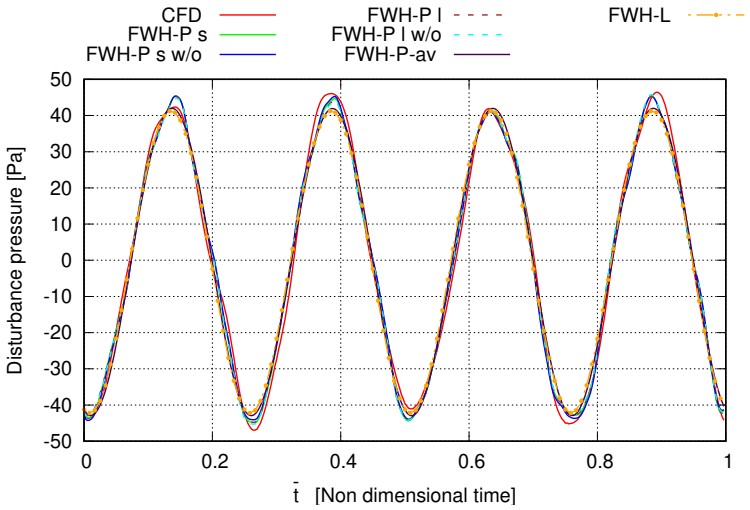

FIGURE 5.105: Observer 2, FWH-P/DES comparison of the unsteady solutions.

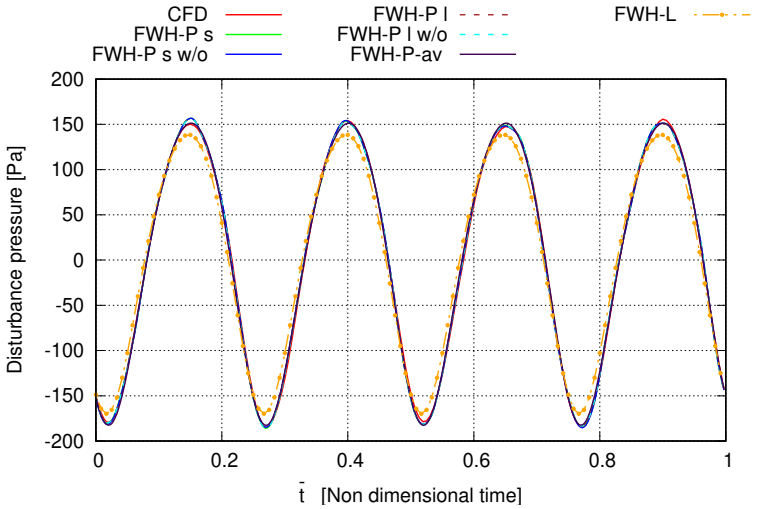

FIGURE 5.106: Observer 3, FWH-P/DES comparison of the unsteady solutions.

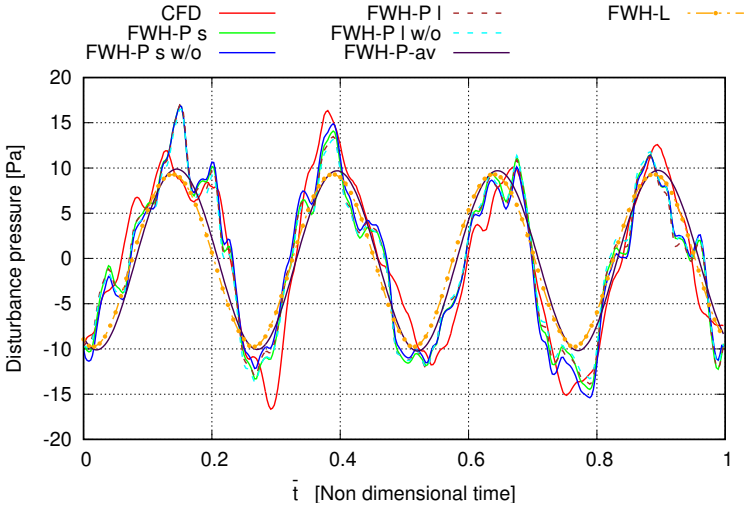

FIGURE 5.107: Observer 4, FWH-P/DES comparison of the unsteady solutions.

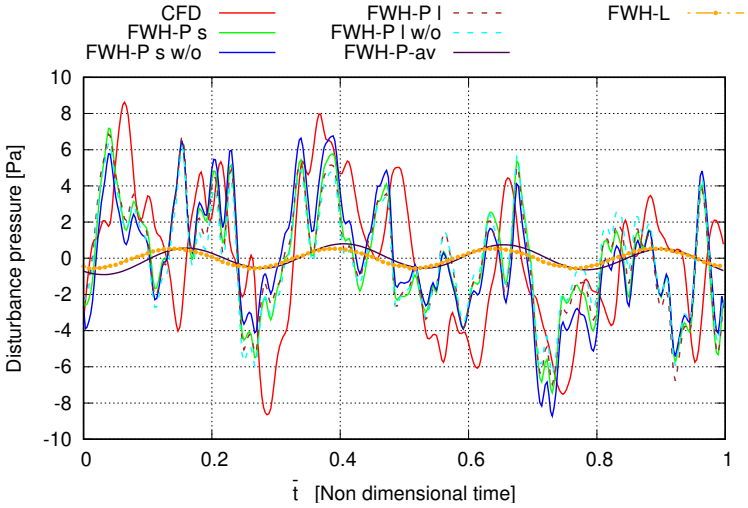

FIGURE 5.108: Observer 5, FWH-P/DES comparison of the unsteady solutions.

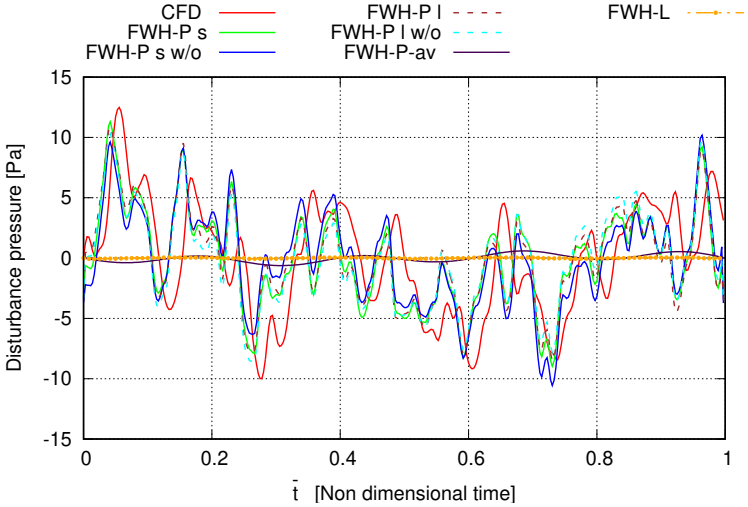

FIGURE 5.109: Observer 6, FWH-P/DES comparison of the unsteady solutions.

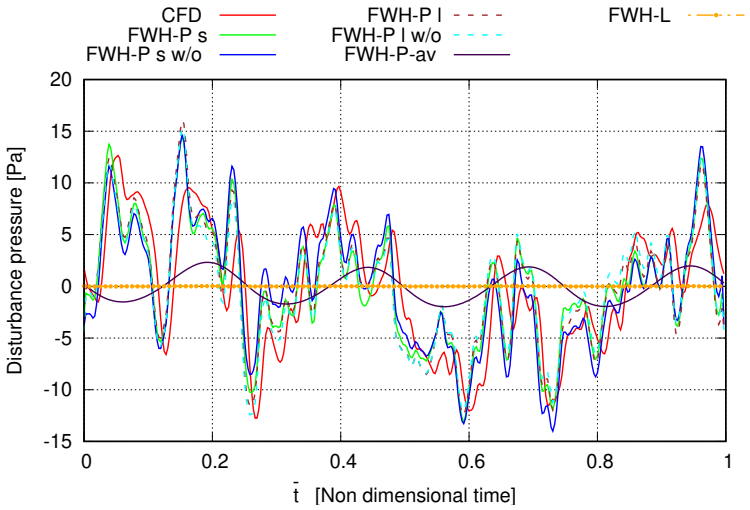

FIGURE 5.110: Observer 7, FWH-P/DES comparison of the unsteady solutions.

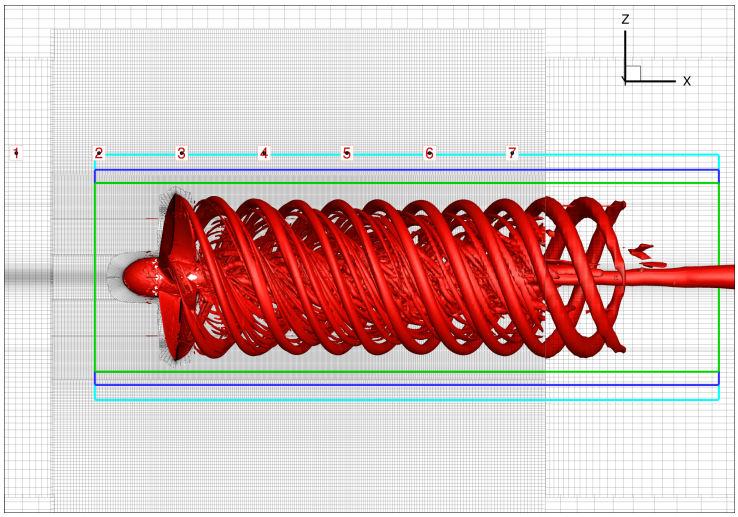

FIGURE 5.111: Vortex core detection Jeong's criterion $\sigma_2 = -0.03$, enlarged acoustic surfaces and observers

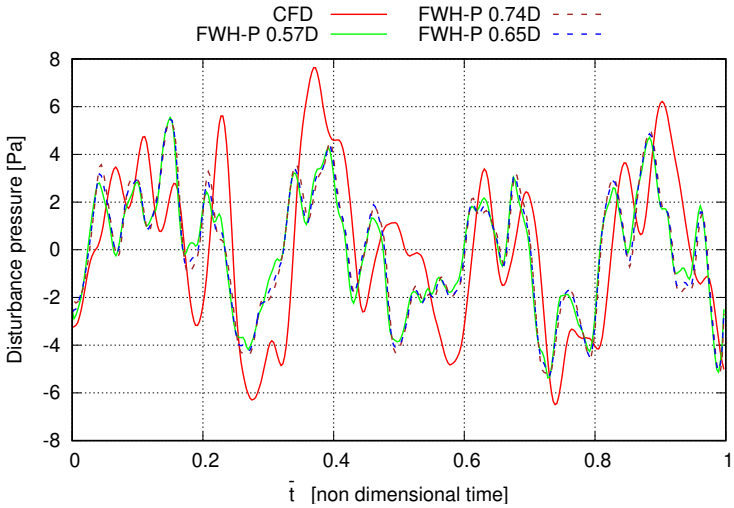

FIGURE 5.112: Observer 1, FWH-P/DES comparison of the unsteady solutions, larger porous surfaces.

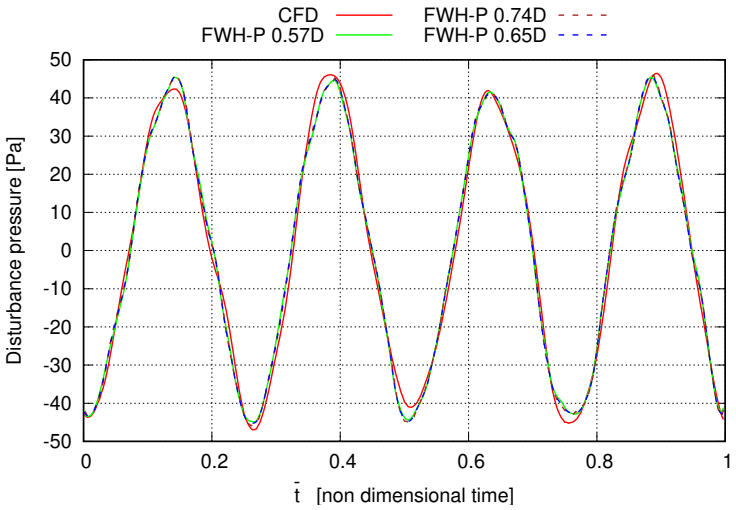

FIGURE 5.113: Observer 2, FWH-P/DES comparison of the unsteady solutions, larger porous surfaces.

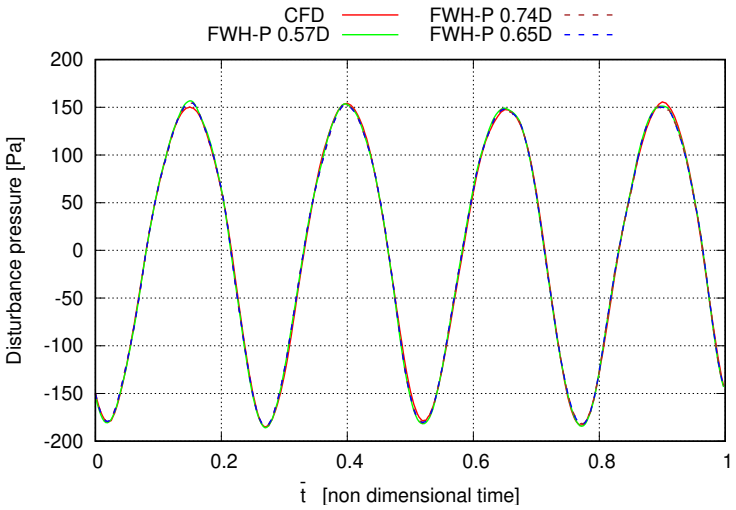

FIGURE 5.114: Observer 3, FWH-P/DES comparison of the unsteady solutions, larger porous surfaces.

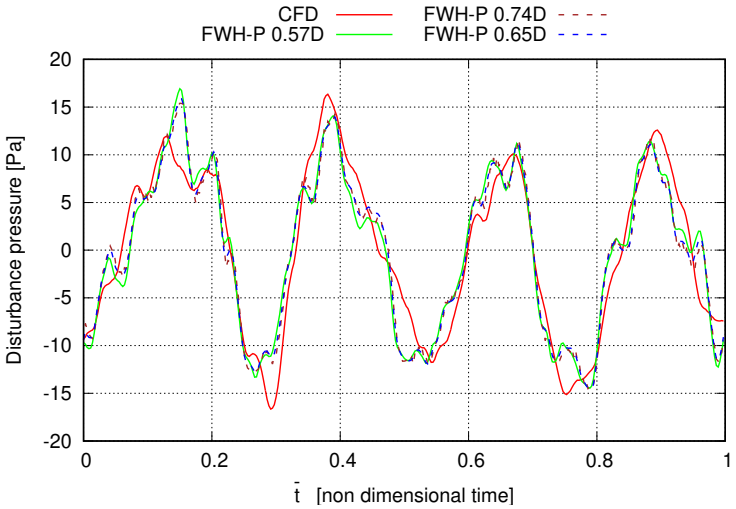

FIGURE 5.115: Observer 4, FWH-P/DES comparison of the unsteady solutions, larger porous surfaces.

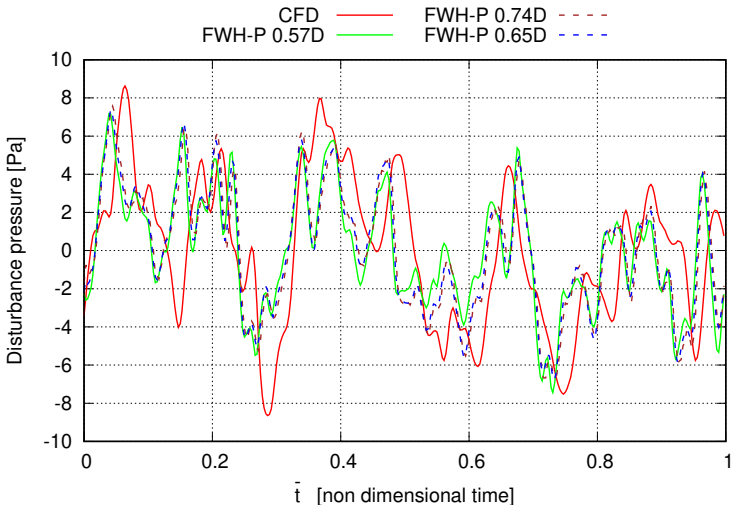

FIGURE 5.116: Observer 5, FWH-P/DES comparison of the unsteady solutions, larger porous surfaces.

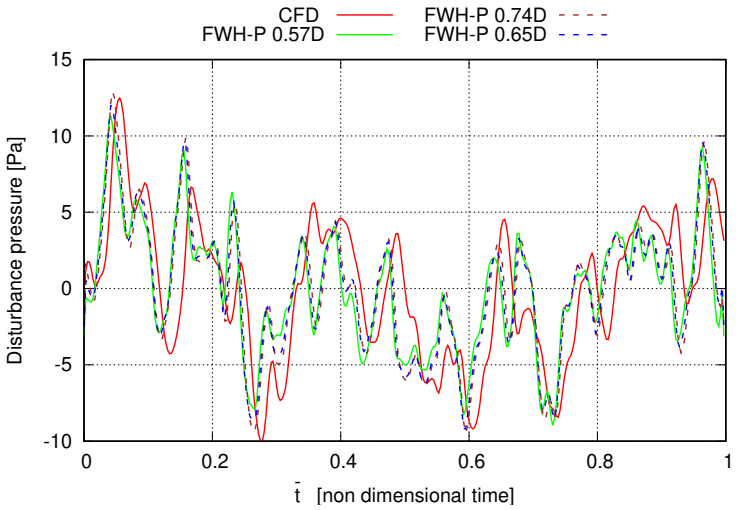

FIGURE 5.117: Observer 6, FWH-P/DES comparison of the unsteady solutions, larger porous surfaces.

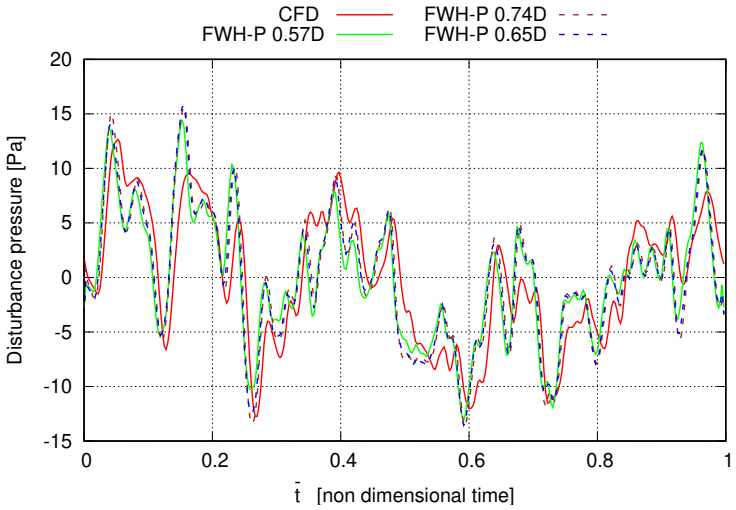

FIGURE 5.118: Observer 7, FWH-P/DES comparison of the unsteady solutions, larger porous surfaces.

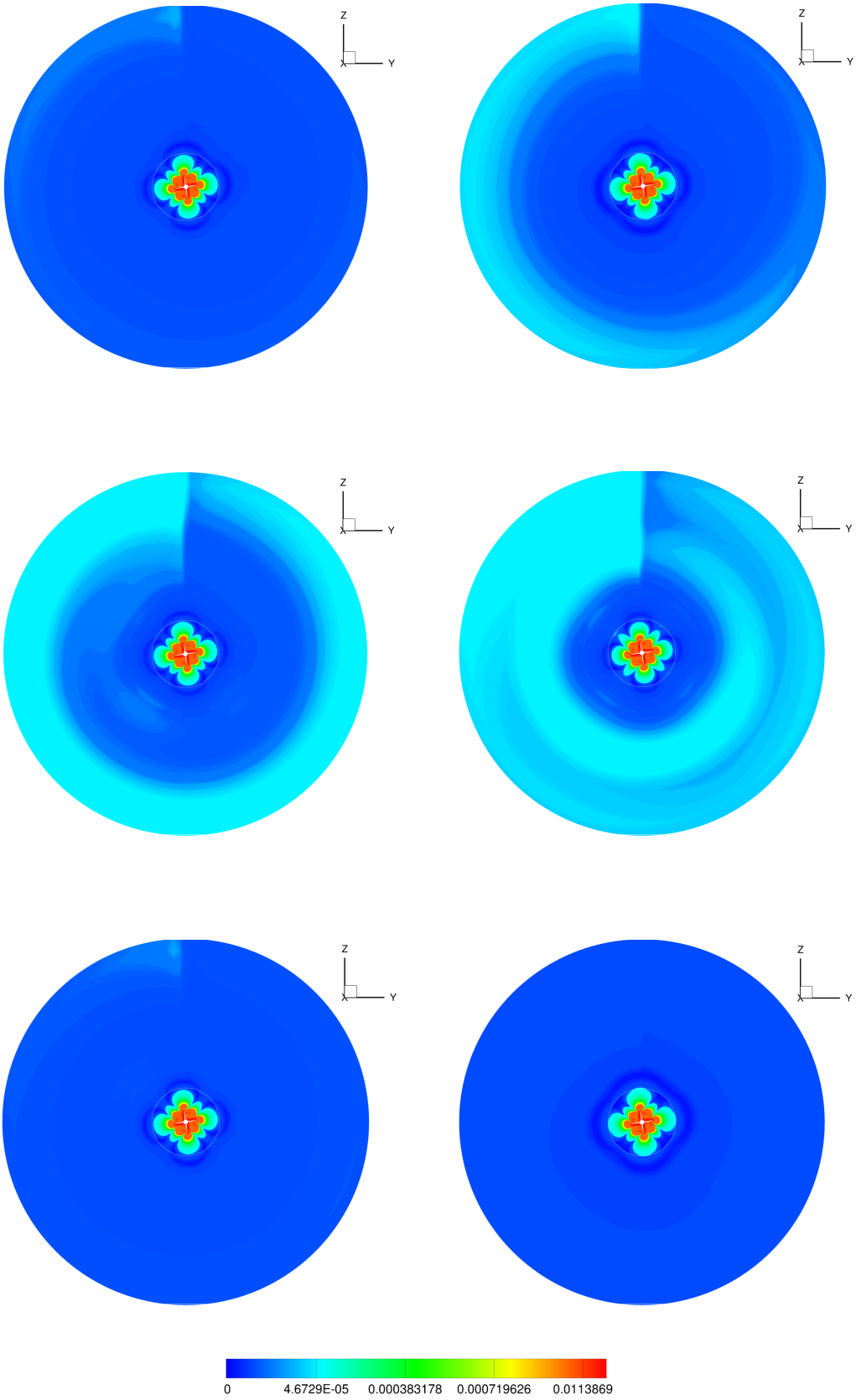

FIGURE 5.119: From top left to bottom right the non dimensional Lighthill tensor norm relative to the angular positions from 49° to 99° over the 16-th revolution,

5.4.4 Four Bladed E779A Propeller, DES vs 3D Panel Method Hydrodynamics

This subsection investigates the capabilities and drawbacks of potential-based hydrodynamic data for the prediction of the noise signatures generated by marine propellers in open water.

A fully-validated, three-dimensional, unsteady, free-wake panel method, along with the Bernoulli Equation, are combined with the Ffowcs Williams and Hawkings Equation for permeable surfaces to yield the sound signals at hydrophones located in the near-field.

A comparison with the pressure disturbances coming directly from a Detached Eddy Simulation (DES) of the propeller and those predicted by a FWH-P/DES approach, for the configuration analyzed in section 5.4.3, is proposed to shed light on the limits of applicability of Boundary Element Method (BEM) hydrodynamics for propeller hydroacoustics.

Here, DES input data over the acoustic surface come from a running-averaged solution of the collected data, yielding a vortical flow filtered by any turbulence-induced effect. Such processing is adequate to investigate the strength of a BEM formulation in capturing the tonal noise hydrodynamic sources.

To this aim, an analysis of the unsteady data set suggests to consider as statistically significant, those hydrodynamic samples ranging from the 6^{th} to the 16^{th} propeller revolution. As depicted in figs. 5.122 to 5.125, respectively from Obs1 to Obs4, the agreement among predictions is excellent: the noise is dominated by vorticity phenomena, well captured by the BEM hydrodynamic solver, as confirmed also by the analysis in the frequency domain highlighted in figs. 5.136 to 5.139 where the frequency content of the signals shows only tones multiples of the shaft frequency $4f_0$.

At Obs5 depicted in fig. 5.126, the waveform and peak-to-peak agreement starts to get worse.

The frequency analysis in fig.5.140 exhibits a contribution at f_0 that is the main responsible of the waveform distortion.

This phenomenon is amplified at Obs6 and Obs7, depicted respectively in Figs. 5.127,5.128 where FWH-P/BEM and FWH-P/DES predictions are no more comparable.

At this position, the FWH-P/DES signature is characterized by an important contribution from the first harmonic differently from the FWH-P/BEM outcome that remains purely dominated by the $4f_0$ frequency. Similar considerations hold at Obs7.

The above results suggest that, within a longitudinal distance of 0.5D $\div$ 1D from the hub, propeller hydroacoustics is dominated by potential wake vorticity effects.

However, moving downstream, the DES averaged field detects important vorticity contributions that deeply modify the overall sound. Although averaged, these contributions are the results of complex interactions among vortices occurring during propeller revolution, that, locally, may give rise to stronger vortex structures inducing higher level of noise behind the disk.

For instance, this happens at Obs7 (see fig.5.128) where the noise magnitude is almost 5 times greater than at Obs6 located one radius upstream.

For completeness, it is of interest to compare the vorticity field predicted by BEM and DES-averaged simulations.

Making reference to the longitudinal XZ plane (see 5.93), up to 2D downstream the propeller disk, Fig. 5.120 compares the contour map of the vorticity component along the Y axis predicted by DES and the trailing wake location carried out by BEM (black lines).

The overall propeller wake features, such as wake contraction, tip-vortices spacing/growth along X and mid-span trailed vorticity, are coherently described by the two solvers in the near wake region (up to 1D downstream).

Further downstream, BEM predicted tip-vortex location shows a slight shift towards the propeller disk which is not present in DES simulation. This is confirmed also by the thrust coefficients values shown in Tab 5.9 where BEM predictions are about 5 % higher than DES outcomes.

DES running average	BEM
K_T=0.1335	K_T=0.1407
$10Q_K$=0.2843	$10Q_K$=0.2971

TABLE 5.9: Thrust and torque numerical predictions

Nevertheless, the general shape of the trailed-wake is satisfactorily described.

Finally, note that BEM-predicted wake tends to roll-up in the region close to the rotation axis similarly to what happens at the blade tip; such an nonphysical solution is mainly due to the lack of a suitable hub-vortex model interacting with blades vorticity. In that flow region DES calculations correctly show the presence of the hub-vortex.

Next, the comparison between FWH-P/BEM results and those carried out through the unsteady DES data set on the acoustic surface, is proposed.

The FWH-P/DES computations in Figs. 5.129 to 5.135, including here turbulence-induced noise effects, oscillate about the predictions provided by the FWH-P/BEM solver, at least up to Obs4 (see Figs 5.129 to 5.132).

At Obs2 and Obs3 (see Figs 5.130 and 5.131), turbulence-induced noise is almost negligible, since the waveforms, noise levels and frequency content of the overall sound are very similar to those predicted by the running averaged technique.

At Obs4, see Fig. 5.132, turbulence sources of sound determine a distortion of the signal; differently from Obs2 and Obs3, the spectrum, (Figs. 5.143 to 5.149) highlights acoustic energy spread out over all the harmonics herein analyzed ($\leq 20 f_0$).

Nevertheless, the FWH-P/BEM signal captures the main features of the noise and provides a sort of average signature about which the FWH-P/DES prediction oscillates.

Akin to the running-averaged case previously discussed, from Obs5 on, the comparison between signals is no more reasonable; broadband noise due to flow field vorticity and turbulence, even the $4f_0$ harmonic, is not well captured by the FWH-P/BEM approach. As a matter of fact, the characterization of the tonal hydrodynamic sources of sound by a potential-based theory is allowed only if the acoustic analysis concerns the very near field, that, for this advancing ratio, is about one radius downstream.

Differently, vorticity and/or turbulence effects have to be modeled by a more suitable hydrodynamic simulations.

At lower advancing ratios, such effects are expected to become more relevant because of the higher thrust delivered by the propeller blades; hence, the use of a BEM hydrodynamics might be not adequate for tonal noise predictions too.

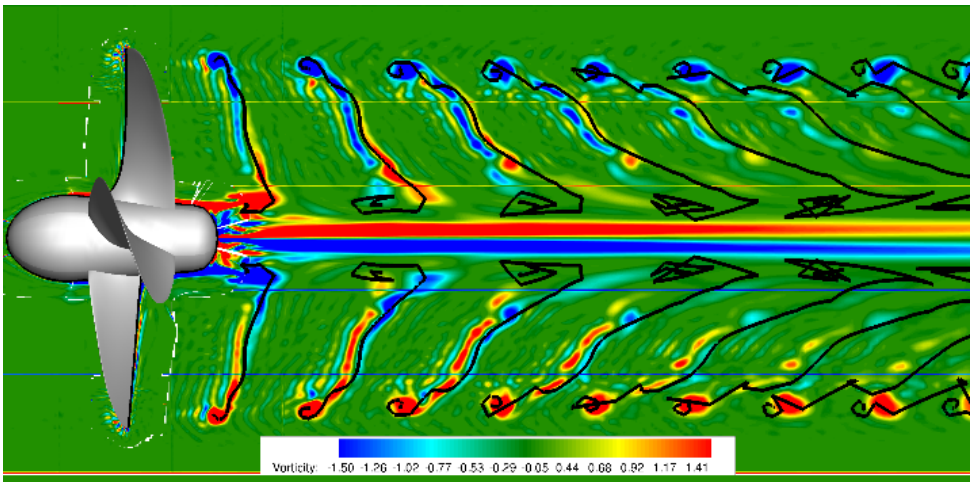

FIGURE 5.120: Vorticity field along the Y axis predicted by DES-averaged simulations compared to trailing wake location by BEM (black lines).

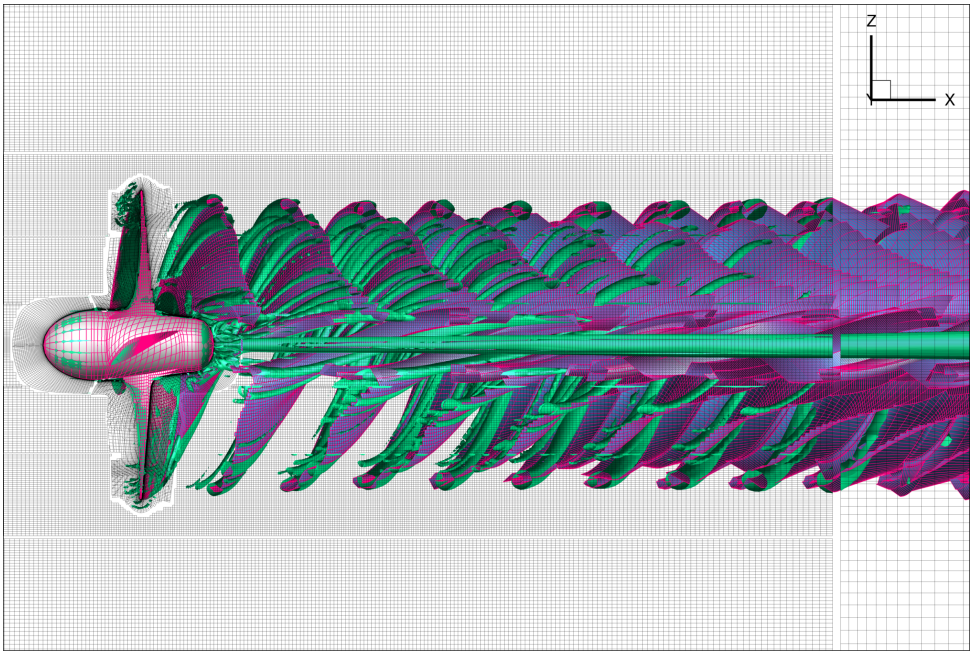

FIGURE 5.121: Section plane y=0; comparison between the vortical structures predicted by the isosurfaces of $\sigma_2 = 0.01$ of the average DES simulation and the free wake predicted by the BEM approach.

However, apart from Obs1, a good agreement between DES and FWH-P/DES signals is observed. At Obs 2 and Obs3, turbulence-induced noise is almost negligible, since the waveforms, noise levels and frequency content of the overall sound, depicted in Fig.7, are very similar to those predicted by the running averaged technique.

At Obs4, turbulence sources of sound determine a distortion of the signal; differently

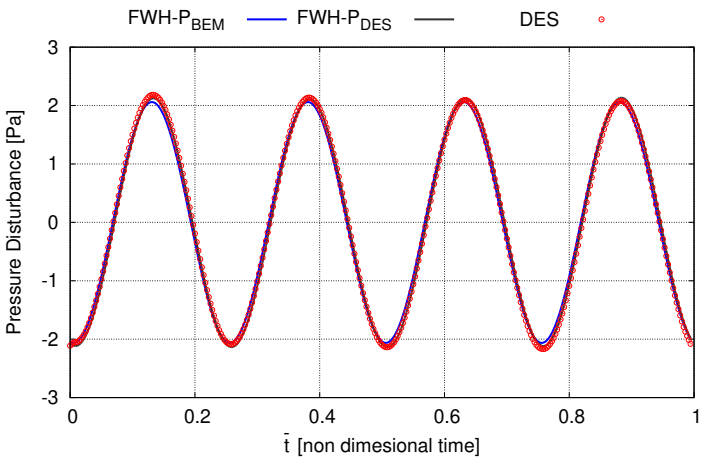

FIGURE 5.122: Comparison among noise signals predicted by DES, $FWH-P/BEM$ and $FWH-P/DES_{Averaged}$ at obs 1.

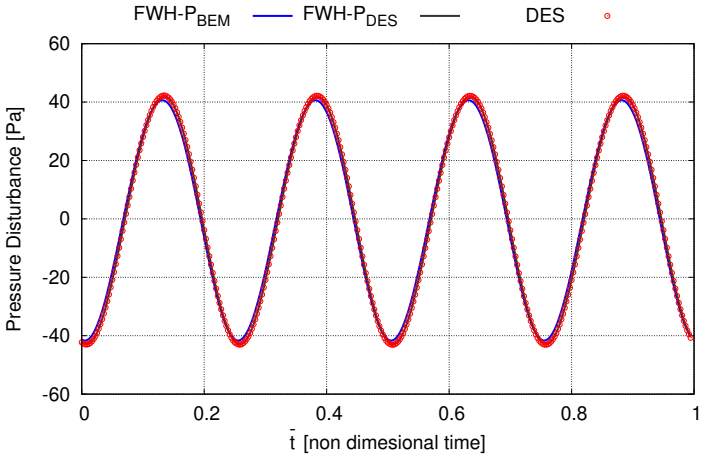

FIGURE 5.123: Comparison among noise signals predicted by DES, $FWH-P/BEM$ and $FWH-P/DES_{Averaged}$ at obs 2.

form Obs2 and Obs3, the spectrum highlights acoustic energy spread out over all the harmonics herein analyzed (up to 20 f_0).

Nevertheless, the FWH-P/BEM signal captures the main features of the noise and provides a sort of average signature about which the FWH-P/DES prediction oscillates.

Akin to the running-averaged data set case previously discussed, from Obs5 on, the comparison between signals is no more reasonable; broadband noise due to flow field vorticity and turbulence is exhibited and the $4f_0$ harmonic is also bad captured by the FWH-P/BEM approach.

In essence, the characterization of the tonal hydrodynamic sources of sound by a potential-based theory is allowed only if the acoustic field concerns with the very near field, that, for this advancing ratio is about one radius downstream. At lower advancing ratios, such effects are expected to become relevant because of the higher thrust delivered by the propeller blades; hence, the use of a BEM hydrodynamics might be not adequate for tonal noise predictions.

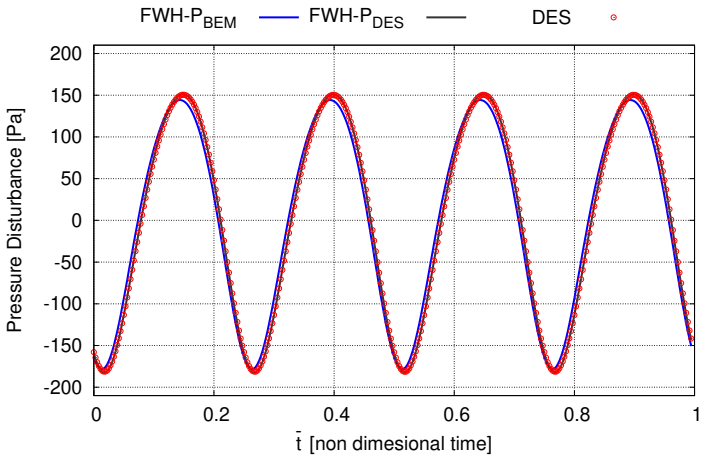

FIGURE 5.124: Comparison among noise signals predicted by DES, $FWH-P/BEM$ and $FWH-P/DES_{Averaged}$ at obs 3.

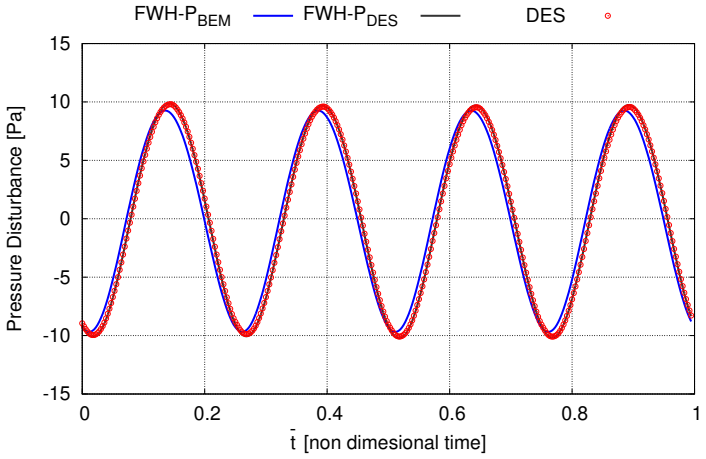

FIGURE 5.125: Comparison among noise signals predicted by DES, $FWH-P/BEM$ and $FWH-P/DES_{Averaged}$ at obs 4.

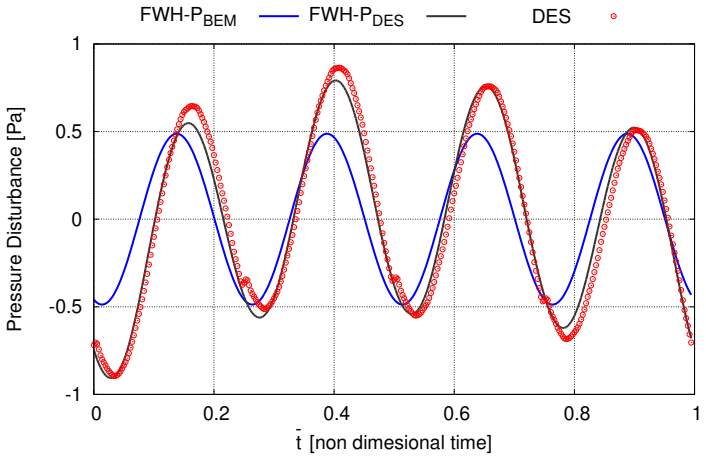

FIGURE 5.126: Comparison among noise signals predicted by DES, $FWH-P/BEM$ and $FWH-P/DES_{Averaged}$ at obs 5.

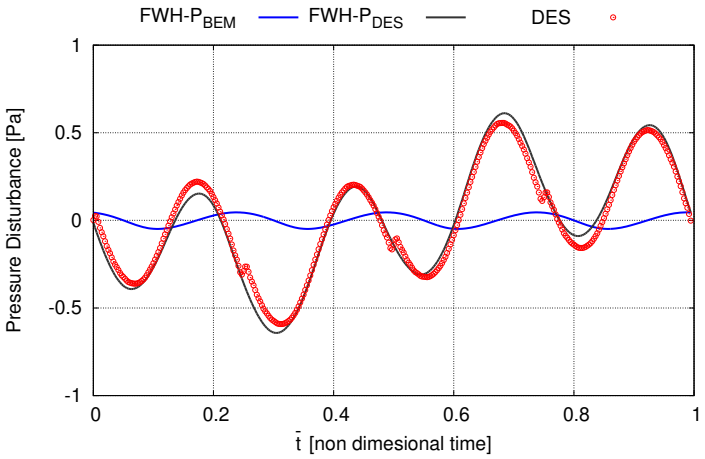

FIGURE 5.127: Comparison among noise signals predicted by DES, $FWH-P/BEM$ and $FWH-P/DES_{Averaged}$ at obs 6.

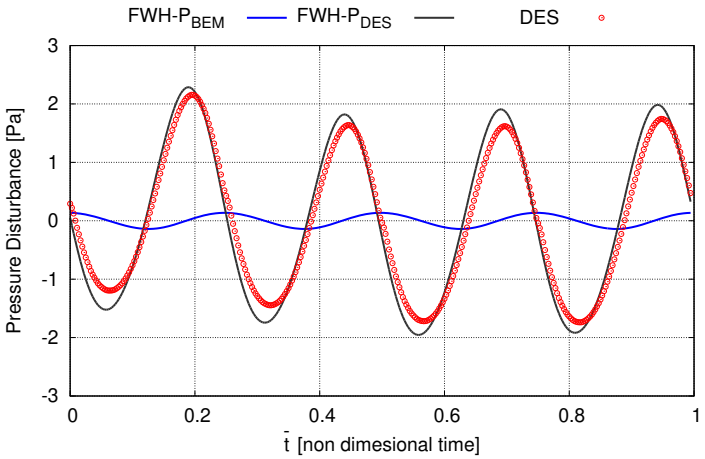

FIGURE 5.128: Comparison among noise signals predicted by DES, $FWH-P/BEM$ and $FWH-P/DES_{Averaged}$ at obs 7.

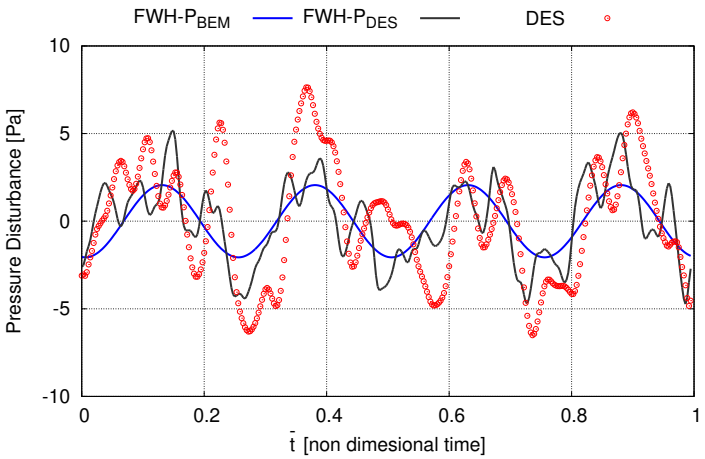

FIGURE 5.129: Comparison among noise signals predicted by DES, $FWH-P/BEM$ and $FWH-P/DES_{Unsteady}$ at obs 1.

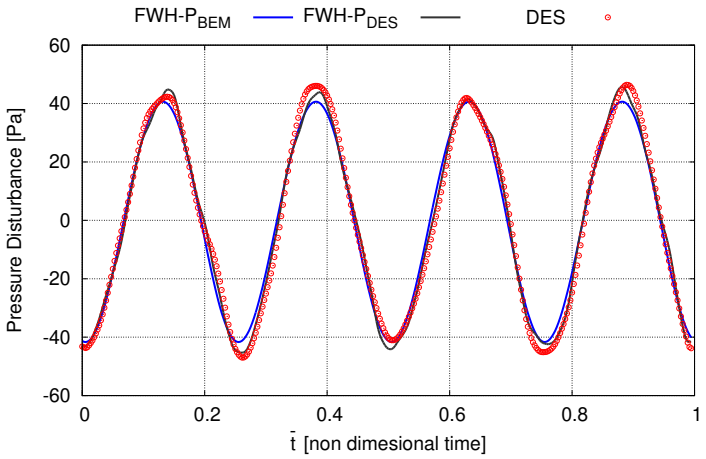

FIGURE 5.130: Comparison among noise signals predicted by DES, $FWH-P/BEM$ and $FWH-P/DES_{Unsteady}$ at obs 2.

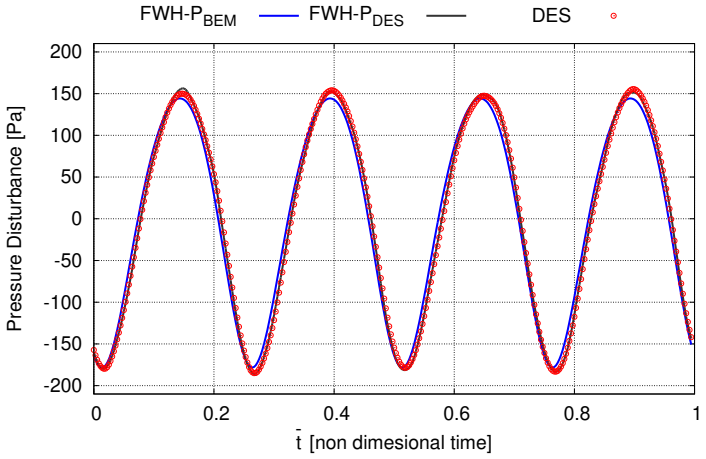

FIGURE 5.131: Comparison among noise signals predicted by DES, $FWH-P/BEM$ and $FWH-P/DES_{Unsteady}$ at obs 3.

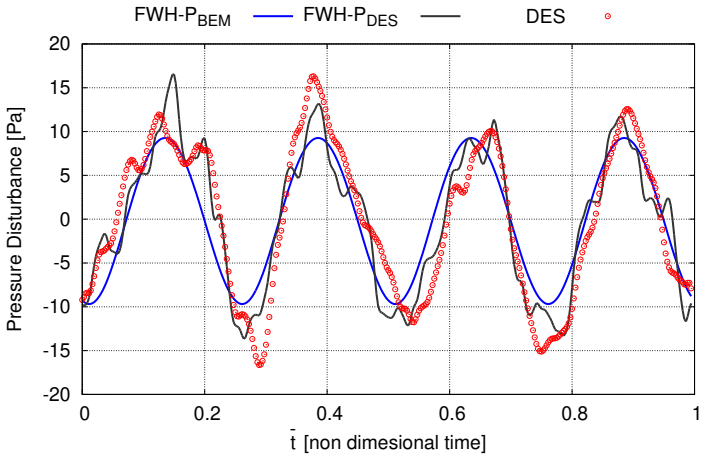

FIGURE 5.132: Comparison among noise signals predicted by DES, $FWH-P/BEM$ and $FWH-P/DES_{Unsteady}$ at obs 4.

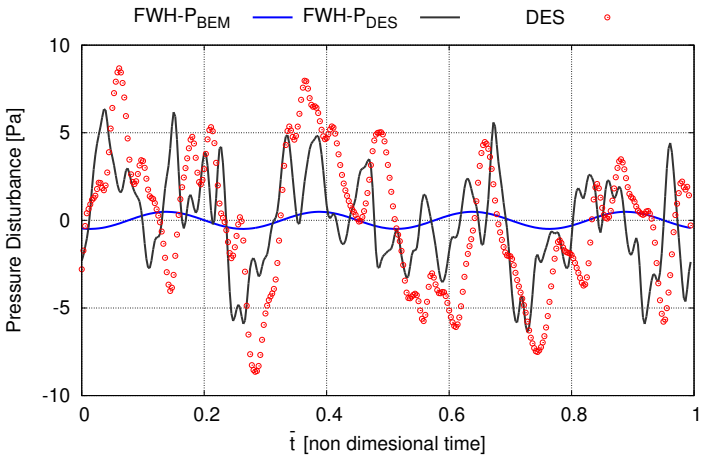

FIGURE 5.133: Comparison among noise signals predicted by DES, $FWH-P/BEM$ and $FWH-P/DES_{Unsteady}$ at obs 5.

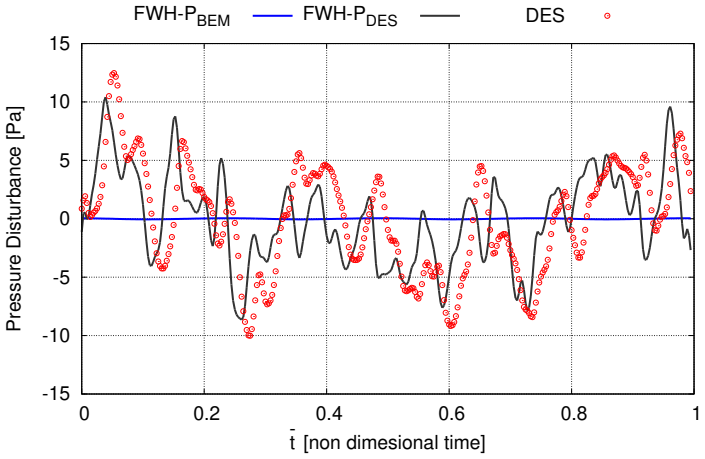

FIGURE 5.134: Comparison among noise signals predicted by DES, $FWH-P/BEM$ and $FWH-P/DES_{Unsteady}$ at obs 6.

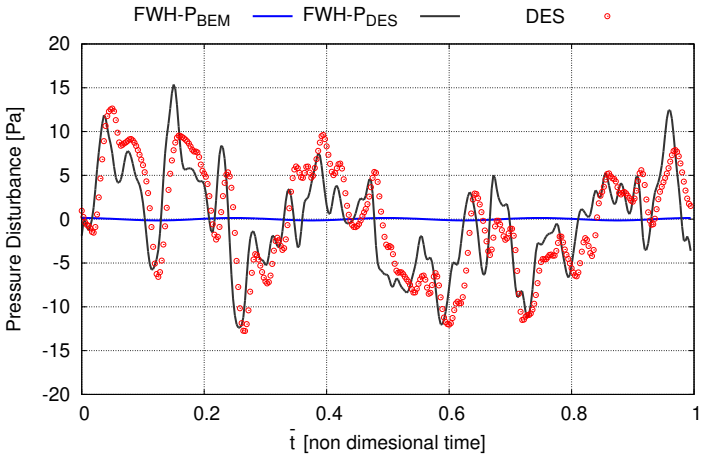

FIGURE 5.135: Comparison among noise signals predicted by DES, $FWH-P/BEM$ and $FWH-P/DES_{Unsteady}$ at obs 7.

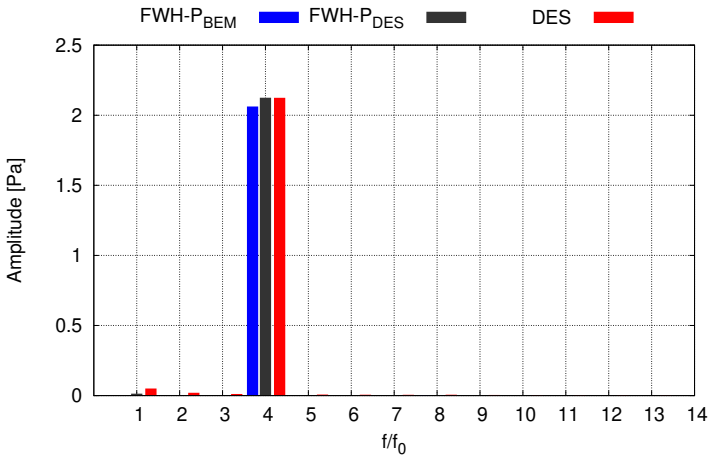

FIGURE 5.136: Comparison among noise spectra predicted by DES, $FWH-P/BEM$ and $FWH-P/DES_{Averaged}$ at obs 1.

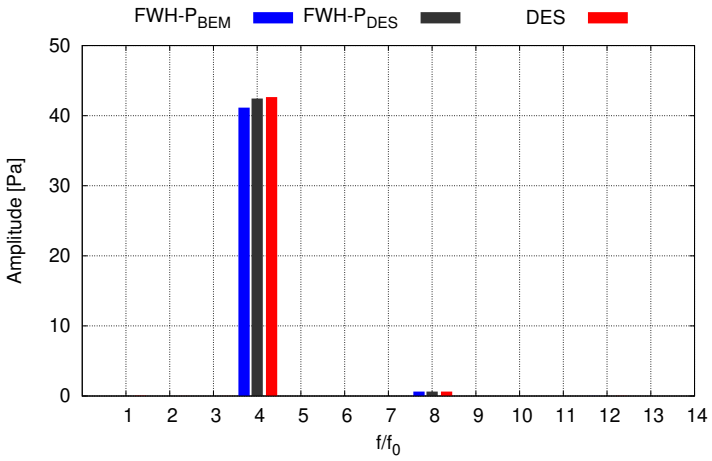

FIGURE 5.137: Comparison among noise spectra predicted by DES, $FWH-P/BEM$ and $FWH-P/DES_{Averaged}$ at obs 2.

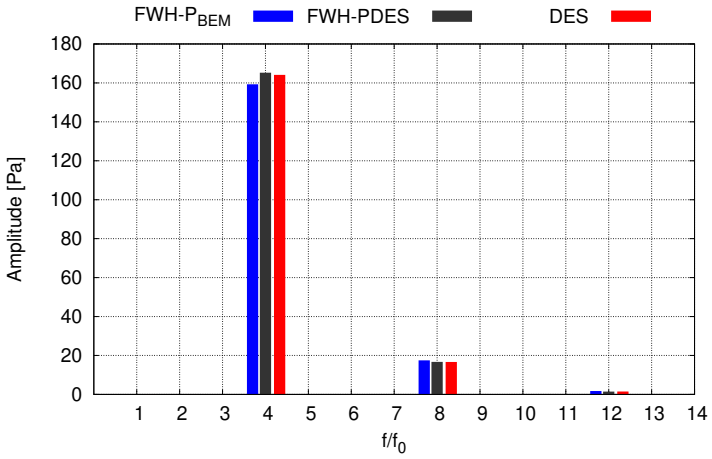

FIGURE 5.138: Comparison among noise spectra predicted by DES, $FWH-P/BEM$ and $FWH-P/DES_{Averaged}$ at obs 3.

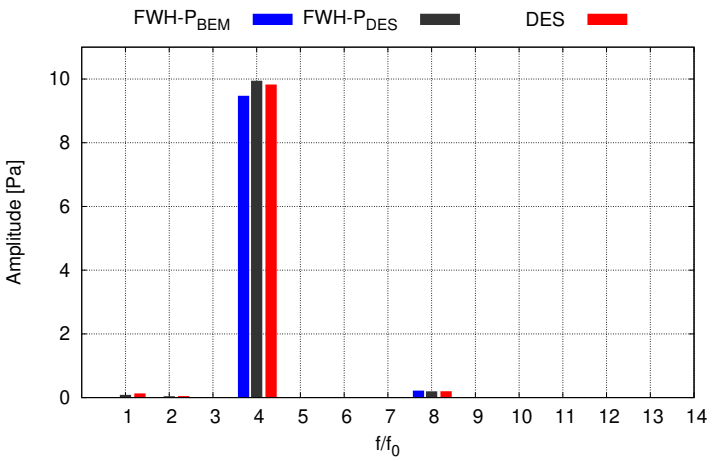

FIGURE 5.139: Comparison among noise spectra predicted by DES, $FWH-P/BEM$ and $FWH-P/DES_{Averaged}$ at obs 4.

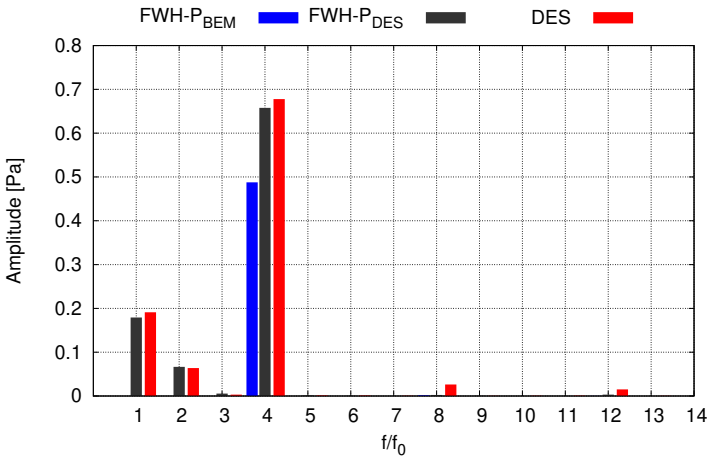

FIGURE 5.140: Comparison among noise spectra predicted by DES, $FWH-P/BEM$ and $FWH-P/DES_{Averaged}$ at obs 5.

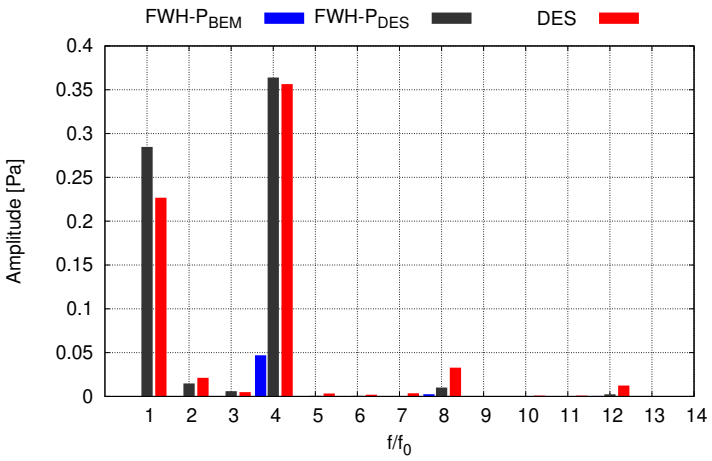

FIGURE 5.141: Comparison among noise spectra predicted by DES, $FWH-P/BEM$ and $FWH-P/DES_{Averaged}$ at obs 6.

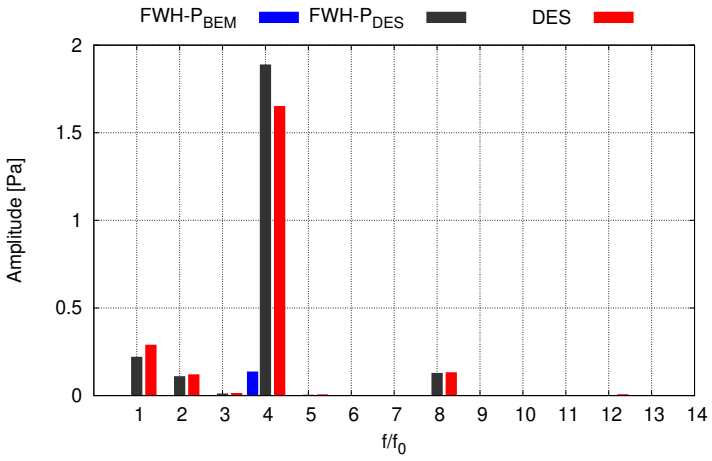

FIGURE 5.142: Comparison among noise spectra predicted by DES, $FWH-P/BEM$ and $FWH-P/DES_{Averaged}$ at obs 7.

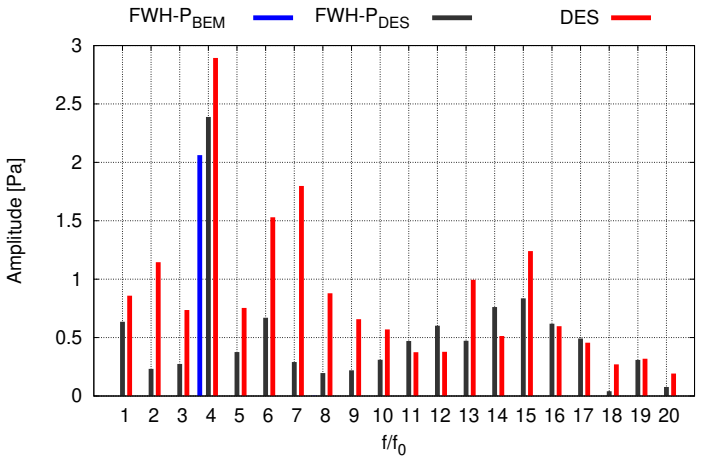

FIGURE 5.143: Comparison among noise spectra predicted by DES, $FWH-P/BEM$ and $FWH-P/DES_{Unsteady}$ at obs 1.

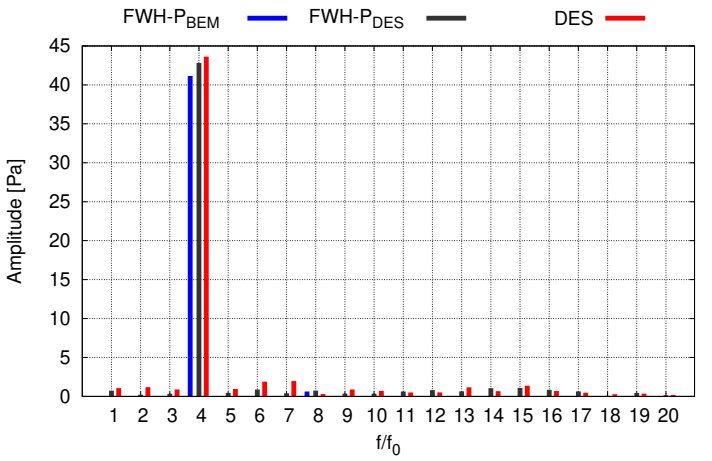

FIGURE 5.144: Comparison among noise spectra predicted by DES, $FWH-P/BEM$ and $FWH-P/DES_{Unsteady}$ at obs 2.

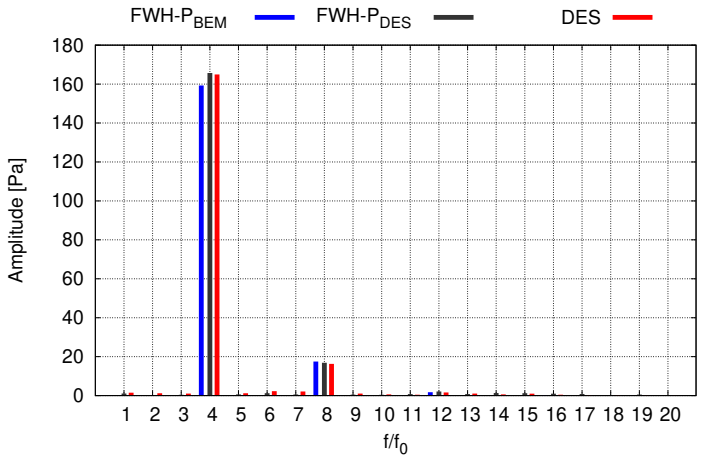

FIGURE 5.145: Comparison among noise spectra predicted by DES, $FWH-P/BEM$ and $FWH-P/DES_{Unsteady}$ at obs 3.

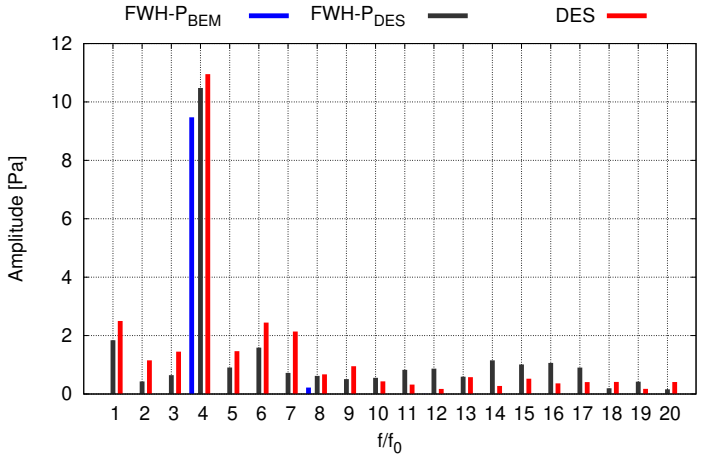

FIGURE 5.146: Comparison among noise spectra predicted by DES, $FWH-P/BEM$ and $FWH-P/DES_{Unsteady}$ at obs 4.

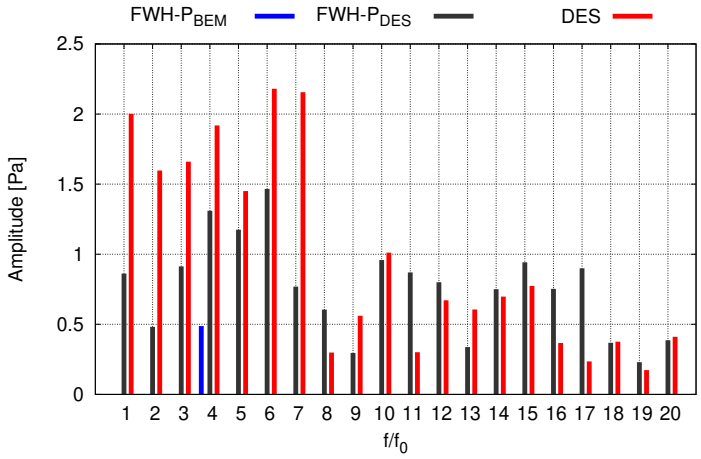

FIGURE 5.147: Comparison among noise spectra predicted by DES, $FWH-P/BEM$ and $FWH-P/DES_{Unsteady}$ at obs 5.

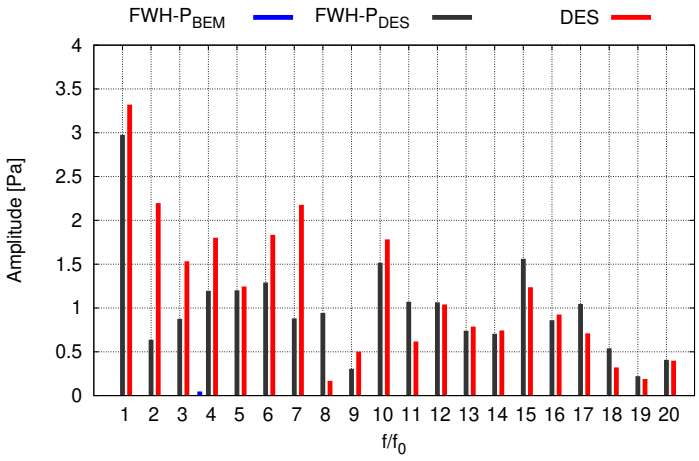

FIGURE 5.148: Comparison among noise spectra predicted by DES, $FWH-P/BEM$ and $FWH-P/DES_{Unsteady}$ at obs 6.

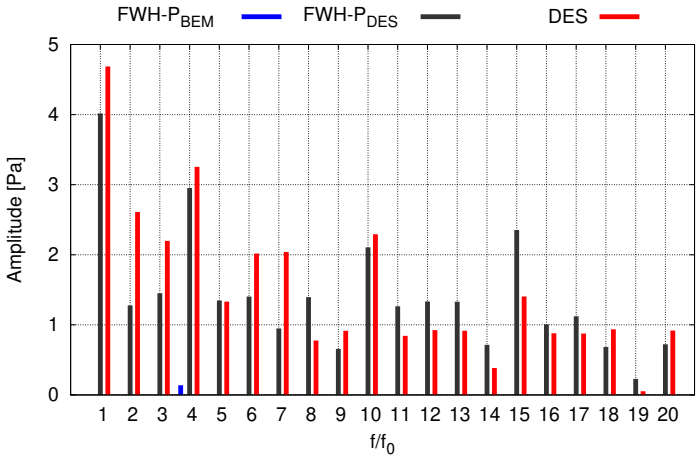

FIGURE 5.149: Comparison among noise spectra predicted by DES, $FWH-P/BEM$ and $FWH-P/DES_{Unsteady}$ at obs 7.

5.4.5 Four Bladed INSEAN E779A by DES Hydrodynamics, Comparisons with the K-Equation

In this subsection the same layout of section 5.4.3 is analyzed through the permeable approach of the Hybrid Lighthill-Ffowcs Williams and Hawkings Equation for moving surfaces (H-FWHE), which recasts into the well known K-Equation (theoretical details are reported in Chapter 3.3).

Comparisons with the solutions carried out by the FWH-P on the same configuration are also proposed.

5.4.5.1 Running Average Based Solution

Akin to subsection 5.4.3.1, let us considered the fluid dynamic data from the CFD-DES running average solution. Figure 5.150 depicts the acoustic surfaces used in the simulations: the longest is the same used with the the FWH-P formulation, having a radius equal to $0.75D$ and a length of $4.72D$. The wider porous surface depicted in red has a radius of $0.67D$ and a length of $3.25D$.

The acoustic pressure signatures reported in Figs. 5.151 to 5.157 are relative to the observers listed in Tab. 5.8. It is worth to note that the comparison between the K-Equation and the CFD based solution are in excellent agreement only for the largest porous surface.

The solution based on the same grid used for the FWH-P simulations, the tighter one, confirms the behaviour shown in the analysis concerning the monopole (see 5.3.1.2.2). It confirms the K-Equation as more demanding model with respect to the surfaces dimension compared to the FWH-P formulation because of the different content in the neglected field contribution (it needs a wider porous surface to produce convergent results). Since the advantages to be as close as possible to the noise sources are relevant, the FWH-P solution represents the best choice also because the data input of the FWH-P solver are easier to get from the CFD code, being the primary outputs.

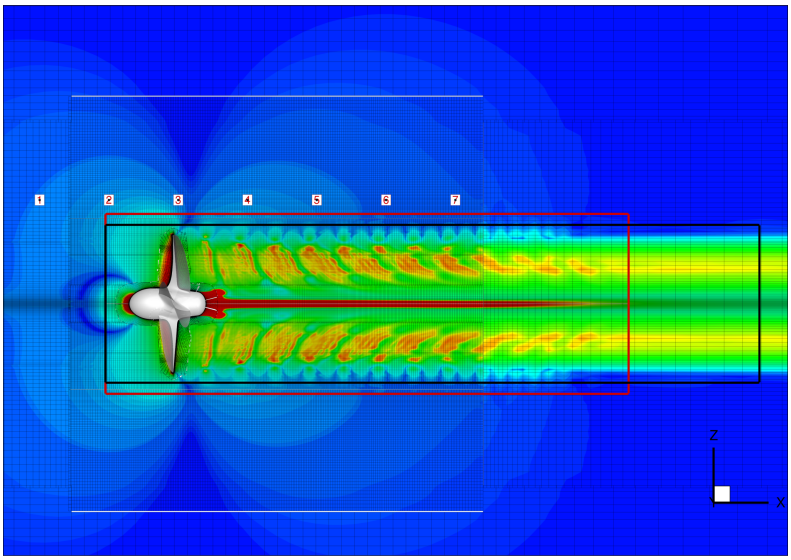

FIGURE 5.150: Porous surfaces, observer and contours of Lighthill stress tensor Frobenius norm

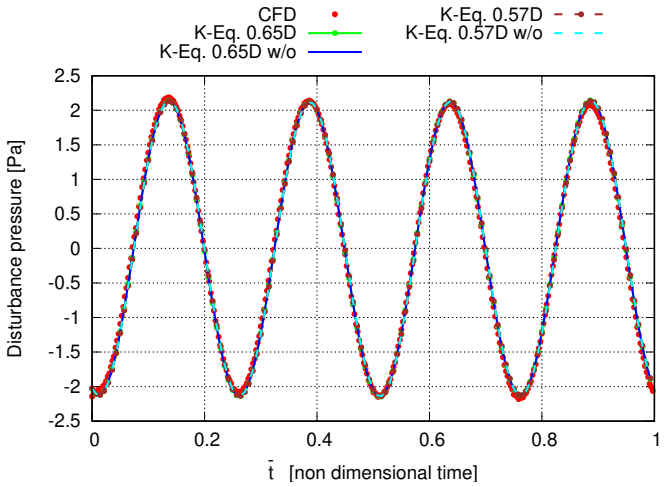

FIGURE 5.151: Observer 1, comparison between the FWH-P, K-Equation and CFD average-based pressure signatures.

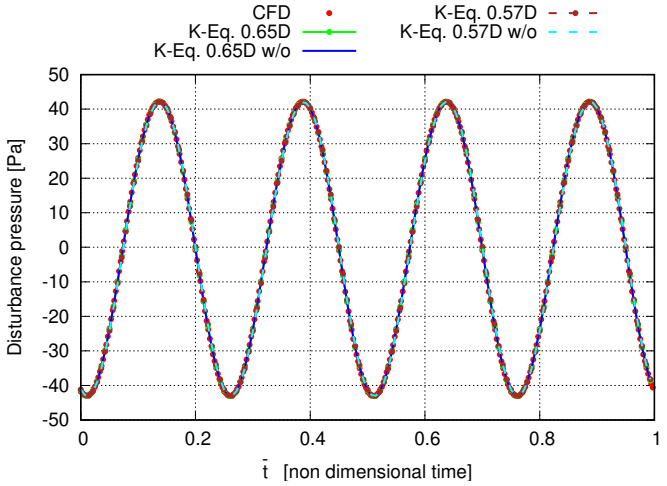

FIGURE 5.152: Observer 2, comparison between the FWH-P, K-Equation and CFD average-based pressure signatures.

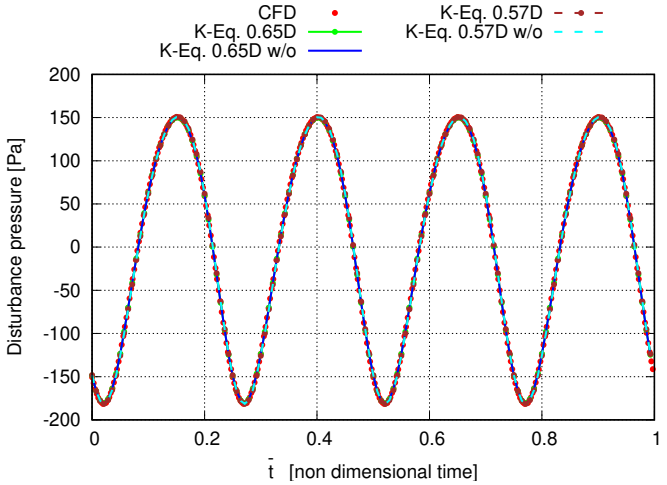

FIGURE 5.153: Observer 3, comparison between the FWH-P, K-Equation and CFD average-based pressure signatures.

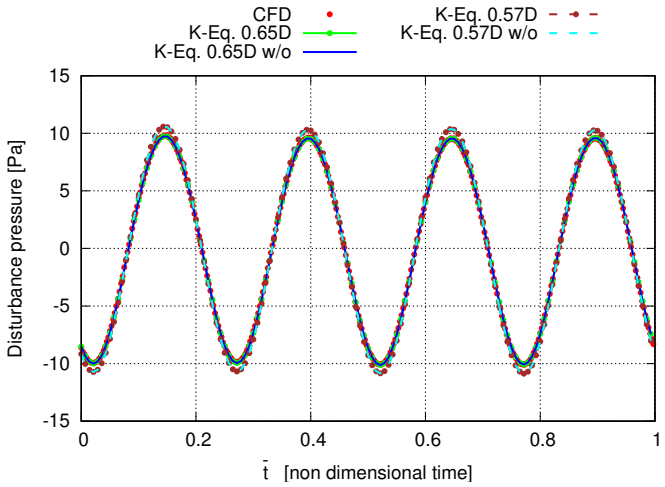

FIGURE 5.154: Observer 4, comparison between the FWH-P, K-Equation and CFD average-based pressure signatures.

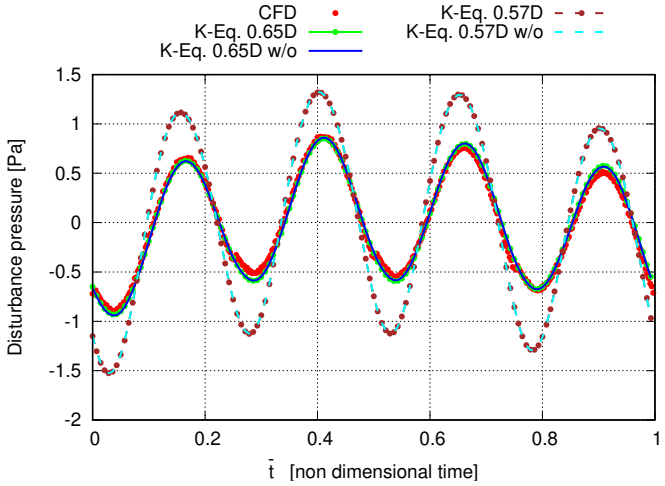

FIGURE 5.155: Observer 5, comparison between the FWH-P, K-Equation and CFD average-based pressure signatures.

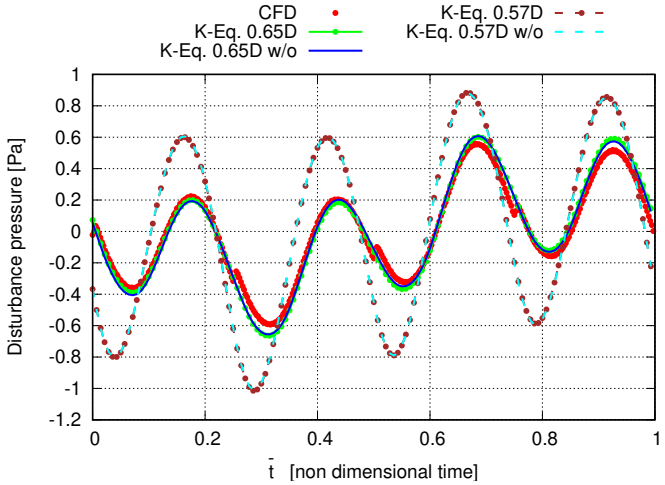

FIGURE 5.156: Observer 6, comparison between the FWH-P, K-Equation and CFD average-based pressure signatures.

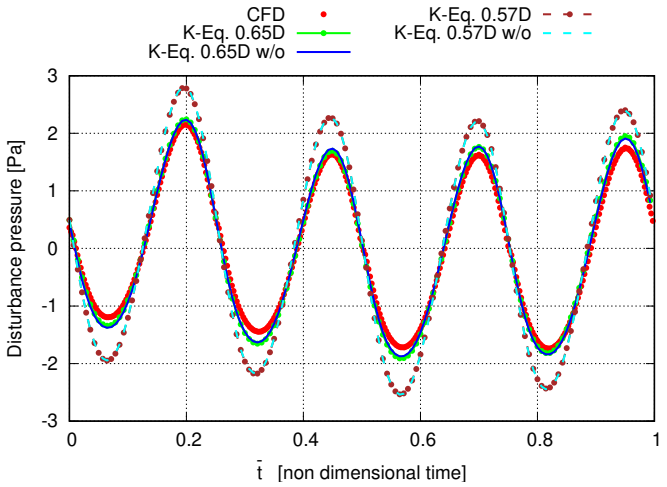

FIGURE 5.157: Observer 7, comparison between the FWH-P, the K-Equation and CFD average-based pressure signatures.

5.4.5.2 Unsteady DES Based Acoustic Simulation

The unsteady DES solution of the INSEAN E779A marine propeller is here used to assess the capabilities of the K-Equation in case of intense quadrupole noise sources induced by a turbulent flow field.

To this aim the same porous surface used in the section 5.4.3.2 is used to carry out the acoustic analysis. Particularly, the cylinder has a radius equal to $0.65D$ and a length of $3.1864D$. The same acoustic observers used in the previous analysis and listed in Tab. 5.8 are here addressed.

For those observers Figs. 5.158 to 5.164 show the comparison between the CFD based solution and those provided by the K-Equation and the FWH-P approach. The results are in excellent agreement for all observers only between the K-Equation and the FWH-P approach whereas differences with the CFD solution are present.

Such differences confirm what said about the effect of the boundary conditions of the CFD based prediction.

The similarities between the FWH-P and the K-Equation also provide further confirmations about the fact that noise sources surrounded by the permeable surface are those effectively generated by the propeller motion; thus, those to account for a physical consistent noise radiation.

Regarding to this, the unsteady case is characterized by intense quadrupole noise sources due to the turbulence; these are localized where the CFD grid is fine enough to well predict the energy cascade (see Fig.5.165, notably the fine block of the CFD solution downstream the rotor).

Unsteady predictions from the K-Equation and FWH-P are therefore in perfect agreement because both are able to embed this zone; otherwise, as shown for the case of the averaged simulation, the solutions would have been different by the virtue of their different capability to account for nonlinearities over the permeable surface.

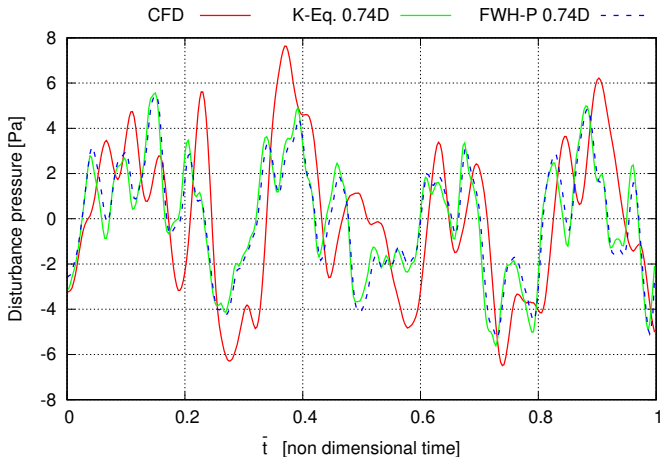

FIGURE 5.158: Observer 1, comparison between the FWH-P, K-Equation and CFD unsteady pressure signatures.

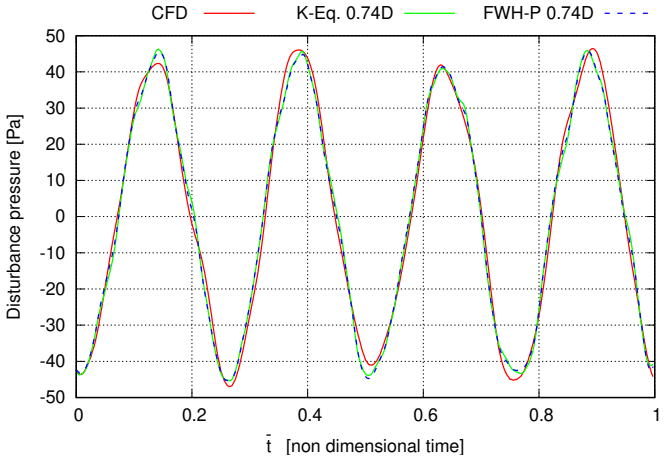

FIGURE 5.159: Observer 2, comparison between the FWH-P, K-Equation and CFD unsteady pressure signatures.

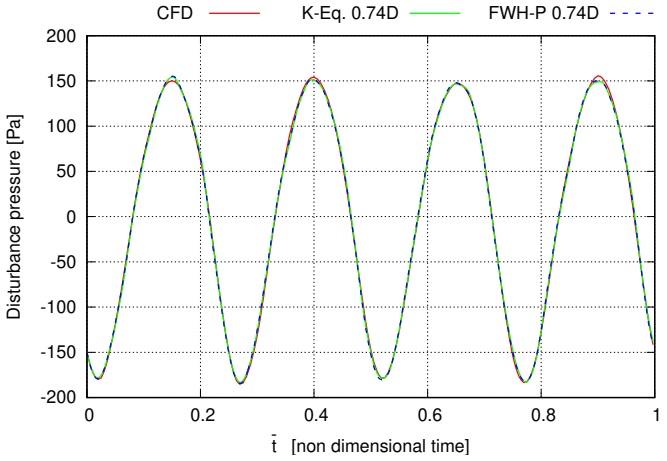

FIGURE 5.160: Observer 3, comparison between the FWH-P, K-Equation and CFD unsteady pressure signatures.

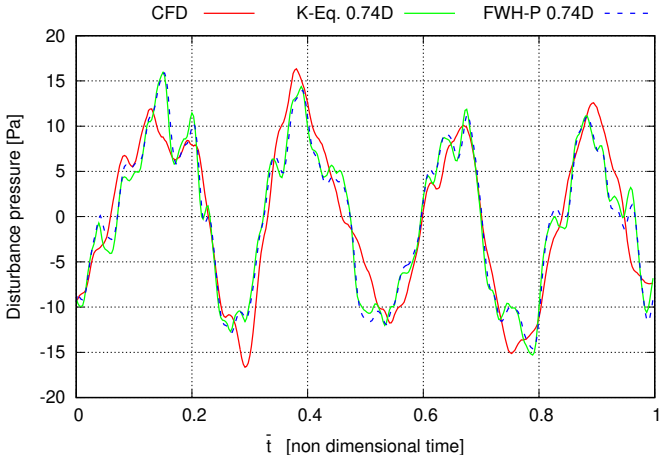

FIGURE 5.161: Observer 4, comparison between the FWH-P, K-Equation and CFD unsteady pressure signatures.

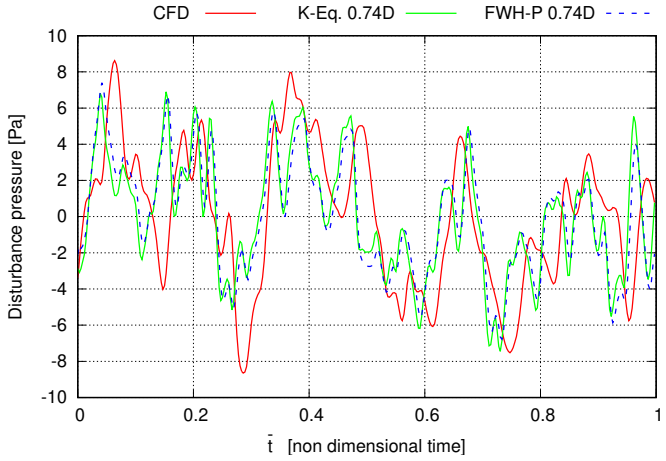

FIGURE 5.162: Observer 5, comparison between the FWH-P, K-Equation and CFD unsteady pressure signatures.

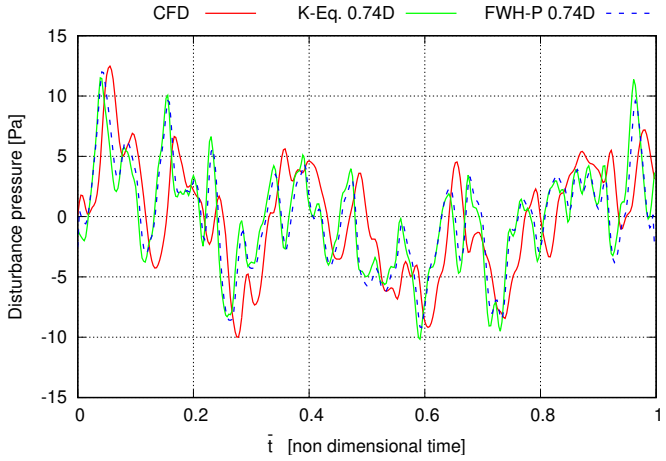

FIGURE 5.163: Observer 6, comparison between the FWH-P, K-Equation and CFD unsteady pressure signatures.

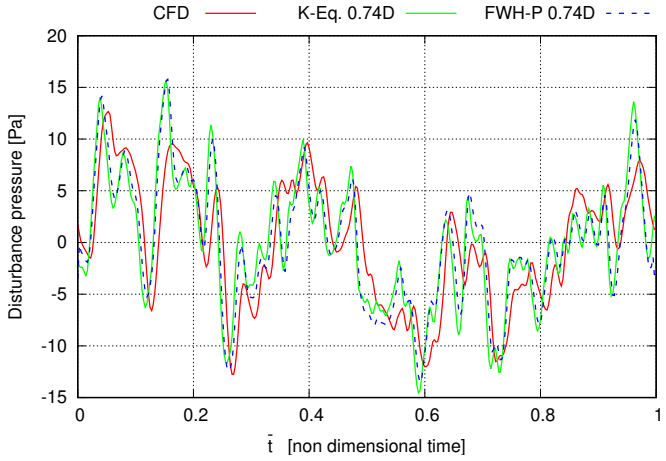

FIGURE 5.164: Observer 7, comparison between the FWH-P, K-Equation and CFD unsteady pressure signatures.

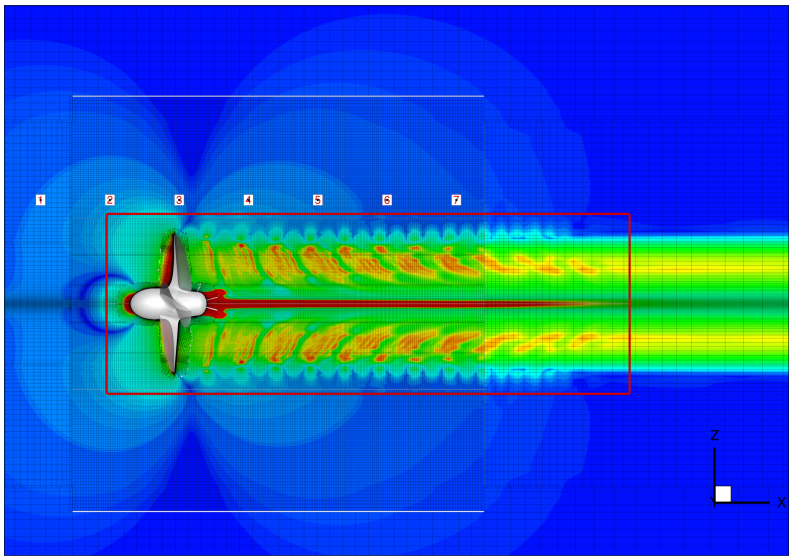

FIGURE 5.165: Permeable surface with respect to contours of Lighthill stress tensor norm.

5.4.6 INSEAN E779A Propeller In Yaw Condition by DES Hydrodynamics

In the following, the hydroacoustic behavior of the INSEAN E779A four-bladed propeller in drifting condition is addressed through the FWH-P approach.

The main geometrical features of this rotating device are given in [69]. It moves horizontally in open water at a yaw angle of 20°, with advance ratio J equal to 0.71 and angular velocity $n = 25$ Hz.

The hydrodynamic data are provided by a Detached Eddy Simulation technique along with the Smagorisky turbulence model. The hydroacoustic analysis is performed for hydrodynamic conditions characterized by a fully-developed propeller wake structure (converged CFD solution).

Noise signatures evaluated at observers translating with the hub are based on the knowledge of the unsteady pressure and velocity field distributions upon a cylindrical acoustic surface S moving with the propeller hub.

The hydrodynamic analysis of the vortical/turbulence structures evolution behind the propeller disk guides the optimal placement of S in order to avoid impact phenomena; to comply with this requirement, S is chosen with generatrix line laying in a horizontal plane and inclined of 13.5° respect to the x axis.

Figure 5.166 shows a top view of the propeller (rotating about the x axis and translating with velocity $U = 4.034$ m/s), enclosed within three different cylindrical surfaces, $14D$ long, with radius equal to $0.8D$, $0.85D$ and $0.9D$, respectively.

These surfaces are used to check the convergence of the noise predictions, that is, to verify that the volume noise contribution, i.e. the Lighthill stress tensor $\mathbf{T}$, is well-captured by the surface integral terms.

The analysis of the unsteady spatial distribution of the $\mathbf{T}$ Frobenius norm (namely $\|\mathbf{T}\|_2$), outside them proves that it is negligible with respect to the values of $\|\mathbf{T}\|_2$ inside. Is also worth to note that, unlike the configurations analyzed before, here the drifting operating conditions produce a finite axial dimension of the Lighthill stress tensor. Indeed the interactions between the flow structures shed downstream of the rotor and the oblique inflow condition give rise to a high turbulent viscosity which quickly dissipate the energy introduced by the propeller in the flow.

Hence, a finite axial zone shows important time space dependencies of the $\|\mathbf{T}\|_2$ also in correspondence of the coarse CFD grid. Therefore its acoustic behaviour may not be a priori neglected; thus, the acoustic grid is located in order to embed all of it despite the cut-off effect of the coarse grid downstream the most refined blocks. For conciseness, Fig. 5.166 depicts the contour plot of $\|\mathbf{T}\|_2$ at the beginning of the $15th$ revolution.

For the sixteen observers co-moving with the propeller hub (shown in Fig 5.167 along with the CFD grid topology), whose coordinates with respect to a rectangular frame of reference centered at the hub are listed in Tabs. 5.10 and 5.11, Figs. 5.170 to 5.185 show the comparison between the time histories of FWH-P and CFD results (time is nondimensional with respect to the shaft period of revolution).

Results are in good agreement only between the FWH-E solutions obtained with the three different porous surfaces.

The FWH-P solutions and those provided by the CFD DES solver are considerably different both in waveform and amplitude for all the acoustic observers.

Upstream microphones			
	x/r	y/r	z/r
Obs1	-1.945	-0.469	2.0
Obs2	-1.945	1.531	0.0
Obs3	-1.945	-0.469	-2.0
Obs4	-1.945	-2.469	0.0

Blade plane microphones			
	x/r	y/r	z/r
Obs5	0.0	0.0	2.0
Obs6	0.0	2.0	0.0
Obs7	0.0	0.0	-2.0
Obs8	0.0	-2.0	0.0

TABLE 5.10: Non dimensional hydrophones coordinates with respect to the propeller radius.

1D downstream microphones			
	x/r	y/r	z/r
Obs9	1.945	0.469	2.0
Obs10	1.945	2.469	0.0
Obs11	1.945	0.469	-2.0
Obs12	1.945	-1.531	0.0

2D downstream microphones			
	x/r	y/r	z/r
Obs13	3.89	0.938	2.0
Obs14	3.89	2.938	0.0
Obs15	3.89	0.938	-2.0
Obs16	3.89	-1.062	0.0

TABLE 5.11: Non dimensional hydrophones coordinates with respect to the propeller radius.

Such discrepancies between the FWH-P based solutions and the CFD DES outcomes are not expected because as may be seen in Figs. 5.166, 5.168 and 5.169 the main noise sources seem to be embed inside the porous surface.

Moreover the finest CFD grid (the only capable to describe the fluctuating velocity and pressure component due to the turbulence phenomena) is quite close to the observers and should contains the most intense noise sources.

On the basis of what seen in section 5.4.3.2, concerning the effect of the CFD boundary conditions, a deep analysis on the hydrodynamic flow field is necessary.

To this aim, Figs. 5.186 and 5.187 show the time evolution of the L2 norm of the Lighthill stress tensor.

Particularly, Fig. 5.186 depicts a time series of images from the non dimensional time $\bar{t} = 0.811$ to $\bar{t} = 0.850$ over the 14-th revolution in which the acoustic analysis is focused. The high part of the figures depict a growth in time of the non dimensional Lighthill stress tensor norm which goes from the top boundary of the CFD grid to the center of the field. Moreover Fig. 5.187 shows a following phase between $\bar{t} = 0.855$ to $\bar{t} = 0.894$ in which $\|\mathbf{T}\|_2$ vanishes from the top boundary and becomes to appear in the bottom going trough a configuration where the Lighthill stress tensor is present almost only near the propeller and wake.

This behaviour is periodic and can be observed about seven times in a revolution time.

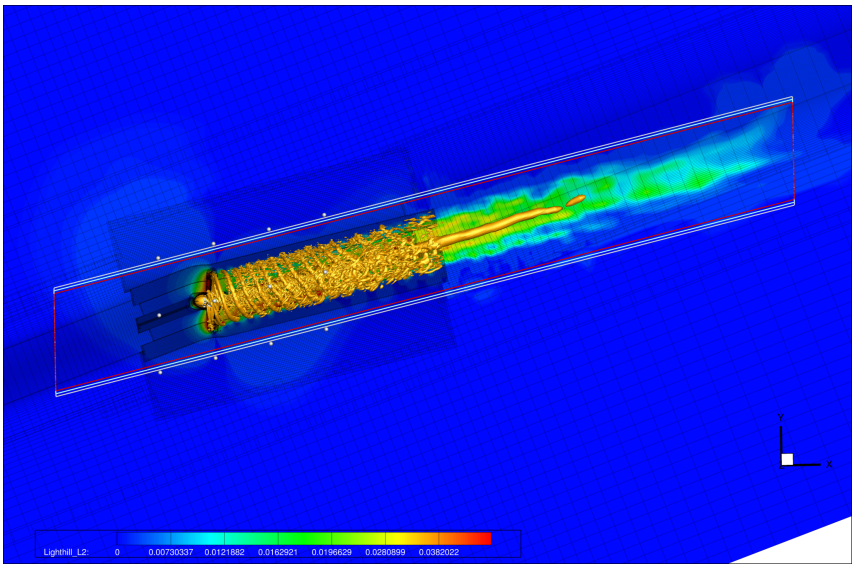

FIGURE 5.166: Nondimensional Frobenius norm $\|T\|_2$ of the Lighthill stress tensor, vortex core detection through the Jeong's $\sigma_2 = -0.2$ and acoustic porous surfaces.

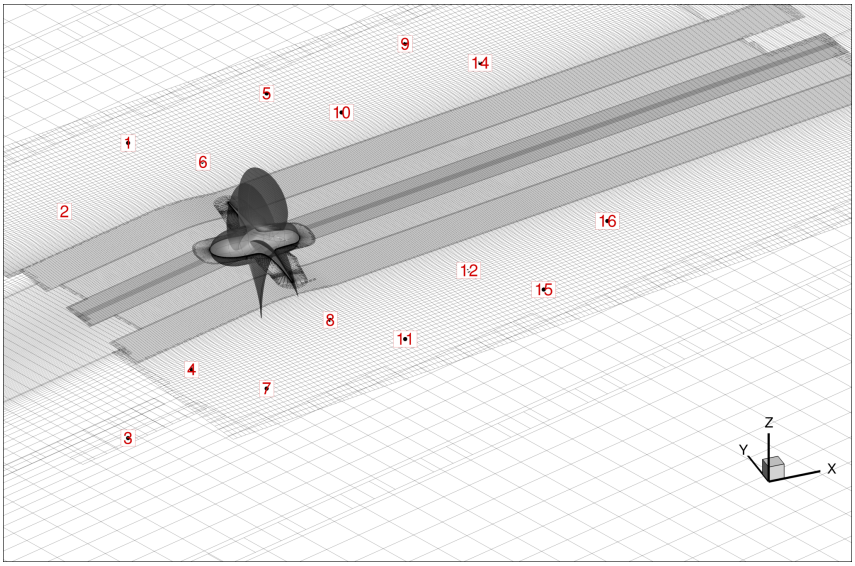

FIGURE 5.167: CFD grid topology and microphones location.

The spatial distribution of these nonphysical noise sources is mainly located at the lateral outflow boundaries where the phenomenon shows the maximum intensity, being null at the inflow boundary.

In order to have an insight into this phenomena we need to recall the definition of the Lighthill stress tensor which reads $\mathbf{T} = \left\{[\rho(\mathbf{u} \otimes \mathbf{u})] + [(p - p_0)\mathbf{I} - c_0^2 (\rho - \rho_0)\mathbf{I}] + \mathbf{V}\right\}$. The first term $\rho\mathbf{u} \otimes \mathbf{u}$ is called the Reynolds stress tensor. It is a nonlinear quantity that can be neglected except where the motion is turbulent; the spatial distribution of the Reynolds stress tensor obtained in the hydrodynamic simulation complies with this statement because weakly affects the flow field far from the propeller-wake and is null at the boundaries.

The most important contribution to the Lighthill tensor at the boundary of computational

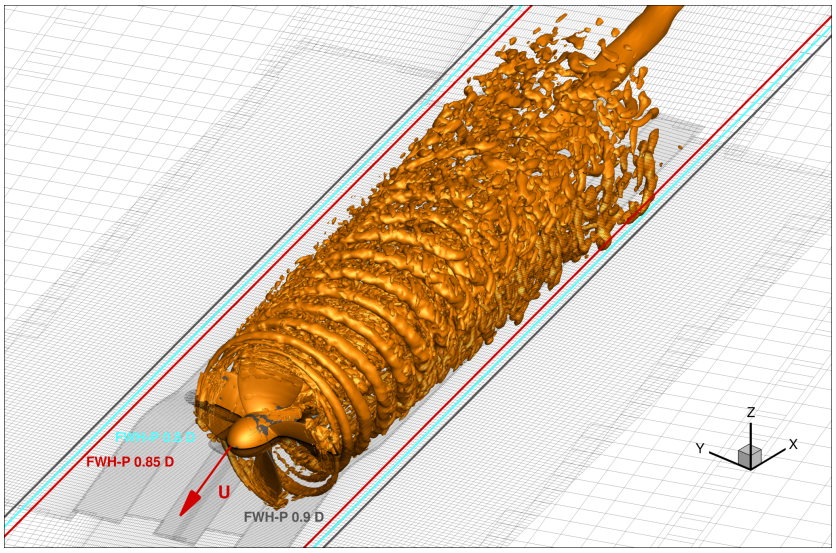

FIGURE 5.168: CFD grid, σ_2=-0.2 vortex core detection and acoustic surfaces

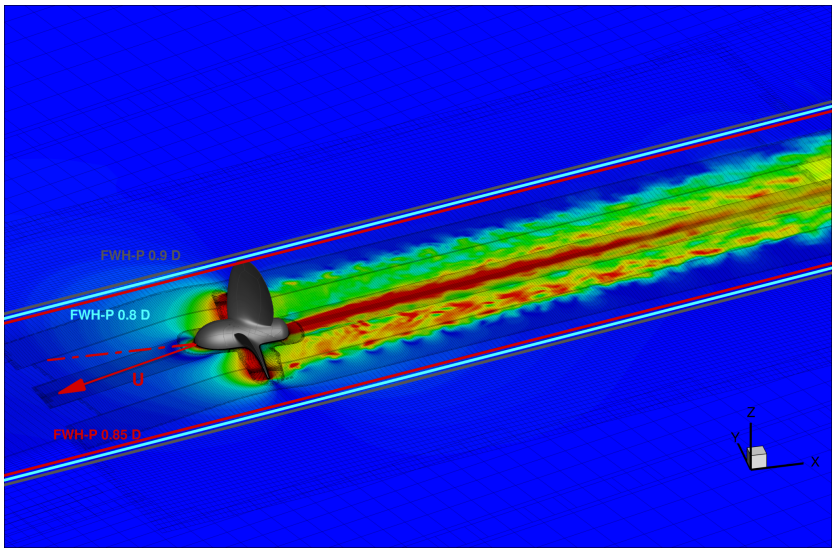

FIGURE 5.169: Enlargement of nondimensional Frobenius norm $\|T\|_2$ of the Lighthill stress tensor and acoustic surfaces.

domain is instead related with the second term, which represents the excess of momentum transfer by the pressure over that in the ideal (linear) fluid of density ρ_0 and sound speed c_0 [57]. This is produced by wave amplitude non-linearity, and by density variations in the source flow.

Being the latter contribution of the Lighthill stress tensor the one showing not physic behaviour at the boundary of the field, we suppose that such issue is related with the handling of the pressure condition at the boundary [68] which, for acoustic purposes, should be treated using suited condition based on the characteristic method.

Nevertheless, the hydrodynamic solution near the body is insulated from the external field by the effect of the discretization strategy. This is well evident in Fig. 5.186 and Fig. 5.187 showing a zone near the body and wake where the Lighthill stress tensor is practically uninfluenced by the effect of the boundary conditions. In other words, the noise sources

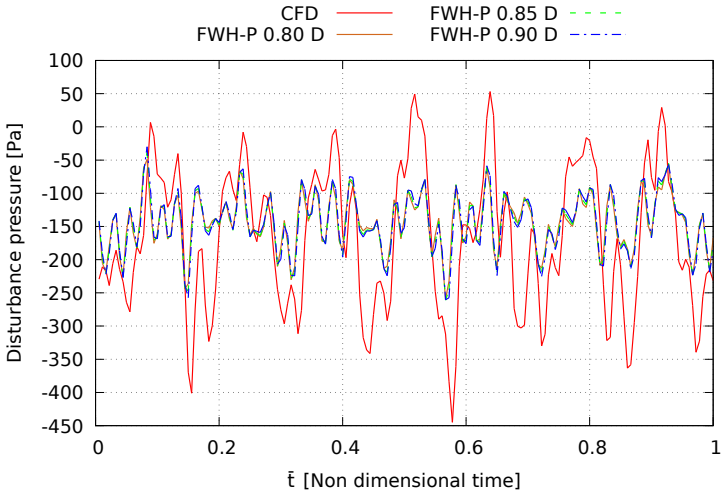

FIGURE 5.170: Comparison between FWH-P and CFD solutions at Obs1.

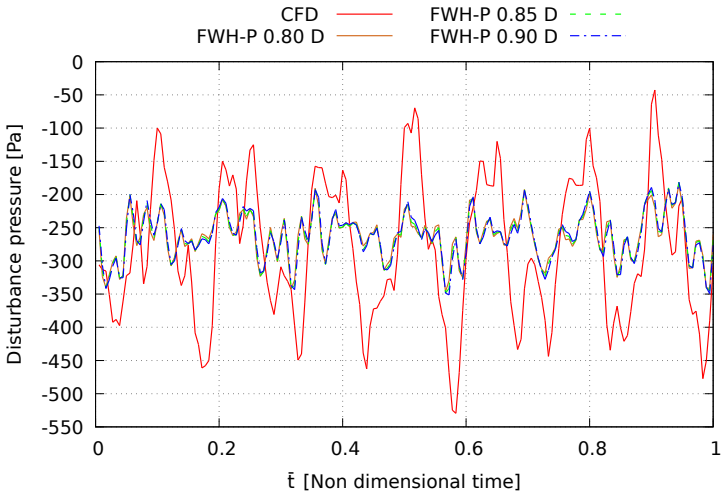

FIGURE 5.171: Comparison between FWH-P and CFD solutions at Obs2.

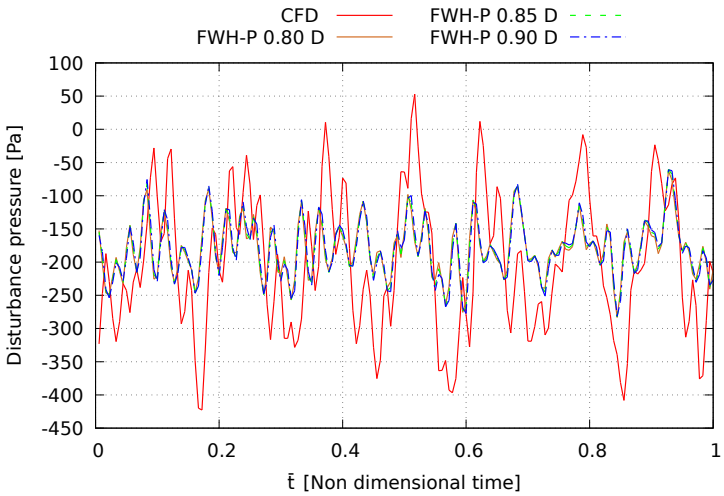

FIGURE 5.172: Comparison between FWH-P and CFD solutions at Obs3.

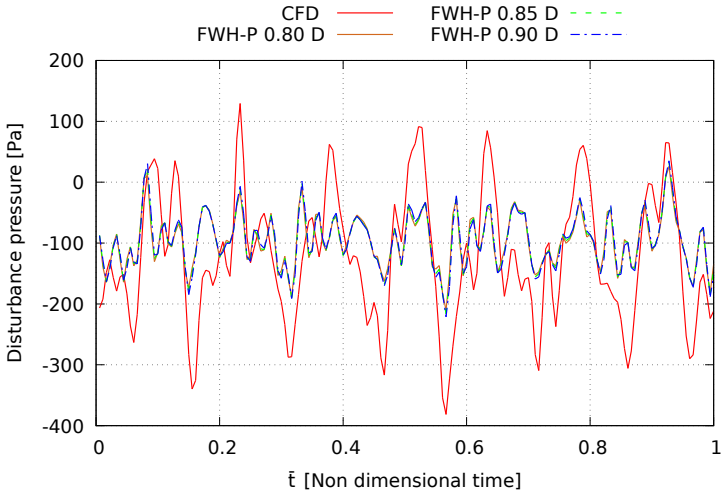

FIGURE 5.173: Comparison between FWH-P and CFD solutions at Obs4.

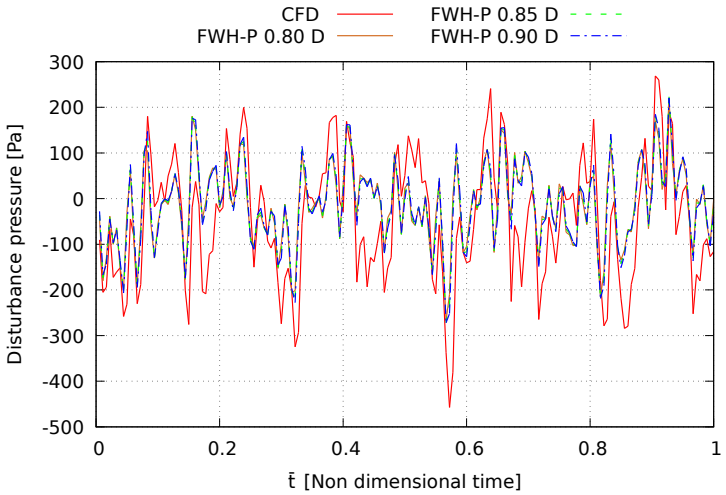

FIGURE 5.174: Comparison between FWH-P and CFD solutions at Obs5.

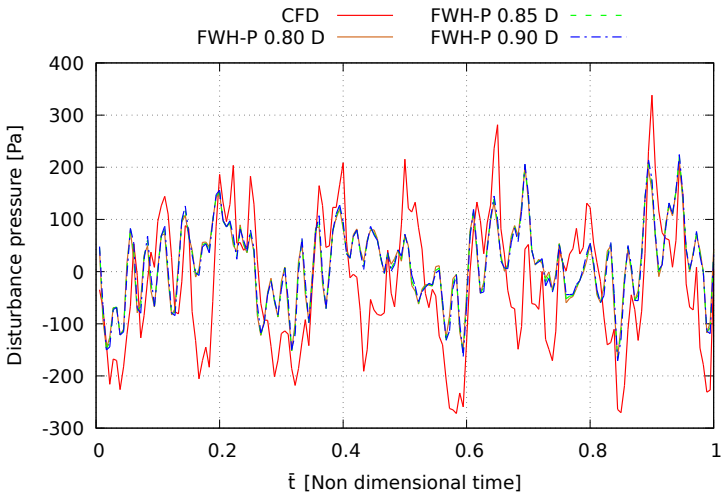

FIGURE 5.175: Comparison between FWH-P and CFD solutions at Obs6.

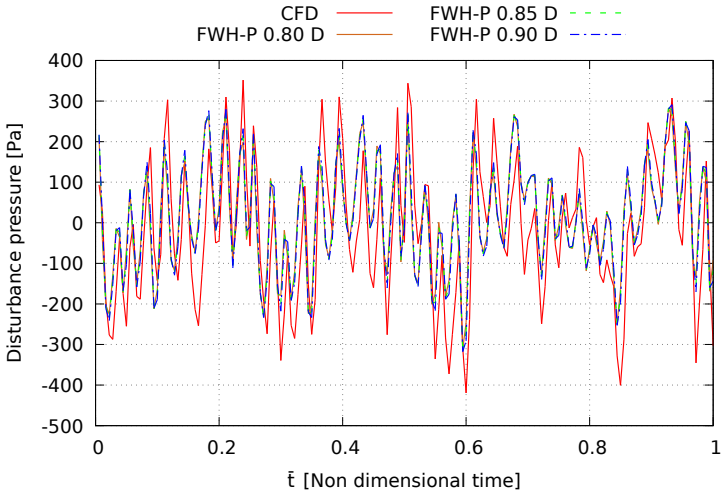

FIGURE 5.176: Comparison between FWH-P and CFD solutions at Obs7.

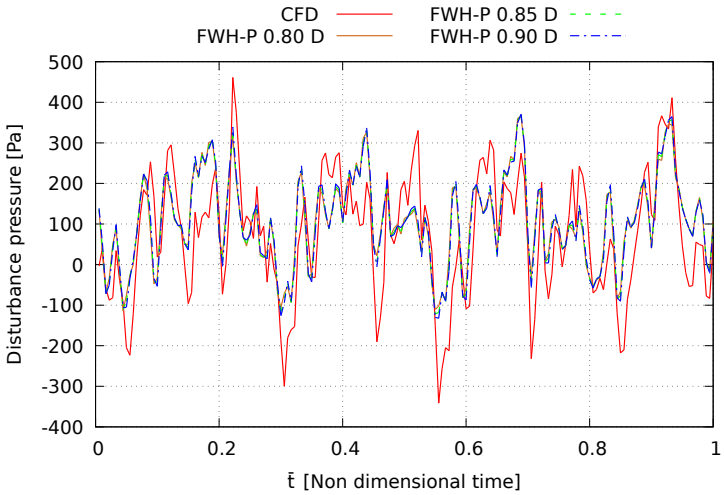

FIGURE 5.177: Comparison between FWH-P and CFD solutions at Obs8.

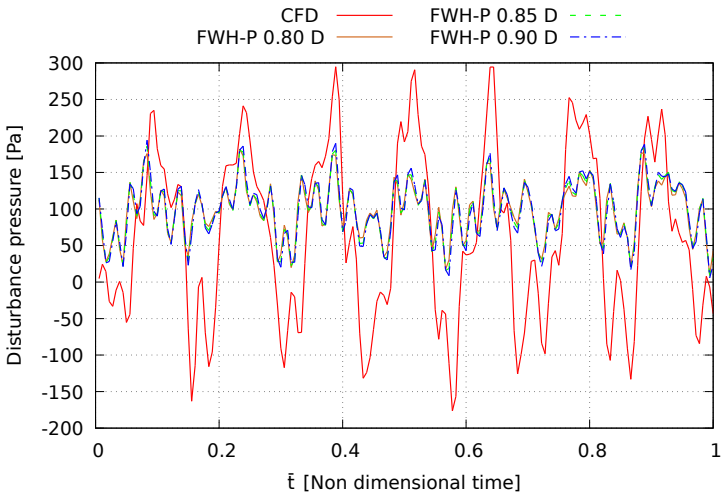

FIGURE 5.178: Comparison between FWH-P and CFD solutions at Obs9.

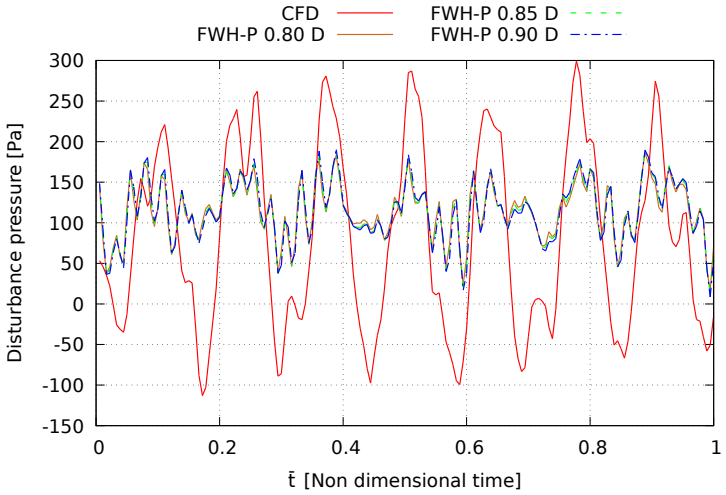

FIGURE 5.179: Comparison between FWH-P and CFD solutions at Obs10.

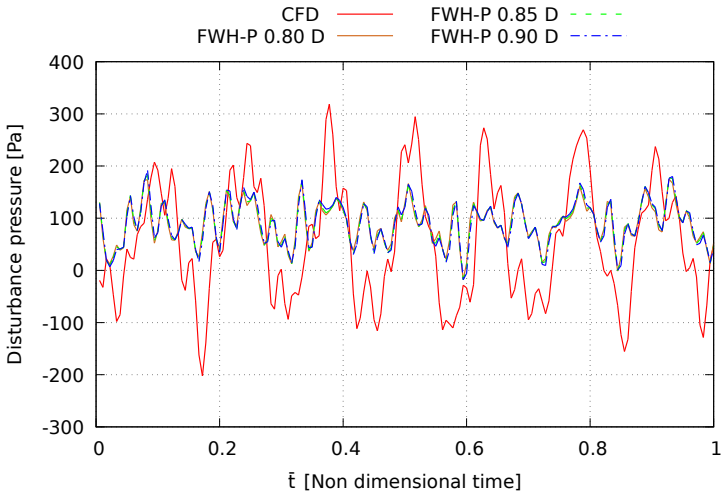

FIGURE 5.180: Comparison between FWH-P and CFD solutions at Obs11.

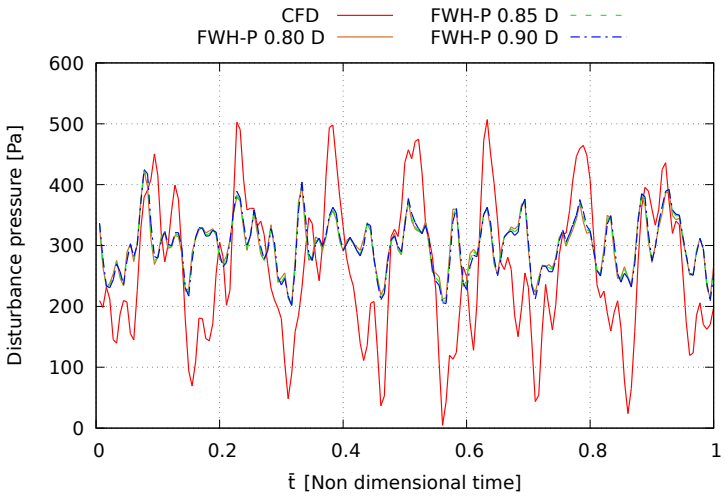

FIGURE 5.181: Comparison between FWH-P and CFD solutions at Obs12.

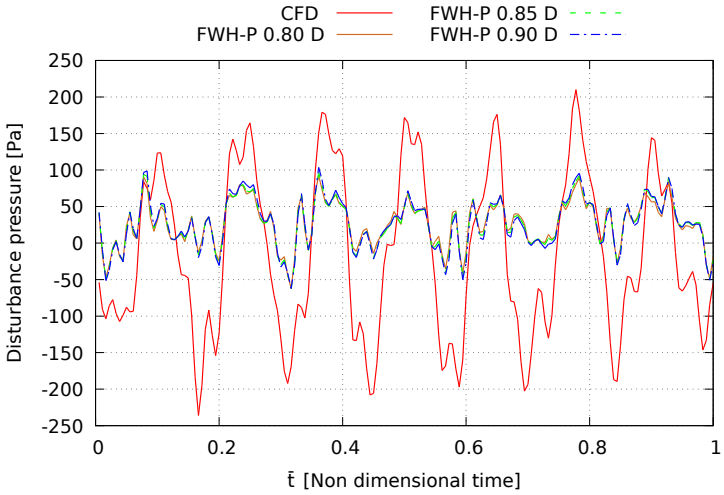

FIGURE 5.182: Comparison between FWH-P and CFD solutions at Obs13.

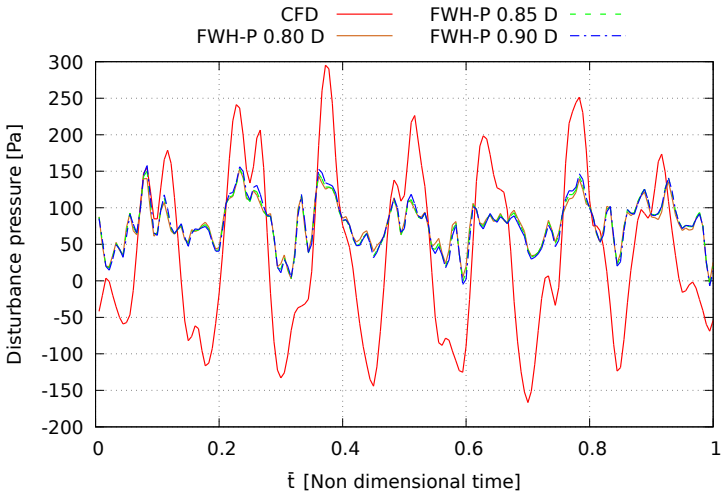

FIGURE 5.183: Comparison between FWH-P and CFD solutions at Obs14.

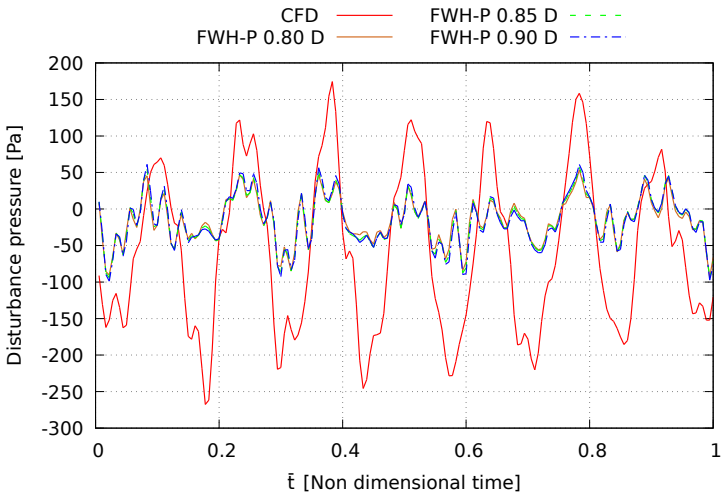

FIGURE 5.184: Comparison between FWH-P and CFD solutions at Obs15.

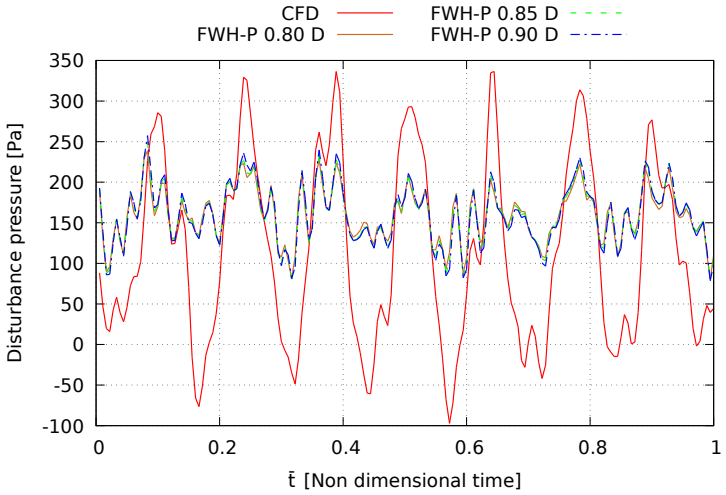

FIGURE 5.185: Comparison between FWH-P and CFD solutions at Obs16.

detection is still good if the porous surface is located tightly around the nonlinear flow field generated by blade and wake.

5.4.6.1 Characterization of the Fictitious Noise Sources

The evaluation of the sound generated by the above mentioned fictitious sources located out from the permeable surface would theoretically require the evaluation of the field contribution which is out of the purposes of this work.

Although this, this subsection proposes an evaluation of such contribution exploiting the embedding procedure definition. Such technique used to derive the FWHE (see Appendix A.1 for theoretical details) implies a discontinuous pattern of the acoustic pressure across the porous surface such that it is zero inside whereas it assumes different values outside.

One of the implications is that, for observers inside the porous surface, the surface integral contributions give rise to an acoustic pressure balanced by the field contribution of the FWHE (see also 3.2.1).

Hence, for observers inside the permeable surface the induced acoustic pressure by external noise sources coincides with the opposite value of the integral surface contribution (for clarity see the prove of such property carried out through the use of monopoles 5.3.1.3).

In order to exploit this property, let us consider the three porous surfaces depicted in Fig. 5.188 which embed the same acoustic observers of the previous analysis listed in Tabs. 5.10 and 5.11.

Figures 5.190 to 5.205 depict the comparison between the acoustic pressure induced at the aforementioned observers by the external noise sources due to the fictitious effect arising by the boundary conditions. For all the observers these contribution play a significant role on the pressure field, thus explaining the differences between the FWH-P based solution and those predicted by the CFD code. Although the intensity of the bouncing pressure may be weak by its own and then difficult to find out in the CFD predicted field, the integral over the whole volume produces fictitious acoustic disturbances up to an order of magnitude greater

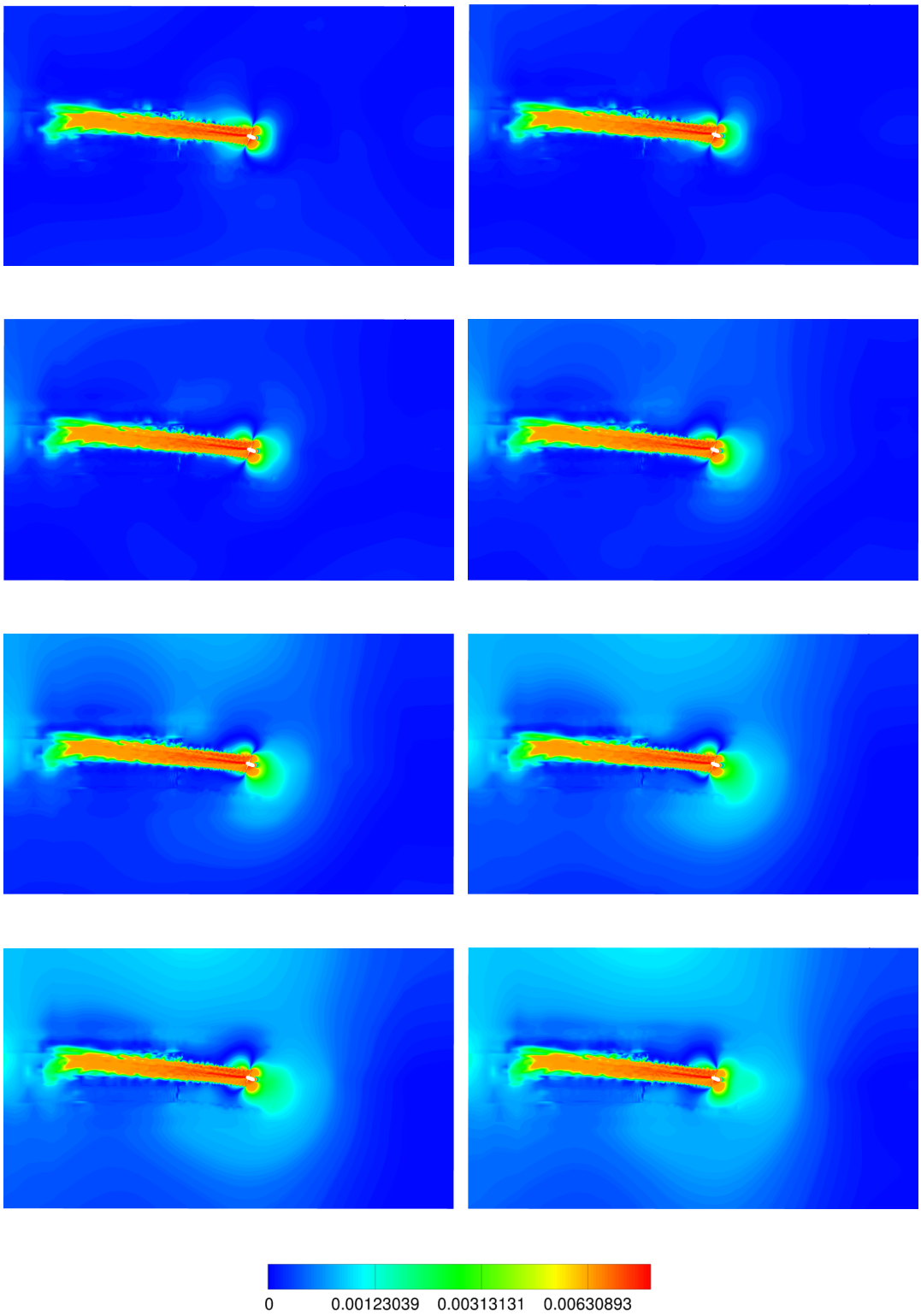

FIGURE 5.186: From top left to bottom right the non dimensional Lighthill tensor norm relative to the non dimensional time $\bar{t} = 0.811$ to $\bar{t} = 0.850$ over the 14-th revolution

respect to the real noise sources. Besides, the acoustic pressure signatures obtained with the external porous surfaces are practically invariant with respect to their axial and radial dimension, thus confirming that the fictitious noise sources are located away from the body

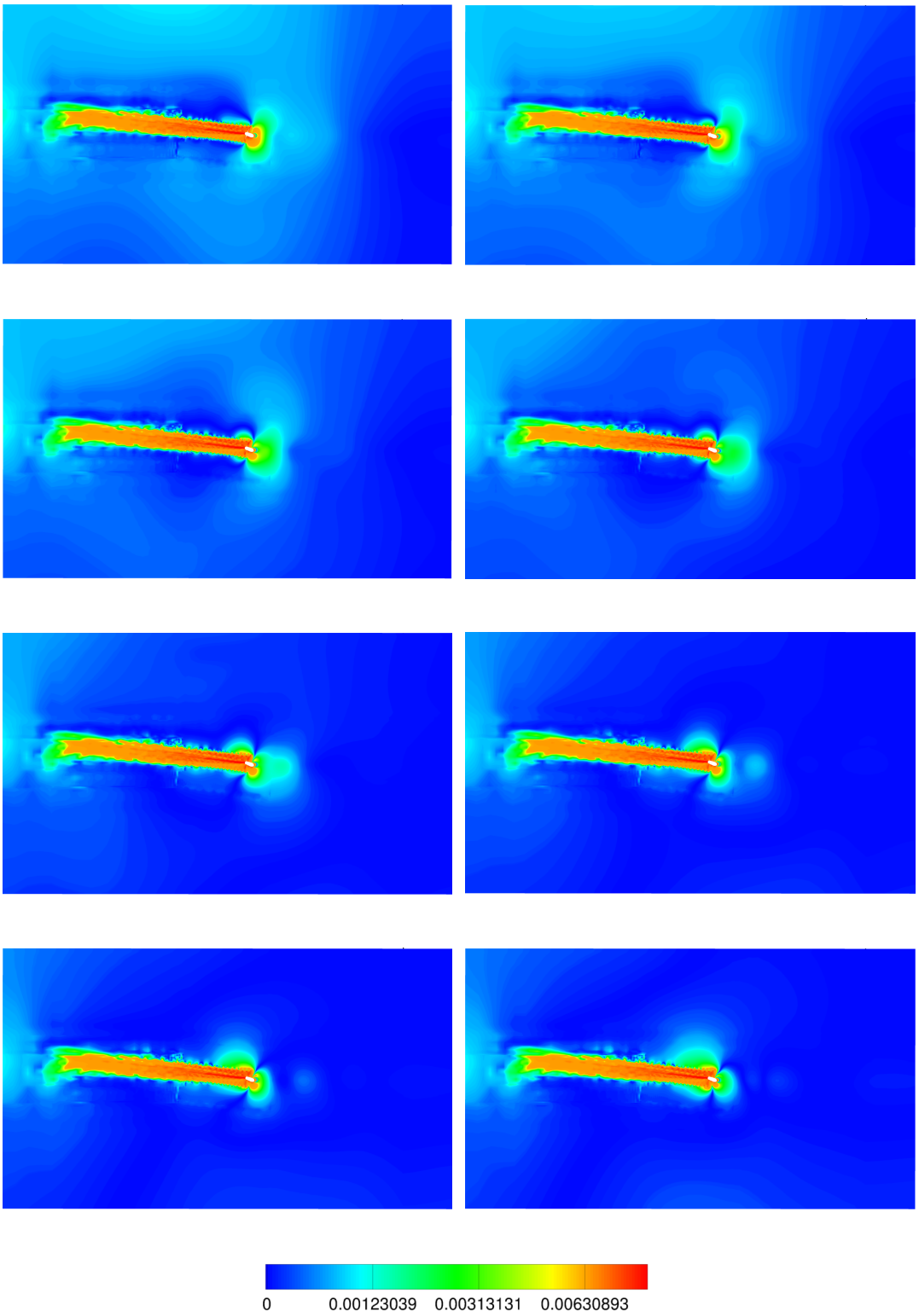

FIGURE 5.187: From top left to bottom right the non dimensional Lighthill tensor norm relative to the non dimensional time $\bar{t} = 0.855$ to $\bar{t} = 0.894$ over the 14-th revolution

and wake, that are the *real* noise sources.

This also prove our suggestion that the effect of the boundaries affects the pressure field of the CFD based solution because it accounts for all the "sources" in the field (i.e. it is

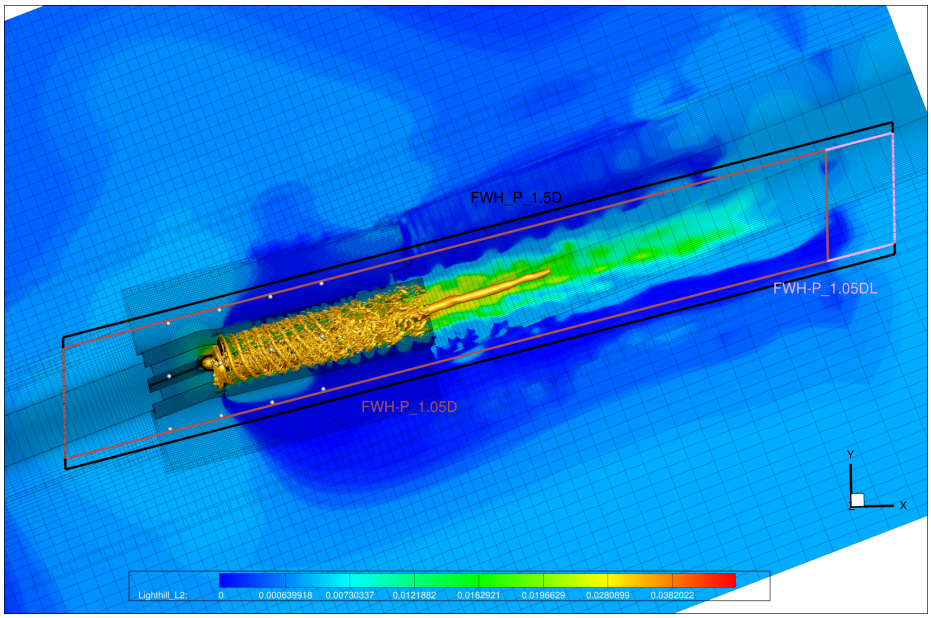

FIGURE 5.188: Porous surfaces embedding the observes, contour of the non dimensional Lighthill stress tensor relative to the non dimensional time $\bar{t} = 0,855$

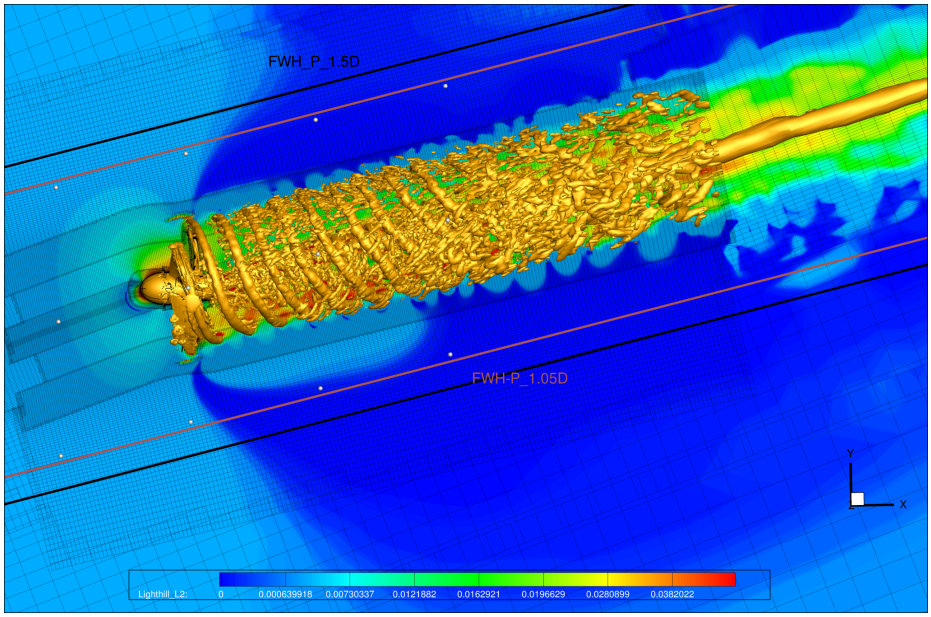

FIGURE 5.189: Enlargement of the porous surfaces embedding the acoustic observers.

elliptical). As already said, the numerical dissipation due to the CFD grid clustering features intentionally introduced to produce a zone of almost *undisturbed flow condition* around the propeller-wake makes the noise source detection reliable.

Based on these considerations, the acoustic signature provided by the FWH-P model is now compared to the CFD disturbance pressure *purged* of the contribution coming from the boundary condition. This contribution comes from the tightest porous surface embedding the observers, called $FWH - P_{1.05D}$.

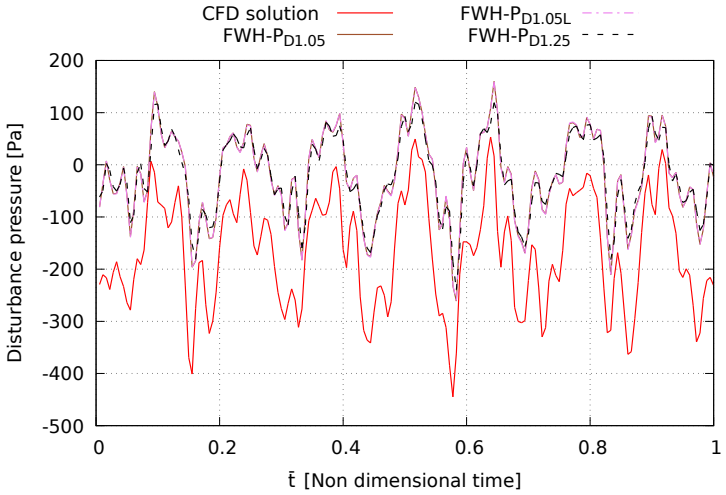

FIGURE 5.190: Comparison between the CFD solutions and the FWH-P related with the external noise sources at Obs1.

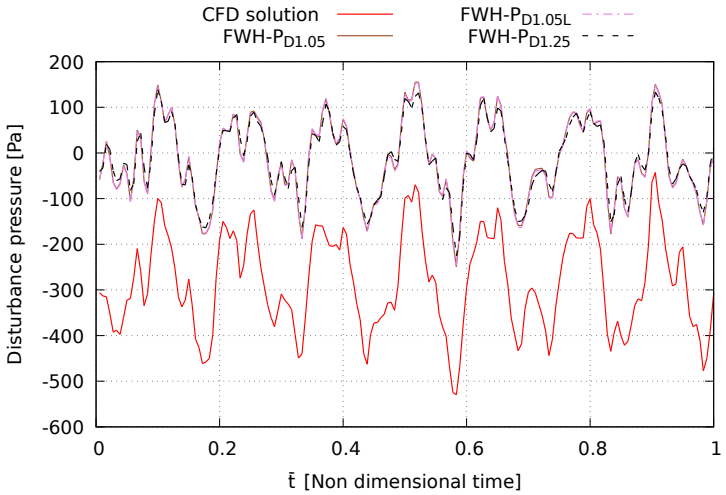

FIGURE 5.191: Comparison between the CFD solutions and the FWH-P related with the external noise sources at Obs2.

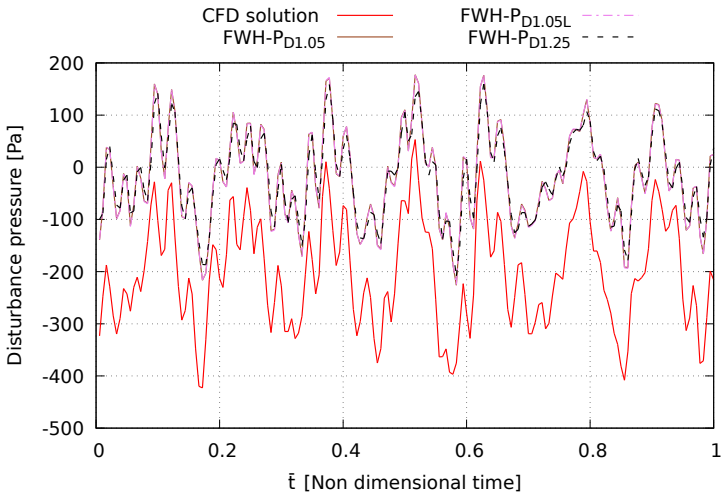

FIGURE 5.192: Comparison between the CFD solutions and the FWH-P related with the external noise sources at Obs3.

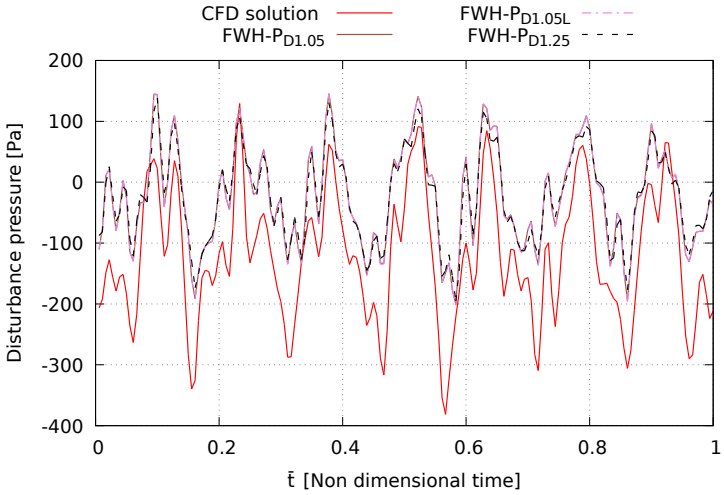

FIGURE 5.193: Comparison between the CFD solutions and the FWH-P related with the external noise sources at Obs4.

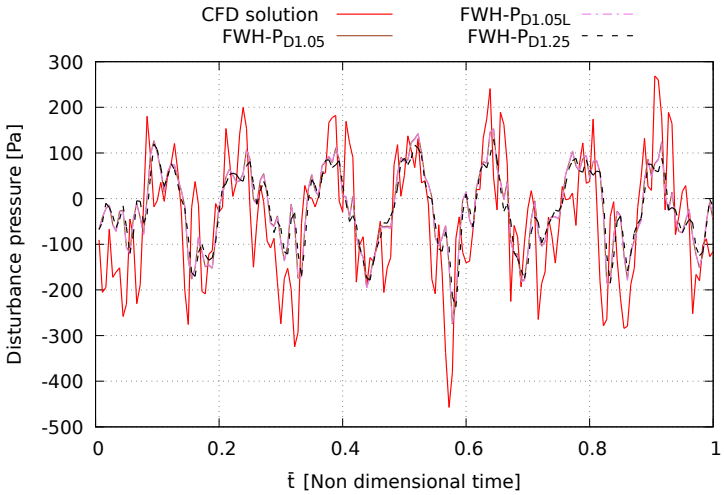

FIGURE 5.194: Comparison between the CFD solutions and the FWH-P related with the external noise sources at Obs5.

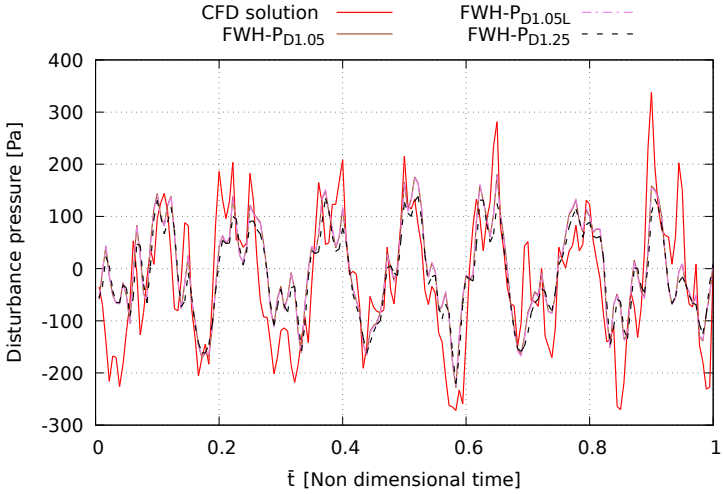

FIGURE 5.195: Comparison between the CFD solutions and the FWH-P related with the external noise sources at Obs6.

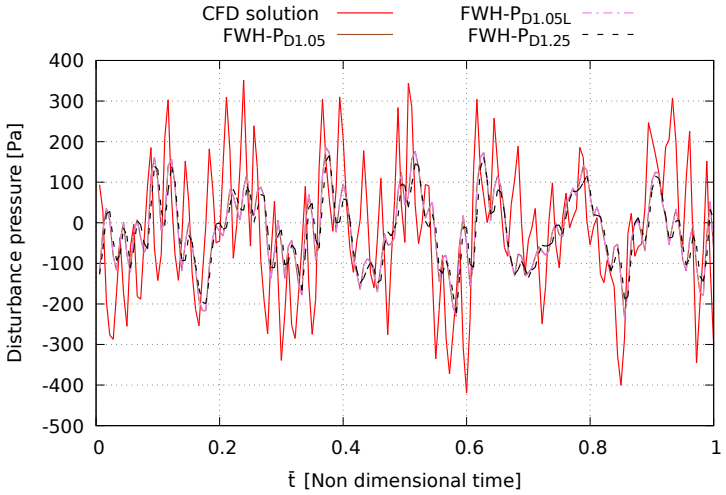

FIGURE 5.196: Comparison between the CFD solutions and the FWH-P related with the external noise sources at Obs7.

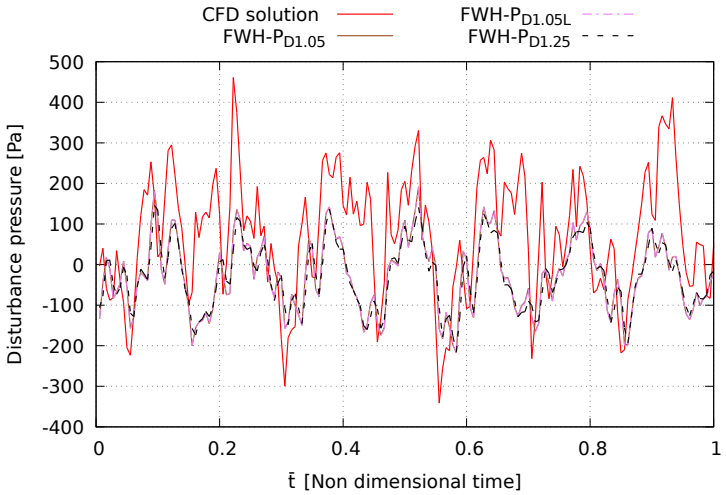

FIGURE 5.197: Comparison between the CFD solutions and the FWH-P related with the external noise sources at Obs8.

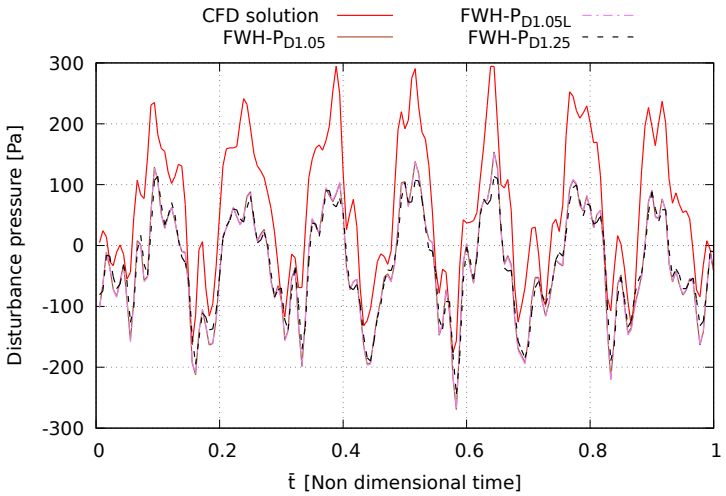

FIGURE 5.198: Comparison between the CFD solutions and the FWH-P related with the external noise sources at Obs9.

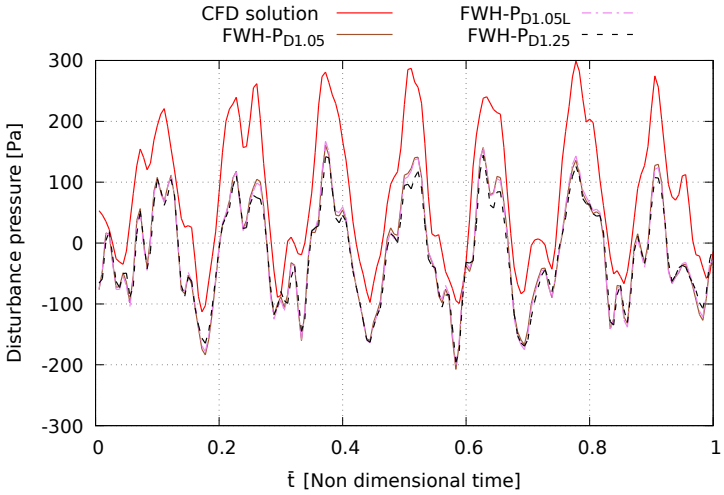

FIGURE 5.199: Comparison between the CFD solutions and the FWH-P related with the external noise sources at Obs10.

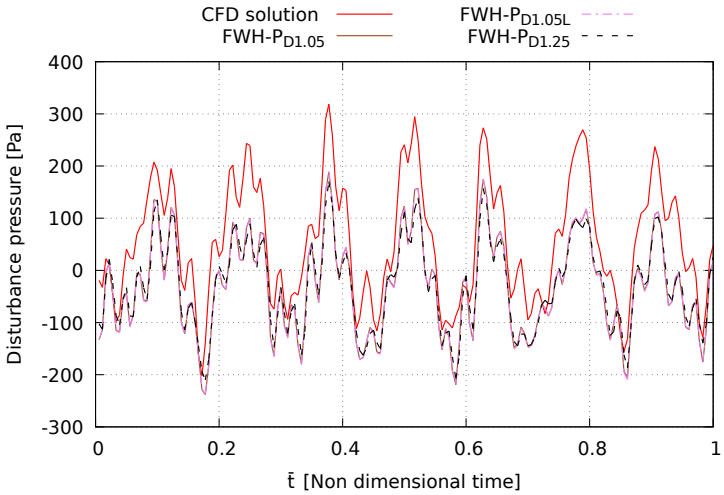

FIGURE 5.200: Comparison between the CFD solutions and the FWH-P related with the external noise sources at Obs11.

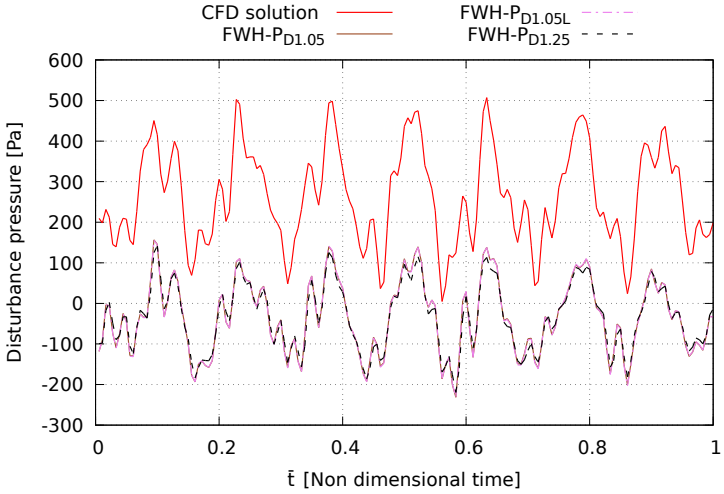

FIGURE 5.201: Comparison between the CFD solutions and the FWH-P related with the external noise sources at Obs12.

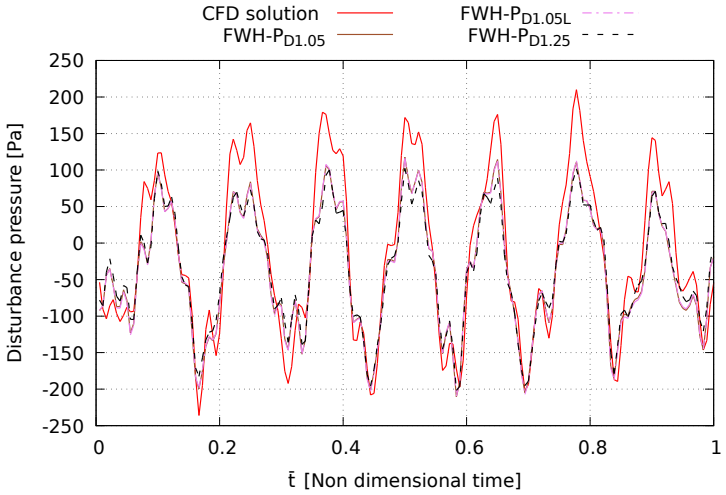

FIGURE 5.202: Comparison between the CFD solutions and the FWH-P related with the external noise sources at Obs13.

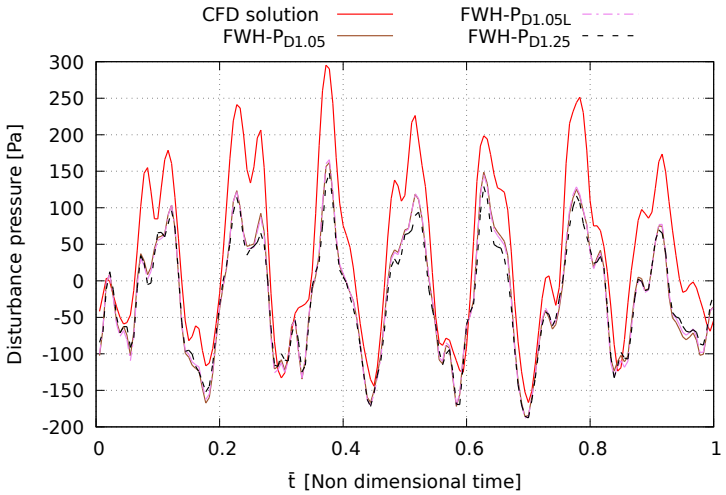

FIGURE 5.203: Comparison between the CFD solutions and the FWH-P related with the external noise sources at Obs14.

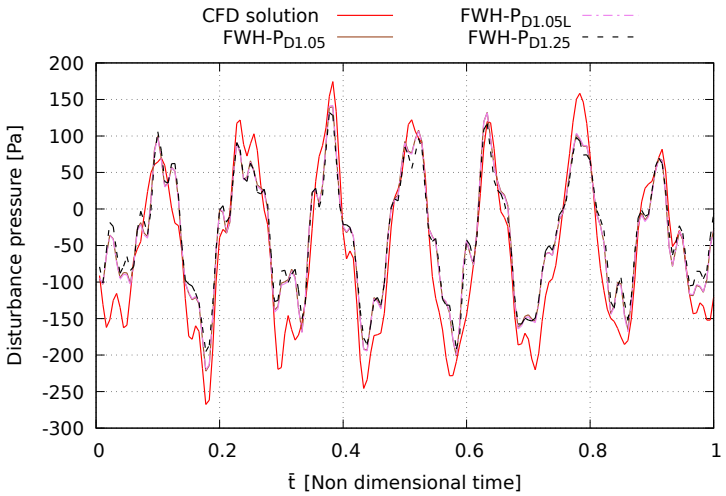

FIGURE 5.204: Comparison between the CFD solutions and the FWH-P related with the external noise sources at Obs15.

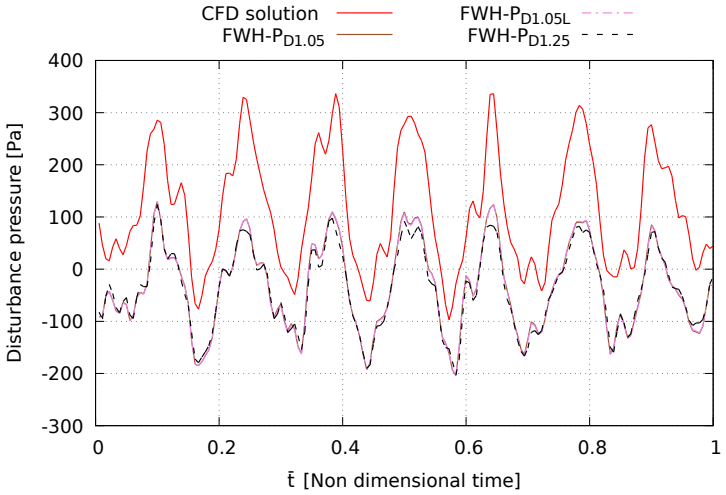

FIGURE 5.205: Comparison between the CFD solutions and the FWH-P related with the external noise sources at Obs16.

This choice is based on the fact that although the solutions coming from the externals (with respect to the acoustic observer) porous surface are very similar, from a theoretical standpoint some noise sources remains trapped between the internal and external porous surfaces (with respect to the observers).

However, the purpose of this technique is *only* to carry out a baseline for comparison for the acoustic solution of the FWH-P technique, since it provides by its own a filtering effect with respect to the external noise sources (for clarity see also 3.2.1).

Figures 5.206 to 5.221 show the above mentioned comparison where the solution called $CFD\ w/o\ outer$ indicates the CFD solution to which has been subtracted the acoustic contribution due to the boundary condition. All the pressure signature are in excellent agreement, thus proving that the porous formulation of FWH equation provide a excellent estimation of the acoustic pressure when coupled with a noise source detection made with the CFD solver.

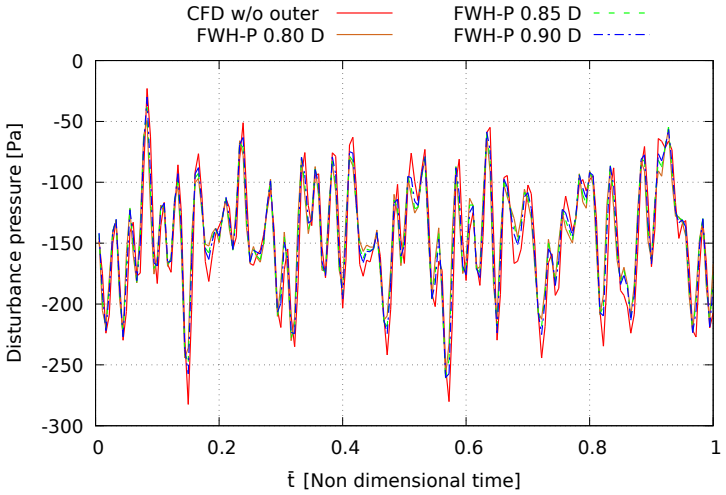

FIGURE 5.206: Comparison between FWH-P and CFD without the boundaries induced noise at Obs1.

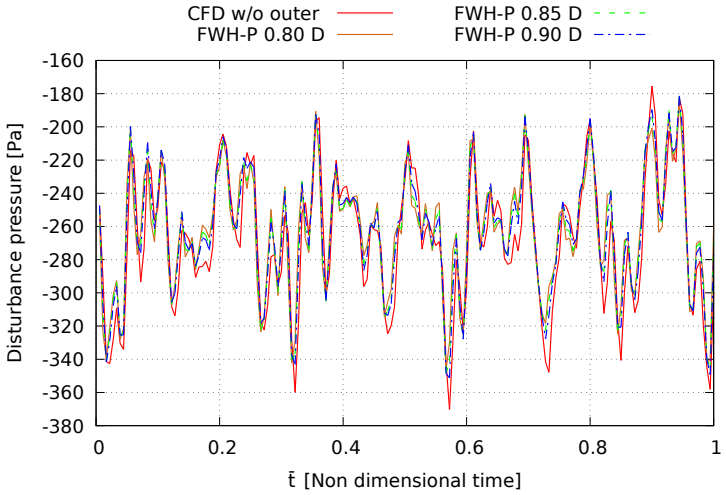

FIGURE 5.207: Comparison between FWH-P and CFD without the boundaries induced noise at Obs2.

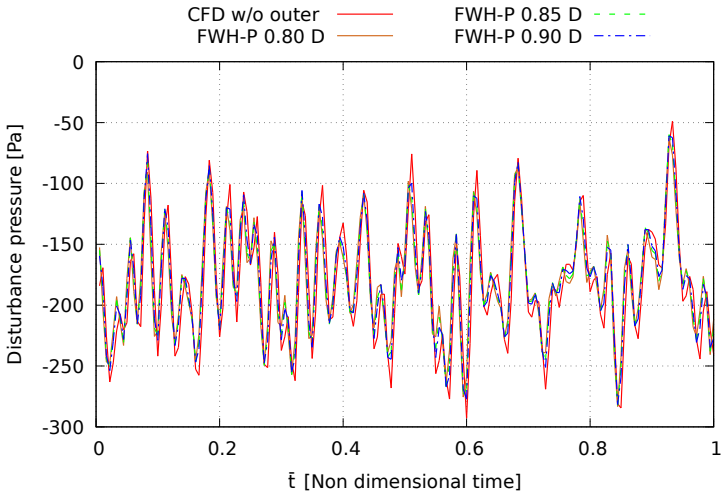

FIGURE 5.208: Comparison between FWH-P and CFD without the boundaries induced noise at Obs3.

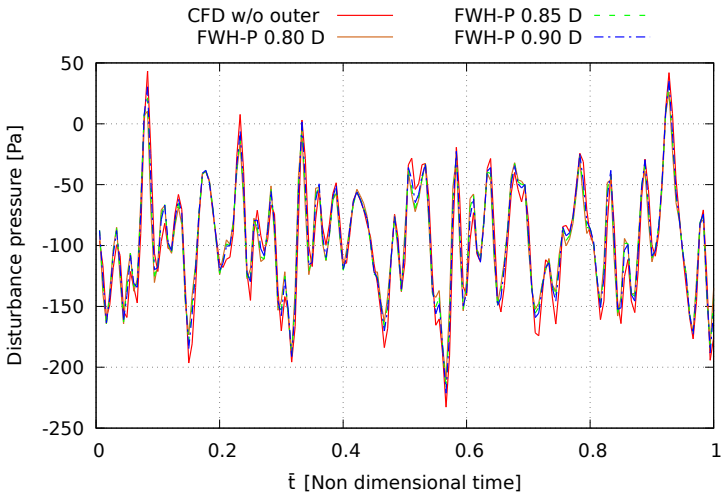

FIGURE 5.209: Comparison between FWH-P and CFD without the boundaries induced noise at Obs4.

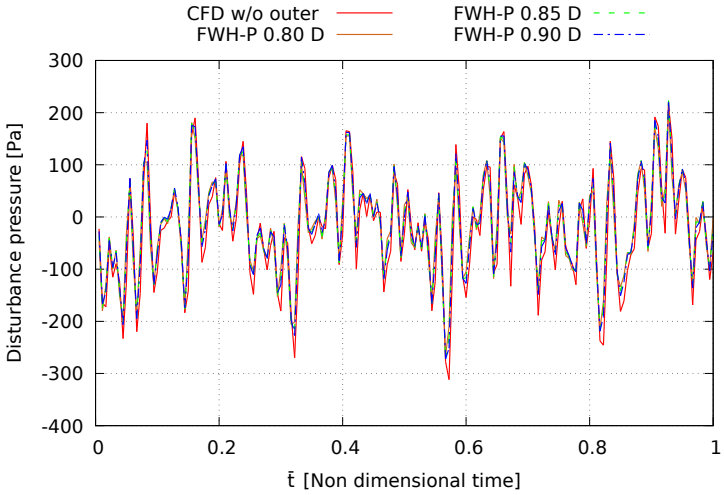

FIGURE 5.210: Comparison between FWH-P and CFD without the boundaries induced noise at Obs5.

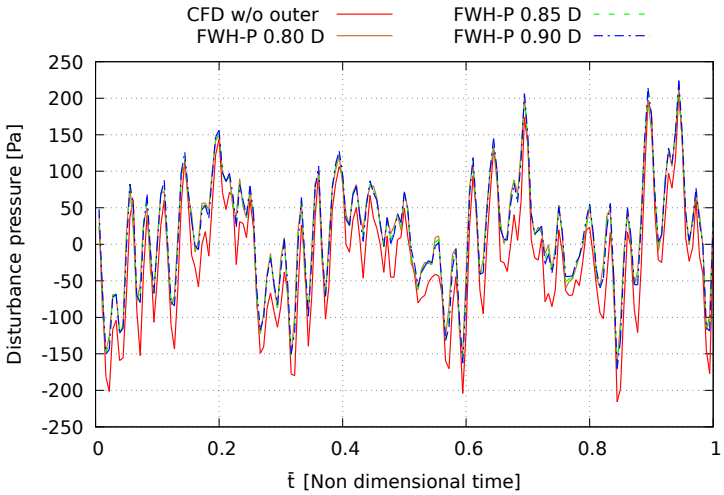

FIGURE 5.211: Comparison between FWH-P and CFD without the boundaries induced noise at Obs6.

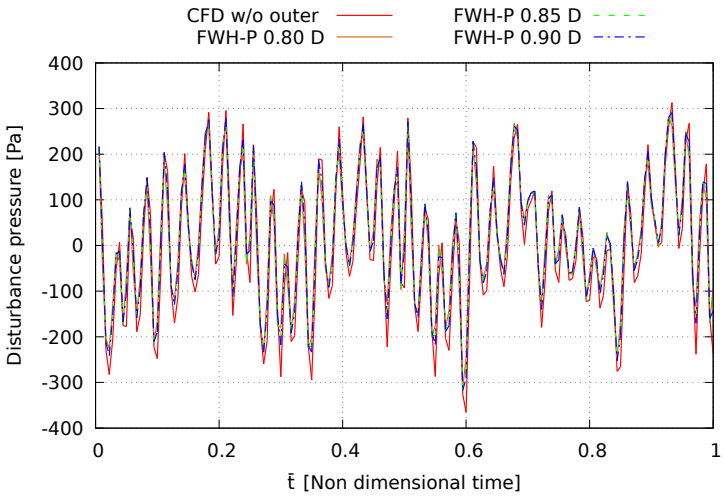

FIGURE 5.212: Comparison between FWH-P and CFD without the boundaries induced noise at Obs7.

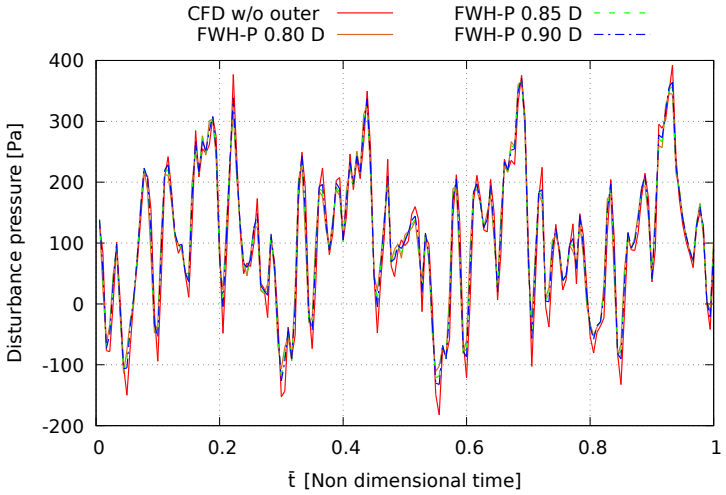

FIGURE 5.213: Comparison between FWH-P and CFD without the boundaries induced noise at Obs8.

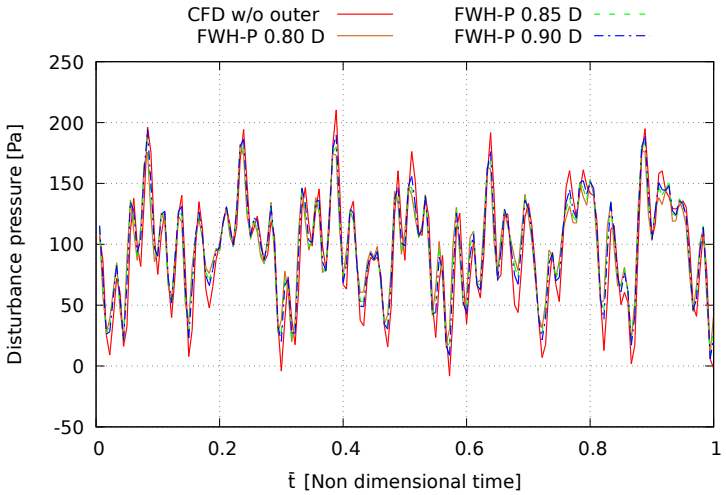

FIGURE 5.214: Comparison between FWH-P and CFD without the boundaries induced noise at Obs9.

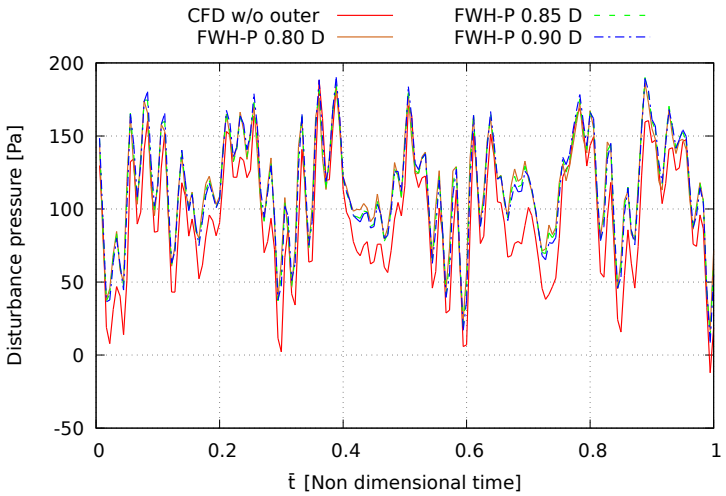

FIGURE 5.215: Comparison between FWH-P and CFD without the boundaries induced noise at Obs10.

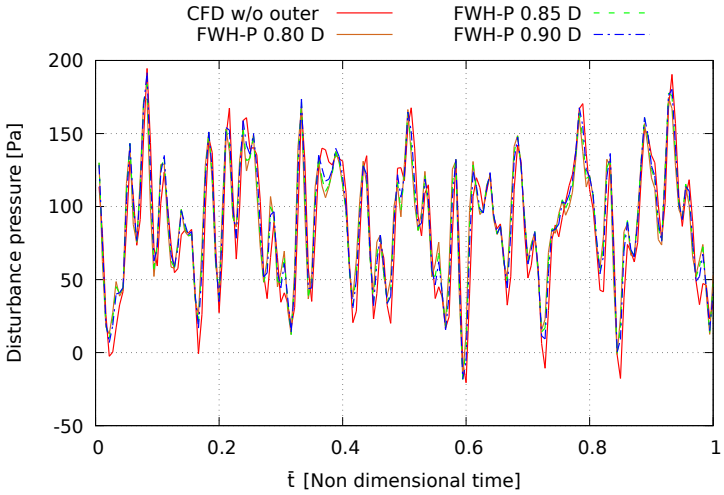

FIGURE 5.216: Comparison between FWH-P and CFD without the boundaries induced noise at Obs11.

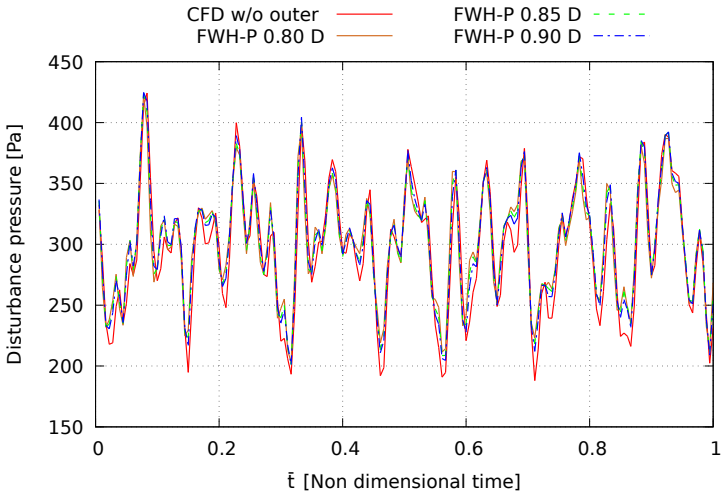

FIGURE 5.217: Comparison between FWH-P and CFD without the boundaries induced noise at Obs12.

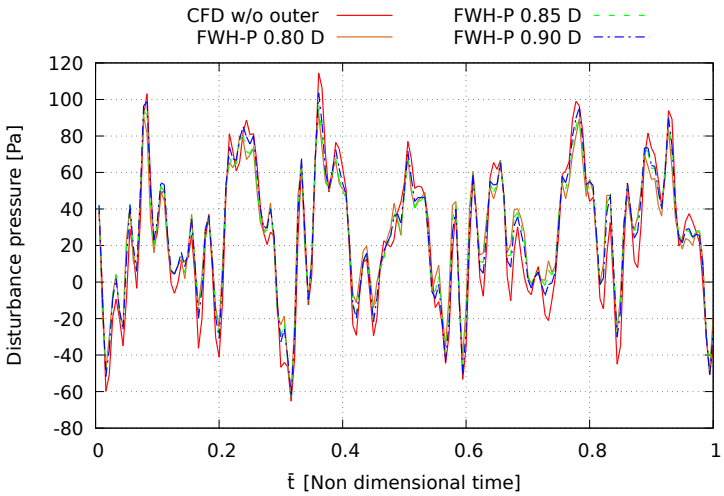

FIGURE 5.218: Comparison between FWH-P and CFD without the boundaries induced noise at Obs13.

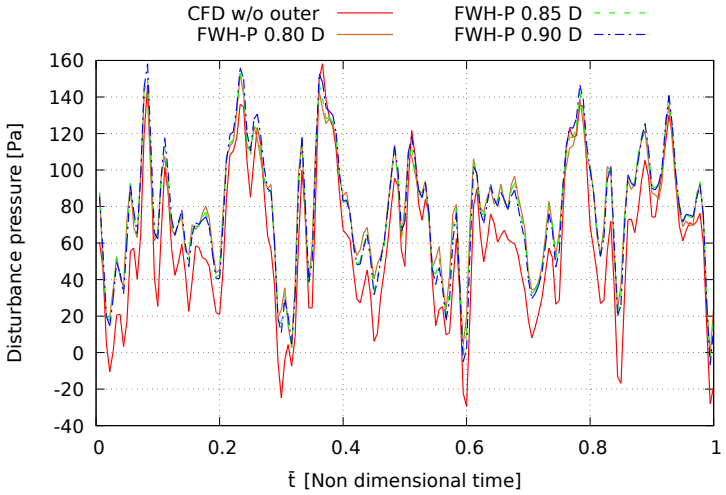

FIGURE 5.219: Comparison between FWH-P and CFD without the boundaries induced noise at Obs14.

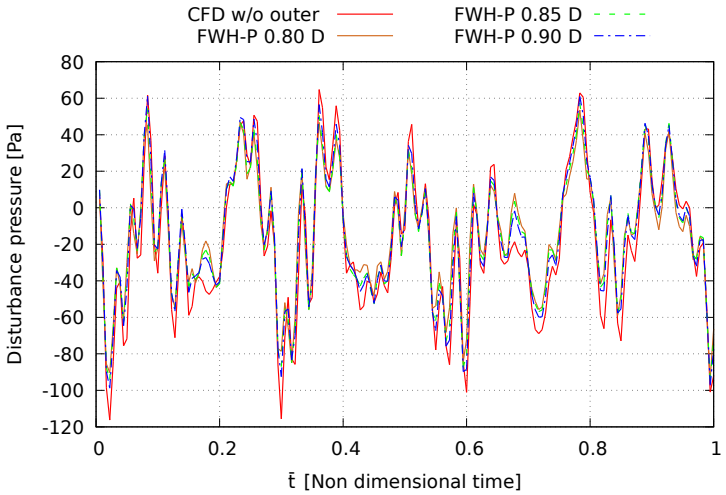

FIGURE 5.220: Comparison between FWH-P and CFD without the boundaries induced noise at Obs15.

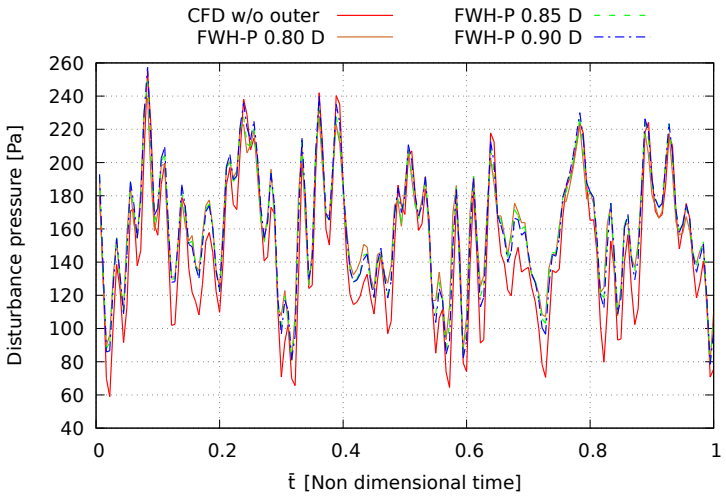

FIGURE 5.221: Comparison between FWH-P and CFD without the boundaries induced noise at Obs16.

5.4.6.2 Frequency Content

Figures 5.222 to 5.237 show the comparison between the frequency content of the pressure signature at microphones listed in Tabs. 5.10 and 5.11.

The sampling frequencies of the CFD simulation is set up to 4500 Hz; then the analyzed frequency range is extended up to the value $\frac{f}{f_0} = 22.5$, where $f_0 = 25$ Hz is the shaft rotational frequency. The spectrum is dominated by a frequency $\frac{f}{f_0} = 7$ of the CFD raw data; it is present for all the observers, even for those located downstream of the rotor, with almost everywhere the same amplitude. Therefore, such frequency content is probably associated with those nonphysical contribution coming from the boundary conditions.

Indeed, the comparisons between the FWH-P solutions and those obtained from the CFD signals without the CFD boundary associated contributions show a very good agreement all over the frequency range of the spectrum.

Besides, the frequency content at $f/f_0 = 7$ is highly attenuated with respect to the solution relative to the raw CFD data for all microphones and in particular for those downstream, whereas the broadband character of the signal is well evident and retained with respect to the raw CFD data.

However, even considering possible coupling phenomena related to the vortical structures downstream the rotor (which may slightly move the frequency tonal content around the $2BPF$) the amplitude relative to $f/f_0 = 7$ is suspiciously high for those microphones located upstream and downstream of the rotor.

Therefore, nevertheless the already cited filtering effects of the CFD computational grid, further investigation are required to verify the genesis of such frequency component.

As a last consideration, at each observer the solution provided by the impermeable FWH configuration, inhere indicated by FWH-linear, is present only in the plane of blades and it is able to predict only the tonal contributions at the first and second BPF.

In conclusion, the sound of the INSEAN 779A in drifting conditions seems to be dominated by the non linear terms which give rise to a signal with a frequency content spread all over the spectrum for all the observers, even those located in the blade plane.

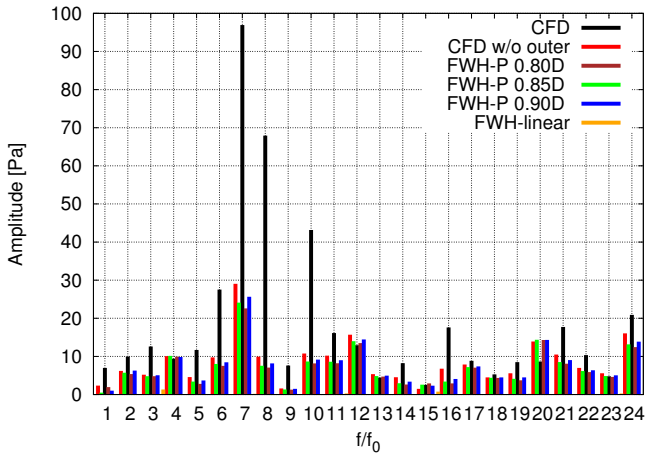

FIGURE 5.222: Comparison between the frequency content of the FWH-P and CFD outcomes at Obs1.

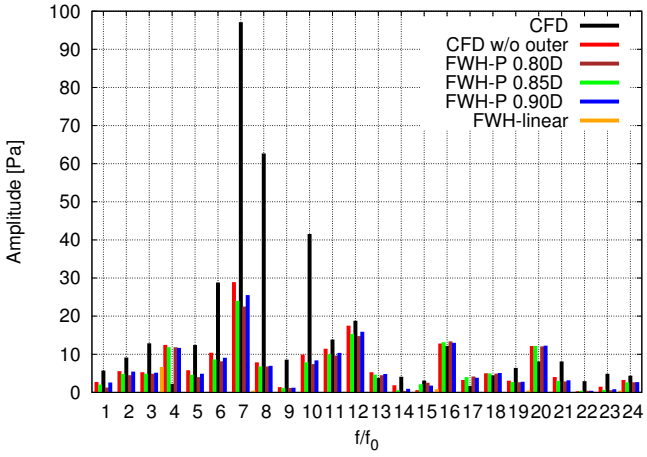

FIGURE 5.224: Comparison between the frequency content of the FWH-P and CFD outcomes at Obs3.

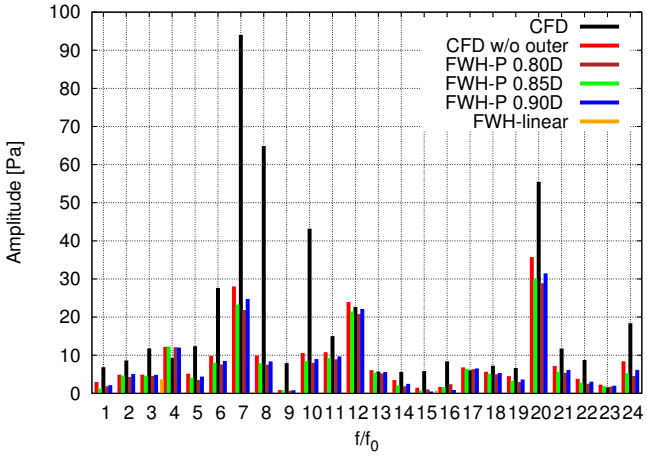

FIGURE 5.225: Comparison between the frequency content of the FWH-P and CFD outcomes at Obs4.

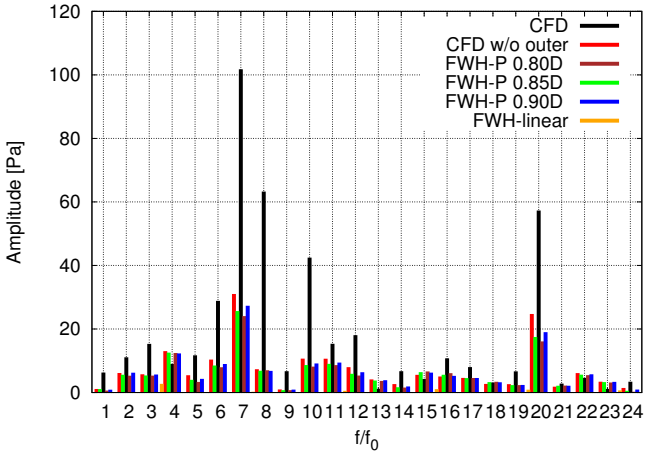

FIGURE 5.223: Comparison between the frequency content of the FWH-P and CFD outcomes at Obs2.

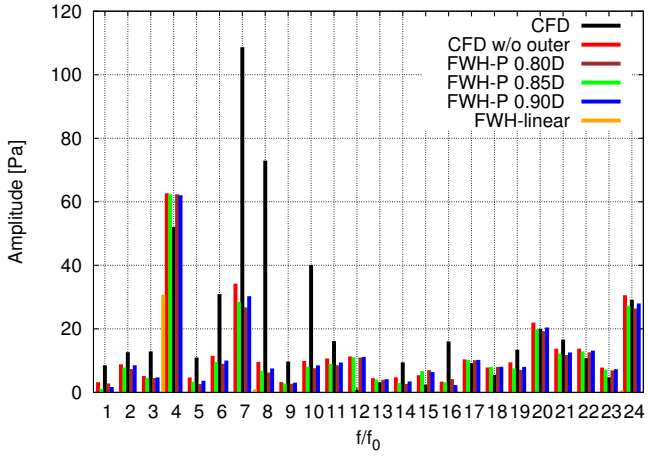

FIGURE 5.226: Comparison between the frequency content of the FWH-P and CFD outcomes at Obs5.

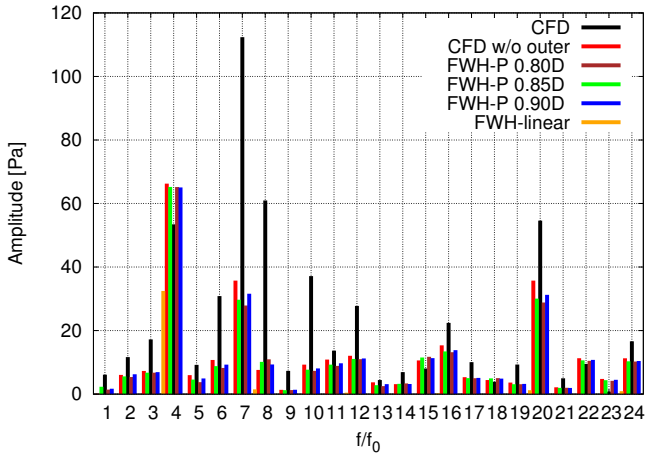

FIGURE 5.227: Comparison between the frequency content of the FWH-P and CFD outcomes at Obs6.

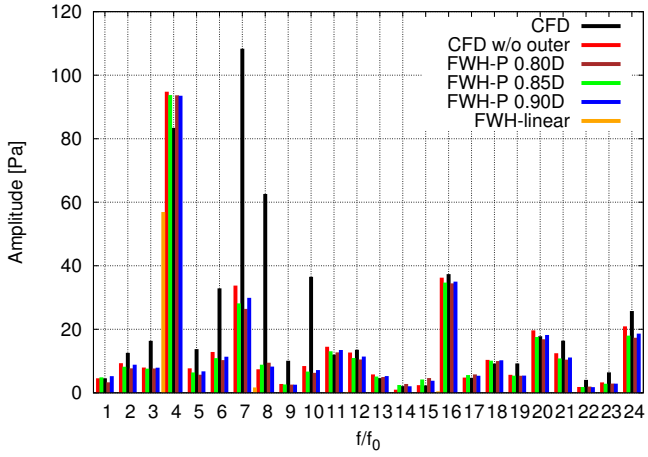

FIGURE 5.228: Comparison between the frequency content of the FWH-P and CFD outcomes at Obs7.

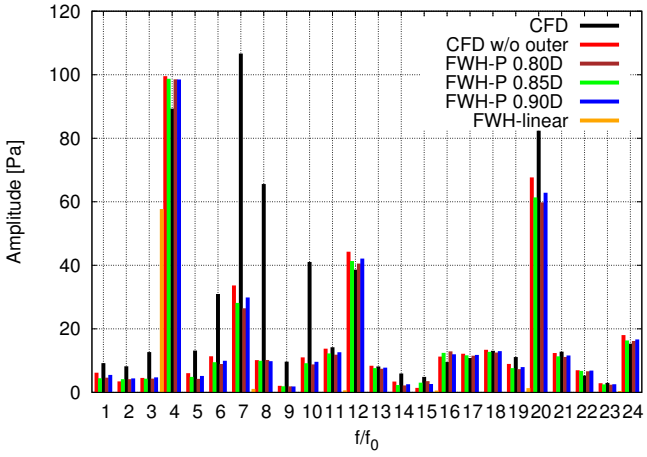

FIGURE 5.229: Comparison between the frequency content of the FWH-P and CFD outcomes at Obs8.

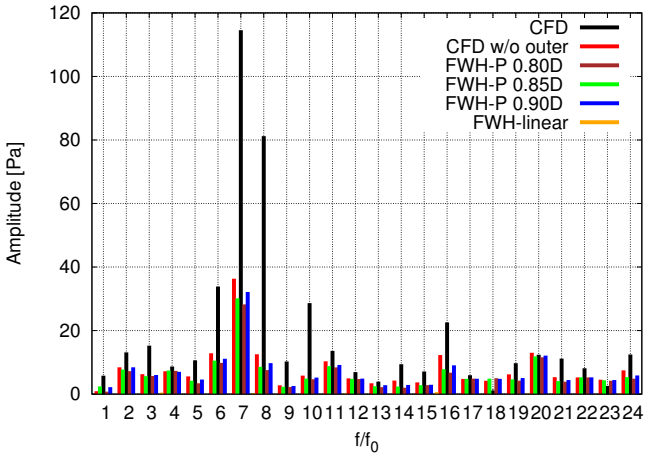

FIGURE 5.230: Comparison between the frequency content of the FWH-P and CFD outcomes at Obs9.

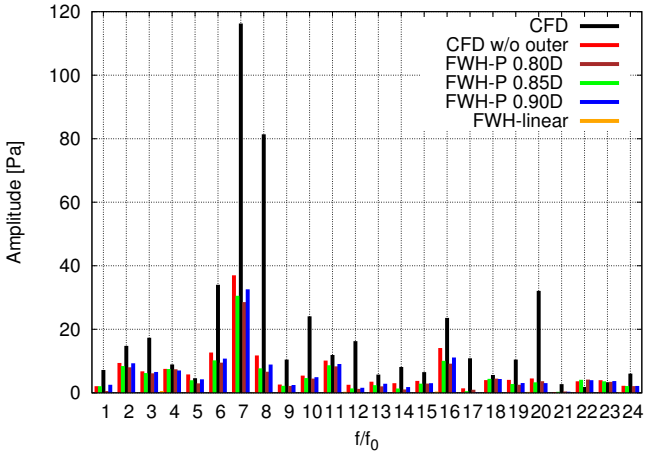

FIGURE 5.231: Comparison between the frequency content of the FWH-P and CFD outcomes at Obs10.

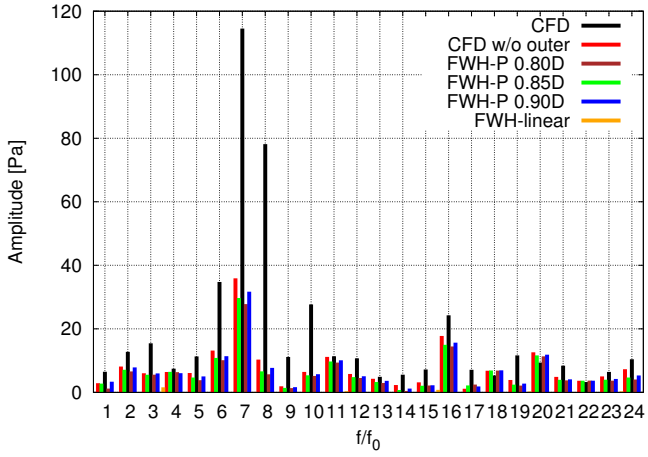

FIGURE 5.232: Comparison between the frequency content of the FWH-P and CFD outcomes at Obs11.

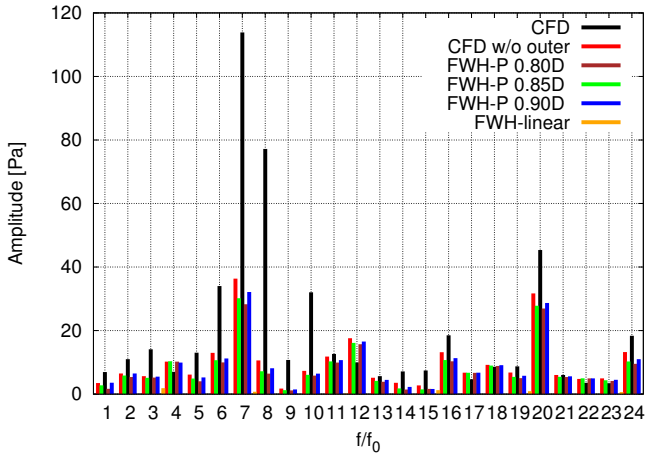

FIGURE 5.233: Comparison between the frequency content of the FWH-P and CFD outcomes at Obs12.

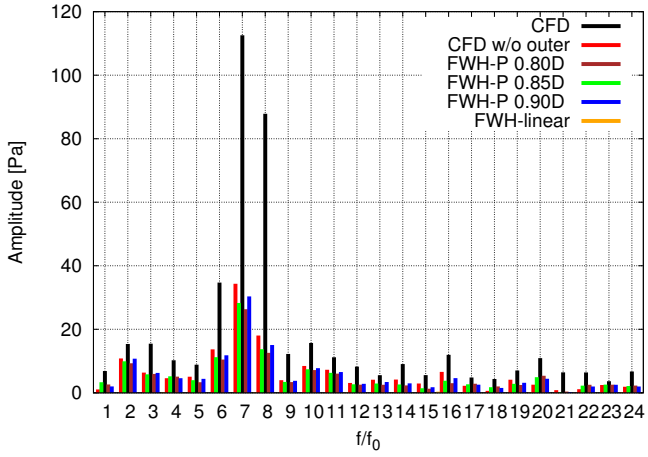

FIGURE 5.234: Comparison between the frequency content of the FWH-P and CFD outcomes at Obs13.

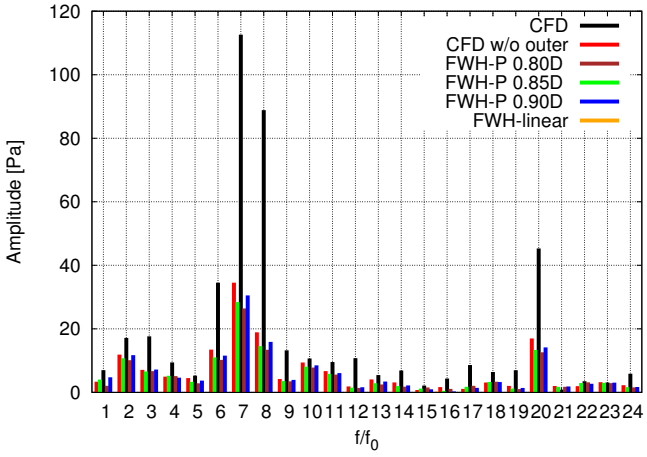

FIGURE 5.235: Comparison between the frequency content of the FWH-P and CFD outcomes at Obs14.

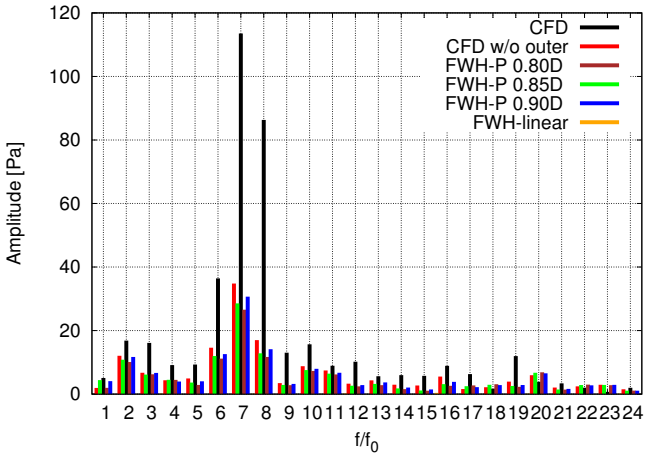

FIGURE 5.236: Comparison between the frequency content of the FWH-P and CFD outcomes at Obs15.

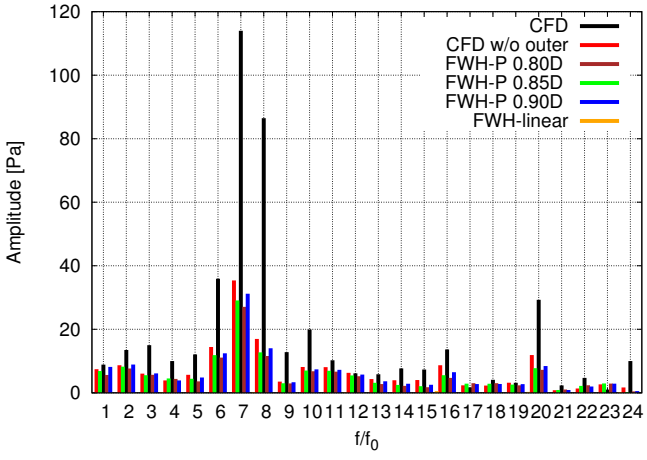

FIGURE 5.237: Comparison between the frequency content of the FWH-P and CFD outcomes at Obs16.

5.5 Assessment of the Combined FWHE/H-FWHE Formulation

In this section the acoustic effects induced by quadrupole source terms over a thin vorticity layer are evaluated following the approach proposed in Chapter 4.

Particularly, the hybrid formulation of Eq. (4.16) is used to extend the FWHE model in order to keep into account disturbance pressure signals from a field surface side of intense non linear noise contribution. It is worth to remind that, unlike to the standard approach followed to evaluate the quadrupole noise contributions (i.e the volume integral or the permeable approach) the purpose inhere is only to assess the effect of quadrupole noise contributions over a surface side of discontinuity for the Lighthill stress tensor (whenever it is identifiable). As highlighted in section C.2, the linear FWHE formulation is not able, by its own, to directly account for these contributions (as in the case of a potential wake convected downstream a lifting body) unless to embed the discontinuity surface inside the porous one. In that regard, it is also shown that thickness and loading noise contributions vanish when integrated over the discontinuity surface.

In view of this, the presented approach proposes to include the effects of quadrupole noise contributions over a potential wake surface through additional noise sources (monopole and dipole over it), whose intensity is derived by a manipulation of the FWHE volume term.

In Appendix C.4 it is also proved that these contributions correspond to the difference between the K-Equation and the linear FWHE (applied to the same surface).

Notably, Eq. (4.16) can be used to achieve the acoustic pressure prediction in applications where a contact discontinuity, as a potential wake, cannot be fully embedded inside the porous surface (see Fig. 5.238).

In a such condition, following the proposed approach, the contribution over the wake outside the porous surface is accounted for by the jump of the normal derivative of the acoustic pressure, namely $\Delta\left(\partial p'/\partial\tilde{n}\right)$, integrated over the wake itself.

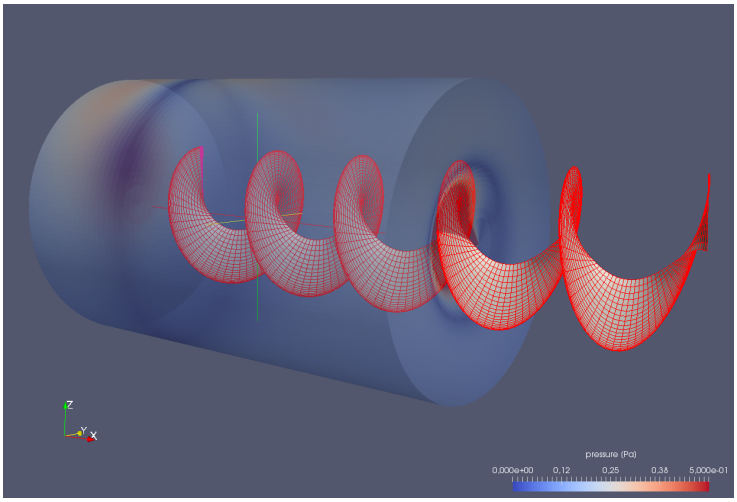

FIGURE 5.238: Discontinuity contact which goes through the porous surface.

Therefore, it represents a possible way to handle the *End Cap* issue in case of potential based applications. Although interesting, the applicability is limited by unquestionable numerical difficulties, such approach is indeed rather difficult to code; besides, the evaluation

	x[m]	y[m]	z[m]
Obs1	-2.0	0.0	2.0
Obs2	0.0	0.0	2.0
Obs3	2.0	0.0	2.0
Obs4	3.0	0.0	2.0
Obs5	6.0	0.0	2.0
Obs6	8.0	0.0	2.0
Obs7	10.0	0.0	2.0

TABLE 5.12: Microphones position.

of aerodynamic input it is not straightforward (because of the rather wide use of differential geometry needed to describe the flow field behaviour across the wake). These issues has to be accounted in the application of this particular acoustic model.

On the other hand, it is worth to note that it is capable of partially retain the quadrupoles outside the permeable surface, and, above all, to maintain the physical consistency in the noise source detection in case of potential vortices crossing the outflow disk.

Keeping in mind these consideration, the application to face the *End Cap* issue is not here carried out; in the following, analysis are limited only to assess the effectiveness to retain a portion of quadrupole sources in the noise prediction.

The best approach, from this standpoint, is the application to a impermeable configuration of the FWHE, since it allows to better evaluate the acoustic effects of non linear contribution over the wake (with respect to the noise sources over the body).

To this aim, the aeroacoustic behavior of a simplified propeller model, composed of a single rectangular blade 1 m long, having constant twist equal to 40°, constant chord $c = 0.1\ m$, root cut-off of 0.2 m and NACA 0012 airfoil sections, is investigated.

Two different operating conditions are defined by the horizontal advance ratio $J = U/nD$ equal to 0.3 and 0.7244, where $n = 4.77$ Hz is the rotational frequency of the shaft, $D = 2$ m indicates the blade diameter and U represents the magnitude of the advancing velocity.

Both the aforementioned advancing conditions refer to axial motion. The wake shape is considered prescribed and composed by 6 turns.

The fluid dynamic data needed by the acoustic model (i.e. the pressure over the blades and the $\Delta(\partial p/\partial \tilde{n})$ across the wake surface) as well as the pressure signatures used as baseline for comparisons are given, in the framework of potential flows, by the use of unsteady 3D panel method along with the Bernoulli Equation (details of the theoretical model are reported in section 2.2).

The observer positions are listed in Tab. 5.12 whereas Fig. 5.239 depicts their relative position with respect to the layout of the blade-wake concerning the advance ratio J=0.7244.

Figures 5.240 to 5.246 show comparisons between the Bernoulli solution, those carried out by the linear formulations of the FWHE and the combined FWHE/H-FWHE, indicated as FWH and FWH-K, respectively, for the advance ratio J=0.7244.

The results show an invariant solution between the FWHE impermeable outcomes and that provided by the FWH-K model for the first three microphones, those near the blade.

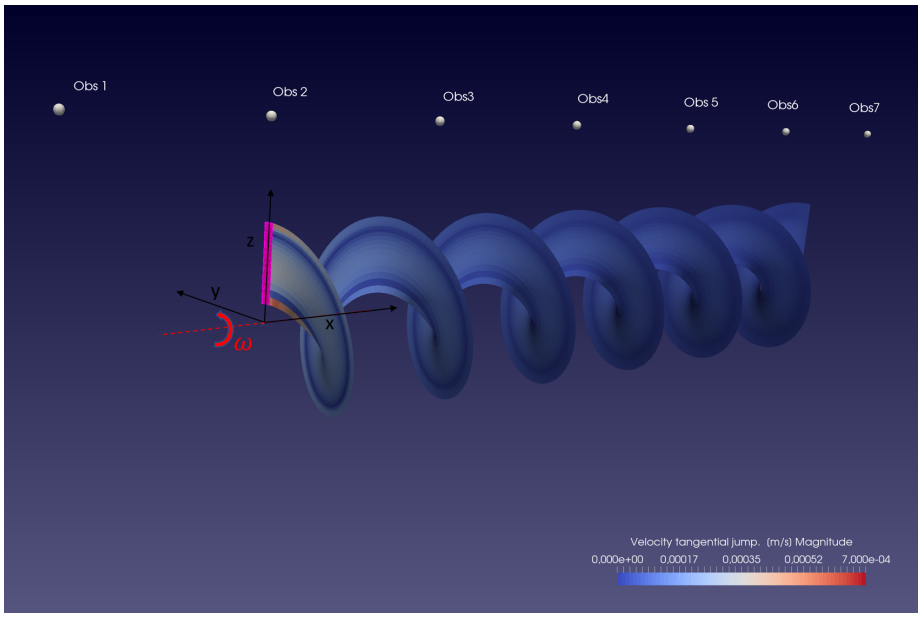

FIGURE 5.239: Layout of the blade, wake and observers at J=0.7244, contours of normal velocity over the wake.

This result is not surprising because in that zone the effect of the blade is of major importance compared to the non linear contribution over the wake.

Besides, the advance ratio $J = 0.7244$ is associated to a low loaded condition of the blade, and then, to a weak velocity jump induced over the wake surface.

However, slightly differences between pressure signature from FWH and the outcomes of FWH-K are present downstream of the blade, thus proving that, the non linear terms provide a not negligible contribution.

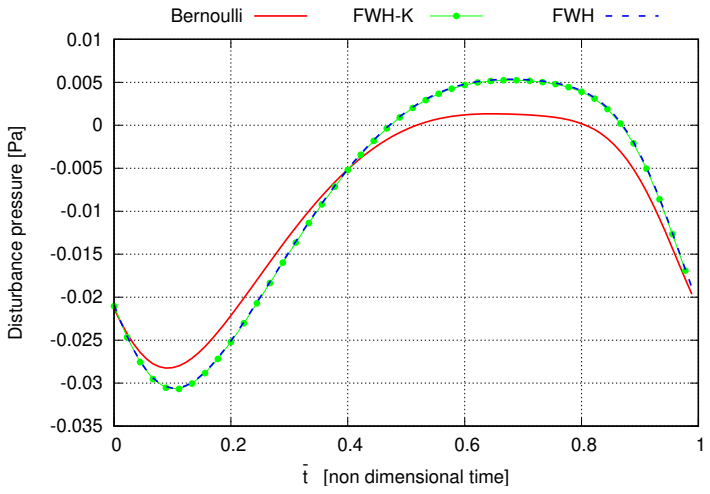

FIGURE 5.240: Comparison between the Bernoulli, the linear FWHE and the FWH-K acoustic predictions at Obs1, J=0.7244.

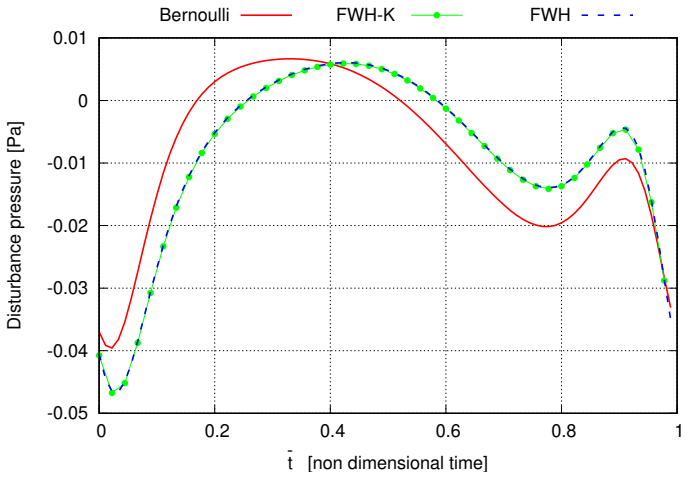

FIGURE 5.241: Comparison between the Bernoulli, the linear FWHE and the FWH-K acoustic predictions at Obs2, J=0.7244.

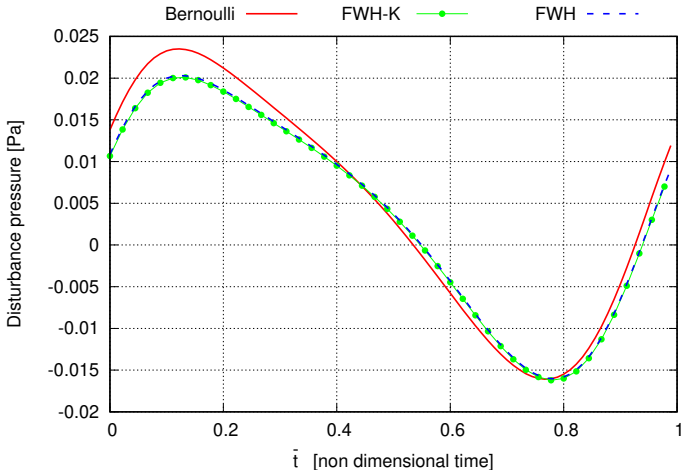

FIGURE 5.242: Comparison between the Bernoulli, the linear FWHE and the FWH-K acoustic predictions at Obs3, J=0.7244.

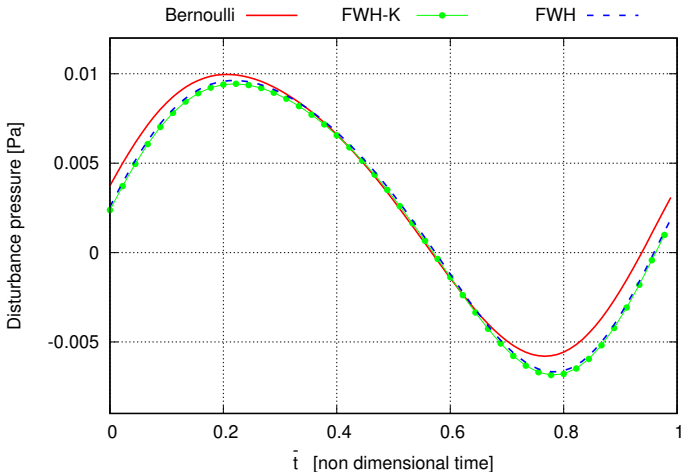

FIGURE 5.243: Comparison between the Bernoulli, the linear FWHE and the FWH-K acoustic predictions at Obs4, J=0.7244.

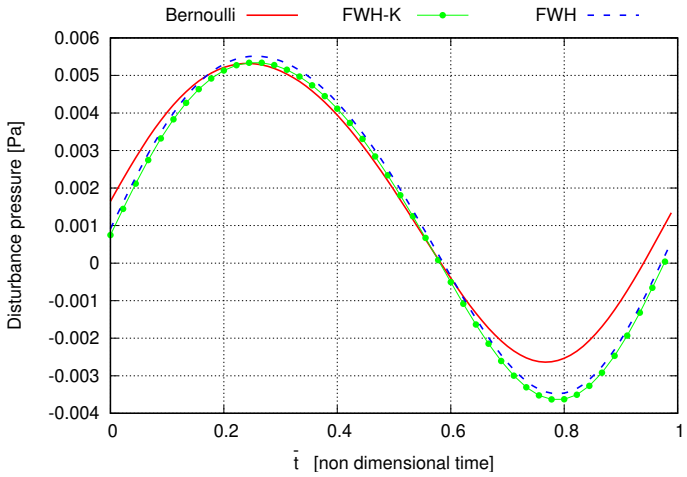

FIGURE 5.244: Comparison between the Bernoulli, the linear FWHE and the FWH-K acoustic predictions at Obs5, J=0.7244.

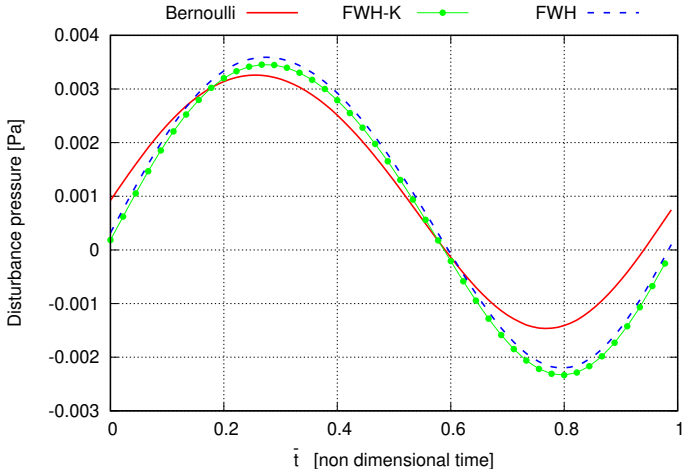

FIGURE 5.245: Comparison between the Bernoulli, the linear FWHE and the FWH-K acoustic predictions at Obs6, J=0.7244.

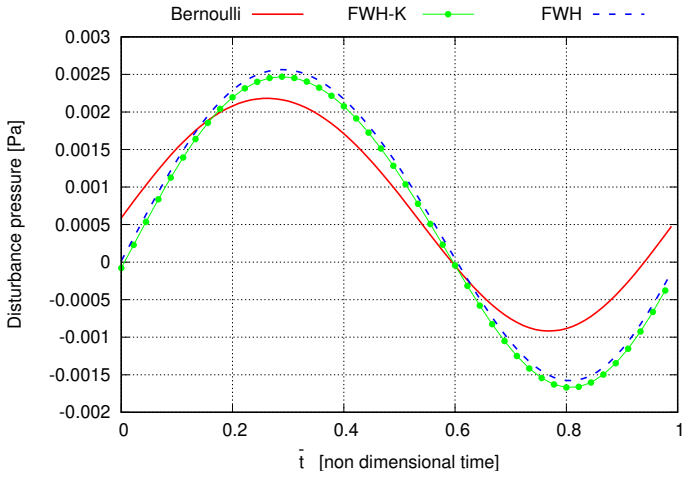

FIGURE 5.246: Comparison between the Bernoulli, the linear FWHE and the FWH-K acoustic predictions at Obs7, J=0.7244.

In order to verify the effect of a greater jump of tangential velocity over the wake a operating condition with $J = 0.3$ is considered.

Figures 5.248 to 5.254 depict the acoustic pressure comparison between the Bernoulli solution, the impermeable FWHE ad the FWH-K Equation for the observers listed in Tab. 5.12.

Similarly to the case study at J=0.7244, the first three microphones are weakly affected by the non-linear sources of noise over the wake.

On the contrary, the microphones Obs5, Obs6 and Obs7 show a consistent contribution to the acoustic pressure induced by the wake, which *moves* the FWHE solution towards the Bernoulli signal.

This is an encouraging result which suggests further investigation on the role plated by the field discontinuity surface of the Lighthill stress tensor. This is also confirms that such technique could be profitably applied to face the *End Cup* issue.

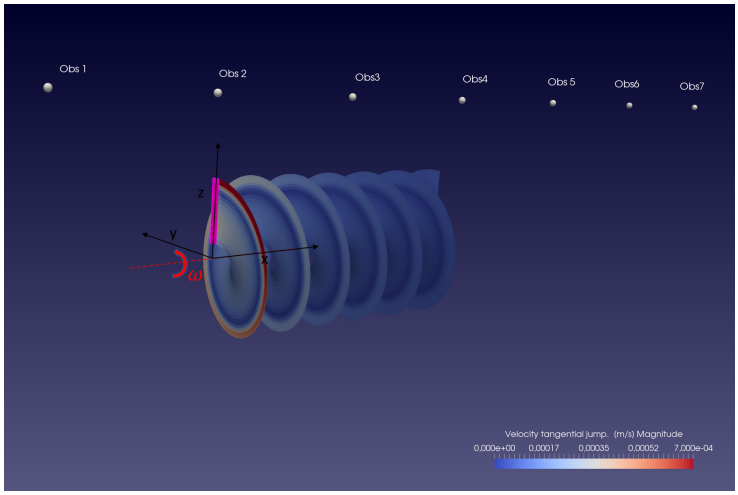

FIGURE 5.247: Layout of the blade, wake and observers at J=0.3, contours of normal velocity over the wake.

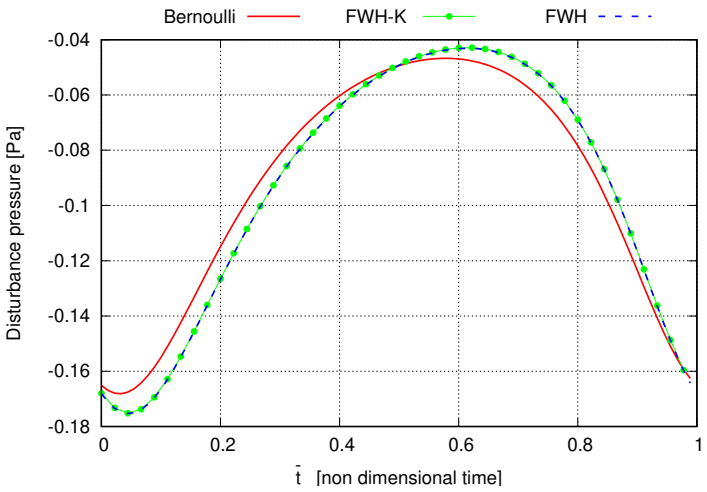

FIGURE 5.248: Comparison between the Bernoulli, the linear FWHE and the FWH-K acoustic predictions at Obs1, J=0.3.

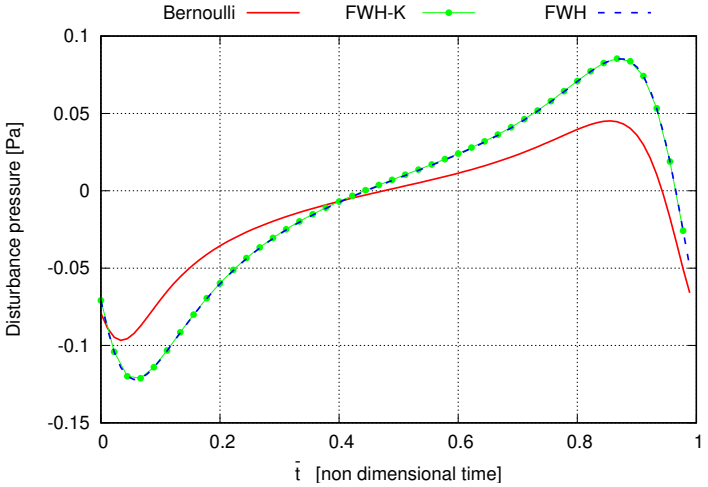

FIGURE 5.249: Comparison between the Bernoulli, the linear FWHE and the FWH-K acoustic predictions at Obs2, J=0.3.

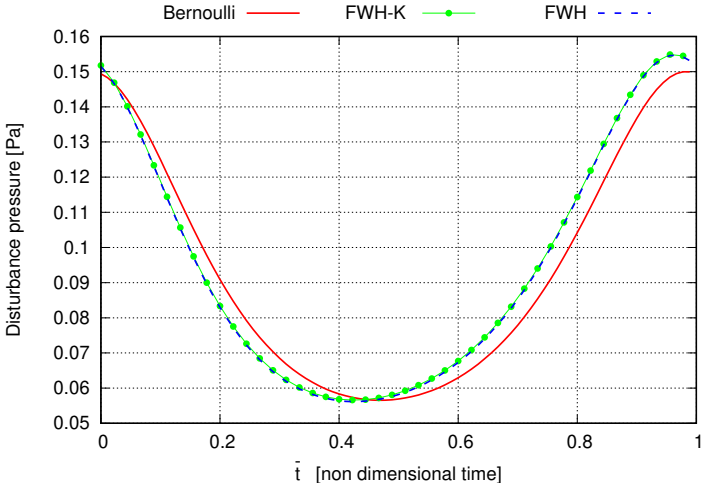

FIGURE 5.250: Comparison between the Bernoulli, the linear FWHE and the FWH-K acoustic predictions at Obs3, J=0.3.

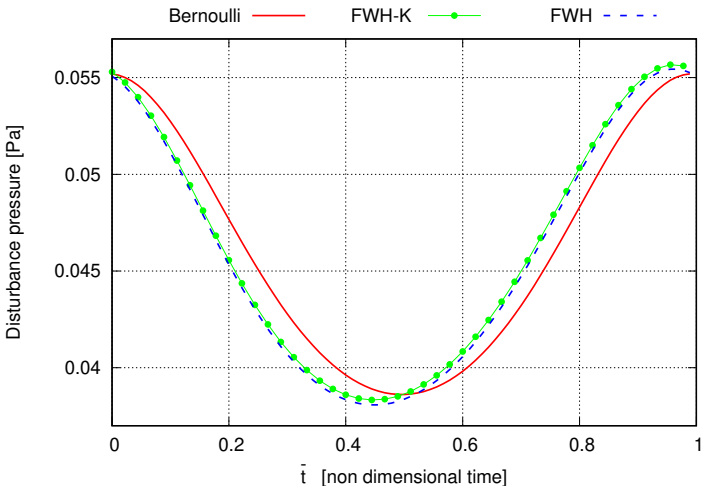

FIGURE 5.251: Comparison between the Bernoulli, the linear FWHE and the FWH-K acoustic predictions at Obs4, J=0.3.

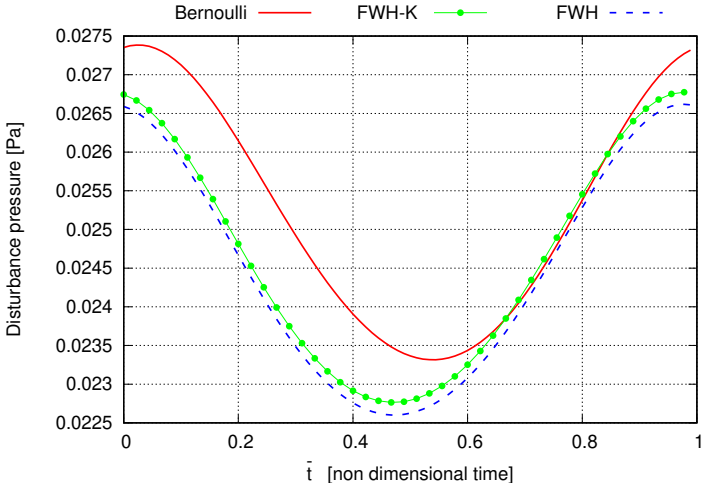

FIGURE 5.252: Comparison between the Bernoulli, the linear FWHE and the FWH-K acoustic predictions at Obs5, J=0.3.

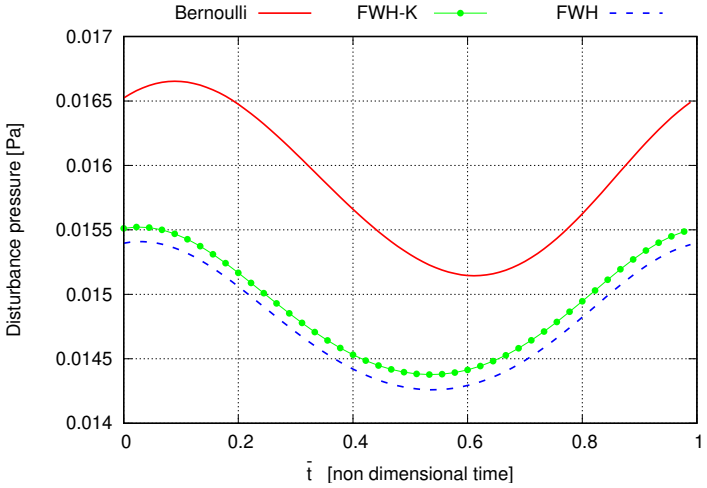

FIGURE 5.253: Comparison between the Bernoulli, the linear FWHE and the FWH-K acoustic predictions at Obs6, J=0.3.

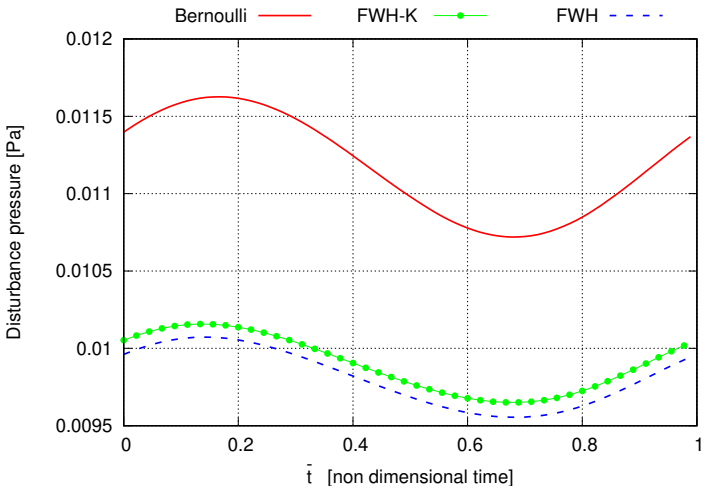

FIGURE 5.254: Comparison between the Bernoulli, the linear FWHE and the FWH-K acoustic predictions at Obs7, J=0.3.

Chapter 6

Concluding Remarks

The present work deals with the noise prediction from rotating-wings devices whose operating conditions induce significant flow field noise sources.

Powerful tools based on the Acoustic Analogy, such as the permeable approach of FWHE and the Hybrid Lighthill-Ffowcs Williams and Hawkings Equation (namely FWH-P and K-Equation, respectively), have been implemented and fruitfully used to predict the noise signature.

In addition, a novel approach has been proposed to extent the application of the porous approach of the FWHE to the presence (outside the permeable surface) of thin layers, where intense gradients of velocity, pressure or density may occur.

The first part of the thesis has been devoted to the methodological approach, as to understand the main features of the porous formulations.

To this aim, their capabilities have been first investigated through the use of singular solutions of the wave equation.

At the first glance, the use of moving monopoles with translating and rototranslating kinematics allowed to compare the outcomes of the acoustic models against analytic baselines. Although excellent results confirmed that, both permeable approaches represent a viable way to achieve the noise prediction of moving sources of sound, differences between the FWH-P and the K-Equation soon have been highlighted. In Particular, numerical results have confirmed (in accordance with literature outcomes) the FWH-P technique as the most effective, in that, capable to provide reliable acoustic predictions when the permeable surface is located *closer*, with respect to the K-Equation, to the noise sources.

The different behaviour between the FWH-P and the K-Equation has been theoretically related to the different non linear contribution which the models are able to account for. Interesting results on that highlight how, even in case of such simple acoustic emitters (i.e the monopoles), the incomplete inclusion (inside the permeable surface) of flow nonlinearities induced by the sources gives rise to a wrong noise prediction. Notably, erroneous predictions concern with the overestimation of specific frequency contents (correlated with the acoustic effects of flow nonlinearities) which would be canceled out by the inclusion of *all* quadrupoles in the acoustic models.

Such statement perfect match with the definition of *spurious noise*, although commonly associated to the acoustic effects of eddies crossing the boundary of the permeable surface.

In order to fill the knowledge gap and get a better insight on the *spurious noise* generation mechanisms a rototranslating potential vortex ring, based on the Biot-Savart law and the Bernoulli Equation, allowed to evaluate the noise effects of a vortex partially embedded inside the permeable surface.

The numerical findings highlight that its genesis is due to a combination of two factors:
i) the partial enclosure of non linear flow field (the phenomenon shown also in the case study of the monopoles)
ii) the effect of the nonphysical (inconsistent) noise source detection arising when only a portion of a vortex falls inside the porous surface (as it violates the Helmholtz's theorem: "A vortex filament cannot end in a fluid; it must extend to the boundaries of the fluid or form a closed path").

Therefore, as in the case study of the monopoles, the spurious noise would be canceled out by the inclusion of the quadrupole field contribution (of the acoustic models) if it were extended up to the end of the vortex.

The numerical results show that the spurious noise represents a non negligible unwanted acoustic effect especially for those observers located near the zone where the interactions between vortex-permeable surface occur.

Possible suggestions to mitigate such issue has been proposed in view of applications to realistic configurations, where the presence of eddies crossing the closure of the porous surface is unavoidable.

The acoustic analysis of rotary wing devices started with a simplified case study concerning a single rotary lifting blade device. In this case the noise sources detection process has been based on the aerodynamic solution provided by a 3D panel method solver based on the potential flows theory along with the Bernoulli Equation.

Akin to the outcomes of the singular sources, the permeable approach of the FWHE proved to well match the reference signals. Hence, its effectiveness in the noise predictions has been confirmed, providing that all noise sources, those over the body and in the flow field are embedded inside the surface.

Besides, similar issues to those encountered with the vortex ring, confirm the *End Cap* issue as the major limitation in the application of the permeable approach.

A very good agreement between the FWH-P predictions and the Bernoulli based solutions have been as well found out for the mono blade case study operating in inclined flow conditions (i.e. a case characterized by rotational axis and hub translation velocity not aligned).

A similar test case, concerning the simplified single blade configuration, has been used to assess the effectiveness of the combined FWHE/H-FWHE. Such formulation represents the most innovative content of the thesis; in fact, it allows to keep into account the noise generated by quadrupole contributions (by their direct integration) over a surface where the Lighthill stress tensor shows a discontinuous pattern.

Numerical results exhibit that, the acoustic effects of potential wakes (side of the tangential velocity jump) assume a considerable importance.

However, although satisfying outcomes, one of the most interesting application of such technique, i.e. the use oriented at the mitigation of the *end cap* phenomenon, has not been verified.

As a matter of fact, it might be a very interesting cue for future works. Indeed, in cases where thin vorticity layers go trough the porous surface, the acoustic effects of quadrupole contributions could be partially retrieved through such technique and, above all, the consistency in the noise detection maintained (as the integration is extended over the whole vortex).

The methodological part of the thesis ends with the aforementioned simplified single blade configurations.

Further numerical investigation concern with a considerable number of cases involving the aero/hydro-acoustics analysis of devices as underwater propellers and wind turbines.

As widely discussed along the thesis, they are acoustically characterised by the effects of the field noise sources, therefore representing an ideal benchmark to assess the effectiveness of the permeable approach of FWHE and the H-FWHE models.

To this aim a fruitful noise sources detection able to characterize the turbulence and vorticity phenomena generated by these devices has been provided by a finite volume fluid dynamic solver (CFD).

Although the high level reached by such techniques, the computational resources needed to perform Direct Numerical Simulation (able to resolve the turbulence scales, thus to fully characterize the quadrupole noise sources) is nowadays unapproachable for applications of industrial interest. Hence, models based on the eddy viscosity have been used to model the energy cascade inside the fluid domain.

Among them the Reynolds Averaged Navier Stokes Equations (RANSE), used in the analysis of the wind turbine, is turned out to be not able to accurately predict the velocity and pressure fluctuations characterizing the turbulent phenomena away from the rotor.

Indeed, the predicted acoustic field by the FWH-P, although showing a complete agreement with the CFD solution, is unable to describe the acoustic effects of the turbulence and weakly able to account with those related with the vorticity field induced by the rotor downstream it (i.e. only the rotational noise sources are well detected).

The high frequencies phenomena expected by the well known swishing character of wind turbines noise are not highlighted. Such result can be ascribed to the following two reasons: i) the first regards the numerical dissipation of the RANSE model, which even if is able to well detect the dynamics of the boundary layer is also prone to filtering effects due both to the eddy viscosity modeling and to the grid features. ii) operating conditions, inhere the nominal tip speed ratio $\lambda = 6$ has been analyzed. In this condition the dynamics of boundary layer weakly interact with the trailing edge of the blades; such behaviour is emphasized by the absence of inflow turbulence. Besides, the acoustic effects related with change in the wind direction as well as those related with the inflow turbulence are not predicted because not accounted by the fluid dynamic simulation.

Thus, further investigations are suggested in order to have a broadband noise characterization of such devices. As a matter of fact, it can be achieved only through turbulence models capable of accurately predict the flow field induced sources.

For what concern the underwater noise predictions of propellers, hydrodynamic simulations based on the DES turbulence model has been used in that able to get the strength points of the RANSE in resolving the boundary layer and the effectiveness of the LES in the solution of the near-mid flow field features.

A considerable advantage of these techniques is the reasonable level of numerical dissipation of the modern numerical integration schemes, in that, they allow to propagate fluctuating phenomena predicted by the turbulence model far enough to reach the permeable surface. For these reasons, the unsteady CFD/DES simulations have proven to be particularly well suited to detect noise sources due to the turbulent phenomena.

In this regard, one of the most interesting outcomes of this work concerns with the decoupling of the acoustic effects of turbulence from those related with the large vortical structure released downstream of the rotor. This has been achieved by exploiting the properties of the DES hydrodynamics of the E779A INSEAN marine propeller in axial motion by the means of the running average process.

Results show how, the effect of turbulence produces disturbance pressure up to an order of magnitude greater then those related with large vortical structures just two diameters downstream of the rotor.

The importance of flow field fluctuating behaviour (i.e. of the quadrupole noise contribution) in the noise generation mechanisms is also highlighted by the spatial identification of the noise sources. Indeed, it comes out that the finest resolved computational CFD domain is the most important acoustic region in the flow field. This comply with the capabilities of the turbulence model, in that, the finer is the gird resolution the better is the energy cascade predicted by the DES model.

On the contrary, the linear contribution of the FWHE, i.e. thickness and loading noise fast decay in space and become negligible just a diameter downstream the propeller.

The outcomes of a 3D panel method hydrodynamics, based on the potential flows theory and the Bernoulli Equation, turn out to well detect only the near field noise sources for the INSEAN E779A propeller operating at the same conditions of the aforementioned analysis. As a matter of fact, the acoustic predictions based on that hydrodynamics well match those from the DES up to approximately a diameter downstream of the rotor. This also confirms how, behind such distance, the major role to the noise generation is played by the turbulence phenomena.

Similar findings came out from the analysis of the E779A INSEAN marine propeller operating in drifting condition (i.e. the condition characterized by rotational axis not aligned with the hub translation velocity). Such a operating condition forces the blades to exchange much more energy with the flow around it producing zones with high velocity and pressure gradients.

As expected, the field noise contributions associated to the turbulence phenomena play an even greater (with respect to the axial case) role in the noise generation mechanisms. The noise signature is indeed dominated by a high broadband content, which is massively present even in the zone near the blades where the thickness and loading noise components are expected to be dominant.

Finally, last but not least outcome concerns with the unexpected role played by the boundary conditions of the CFD/DES field solution in the noise sources detection process.

Throughout the thesis is highlighted how, especially in case of unsteady simulations, reflective effects at the boundaries of the CFD computational domain can lead to wrong acoustic predictions. Essentially, being them not *transparent*, as should be, produce unwanted bouncing of pressure perturbations coming from inside the field. As a matter of fact, the pressure waves bounced at the boundaries turn out to have weak intensity by its own, thus being substantially ineffective from the hydrodynamic point of view (at least for the hydro loads evaluation, may instead be dangerous for the convergence of the solution). On the contrary, the CFD/DES pressure predictions far from the body are deeply affected by the reflective effects, since them account for all contributions (i.e. even if the bouncing are weak the solution accounts for all the computational domain).

Using some interesting mathematical properties of the FWH-P formulation has been possible to characterize acoustically they overall intensity without computing any field contribution. It turns out that, sometimes, the integral contribution of the fictitious noise sources associated to the boundary of the CFD domain is even greater than those of the rotor and wake.

However, in this regard, is important to keep in mind the two following considerations:
i) the capability of the permeable approach to account only with the internal noise sources allows to neglect in the acoustic prediction the presence of the fictitious CFD noise sources at the boundary condition;
ii) besides, the clustering grid strategy of the CFD computational domain insulates the zone near the rotor and wake by the external field in a way to let the effects of fictitious boundary condition outside to the zone of interest for the hydrodynamic solution. This means that, theoretically, the presence of reflecting boundaries weakly or not at all influence the noise source detection near the body (similarly to what happened for the hydro loads evaluation).

Hence, at the first glance, the aforementioned effects can be considered ineffective for the acoustic prediction if the permeable surface is located tightly around the most intense noise sources.

On the contrary the CFD solution, far from the body, is deeply affected by such condition making prohibitive any comparisons with the FWH-P outcomes.

The assessment of the effectiveness in the filtering process due to the clustering grid strategy could represents a cue for future works. In particular, specific adaptations of the CFD solvers, for instance with the inclusion of particular boundary condition techniques suited for acoustic purposes, might clarify the effectiveness of standard approaches in the near field noise source detection.

Concerning the future possible works, analysis on the acoustic effects of turbulence for propellers working at lower advancing ratio, even in case of non isolated configuration, may confirm (as we expect) the outcomes of this thesis for a wider range of operating conditions.

Appendix A

Appendix A

A.1 The Differential Problem

Here the general form of the Ffowcs Williams Hawkings and Hybrid Lighthill-Ffowcs Williams and Hawkings Equations is derived.

Let us assume that the fluid is compressible and undergoes to transformations with negligible entropy changes; by combining the continuity and momentum equations

$$\begin{aligned} \frac{d\rho}{dt} + \nabla \cdot (\rho \mathbf{u}) &= 0 \\ \frac{d(\rho \mathbf{u})}{dt} + \nabla \cdot (\rho \mathbf{u} \otimes \mathbf{u}) &= \nabla \cdot (-p\mathbf{I} + \mathbf{V}) \end{aligned} \tag{A.1}$$

the following Lighthill equation is obtained

$$\Box^2 p' = \frac{1}{c_0^2} \frac{\partial^2 p'}{\partial t^2} - \nabla^2 p' = \nabla \cdot \nabla \cdot \mathbf{T} \tag{A.2}$$

where $\mathbf{u}$, ρ, and p are the flow field velocity, density and pressure, respectively. Besides, c_0 is the sound speed in the medium at rest, $p' = c_0^2(\rho - \rho_0) = c_0^2 \rho'$ denotes the acoustic pressure, $\mathbf{V}$ is the viscous stress tensor, $\mathbf{T} = \left[\rho \mathbf{u} \otimes \mathbf{u} + (p' - c_0^2 \rho')\mathbf{I} - \mathbf{V}\right]$ is the Lighthill stress tensor whereas p_0 and ρ_0 are the pressure and density fields in the undisturbed medium, respectively.

Furthermore, let us consider a moving permeable surface S enclosing both the flow field noise sources and solid surfaces (*i.e.* the bodies surfaces) in a volume $\mathcal{V}$. By the introduction of a domain function $E(\mathbf{x}, t)$ such that

$$E(\mathbf{x}, t) = \begin{cases} 1 & \text{if} \quad \mathbf{x} \in \Re^3 \setminus \mathcal{V} \\ 0 & \text{if} \quad \mathbf{x} \in \mathcal{V} \end{cases} \tag{A.3}$$

the *embedding* procedure allows to recast the original Lighthill equation in an unbounded problem through the following expression for the acoustic pressure

$$\hat{p}'(\mathbf{x}, t) = E(\mathbf{x}, t) p'(\mathbf{x}, t) \tag{A.4}$$

Combining Eq. (A.2) with Eq. (A.4) the following infinite–space problem is obtained

$$\Box^2 \hat{p}' = E\,\nabla\cdot\nabla\cdot\mathbf{T} - \nabla p'\cdot\nabla E - \nabla\cdot(p'\nabla E)\frac{1}{c_0^2}\left[\dot{p}'\dot{E} + (p'\dot{E})^{\cdot}\right] \tag{A.5}$$

representing the extension of the Lighthill equation to account for the presence of moving bodies, hereafter referred as Hybrid Lighthill-Ffowcs Williams and Hawkings Equation for Moving Surfaces (H-FWHE).

A.1.1 The Ffowcs Williams and Hawkings Equation

The Ffowcs Williams and Hawkings Equation (FWHE) is obtained from Eq. (A.5) by recasting the quadrupole source term as follows

$$E\,\nabla\cdot\nabla\cdot\mathbf{T} = \nabla\cdot\nabla\cdot(E\mathbf{T}) - (\nabla\cdot\mathbf{T})\cdot\nabla E - \nabla\cdot(\mathbf{T}\nabla E) \tag{A.6}$$

recalling that $p' = c_0^2(\rho-\rho_0)$ and $\mathbf{T} + p'\mathbf{I} = \mathbf{P} + \rho\mathbf{u}\otimes\mathbf{u}$ where $\mathbf{P} = [(p-p_0)\mathbf{I} - \mathbf{V}]$ is the compressive stress tensor, combining Eq. (A.5) and Eq. (A.6) one obtains

$$\begin{aligned}\Box^2\hat{p}' = \nabla\cdot\nabla\cdot(E\,\mathbf{T}) - \left[\nabla\cdot(p'\mathbf{I}+\mathbf{T})\right]\cdot\nabla E + \\ - \nabla\cdot[(p'\mathbf{I}+\mathbf{T})\nabla E] + 2\dot{\rho}\dot{E} + \rho\ddot{E} - \rho_0\ddot{E}\end{aligned} \tag{A.7}$$

Through the use of the continuity and momentum equations Eq. (A.7) recasts as

$$\begin{aligned}\Box^2\hat{p}' &= \nabla\cdot\nabla\cdot(E\mathbf{T}) - \nabla\cdot(\mathbf{P}\nabla E) + \rho\dot{\mathbf{u}}\cdot\nabla E + 2\dot{\rho}\mathbf{u}\cdot\nabla E + \\ &- \rho\mathbf{u}\cdot\nabla(\mathbf{u}\cdot\nabla E) + 2\dot{\rho}\dot{E} + \rho\ddot{E} - \rho_0\ddot{E}\end{aligned} \tag{A.8}$$

Moreover noting that the material derivative $\dfrac{DE}{Dt}$ following a flow field point is given by

$$\frac{DE}{Dt} = \dot{E} + \mathbf{u}\cdot\nabla E \tag{A.9}$$

and its time derivative

$$\left(\frac{\dot{DE}}{Dt}\right) = \ddot{E} + \dot{\mathbf{u}}\cdot\nabla E + \mathbf{u}\cdot\nabla\dot{E}^{\cdot} \tag{A.10}$$

one obtains

$$2\dot{\rho}(\dot{E}+\mathbf{u}\cdot\nabla E) + \rho[\ddot{E} + \dot{\mathbf{u}}\nabla E - \mathbf{u}\cdot\nabla(\mathbf{u}\cdot\nabla E)] = 2\frac{\partial}{\partial t}(\rho\frac{DE}{Dt}) - \rho\frac{D^2E}{Dt^2} \tag{A.11}$$

Combining Eq. (A.8) with Eq. (A.11) yields

$$\Box^2\hat{p}' = \nabla\cdot\nabla(E\mathbf{T}) - \rho_0\ddot{E} - \nabla\cdot(\mathbf{P}\nabla E) + 2\frac{\partial}{\partial t}(\rho\frac{DE}{Dt}) - \rho\frac{D^2E}{Dt^2} \tag{A.12}$$

Eq. (A.12) represents the Ffowcs Williams and Hawkings equation for permeable surfaces, governing the aeroacoustic field around a volume $\mathcal{V}$ moving in arbitrary motion with respect to the air space.
In order to re-write the FWHE in a more suitable mathematical form, let the boundary of S be mathematically defined by $f(\mathbf{x},t) = 0$, with $f > 0$ outside S and such that $\nabla f = \mathbf{n}$, where $\mathbf{n}$ is the outward unit normal vector. Observing that $E(\mathbf{x},t) = H[f(\mathbf{x},t)]$, where H denotes the Heaviside function, the following relations hold

$$\nabla E = \frac{dH}{df}\,\nabla f = \delta(f)\,\mathbf{n} \tag{A.13}$$

$$\frac{DE}{Dt} = \frac{dH}{df}\,\frac{Df}{Dt} = \delta(f)\frac{Df}{Dt} \tag{A.14}$$

The material time derivative, following a fluid particle, is given by

$$\frac{Df}{Dt} = \frac{\partial f}{\partial t} + \mathbf{u}\cdot\nabla f \tag{A.15}$$

where $\dfrac{\partial f}{\partial t}$ indicates the Eulerian derivative; furthermore, following a material point on the surface S that moves with velocity $\mathbf{v}$, the time derivative of $f(\mathbf{x},t)$ is equal to

$$\frac{Df}{Dt} = \frac{\partial f}{\partial t} + \mathbf{v}\cdot\nabla f = 0 \tag{A.16}$$

It results that following a fluid particle, the material derivative may be written as

$$\frac{Df}{Dt} = (\mathbf{u}-\mathbf{v})\cdot\mathbf{n} \tag{A.17}$$

Thus, accounting for Eqs. (A.13), (A.14) and (A.17), the material derivative $\dfrac{DE}{Dt}$ may be written as

$$\frac{DE}{Dt} = (\mathbf{u}-\mathbf{v})\cdot\ \nabla E \tag{A.18}$$

Moreover combining the continuity equation with the Eq. (A.18) yields

$$2\frac{\partial}{\partial t}(\rho\frac{DE}{Dt}) - \rho\frac{D^2E}{Dt^2} = \frac{\partial}{\partial t}\left[\rho(\mathbf{u}-\mathbf{v})\cdot\nabla E\right] - \nabla\cdot\left[\rho\mathbf{u}\left[(\mathbf{u}-\mathbf{v})\cdot\nabla E\right]\right] \tag{A.19}$$

Thus, rearranging Eq. (A.12) using Eq. (A.19) and recalling that, for any vector field $\mathbf{a},\mathbf{b},\mathbf{c}$, $(\mathbf{a}\otimes\mathbf{b})\,\mathbf{c} = (\mathbf{b}\cdot\mathbf{c})\,\mathbf{a}$ the following form of the FWHE is obtained

$$\begin{aligned}\Box^2\hat{p}' &= \nabla\cdot\nabla\cdot(E\mathbf{T}) - \frac{\partial}{\partial t}(\rho_0\frac{\partial E}{\partial t}) - \nabla\cdot(\mathbf{P}\nabla E) + \frac{\partial}{\partial t}\left[\rho(\mathbf{u}-\mathbf{v})\cdot\nabla E)\right] \\ &- \nabla\cdot[\rho\mathbf{u}\otimes(\mathbf{u}-\mathbf{v})\nabla E)] \quad \forall\mathbf{x}\in\Re^3\end{aligned} \tag{A.20}$$

Accounting for Eqs. (A.9), (A.13) and (A.18), it comes out that $\dot{E} = -\mathbf{v}\cdot\mathbf{n}\,\delta(f)$ and hence

$$-\rho_0\ddot{E} = \frac{\partial}{\partial t}\left[-\rho_0\frac{\partial E}{\partial t}\right] = \frac{\partial}{\partial t}\left[\rho_0\,\mathbf{v}\cdot\mathbf{n}\,\delta(f)\right] \tag{A.21}$$

Thus substituting Eq. (A.21) in Eq. (A.20) and accounting for Eq. (A.13) the FWHE recasts as follows

$$\begin{aligned}\Box^2 p' &= \frac{\overline{\partial}}{\overline{\partial} t}\left[\rho_0\,\mathbf{v}\cdot\nabla f\,\delta(f)\right] + \frac{\overline{\partial}}{\overline{\partial} t}\left[\rho\,(\mathbf{u}-\mathbf{v})\cdot\nabla f\,\delta(f)\right] \\ &- \overline{\nabla}\cdot\left[\mathbf{P}\,\nabla f\,\delta(f)\right] - \overline{\nabla}\cdot\left[\rho\,\mathbf{u}\otimes(\mathbf{u}-\mathbf{v})\,\nabla f\,\delta(f)\right] \\ &+ \overline{\nabla}\cdot\left\{\overline{\nabla}\cdot\left[\mathbf{T}\,H(f)\right]\right\} \quad \forall\mathbf{x}\in\Re^3\end{aligned} \tag{A.22}$$

where the bar over the derivative symbol denotes generalized differentiation. Equation (A.22) is written by using the typical notation for the FWHE.

If the surface S, moving with velocity $\mathbf{v}$, is impermeable, $\dfrac{DE}{Dt} = 0$ and Eq. (A.20) reduces to

$$\Box^2\hat{p}' = \nabla\cdot\nabla\cdot(E\mathbf{T}) - \rho_0\ddot{E} - \nabla\cdot(\mathbf{P}\nabla E) \tag{A.23}$$

that is

$$\begin{aligned}\Box^2 p' &= \frac{\overline{\partial}}{\overline{\partial} t}\left[\rho_0\,\mathbf{v}\cdot\nabla f\,\delta(f)\right] - \overline{\nabla}\cdot\left[\mathbf{P}\,\nabla f\,\delta(f)\right] + \\ &+ \overline{\nabla}\cdot\left\{\overline{\nabla}\cdot\left[\mathbf{T}\,H(f)\right]\right\} \qquad\qquad \forall\mathbf{x}\in\Re^3\end{aligned} \tag{A.24}$$

A.1.2 Hybrid Lighthill-Ffowcs Williams and Hawkings Equation for Moving Surfaces

A re-writing of Eq. (A.5), namely (H-FWHE), in a most known form is hereafter proposed.

To this aim let the boundary of S be mathematically defined by $f(\mathbf{x},t) = 0$, with $f > 0$ outside S and such that $\nabla f = \mathbf{n}$, where $\mathbf{n}$ is the outward unit normal vector.

Observing that $E(\mathbf{x},t) = H[f(\mathbf{x},t)]$ and recalling that $\dfrac{\partial H}{\partial t} = -\mathbf{n}\cdot\mathbf{v}\delta(f)$ and $\nabla H(f) = \mathbf{n}\delta(f)$ the following form of Eq. (A.5) is obtained

$$\begin{aligned}\overline{\Box}^2 p' = &- \overline{\nabla} p'\cdot\mathbf{n}\delta(f) - \overline{\nabla}\cdot\left[p'\mathbf{n}\delta(f)\right] + \\ &- \frac{1}{c_0^2}\left[\frac{\overline{\partial} p'}{\overline{\partial} t}\delta(f)\mathbf{n}\cdot\mathbf{v} + \frac{\overline{\partial}}{\overline{\partial} t}(p'\delta(f)\mathbf{n}\cdot\mathbf{v})\right] + H\,\overline{\nabla}\cdot\overline{\nabla}\cdot\mathbf{T}\end{aligned} \tag{A.25}$$

which recasts as follows

$$\begin{aligned}\overline{\Box}^2 p' = &- \left(\frac{\overline{\partial} p'}{\overline{\partial} n} + \frac{1}{c_0}\frac{\overline{\partial} p'}{\overline{\partial} t}M_n\right)\delta(f) - \overline{\nabla}\cdot\left[p'\mathbf{n}\delta(f)\right] + \\ &- \frac{1}{c_0}\frac{\overline{\partial}}{\overline{\partial} t}\left[p' M_n\delta(f)\right] + H\,\overline{\nabla}\cdot\overline{\nabla}\cdot\mathbf{T}\end{aligned} \tag{A.26}$$

Eq. (A.26) is a rearrangement of the Lighthill equation for moving surfaces where the linear part represents the well known *Kirchhoff formula for moving surfaces* also called *K equation* [61]. Note that the linear source terms of Eq. (A.26) are related with the acoustic pressure p' and its time and normal derivative over $f(\mathbf{x},t)$ whereas the quadrupole is related with the flow field noise sources outside the acoustic surface.

A.2 General Integral Solution

For a surface $\mathcal{S}$ in rigid–body motion with respect to the air space (SRA) and subject to a distribution of noise sources over it, in addition to those present outside, the inhomogeneous wave equation given by Eq. (A.22) or Eq. (A.26) govern the propagation of an acoustic disturbance throughout the fluid domain. Thus, to derive the general structure of integral solution for both equations, let us consider the following inhomogeneous wave equation

$$\begin{aligned} -\Box^2\hat{u} = \chi + \mathbf{z}\cdot\nabla E + \nabla\cdot(\mathbf{Z}\nabla E) + \frac{\partial}{\partial t}(k_2\frac{\partial E}{\partial t}) \\ + k_1\frac{\partial E}{\partial t} - \frac{\partial}{\partial t}(\mathbf{z}_1\cdot\nabla E) \end{aligned} \tag{A.27}$$

forced by generic vectorial and tensorial fields $\mathbf{z}$, $\mathbf{z}_1$ and $\mathbf{Z}$, respectively, where E denotes the Heaviside $H(f(\mathbf{x},t))$ *function* and $\hat{u} = u\ E$ a generic variable to be propagated. In addition, let the boundary conditions at infinity and the initial conditions be homogeneous for all the perturbative quantities involved.

The application of the Green function method that combines Eq. (A.27) with the fundamental wave equation problem

$$\begin{aligned} -\Box^2 G &= \delta(\mathbf{x}-\mathbf{x}^*, t-t^*) \\ G &= 0 \qquad \forall\mathbf{x}\in\infty \\ G &= 0 \qquad t=\infty \\ \frac{\partial G}{\partial t} &= 0 \qquad t=\infty \end{aligned} \tag{A.28}$$

yields the following integral solution of the Eq. (A.27) in the SRA

$$\begin{aligned} E(\mathbf{x}^*,t^*)\,u(\mathbf{x}^*,t^*) &= \int_0^\infty\int_{\Re^3} G\,\chi\,\mathrm{d}V dt \\ &+ \int_0^\infty\int_{\Re^3} \nabla\cdot(\mathbf{Z}\nabla E)\,G\mathrm{d}V dt \\ &+ \int_0^\infty\int_{\Re^3} \frac{\partial}{\partial t}(k_2\frac{\partial E}{\partial t})\,G\mathrm{d}V dt \\ &- \int_0^\infty\int_{\Re^3} \frac{\partial}{\partial t}(\mathbf{z}_1\cdot\nabla E)\,G\mathrm{d}V dt \\ &+ \int_0^\infty\int_{\Re^3} k_1\frac{\partial E}{\partial t}\mathrm{d}V dt \\ &+ \int_0^\infty\int_{\Re^3} \mathbf{z}\cdot\nabla E\,G\mathrm{d}V\,dt \end{aligned} \tag{A.29}$$

where

$$G(\mathbf{x}^* - \mathbf{x}, t - t^*) = \frac{-1}{4\pi r}\delta(t - t^* + \frac{r}{c_0}) \tag{A.30}$$

being $\mathbf{x}$ and $\mathbf{x}^*$ the source and observer positions in the SRA, respectively, t^* the time of observation, t the emission time of the signal and $r = |\mathbf{x}^* - \mathbf{x}|$. Since the surface $\mathcal{S}$ moves like a rigid–body, in the space rigidly connected with it (referred as body–space, SRC) E is time-independent; thus, it is convenient to transform the above air–space solution into one expressed in the SRC space.

To distinguish the air–space from the body–space, from here on $(\mathbf{x}, t)$ indicates an event in the air space whilst $(\mathbf{y}, \bar{t})$ is used for an event in the body space; moreover, the pedix y is used to denote tensorial and vectorial quantities whose images is referred to the body–space. In the air–space, the fundamental equation for rigid-body motion yields

$$\mathbf{x}(\mathbf{y}, \bar{t}) = \mathbf{x}_0(\bar{t}) + \mathbf{R}(\bar{t})\mathbf{y} \tag{A.31}$$

where $\mathbf{x}_0$ denotes the air–space image of the body point $\mathbf{y} = 0$ and $\mathbf{R}$ is an orthogonal tensor representing a rigid–body rotation around $\mathbf{x}_0$ (the Jacobian of the rigid–body transformation is equal to one). In addition, the time derivatives between the two spaces are related by

$$\frac{\partial}{\partial t} = \frac{\partial}{\partial \bar{t}} - \mathbf{v}_y \cdot \nabla_y \tag{A.32}$$

where $\nabla_y = \mathbf{R}^T \nabla$ denotes the body–space gradient operator and $\mathbf{v}_y = \mathbf{R}^T \frac{\partial \mathbf{x}}{\partial \bar{t}}$ the body–space vector of the velocity of $\mathbf{y}$ relative to the air space. For the next mathematical manipulations let us observe that, for any function $h(\bar{t})$ and $g(\bar{t})$

$$\int_0^\infty h(\bar{t})\delta[g(\bar{t})]d\bar{t} = \sum_k \int_0^\infty \frac{h(\bar{t})}{\dot{g}(\bar{t})}\delta(\bar{t} - \bar{t}_k)d\bar{t} \tag{A.33}$$

where $\bar{t}_k$ represents a roots of $g(\bar{t}) = 0$. Referring to the body–space and combining Eq. A.29 with Eqs. A.30, A.33, the support of the Dirac delta function and its time derivative are easily identified, being $g = (\bar{t} - \bar{t}^* + \frac{|\mathbf{r}_y|}{c_0})$, $\dot{g} = 1 - \mathbf{r}_y \cdot \frac{\mathbf{v}_y}{c_0|\mathbf{r}_y|}$ with $\mathbf{r}_y = \mathbf{R}^T[\mathbf{x}(\mathbf{y}^*, \bar{t}^*) - \mathbf{x}(\mathbf{y}, \bar{t})]$ and $\dot{g} = 1 - \mathbf{r}_y \cdot \frac{\mathbf{v}_y}{c_0|\mathbf{r}_y|}$. Hence, by combining the above relations with Eq. A.29 and performing an integration by parts (with the condition $\hat{u} = 0$ at infinity), the integral solution of

Eq. A.27 in the body–space reads

$$\begin{aligned} E(\mathbf{y}^*)\, u(\mathbf{y}^*, t^*) &= \int_0^\infty \int_{\Re^3} \check{G}\, \chi \mathrm{d}V d\bar{t} + \\ &- \int_0^\infty \int_{\Re^3} (\mathbf{Z}_y \nabla_y E)\, \nabla_y \check{G} \mathrm{d}V d\bar{t} \\ &- \int_0^\infty \int_{\Re^3} k_2 \frac{d_B E}{d\bar{t}} (\frac{d_B \check{G}}{d\bar{t}}) \mathrm{d}V d\bar{t} \\ &+ \int_0^\infty \int_{\Re^3} (\mathbf{z}_{1y} \cdot \nabla_y E)\, \frac{d_B \check{G}}{d\bar{t}} \mathrm{d}V d\bar{t} \\ &+ \int_0^\infty \int_{\Re^3} k_1 \frac{d_B E}{d\bar{t}}\, \check{G} \mathrm{d}V d\bar{t} \\ &+ \int_0^\infty \int_{\Re^3} (\mathbf{z}_y \cdot \nabla_y E)\, \check{G} \mathrm{d}V d\bar{t} \end{aligned} \tag{A.34}$$

where the (Eulerian) time derivative $d_B/d\bar{t}$ is expressed as

$$\frac{d_B}{d\bar{t}} = \frac{\partial}{\partial \bar{t}} - \mathbf{v}_y \cdot \nabla_y \tag{A.35}$$

being $\partial/\partial\bar{t}$ the material derivative (that is following a body point), $\mathbf{z}_y = \mathbf{R}^T\mathbf{z}$, $\mathbf{Z}_y = \mathbf{R}^T\mathbf{Z}\mathbf{R}$ whereas $\check{G}(\mathbf{y} - \mathbf{y}^*, \bar{t} - \bar{t}^*) = \hat{G}\, \delta(\bar{t} - \bar{t}^* + \vartheta)$ with

$$\hat{G} = \left[\left| 1 - \frac{\mathbf{r}_y \cdot \mathbf{v}_y}{c_0 |\mathbf{r}_y|} \right|^{-1} \frac{-1}{4\pi |\mathbf{r}_y|} \right]_\theta \tag{A.36}$$

In Eq. A.36, $[...]_\theta$ denotes that $\hat{G}$ is a retarded function since it is evaluated at the emission time $(\bar{t}^* - \vartheta)$ that, for subsonic flows, is given by the (unique) root of the equation $g(\bar{t}) = 0$.

Although mathematically consistent, the use of Eq. A.34 in acoustic calculations is impractical. However, a form of solution suitable for numerical purposes is easily obtained noting that

- $\nabla_y E = \delta(f)\mathbf{n}_y |\nabla_y f|$ so, for any body–space vector $\mathbf{a}(\mathbf{y}, t)$

$$\int_0^\infty \int_{\Re^3} \mathbf{a} \cdot \nabla_y E\, \delta(\bar{t} - \bar{t}^* + \vartheta) \mathrm{d}V d\bar{t} = \int_S \left[\mathbf{a} \cdot \mathbf{n}_y \right]_\theta \mathrm{d}S \tag{A.37}$$

- the time-independence of E implies $\dfrac{d_B E}{d\bar{t}} = -\mathbf{v}_y \cdot \nabla_y E$; hence, for any $f(\mathbf{y}, \bar{t})$ Eq. A.37 yields

$$\int_0^\infty \int_{\Re^3} f \frac{d_B E}{d\bar{t}}\, \delta(\bar{t} - \bar{t}^* + \vartheta) \mathrm{d}V\, d\bar{t} = -\int_S \left[f\, \mathbf{v}_y \cdot \mathbf{n}_y \right]_\theta \mathrm{d}S \tag{A.38}$$

- since $\vartheta = \vartheta(\mathbf{y}, \mathbf{y}^*, \bar{t}^*)$, the relation $\nabla_y \check{G} = \nabla_y \hat{G}\, \delta + \hat{G}\, \nabla_y \delta$ recasts

$$\nabla_y \check{G} = \nabla_y \hat{G}\, \delta(\bar{t} - \bar{t}^* + \vartheta) + \hat{G}\, \dot{\delta}(\bar{t} - \bar{t}^* + \vartheta) \nabla_y \vartheta \tag{A.39}$$

- $\dfrac{d_B \check{G}}{d\bar{t}} = \hat{G}\, \dot{\delta} - \mathbf{v}_y \cdot \nabla_y \check{G}$

- $\int_{-\infty}^{\infty} f\dot{\delta}d\bar{t} = -\dot{f}(0)$

Accounting for the above relations, the integrals at the left-hand-side of Eq. A.34 are transformed into

$$
\begin{aligned}
I_1 &= \int_0^{\infty}\int_{\Re^3}(\mathbf{Z}_y\nabla_y E)\,\nabla_y\check{G}\,\mathrm{d}V d\bar{t} = \\
&= \int_S \left[(\mathbf{Z}_y\mathbf{n}_y)\cdot\nabla_y\hat{G} - (\dot{\mathbf{Z}}_y\mathbf{n}_y)\cdot\nabla_y\vartheta\,\hat{G}\right]_\vartheta \mathrm{d}S \\
I_2 &= \int_0^{\infty}\int_{\Re^3} k_2\,\frac{d_B E}{d\bar{t}}\left(\frac{d_B\check{G}}{d\bar{t}}\right)\mathrm{d}V d\bar{t} = \\
&= \int_S \left\{k_2\,\mathbf{v}_y\cdot\mathbf{n}_y\mathbf{v}_y\cdot\nabla_y\hat{G} + \left[k_2\,\mathbf{v}_y\cdot\mathbf{n}_y(1-\mathbf{v}_y\cdot\nabla_y\vartheta)\right]^{\cdot}\,\hat{G}\right\}_\theta \mathrm{d}S \\
I_3 &= \int_0^{\infty}\int_{\Re^3}(\mathbf{z}_{1y}\cdot\nabla_y E)\,\frac{d_B\check{G}}{d\bar{t}}\,\mathrm{d}V d\bar{t} = \\
&= -\int_S \left\{\left[\mathbf{z}_{1y}\cdot\mathbf{n}_y(1-\mathbf{v}_y\cdot\nabla_y\vartheta)\right]^{\cdot}\hat{G} + \mathbf{z}_{1y}\cdot\mathbf{n}_y\mathbf{v}_y\cdot\nabla_y\hat{G}\right\}_\theta \mathrm{d}S
\end{aligned}
$$

$$
\begin{aligned}
I_4 &= \int_0^{\infty}\int_{\Re^3} k_1\,\frac{d_B E}{d\bar{t}}\check{G}\,\mathrm{d}V d\bar{t} = -\int_S \hat{G}\left[k_1\,\mathbf{v}_y\cdot\mathbf{n}_y\right]_\theta \mathrm{d}S \\
I_5 &= \int_0^{\infty}\int_{\Re^3}(\mathbf{z}_y\cdot\nabla_y E)\,\check{G}\,\mathrm{d}V d\bar{t} = \int_S \left[\mathbf{z}_y\cdot\mathbf{n}_y\hat{G}\right]_\theta \mathrm{d}S
\end{aligned}
$$

where all the time derivatives are performed in the body–space. Finally, combining the above integrals, the boundary integral solution of Eq. (A.27) everywhere in $\Re^3$ yields

$$
E(\mathbf{y}^*)u(\mathbf{y}^*,t^*) = \int_0^{\infty}\int_{\Re^3}\check{G}\,\chi\,\mathrm{d}V d\bar{t} - I_1 - I_2 + I_3 - I_4 + I_5 \tag{A.40}
$$

From here on, without any ambiguity or possibility of confusion, the notation is simplified to avoid the proliferation of symbols.

application to the FWHE

By assuming $\hat{u} = \bar{p}'$, $\mathbf{Z} = \mathbf{P} + \rho\mathbf{u}\otimes(\mathbf{u}-\mathbf{v})$, $\chi = -\nabla\cdot\nabla\cdot(E\mathbf{T})$, $k_2 = \rho_0$, $\mathbf{z}_1 = \rho(\mathbf{u}-\mathbf{v})$, $k_1 = 0$ and $\mathbf{z} = 0$, Eq. (A.22) is represented by Eq. (A.27). Noting that $(\mathbf{a}\otimes\mathbf{b})\mathbf{c} = (\mathbf{b}\cdot\mathbf{c})\mathbf{a}$ and $I_4 = I_5 = 0$, for $\mathbf{u}^- = (\mathbf{u}-\mathbf{v})$ and $\mathbf{u}^+ = (\mathbf{u}+\mathbf{v})$ the integral

solution for the permeable FWHE, written in the space rigidly moving with $\mathcal{S}$ reads

$$\begin{aligned} E(\mathbf{y}^*)p'(\mathbf{y}^*,t^*) &= \int_0^\infty \int_{\Re^3} \check{G}\,\chi \,\mathrm{d}V d\bar{t} \\ &- \int_S \left[(\mathbf{P}\mathbf{n})\cdot\nabla\hat{G} - (\dot{\mathbf{P}}\mathbf{n})\cdot\nabla\vartheta\,\hat{G}\right]_\theta \mathrm{d}S \\ &- \rho_0 \int_S \left\{\mathbf{v}\cdot\mathbf{n}\mathbf{v}\cdot\nabla\hat{G} + \left[\mathbf{v}\cdot\mathbf{n}(1-\mathbf{v}\cdot\nabla\vartheta)\right]^{\cdot}\,\hat{G}\right\}_\theta \mathrm{d}S \\ &- \int_S \left\{\rho\mathbf{u}^-\cdot\mathbf{n}\,\mathbf{u}^+\cdot\nabla\hat{G}\right\}_\theta \mathrm{d}S \\ &+ \int_S \left\{\left[\rho\mathbf{u}^-\cdot\mathbf{n}(1-\mathbf{u}^+\cdot\nabla\vartheta)\right]^{\cdot}\,\hat{G}\right\}_\theta \mathrm{d}S \end{aligned} \tag{A.41}$$

application to the H-FWHE

Equations A.5 and A.27 matches for $\hat{u} = \bar{p}'$, $\chi = E\,\nabla\cdot\nabla\cdot\mathbf{T}$, $\mathbf{z} = \nabla\bar{p}'$, $\mathbf{Z} = \mathbf{I}\bar{p}'$, $k_1 = -\dfrac{\partial\bar{p}'}{\partial t}/c^2$, $k_2 = -\bar{p}'/c^2$, $\mathbf{z}_1 = 0$. In this case, $I_3 = 0$ and the following boundary integral representation in the body space is obtained

$$\begin{aligned} E(\mathbf{y}^*,t^*)\bar{p}'(\mathbf{y}^*,t^*) = &- \int_V \hat{G}\,[\nabla\cdot\nabla\cdot\mathbf{T}]_\theta\,\mathrm{d}V + \int_S \left[\frac{\partial\bar{p}'}{\partial\tilde{n}}\hat{G} - \bar{p}'\frac{\partial\hat{G}}{\partial\tilde{n}}\right]_\theta \mathrm{d}S \\ &+ \int_S \left[\hat{G}\frac{\partial\bar{p}'}{\partial\bar{t}}\left(\frac{\partial\vartheta}{\partial\tilde{n}} + 2\frac{\mathbf{v}\cdot\mathbf{n}}{c_0^2}\right)\right]_\theta \\ &+ \frac{1}{c_0^2}\int_S \left[\bar{p}'\,\hat{G}\frac{\partial}{\partial\bar{t}}[\mathbf{v}\cdot\mathbf{n}(1-\mathbf{v}\cdot\nabla\vartheta)]\right]_\theta \mathrm{d}S \end{aligned} \tag{A.42}$$

where $\dfrac{\partial}{\partial\tilde{n}} = \dfrac{\partial}{\partial n} - \dfrac{1}{c_0^2}\,(\mathbf{v}\cdot\mathbf{n})\,(\mathbf{v}\cdot\nabla)$.

A.3 Kinematic of the Acoustic Surface

In the following two different expressions of Eq. (A.41) are proposed to account with rototranslating or translating motion of $f(\mathbf{x},t) = 0$.

A.3.1 Roto-translating Motion

In this subsection an expression of Eq. (A.41) suitable for porous surfaces enclosing rotating blade devices is proposed. To this aim $\mathbf{v}$ and $\mathbf{n}$, the singularities $\hat{G}, \nabla\hat{G}$ and quantities related to the compressibility delay ϑ, $\nabla\vartheta$ are here written with respect to the rotating reference system rigidly connected with the surface S. The relations between air-space and body-space here used as introduced in Appendix A.2 with the same meaning of symbols.

To this aim the kinematic of the acoustic surface is described by $\mathbf{x}(\mathbf{y},\bar{t}) = \mathbf{x}_0(\bar{t}) + \mathbf{R}(\bar{t})\mathbf{y}$ where $\mathbf{y}$ represents the position of the acoustic surface respect to the reference frame moving

with it. Besides, $\mathbf{R}$ is an orthogonal tensor representing a rigid–body rotation around $\mathbf{x}_0$ at the angular velocity of the body $\boldsymbol{\omega}$. The surface points velocity is obtained by the time derivative of $\mathbf{x}(\mathbf{y},\bar{t})$ with respect to the air frame reference, namely $\mathbf{v} = \dfrac{\partial \mathbf{x}(\mathbf{y},\bar{t})}{\partial \bar{t}} = \mathbf{v}_0 + \boldsymbol{\Omega}\mathbf{R}(\bar{t})\mathbf{y}$ where $\mathbf{v}_0$ is the translating velocity, $\boldsymbol{\Omega}$ the skew-tensor such that, for any vector $\mathbf{c}$, $\boldsymbol{\omega} \times \mathbf{c} = \boldsymbol{\Omega}\mathbf{c}$. Therefore $\mathbf{v}_y(\mathbf{y},\bar{t}) = \mathbf{R}^T(\bar{t})\mathbf{v}_0 + \boldsymbol{\Omega}_y\mathbf{y}$ represents the body space image of $\mathbf{v}$ where $\boldsymbol{\Omega}_y = \mathbf{R}^T(\bar{t})\boldsymbol{\Omega}$.

The velocity time derivative with respect to the rotating reference frame provides $\dot{\mathbf{v}}_y = -\boldsymbol{\Omega}_y\mathbf{R}^T(\bar{t})\mathbf{v}_0$, furthermore the body space image of the normals $\mathbf{n}_y = \mathbf{R}^T(\bar{t})\mathbf{n}$ is time invariant, thus $\dot{\mathbf{n}}_y = 0$.

The compressibility delay is obtained by the solution of $\vartheta = \dfrac{|\mathbf{x}(\bar{t}^*) - \mathbf{y}(\bar{t}^* - \vartheta)|}{c_0}$ which is a non linear equation; due to the transcendental functions involved in the rotational motion the solution is obtained by the means of the Newton-Raphson iterative method. Furthermore $\dfrac{\partial \vartheta}{\partial \bar{t}} = 0$ since $\vartheta = \vartheta(\mathbf{y},\mathbf{y}^*,\bar{t}^*)$ has not functional dependencies on $\bar{t}$, thus also $\nabla\vartheta^{\cdot} = 0$.

In order to determine a suitable expression for $\nabla\hat{G}$ note that $\hat{G}$ is a retarded function, thus the following functional dependencies $\hat{G} = \hat{G}\left(\mathbf{y},\mathbf{y}^*,\bar{t}^*,\bar{t}^* - \vartheta(\mathbf{y},\mathbf{y}^*,\bar{t}^*)\right)$ must be take into account in the derivation process. To this aim if f^{ϑ} is a retarded function, the application of the multiple chain differentiation rule allows to obtain the following expression

$$\nabla_y f^{\vartheta}\left(\mathbf{y},\bar{t}^* - \vartheta(\mathbf{y},\mathbf{y}^*,\bar{t}^*)\right) = \left.\frac{\partial f}{\partial \mathbf{y}}\right|_{\tau} + \left.\frac{\partial f}{\partial \tau}\right|_{\mathbf{y}} \frac{\partial \tau}{\partial \vartheta}\frac{\partial \vartheta}{\partial \mathbf{y}} \tag{A.43}$$

where $\mathbf{r}_y = \mathbf{R}(\tau)[\mathbf{x}(\bar{t}^*) - \mathbf{y}(\tau)]$ represents the body space image of the observer source radius, $M_r = \dfrac{\mathbf{v}_y}{c_0}\cdot\hat{\mathbf{r}}_y$, $\hat{\mathbf{r}}_y = \dfrac{\mathbf{r}_y}{|\mathbf{r}_y|}$ whereas $\tau = (\bar{t}^* - \vartheta)$ is the emission time.

The application of the Eq. (A.43) provides (see, Ref.([41]))

$$\nabla_y\vartheta = -\frac{\hat{\mathbf{r}}_y}{c_0\left(1 - M_r\right)} \tag{A.44}$$

and

$$\begin{aligned}\nabla_y\hat{G} = &-\frac{1}{4\pi}\left[\frac{\hat{\mathbf{r}}_y}{|\mathbf{r}_y|^2\left(1-M_r\right)} - \frac{\boldsymbol{\Omega}_y\hat{\mathbf{r}}_y}{c_0|\mathbf{r}_y|\left(1-M_r\right)^2} - \frac{\mathbf{v}_y - 2\,v_r\hat{\mathbf{r}}_y}{c_0|\mathbf{r}_y|^2\left(1-M_r\right)^2}\right] \\ &-\frac{1}{4\pi}\left[\frac{\mathbf{R}^T\dot{\mathbf{v}}\cdot\hat{\mathbf{r}}_y}{c_0^2|\mathbf{r}_y|\left(1-M_r\right)^3}\hat{\mathbf{r}}_y - \frac{v_y^2 - v_r^2}{c_0^2|\mathbf{r}_y|^2\left(1-M_r\right)^3}\hat{\mathbf{r}}_y\right]\end{aligned} \tag{A.45}$$

A.3.2 Translating Motion

It may be obtained as particular case of the solution presented in A.3.1 for the rototranslating motion in which $\mathbf{R} = \mathbf{I}$ $\boldsymbol{\Omega}_y = \mathbf{0}$ and $\dot{\mathbf{n}} = 0$. The compressibility delay comes from $\vartheta = \dfrac{|\mathbf{x}(\bar{t}^*) - \mathbf{y}(\bar{t}^* - \vartheta)|}{c_0}$, that reduces to a second order algebraic equation in ϑ.

Appendix B

Appendix B

B.1 Monopole in Helicoidal Motion

The acoustic pressure induced by a steady-state subsonic rototranslating monopole is herein derived. To this aim, let us consider a source of mass, pulsating at angular frequency ω_p in a fluid at rest, moving, throughout it, with velocity $\mathbf{v}$ respect to a frame of reference connected to the undisturbed fluid medium (SRA). Under these assumptions the equation governing the propagation of the velocity potential field is

$$-\Box^2\phi \quad = \quad \sin(\omega_p\tau)\delta(\mathbf{x}-\mathbf{x}^*,\tau-t) \tag{B.1}$$

where where $\Box^2$ is the D'Alambertian operator, $\mathbf{x}$ and $\mathbf{x}^*$ identify source and receiver positions, respectively, in the SRA, whilst t denotes the *current* time at which the disturbance generated in $\mathbf{x}$ at time τ is received. The integral solution of Eq. (B.1) by the Green function technique yields [38]

$$\phi(\mathbf{x}^*,t) = \int_0^\infty \int_{\Re^3} \hat{G}\sin(\omega_p\tau)\delta(\tau-t+\vartheta)\delta(\mathbf{x}-\mathbf{x}^*)\mathrm{d}V(\mathbf{x})d\tau = \hat{G}\sin\left[k\left(c_0t-\hat{\vartheta}\right)\right] \tag{B.2}$$

where $k=\omega_p/c_0$ is the wave number and

$$\hat{G} = -\frac{1}{4\pi r\mid(1+M_r)\mid}\bigg|_{ret} \tag{B.3}$$

is the retarded Green function with $\mathbf{r}=\mathbf{x}(\tau)-\mathbf{x}^*(t)$, $r=|\mathbf{r}|$ and $M_r=\mathbf{v}\cdot(\mathbf{r}/|\mathbf{r}|)=\mathbf{v}\cdot\hat{\mathbf{r}}$. The subscript $|_{ret}$ states that quantities are computed at the emission time $\tau=t-\vartheta$, where $\vartheta=|\mathbf{r}|c_0$ is the compressibility time delay, that is the time required to a signal generated at $\mathbf{x}$ to reach the observer location in $\mathbf{x}^*$. The linearized Bernoulli equation for compressible unsteady isentropic flows yields the acoustic pressure everywhere in the field; by assuming the observer undergoing an arbitrary steady motion with velocity $\mathbf{v}_{obs}$ it reads

$$\frac{p'}{\rho_0} = -\left.\frac{\partial\phi}{\partial t}\right|_b + \mathbf{v}_{obs}\cdot\nabla_*\phi - \frac{\nabla_*\phi\cdot\nabla_*\phi}{2} \tag{B.4}$$

where the subscript $*$ indicates that the gradient operator is performed respect to the observer position and $|_b$ states that the time derivative is computed following it. In order to apply Eq. (B.4), it is convenient to refer to a frame of reference rigidly connected to the monopole

(SRC); to this aim, in analogy with the developments addressed in Appendix A.2, from here on subscript y represents the body space image of a air-space physical quantity.
In the air–space, the rigid-body motion for both the source and observer is given by

$$\mathbf{x}(\mathbf{y},\tau) = \mathbf{x}_0(\tau) + \mathbf{R}(\tau)\mathbf{y}$$
$$\mathbf{x}^*(\mathbf{y}^*,t) = \mathbf{x}_0(t) + \mathbf{R}(t)\mathbf{y}^*(t)$$

where $\mathbf{x}_0$ denotes the air–space image of the body point $\mathbf{y} = 0$, $\mathbf{R}$ is an orthogonal tensor representing a rigid–body rotation around $\mathbf{x}_0$ (the Jacobian of the rigid–body transformation is equal to one) whilst $\mathbf{y}$ and $\mathbf{y}^*$ identify the SRC placements of the monopole and observer, respectively. Moreover, noting that $\mathbf{r}_y = \mathbf{R}(\tau)\left[\mathbf{x}(\mathbf{y},\tau) - \mathbf{x}^*(\mathbf{y}^*,t)\right]$ Eq. (B.3) becomes equivalent to

$$\hat{G} = -\frac{1}{4\pi r_y \mid (1+M_r) \mid}\bigg|_{ret} \tag{B.5}$$

with $M_r = (\mathbf{v}_y \cdot \hat{\mathbf{r}}_y)/c_0$ and $\mathbf{v}_y = \mathbf{R}^T(\tau)\mathbf{v}$ the SRC image of the absolute velocity $\mathbf{v}$. Letting $\mathbf{v}_0$ be the translating speed of the monopole along a generic direction in the 3D space and $\boldsymbol{\omega}$ its rotational velocity about a spinning axis (in general different from the advancing direction) $\mathbf{v}_y = \mathbf{R}^T(\tau)\mathbf{v}_0 + \boldsymbol{\Omega}_y\mathbf{y}$ where $\boldsymbol{\Omega}_y$ denotes the body-space image of the skew-tensor $\boldsymbol{\Omega}$ such that, for any vector $\mathbf{c}$, $\boldsymbol{\omega}\times\mathbf{c} = \boldsymbol{\Omega}\mathbf{c}$. Observing that a generic retarded function $\mathcal{F}$ is such that $\mathcal{F} = \mathcal{F}\left[\mathbf{y},\mathbf{y}^*(t),t,t-\vartheta(\mathbf{y},\mathbf{y}^*,t)\right]$, the application of the multiple chain differentiation rule provides

$$\nabla_*\mathcal{F} = \frac{\partial\mathcal{F}}{\partial\mathbf{y}^*}\bigg|_{ret} + \left[\frac{\partial\mathcal{F}}{\partial\tau}\bigg|_{\mathbf{y}^*}\frac{\partial\tau}{\partial\vartheta}\right]_{ret}\frac{\partial\vartheta}{\partial\mathbf{y}^*} \tag{B.6}$$

and

$$\frac{\partial\mathcal{F}}{\partial t} = \left[\frac{\partial\mathcal{F}}{\partial t}\bigg|_{\mathbf{y}^*}\right]_{ret} + \left[\frac{\partial\mathcal{F}}{\partial\mathbf{y}^*}\bigg|_t\cdot\frac{\partial\mathbf{y}^*}{\partial t}\right]_{ret} + \frac{\partial\mathcal{F}}{\partial\tau}\bigg|_{t,\mathbf{y}^*}\frac{\partial\tau}{\partial t} \tag{B.7}$$

that, applied to Eq. (B.2) provides

$$\nabla_*\phi(\mathbf{x},t) = \nabla_*\hat{G}\sin\left[kc_0(t-\vartheta)\right] - kc_0\hat{G}\cos\left[kc_0(t-\vartheta)\right]\nabla_*\vartheta \tag{B.8}$$

and

$$\frac{\partial\phi}{\partial t} = \frac{\partial\hat{G}}{\partial t}\cos\left[kc_0(t-\vartheta)\right] + \hat{G}kc_0\cos\left[kc_0(t-\vartheta)\right]\left(1-\frac{\partial\vartheta}{\partial t}\right) \tag{B.9}$$

respectively. In the following steps, the mathematical operators of Eq. (B.6) and Eq. (B.7) applied for $\mathcal{F} = \vartheta$ and $\mathcal{F} = \hat{G}$ are briefly outlined.

- $\nabla_*\vartheta$

  By applying the multiple chain rule to the delay function and noting that $\nabla_*\mathbf{r}_y = -\mathbf{R}(\vartheta)$, it derives

$$\nabla_*\vartheta = -\frac{\mathbf{R}^T(\vartheta)\hat{\mathbf{r}}_y}{c_0(1+M_r)} \tag{B.10}$$

- $\nabla_* \hat{G}$

The first term at RHS of Eq. (B.6) may be written as

$$\nabla_* \hat{G}\big|_{ret} = \frac{\nabla_* \mid \mathbf{r}_y \mid}{4\pi \mid \mathbf{r}_y \mid^2 (1+M_r)} + \frac{\nabla_* M_r}{4\pi \mid \mathbf{r}_y \mid (1+M_r)^2} \tag{B.11}$$

where

$$\nabla_* M_r = \frac{1}{c_0}\nabla_*[\mathbf{v}_y \cdot \hat{\mathbf{r}}] = \frac{1}{c_0}[\nabla_* \mathbf{v}_y]^T \hat{\mathbf{r}}_y + \frac{1}{c_0}[\nabla_* \mathbf{r}_y]^T \mathbf{v}_y \tag{B.12}$$

$$\nabla_* \hat{\mathbf{r}}_y = \nabla_* \frac{\mathbf{r}_y}{\mid \mathbf{r}_y \mid} = \frac{\nabla_* \mathbf{r}_y \mid \mathbf{r}_y \mid - \mathbf{r}_y \otimes \nabla_* \mid \mathbf{r}_y \mid}{\mid \mathbf{r}_y \mid^2} \tag{B.13}$$

Noting that $\nabla_* \mid \mathbf{r}_y \mid = -\mathbf{R}^T(\vartheta)\hat{\mathbf{r}}_y$, $\nabla_* \mathbf{v}_y = 0$ and $(\mathbf{a} \otimes \mathbf{b}) \cdot \mathbf{c} = (\mathbf{b} \cdot \mathbf{c})\,\mathbf{a}$ for any vectors $\mathbf{a}$, $\mathbf{b}$, $\mathbf{c}$, the combination of Eq. (B.11) with Eqs. (B.12), (B.13) yields

$$\nabla_* \hat{G}\big|_{ret} = \frac{-\mathbf{R}^T(\vartheta)\hat{\mathbf{r}}_y}{4\pi \mid \mathbf{r}_y \mid^2 (1+M_r)} + \frac{\left[(\mathbf{v}_y \cdot \hat{\mathbf{r}}_y)\,\mathbf{R}^T(\vartheta)\hat{\mathbf{r}}_y - \mathbf{R}^T(\vartheta)\mathbf{v}_y\right]}{4\pi \mid \mathbf{r}_y \mid^2 c_0 (1+M_r)^2} \tag{B.14}$$

Furthermore, the derivative of $\hat{G}$ respect to the retarded time $\tau = t - \vartheta$ reads

$$\left.\frac{\partial \hat{G}}{\partial \tau}\right|_{\mathbf{y}^*} = \frac{\frac{\partial |\mathbf{r}_y|}{\partial \tau}}{4\pi \mid \mathbf{r}_y \mid^2 (1+M_r)} + \frac{\frac{\partial M_r}{\partial \tau}}{4\pi \mid \mathbf{r}_y \mid (1+M_r)^2} \tag{B.15}$$

being

$$\begin{aligned} \frac{\partial \mid \mathbf{r}_y \mid}{\partial \tau} &= \mathbf{v}_y \cdot \hat{\mathbf{r}}_y = v_r \\ \frac{\partial M_r}{\partial \tau} &= \frac{1}{c_0}\left[\dot{\mathbf{v}}_y \cdot \hat{\mathbf{r}}_y + \frac{\mid \mathbf{v}_y \mid^2 - v_r^2 - \Omega_y \mathbf{r}_y \cdot \mathbf{v}_y}{\mid \mathbf{r}_y \mid}\right] \end{aligned} \tag{B.16}$$

Finally, by combining Eq. (B.14) with Eq. (B.15) and $\partial\tau/\partial\theta = -1$, the following expression is derived

$$\begin{aligned} \nabla_* \hat{G} = &- \frac{\mathbf{R}^T(\vartheta)\left(\hat{\mathbf{r}}_y + \mathbf{M}_y\right)}{4\pi \mid \mathbf{r}_y \mid^2 (1+M_r)^2} + \frac{\mathbf{R}^T(\vartheta)\hat{\mathbf{r}}_y\left(M^2 + M_r\right)}{4\pi \mid \mathbf{r}_y \mid^2 (1+M_r)^3} \\ &+ \frac{\mathbf{R}^T(\vartheta)\hat{\mathbf{r}}_y\left(\dot{\mathbf{M}}_y \cdot \hat{\mathbf{r}}_y - \mathbf{M}_y \cdot \boldsymbol{\Omega}_y \hat{\mathbf{r}}_y\right)}{4\pi c_0 \mid \mathbf{r}_y \mid (1+M_r)^3} \end{aligned} \tag{B.17}$$

where $\mathbf{M}_y = \mathbf{v}_y/c_0$, $M^2 = (\mathbf{v}_y \cdot \mathbf{v}_y)/c_0^2$ and $\dot{\mathbf{M}}_y = \dot{\mathbf{v}}_y/c_0$.

- $\dfrac{\partial \hat{G}}{\partial t}$

The first term at RHS of Eq. (B.7) may be written as

$$\left[\left.\frac{\partial \hat{G}}{\partial t}\right|_{\mathbf{y}^*}\right]_{ret} = \frac{\frac{\partial |\mathbf{r}_y|}{\partial t}}{4\pi \mid \mathbf{r}_y \mid^2 (1+M_r)} + \frac{\frac{\partial M_r}{\partial t}}{4\pi \mid \mathbf{r}_y \mid (1+M_r)^2} \tag{B.18}$$

with

$$\begin{aligned}
\frac{\partial \mathbf{r}_y}{\partial t} &= -\mathbf{R}^T(\tau)\mathbf{v}_0 - \mathbf{R}(\vartheta)\mathbf{\Omega}\mathbf{y}^* \\
\frac{\partial \mid \mathbf{r}_y \mid}{\partial t} &= \frac{\partial \mathbf{r}_y}{\partial t} \cdot \hat{\mathbf{r}}_y \\
\frac{\partial M_r}{\partial t} &= \frac{1}{c_0}\left[\frac{\partial \mathbf{v}_y}{\partial t} \cdot \hat{\mathbf{r}}_y + \mathbf{v}_y \cdot \frac{\partial \hat{\mathbf{r}}_y}{\partial t}\right]
\end{aligned} \tag{B.19}$$

Finally, by combining Eq. (B.14) and Eq. (B.15) with Eq. (B.18) one obtains

$$\begin{aligned}
\frac{\partial \hat{G}}{\partial t} =& \frac{\mathbf{R}^T(\vartheta)\left(\hat{\mathbf{r}}_y + \mathbf{M}_y\right)}{4\pi \mid \mathbf{r}_y \mid^2 (1+M_r)^2} \cdot \frac{\partial \mathbf{y}^*}{\partial t} \\
&+ \frac{\left(1 - \frac{\partial \vartheta}{\partial t}\right)}{4\pi \mid \mathbf{r}_y \mid (1+M_r)}\left[\frac{v_r}{\mid \mathbf{r}_y \mid} + \frac{\dot{\mathbf{v}}_y \cdot \hat{\mathbf{r}}_y}{c_0(1+M_r)} + \frac{\mid \mathbf{v}_y \mid^2 - v_r^2 - \Omega \mathbf{r}_y \cdot \mathbf{v}_y}{c_0 \mid \mathbf{r}_y \mid (1+M_r)}\right] \\
&- \frac{\left[\mathbf{R}^T(\tau)\mathbf{v}_0 + \mathbf{R}(\vartheta)\mathbf{\Omega}\mathbf{y}^*\right]}{4\pi \mid \mathbf{r}_y \mid^2 (1+M_r)} \cdot \left[\hat{\mathbf{r}}_y + \left(\frac{\mathbf{v}_y - v_r \hat{\mathbf{r}}_y}{c_0 (1+M_r)}\right)\right]
\end{aligned} \tag{B.20}$$

The pressure disturbance at $(\mathbf{x}^*, t)$ depends on the observer kinematics (see Eq. (B.4)) that, in the SRC, is described by $\mathbf{y}^*(t)$. Two kinds of motion are hereafter considered: i) a steady-state translation in the same direction of the monopole advancing speed; ii) a rototranslation rigidly connected with the monopole. In the first case, for $\mathbf{x}^*(t=0)$ defying the SRA observer position at the initial time, the equation of motion, referred to the SRC is defined by $\mathbf{y}^*(t) = \mathbf{R}^T(t)\mathbf{x}^*(t=0)$ whereas $\partial \mathbf{y}^*/\partial t = -\mathbf{\Omega}_y \mathbf{R}^T(t)\mathbf{x}^*(t=0)$. Differently, in the second case, the observer moves in connection to the monopole; thus, without loss of generality, by assuming the SRC and SRA coincident at $t=0$, $\mathbf{y}^*(t) = \mathbf{I}\mathbf{x}^*(t=0)$ whereas $\partial \mathbf{y}^*/\partial t = 0$, being $\mathbf{I}$ the unit tensor.

The particular case of a monopole in uniform translation may be easily obtained from the above considerations by imposing $\mathbf{\Omega} = \mathbf{0}$ and $\mathbf{R}(t) = \mathbf{I}$. However, since compressibility delays are analytic, in the next section an equivalent derivation is shown for completeness.

B.2 Translating Monopole: an Equivalent Derivation

For a pulsating monopole in uniform translation at velocity $\mathbf{v}$, the solution of Eq. (B.2) is given by

$$\phi(\mathbf{x}^*, t) = -\frac{1}{4\pi r_\beta} \sin\left[k\left(c_0 t - \hat{\vartheta}\right)\right] \tag{B.21}$$

where the retarded Green function of Eq. (B.5) recasts

$$\hat{G} = -\frac{1}{4\pi r_\beta} \tag{B.22}$$

For the next steps, let $\mathbf{e}_1, \mathbf{e}_2, \mathbf{e}_3$ be the unit vectors of a Cartesian frame of reference x_1, x_2, x_3, rigidly connected with the monopole. Assuming $\mathbf{v} = -v_0\mathbf{e}_1$, $r_\beta = \sqrt{(M_0^2 \Delta x_1^2 + \beta^2 r^2)}$,

$\beta^2 = (1 - M_0^2)$, $\Delta x_k = (\mathbf{y} - \mathbf{y}^*) \cdot \mathbf{e}_k \quad k = (1,2,3)$, $\mathbf{r} = \mathbf{y} - \mathbf{y}^*, r = |\mathbf{r}|$ and $M_0 = |-v_0 \mathbf{e}_1 / c_0|$, it is easy to show that, for the case here considered, the compressibility delay comes from the acoustically-consistent solution of an algebraic quadratic equation, whose solution is

$$\hat{\vartheta}_{1/2} = \frac{M_0 \Delta x \pm \sqrt{M_0^2 \Delta x^2 + \beta^2 r^2}}{\beta^2} \tag{B.23}$$

Akin to section B.1, the application of the Bernoulli Equation requires the knowledge of the mathematical operators defined in Eq. (B.4); to this aim, details are summarized in the following steps.

- $\nabla_* \phi$

  From Eq. (B.21) one obtains

  $$\nabla_* \phi = \frac{\nabla_* r_\beta}{4\pi r_\beta^2} \sin\left[k\left(c_0 t - \hat{\vartheta}\right)\right] + \frac{k \cos\left[k\left(c_0 t - \hat{\vartheta}\right)\right]}{4\pi r_\beta^2} \nabla_* \hat{\vartheta} \tag{B.24}$$

  where

  $$\nabla_* r_\beta = \frac{-\left[\beta^2 r \nabla_* r + M_0^2 \Delta x_1 \nabla_* \Delta x_1\right]}{r_\beta} \tag{B.25}$$

  and

  $$\nabla_* \hat{\vartheta} = \frac{\nabla_* r_\beta + M_0 \nabla_* \Delta x_1}{\beta^2} \tag{B.26}$$

- $\dfrac{\partial \phi}{\partial t}$

  From Eq. (B.21) one obtains

  $$\frac{\partial \phi}{\partial t} = \frac{\frac{\partial r_\beta}{\partial t}}{4\pi r_\beta^2} \sin\left[k\left(c_0 t - \hat{\vartheta}\right)\right] - \frac{k \cos\left[k\left(c_0 t - \hat{\vartheta}\right)\right]}{4\pi r_\beta^2} \left(k c_0 - \frac{\partial \hat{\vartheta}}{\partial t}\right) \tag{B.27}$$

  with

  $$\frac{\partial r_\beta}{\partial t} = \frac{\beta^2}{r_\beta} \frac{\partial r}{\partial t}; \qquad \frac{\partial \hat{\vartheta}}{\partial t} = \frac{1}{r_\beta} \frac{\partial r}{\partial t} \tag{B.28}$$

Similarly to section B.1, the pressure disturbance at $(\mathbf{x}^*, t)$ depends on the observer kinematics; for a steady-state translation in rigid connection with the monopole, $\mathbf{y}^* = \mathbf{y}^*(t = 0)$ whilst $\partial r / \partial t = 0$. Differently, for an observer that translates at the same velocity of the monopole, spinning about the direction of $\mathbf{v}$ at angular velocity ω, the observer location is defined by $\mathbf{y}^*(t) = \mathcal{R}^T(t) \mathbf{y}^*(t = 0)$ where

$$\mathcal{R}(t) = \begin{bmatrix} 1 & 0 & 0 \\ 0 & cos(\omega t) & -sin(\omega t) \\ 0 & sin(\omega t) & cos(\omega t) \end{bmatrix} \tag{B.29}$$

defines the rotation matrix around the x_1 axis. Therefore

$$\frac{\partial r}{\partial t} = \hat{\mathbf{r}} \cdot \frac{\partial \mathbf{r}}{\partial t} = \hat{\mathbf{r}} \cdot \frac{d\mathcal{R}}{dt}\mathbf{y}^*(t=0) \tag{B.30}$$

providing

$$\frac{\partial \phi}{\partial t} = -\frac{\frac{\partial r}{\partial t}}{4\pi r_\beta^3}\left(\beta^2 \sin\left[k\left(c_0 t - \hat{\vartheta}\right)\right] + k\cos\left[k^2\left(c_0 t - \hat{\vartheta}\right)\right]\right) - \frac{k^2\cos\left[k\left(c_0 t - \hat{\vartheta}\right)\right]}{4\pi r_\beta^3} \tag{B.31}$$

Appendix C

Appendix C

C.1 Jump Relation Across the Wake

The analytic description of the potential wake behaviour is made using the continuity and momentum equations (see Eq.(C.1) and Eq. (C.2), respectively) that for a generic discontinuity surface read

$$\Delta[\rho(\mathbf{u}-\mathbf{v})\cdot\mathbf{n}] = 0 \tag{C.1}$$

$$\Delta[\rho\mathbf{u}(\mathbf{u}-\mathbf{v})\cdot\mathbf{n}-\mathbf{P}\mathbf{n}] = 0 \tag{C.2}$$

Where $\mathbf{P} = -p\mathbf{I}+\mathbf{V}$ is the compressive stress tensor, $\mathbf{u}$ is the flow field velocity on a material point over the wake surface and $\mathbf{v}$ is the kinematic velocity of a geometric point belonging to the discontinuity surface.

Under the assumption of constant density across it (i.e. it is not side of shocks), the Eq. (C.1) provides $\Delta\mathbf{u}_n = \Delta\mathbf{v}_n = 0$. This implies that the wake is an impermeable surface, thus having a null jump of normal velocity across it. For further discussions let us consider the wake as surface of class C^2 embedded in a 3D Euclidean space using a Cartesian coordinate system. Considering also a parametric representation of the surface such that each space coordinate (x,y,z) is a continuous real differentiable function of two curvilinear coordinate ξ^1 and ξ^2 given by:

$$\mathbf{x}(\xi^1,\xi^2) = x(\xi^1,\xi^2)\mathbf{e}_1 + y(\xi^1,\xi^2)\mathbf{e}_2 + z(\xi^1,\xi^2)\mathbf{e}_3 \tag{C.3}$$

From this standpoint a covariant base such that $\mathbf{g}_\alpha = \dfrac{\partial\mathbf{x}}{\partial\xi^\alpha}$ and the contra variant $\mathbf{g}^\gamma$ such that $\mathbf{g}_\alpha\cdot\mathbf{g}^\gamma = \delta_\alpha^\gamma$ define the metric of surface over a local tangent plane. The local normal direction is defined as $\mathbf{n} = \dfrac{\mathbf{g}_1\times\mathbf{g}_2}{\sqrt{a}}$ where a is the determinant of the surface covariant metric tensor [70]. The velocity field onto a certain material point of the wake is expressed in terms of covariant base as $\mathbf{u} = u_n\mathbf{n}+u^\alpha\mathbf{g}_\alpha$, where $u_n = \mathbf{u}\cdot\mathbf{n}$ and $u^\alpha = \mathbf{u}\cdot\mathbf{g}^\alpha$ represent respectively the normal and tangential velocity field respect to the wake surface.

Thus, the jump velocity across the wake reads $\Delta\mathbf{u} = \Delta u_n\mathbf{n}+\Delta u^\alpha\mathbf{g}_\alpha$ and being $\Delta\mathbf{u}_n = 0$ only the tangential component is present, namely $\Delta\mathbf{u} = \Delta u^\alpha\mathbf{g}_\alpha$. Moreover the projection of

Eq. (C.2) over the normal direction yields

$$\rho\Delta\mathbf{u}_n(\mathbf{u}_n-\mathbf{v}_n)+\mathbf{u}_n\rho\Delta(\mathbf{u}_n-\mathbf{v}_n)+\Delta p=0 \tag{C.4}$$

recalling that $\Delta\mathbf{u}_n = 0$, the combination of Eq. C.4 with the continuity equation yields a null pressure jump across the wake, namely $\Delta p = 0$. Moreover the time derivative of Eq.C.4 yields the following result

$$\dot{\Delta p} = -\mathbf{u}_n\,\Delta[\rho(\mathbf{u}_n-\mathbf{v}_n)]^{\cdot}-\Delta\mathbf{u}_n[\rho(\mathbf{u}_n-\mathbf{v}_n)]^{\cdot}-\Delta\dot{\mathbf{u}}_n[\rho(\mathbf{u}-\mathbf{v})\cdot\mathbf{n}]-\dot{\mathbf{u}}_n\,\Delta[\rho(\mathbf{u}-\mathbf{v})\cdot\mathbf{n}] \tag{C.5}$$

Combining the Eq. (C.5) with Eqs. (C.1) and (C.2) yields $\dot{\Delta p} = 0$, meaning that the time derivative of the pressure jump over the wake is equal to zero.

The following of this section is devoted to the determination of an analytical expression of $\Delta(\partial p'/\partial\tilde{n})$ required by Eq. (4.16). Recalling that

$$\frac{\partial p'}{\partial\tilde{n}}=\frac{\partial p'}{\partial n}-\nabla p\cdot\mathbf{MM}\cdot\mathbf{n} \tag{C.6}$$

the Euler equation under the hypothesis of negligible mass forces may be used to express the pressure gradient as follows

$$\rho\frac{D\mathbf{u}}{Dt}=-\nabla p \tag{C.7}$$

Moreover, for the purposes of the thesis the time derivative in Eq. (C.7) is expressed in terms of a Lagrangian reference system as follows

$$\frac{d\,\mathbf{u}}{dt}=\frac{\partial\mathbf{u}}{\partial t}-(\mathbf{v}\cdot\nabla)\,\mathbf{u} \tag{C.8}$$

where $\partial\,\mathbf{u}/\partial t$ and $d\mathbf{u}/dt$ are the time derivative made with respect to a Lagrangian and Eulerian observer, respectively. In addition $\mathbf{v}$ is the velocity of geometric point in which the time derivative is evaluated, thus combining Eq. (C.8) with Eq. (C.7) the Euler equation for a Lagrangian observer reads

$$\rho\left[\frac{\partial\mathbf{u}}{\partial t}+(\mathbf{u}^{-}\cdot\nabla)\mathbf{u}\right]=-\nabla p \tag{C.9}$$

where $\mathbf{u}^{-}=\mathbf{u}-\mathbf{v}$. The projection of Eq. (C.9) over the normal direction yields the following expression of the normal pressure derivative

$$\rho\frac{\partial\mathbf{u}}{\partial t}\cdot\mathbf{n}+\rho\left[(\mathbf{u}^{-}\cdot\nabla)\mathbf{u}\right]\cdot\mathbf{n}=-\frac{\partial p}{\partial n} \tag{C.10}$$

In order to obtain the jump of the normal derivative across the wake the Eq. (C.10) is turned in terms of a covariant base defined over the wake surface.

Considering the covariant base defined in Eq. (C.3) such that $\mathbf{g}_\alpha = \dfrac{\partial \mathbf{x}}{\partial \xi^\alpha}$ and the resulting contra variant $\mathbf{g}^\gamma = \mathbf{g}_\alpha g^{\alpha\gamma}$ where $g^{\alpha\gamma}$ indicates the inverse local metric tensor, the gradient operator may be expressed as $\nabla = \dfrac{\partial}{\partial \xi^\alpha}\mathbf{g}^\alpha + \dfrac{\partial}{\partial n}\mathbf{n}$. The same covariant base is also used to express all the other vector quantities involved in the Eq. (C.10). Thus, in terms of covariant base the flow field velocity time derivative in Eq. (C.9) reads

$$\frac{\partial \mathbf{u}}{\partial t} = \frac{\partial u^\alpha}{\partial t}\mathbf{g}_\alpha + \frac{\partial \mathbf{g}_\alpha}{\partial t}u^\alpha + \frac{\partial u_n}{\partial t}\mathbf{n} + \frac{\partial \mathbf{n}}{\partial t}u_n \tag{C.11}$$

Moreover being

$$(\mathbf{u}^- \cdot \nabla)\mathbf{u} = \left[(u^{\beta\,(-)}\mathbf{g}_\beta + u_n^{(-)}\mathbf{n}) \cdot (\frac{\partial}{\partial \xi^\alpha}\mathbf{g}^\alpha + \frac{\partial}{\partial n}\mathbf{n})\right](u^\gamma \mathbf{g}_\gamma + u_n\mathbf{n}) \tag{C.12}$$

considering that $\mathbf{g}_\alpha \cdot \mathbf{g}^\beta = \delta_\alpha^\beta$ and $\mathbf{g}_\alpha \cdot \mathbf{n} = \mathbf{g}^\gamma \cdot \mathbf{n} = 0$

$$(\mathbf{u}^- \cdot \nabla)\mathbf{u} = (u^{\alpha\,(-)}\frac{\partial}{\partial \xi^\alpha} + u_n^{(-)}\frac{\partial}{\partial n})(u^\gamma \mathbf{g}_\gamma + u_n\mathbf{n}) \tag{C.13}$$

In addition noting that

- $\dfrac{\partial \mathbf{g}_\gamma}{\partial \xi^\alpha} = \dfrac{\partial \mathbf{g}_\alpha}{\partial \xi^\gamma} = \Gamma^\beta_{\alpha\gamma}\mathbf{g}_\beta + b_{\alpha\gamma}\mathbf{n}$, where $b_{\alpha\gamma} = \dfrac{\partial \mathbf{g}_\alpha}{\partial \xi_\gamma} \cdot \mathbf{n}$ and $\Gamma^\beta_{\alpha\gamma} = \dfrac{\partial \mathbf{g}_\alpha}{\partial \xi_\gamma} \cdot \mathbf{g}_\beta$
- $\dfrac{\partial \mathbf{n}}{\partial \xi_\alpha} = -b_\alpha^\beta \mathbf{g}_\beta$, where b_α^β is the mixed surface curvature tensor such that $b_\alpha^\beta = b_{\alpha\gamma}g^{\gamma\beta}$
- $\dfrac{\partial \mathbf{n}}{\partial n} = 0$ and $\dfrac{\partial \mathbf{g}_\gamma}{\partial n} = 0$

the Eq. (C.13) reads

$$\begin{aligned}(\mathbf{u}^- \cdot \nabla)\mathbf{u} = {} & u^{\alpha\,(-)}\frac{\partial u^\gamma}{\partial \xi^\alpha}\mathbf{g}_\gamma + u^{\alpha\,(-)}u^\gamma(\Gamma^\beta_{\alpha\gamma}\mathbf{g}_\beta + b_{\alpha\gamma}\mathbf{n}) + u_n^{(-)}\frac{\partial u_\gamma}{\partial n}\mathbf{g}_\gamma + \\ & u_n^{(-)}\frac{\partial u_n}{\partial n}\mathbf{n} - u_n u^{\alpha\,(-)}b_\alpha^\gamma \mathbf{g}_\gamma + u^{\alpha\,(-)}\frac{\partial u_n}{\partial \xi_\alpha}\mathbf{n}\end{aligned} \tag{C.14}$$

Finally, combining Eq. (C.11) with Eq. (C.14) [1] the projection of Eq. (C.10) over the normal direction yields the following expression

$$-\frac{1}{\rho}\frac{\partial p}{\partial n} = \frac{\partial u_n}{\partial t} + u^{\alpha\,(-)}u^\gamma b_{\alpha\gamma} + u_n^{(-)}\frac{\partial u_n}{\partial n} + u^{\alpha\,(-)}\frac{\partial u_n}{\partial \xi_\alpha} \tag{C.15}$$

The application of jump condition to the Eq.(C.15) recalling that $\Delta u_n = 0$ and noting that the surface curvature tensor $b_{\alpha\gamma}$ is a continuous function though the wake surface yields the following expression of the jump for the normal derivative of the pressure

$$-\frac{1}{\rho}\Delta\left(\frac{\partial p}{\partial n}\right) = \Delta\left(u^{\alpha\,(-)}u^\gamma\right)b_{\alpha\gamma} + u_n^{(-)}\Delta\left(\frac{\partial u_n}{\partial n}\right) + \Delta\left(u^{\alpha\,(-)}\right)\frac{\partial u_n}{\partial \xi_\alpha} \tag{C.16}$$

[1] The proposed expression is valid only for axial flow condition with a prescript time independent wake model

The last step is represented by the application to the jump operator to the Eq. (C.6) which yields

$$\Delta\left(\frac{\partial p'}{\partial \tilde{n}}\right) = \Delta\left(\frac{\partial p'}{\partial n}\right) - \Delta\left(\nabla p\right)\cdot\mathbf{MM}\cdot\mathbf{n} \tag{C.17}$$

noting that the expression of the jump pressure gradient over the wake in terms of curvilinear coordinate yields $\Delta(\nabla p) = \Delta\frac{\partial p}{\partial \xi_\alpha}\mathbf{g}^\alpha + \Delta\frac{\partial p}{\partial n}\mathbf{n}$ and recalling that the jump condition occurs only over the normal local direction, i.e. $\Delta(\frac{\partial p}{\partial \xi_\alpha}) = 0$, the following relation is obtained

$$\Delta\left(\frac{\partial p'}{\partial \tilde{n}}\right) = \Delta\left(\frac{\partial p'}{\partial n}\right)\left(1 - M_n^2\right) \tag{C.18}$$

Finally, combining Eq. (C.16) and Eq. (C.6) yields

$$\Delta\left(\frac{\partial p'}{\partial \tilde{n}}\right) = -\rho\left[\Delta\left(u^{\alpha\,(-)}u^\gamma\right)b_{\alpha\gamma} + u_n^{(-)}\Delta\left(\frac{\partial u_n}{\partial n}\right) + \Delta\left(u^{\alpha\,(-)}\right)\frac{\partial u_n}{\partial \xi_\alpha}\right]\left(1 - M_n^2\right) \tag{C.19}$$

In Eq. (C.19) b_{α_β} is the surface covariant curvature tensor whereas $u^{\alpha\,(-)} = u^\alpha - v^\alpha$ and $u_n^{(-)} = u_n - v_n$. Moreover Δu^β represent the jump of the flow field velocity in tangential direction and $\dfrac{\partial u_n}{\partial \xi_\alpha}$ represent the tangential derivative of the normal flow field velocity over the contact discontinuity. Finally $\Delta(\frac{\partial u_n}{\partial n})$ is the jump across the discontinuity for the the normal derivative of the normal flow field velocity.

C.2 The Linear FWHE Across a Potential Wake

The particularization of the linear FWHE (i.e. the Eq. (3.5) neglecting the quadrupole source term) over a potential wake is here carried out. For such configuration it reads

$$\begin{aligned} p'_{FWH_k}(\mathbf{x},t) &= -\rho_0\int_{S_k}\Delta\left[\mathbf{v}\cdot\mathbf{n}\,\mathbf{v}\cdot\nabla\hat{G} + \left(\mathbf{v}\cdot\mathbf{n}\left(1-\mathbf{v}\cdot\nabla\vartheta\right)\right)^{\cdot}\hat{G}\right]_\vartheta \mathrm{d}S \\ &- \int_{S_k}\Delta\left[\left(\mathbf{Pn}\right)\cdot\nabla\hat{G} - \left(\mathbf{Pn}\right)^{\cdot}\cdot\nabla\vartheta\,\hat{G}\right]_\vartheta \mathrm{d}S \\ &- \int_{S_k}\Delta\left[\rho\mathbf{u}^-\cdot\mathbf{n}\,\mathbf{u}^+\cdot\nabla\hat{G} + \left(\rho\mathbf{u}^-\cdot\mathbf{n}\left(1-\mathbf{u}^+\cdot\nabla\vartheta\right)\right)^{\cdot}\hat{G}\right]_\vartheta \mathrm{d}S \end{aligned} \tag{C.20}$$

where $\Delta = [.]_u - [.]_l$ and subscripts refer to the two sides of the discontinuity surface. Without ambiguity, the upper side of $k(\mathbf{x},t)$ is associated to the direction of the normal $\mathbf{n} = \nabla k$. Moreover, noting that $\mathbf{v}$, $\nabla\hat{G}$ and $\nabla\vartheta$ are continuous functions through the jump surface, the first integral of Eq. (C.20) gives rise to a null contribution. This results perfectly match with the physics of the contact discontinuity surface, which has not thickness by definition. Furthermore, recalling that the quantities $\Delta\mathbf{P} = 0$, $(\Delta\mathbf{P})^{\cdot} = 0$, $\Delta(\rho\mathbf{u}^-) = 0$ and $\Delta(\rho\mathbf{u}^-)^{\cdot} = 0$ (see Appendix C.1 for theoretical details) also the second and third integral contribution do not provide any contribution to the acoustic pressure. This is a very important results because

it proof that the acoustic pressure provided by the linear configuration of the FWHE over a *contact discontinuity* is identically null.

C.3 The K-Equation Across a Potential Wake

The particularization of the linear H-FWHE (i.e. the Eq. (3.8) neglecting the quadrupole source term) across a potential wake is hereafter carried out. For a such configuration it reads

$$\begin{aligned} p'_{K_k}(\mathbf{x},t) &= \int_{\mathcal{S}_k} \Delta\left[\frac{\partial p'}{\partial \tilde{n}}\hat{G} - \frac{\partial \hat{G}}{\partial \tilde{n}}p'\right]_\theta \mathrm{d}S(\mathbf{y}) \\ &+ \int_{\mathcal{S}_k} \Delta\left[\hat{G}\frac{\partial p}{\partial t}\left(\frac{\partial \vartheta}{\partial \tilde{n}} + 2\frac{\mathbf{v}\cdot\mathbf{n}}{{c_0}^2}\right)\right]_\theta \mathrm{d}S(\mathbf{y}) \\ &+ \frac{1}{{c_0}^2}\int_{\mathcal{S}_k} \Delta\left[p'\hat{G}\frac{\partial}{\partial t}[\mathbf{v}\cdot\mathbf{n}(1-\mathbf{v}\cdot\nabla\vartheta)]\right]_\theta \mathrm{d}S(\mathbf{y}) \end{aligned} \tag{C.21}$$

where $\Delta = [.]_u - [.]_l$ and subscripts refer to the two sides of the discontinuity surface. Without ambiguity, the upper side of $k(\mathbf{x},t)$ is associated to the direction of the normal $\mathbf{n} = \nabla k = 0$. Moreover, akin to the FWHE see Appendix C.2, noting that: i) $\mathbf{v}$, $\nabla\hat{G}$ and $\nabla\vartheta$ are continuous functions through the jump surface, thus their jump across the wake is null. ii) $\Delta\mathbf{P} = 0$ and $(\Delta\mathbf{P})^{\cdot} = 0$, see Appendix C.1. Taking into account the above considerations the specification of Eq. (C.21) across a potential wake reads

$$p'_{K_k}(\mathbf{x},t) = \int_{S_w}\left[\Delta\left(\frac{\partial p'}{\partial \tilde{n}}\right)\hat{G}\right]_\vartheta \mathrm{d}S(\mathbf{y}) \tag{C.22}$$

An expression suitable for numerical applications of $\Delta\left(\partial p'/\partial\tilde{n}\right)$ is reported in Appendix C.19.

C.4 An Insight into the Quadrupole Surface Sources

In this section the quadrupole source contribution of the FWHE, (see Eq. 3.2) is recast into the Lighthill-like jet noise term in addition to surface contribution throughout a suitable combination of the H-FWHE and the FWHE. (see Eqs. (3.2) and (3.7), respectively). By subtracting the Eq. (3.2) to Eq. (3.7), i.e the FWHE to H-FWHE, the following equation is obtained

$$\begin{aligned} \square^2\left(p'_{H-FWHE} - p'_{FWHE}\right) &= \left\{\left(\frac{\overline{\partial} p'}{\overline{\partial} n} + \frac{1}{c_0}\frac{\overline{\partial} p'}{\overline{\partial} t}M_n\right)\delta(f) - \overline{\nabla}\cdot[p'\mathbf{n}\delta(f)]\right. \\ &\left. - \frac{1}{c_0}\frac{\overline{\partial}}{\overline{\partial} t}\left[p'M_n\delta(f)\right] + H\,\overline{\nabla}\cdot\overline{\nabla}\cdot\mathbf{T}\right\} - \left\{\frac{\overline{\partial}}{\overline{\partial} t}\left[\rho_0\,\mathbf{v}\cdot\nabla f\,\delta(f)\right] + \frac{\overline{\partial}}{\overline{\partial} t}\left[\rho\,(\mathbf{u}-\mathbf{v})\cdot\nabla f\,\delta(f)\right]\right. \\ &\left. - \overline{\nabla}\cdot[\mathbf{P}\,\nabla f\,\delta(f)] - \overline{\nabla}\cdot[\rho\,\mathbf{u}\otimes(\mathbf{u}-\mathbf{v})\,\nabla f\,\delta(f)] + \overline{\nabla}\cdot\overline{\nabla}\cdot[\mathbf{T}\,H(f)]\right\} = 0 \end{aligned} \tag{C.23}$$

where the RHS of Eq. (C.23) represent the difference between the forcing terms relative to the H-FWHE and FWHE, contained in the first and second couple of curly brackets, respectively. Similarly, the LHS represents the difference of D'Alambertian operator forced by the above mentioned forcing terms. Since both are an exact rearrangement of the Lighthill equation (see Appendix A.1), the difference is identically null. Therefore, recasting the Eq. (C.23) as difference between the non-linear and linear contribution one obtains

$$\begin{aligned}\overline{\nabla}\cdot\overline{\nabla}\cdot[\mathbf{T}\,H(f)]-H\,\overline{\nabla}\cdot\overline{\nabla}\cdot\mathbf{T}=&\left\{\left(\frac{\overline{\partial}p'}{\overline{\partial}n}+\frac{1}{c_0}\frac{\overline{\partial}p'}{\overline{\partial}t}M_n\right)\delta(f)-\overline{\nabla}\cdot[p'\mathbf{n}\delta(f)]\right.\\&\left.-\frac{1}{c_0}\frac{\overline{\partial}}{\overline{\partial}t}\left[p'M_n\delta(f)\right]\right\}-\left\{\frac{\overline{\partial}}{\overline{\partial}t}\left[\rho_0\,\mathbf{v}\cdot\nabla f\,\delta\left(f\right)\right]+\frac{\overline{\partial}}{\overline{\partial}t}\left[\rho\left(\mathbf{u}-\mathbf{v}\right)\cdot\nabla f\,\delta\left(f\right)\right]\right.\\&\left.-\overline{\nabla}\cdot\left[\mathbf{P}\,\nabla f\,\delta\left(f\right)\right]-\overline{\nabla}\cdot\left[\rho\,\mathbf{u}\otimes\left(\mathbf{u}-\mathbf{v}\right)\nabla f\,\delta\left(f\right)\right]\right\}\end{aligned}\tag{C.24}$$

Thus, noting that

$$\overline{\nabla}\cdot\overline{\nabla}\cdot(H\mathbf{T})=H\overline{\nabla}\cdot\overline{\nabla}(\mathbf{T})+\overline{\nabla}\cdot\left(\mathbf{T}\overline{\nabla}H\right)+\overline{\nabla}H\cdot\left(\overline{\nabla}\cdot\mathbf{T}\right)\tag{C.25}$$

Moreover, combining Eq. (C.24) with Eq. (C.25) yields

$$\begin{aligned}\overline{\nabla}\cdot\left(\mathbf{T}\overline{\nabla}H\right)+\overline{\nabla}H\cdot\left(\overline{\nabla}\cdot\mathbf{T}\right)=&\left\{\left(\frac{\overline{\partial}p'}{\overline{\partial}n}+\frac{1}{c_0}\frac{\overline{\partial}p'}{\overline{\partial}t}M_n\right)\delta(f)-\overline{\nabla}\cdot[p'\mathbf{n}\delta(f)]\right.\\&\left.-\frac{1}{c_0}\frac{\overline{\partial}}{\overline{\partial}t}\left[p'M_n\delta(f)\right]\right\}-\left\{\frac{\overline{\partial}}{\overline{\partial}t}\left[\rho_0\,\mathbf{v}\cdot\nabla f\,\delta\left(f\right)\right]+\frac{\overline{\partial}}{\overline{\partial}t}\left[\rho\left(\mathbf{u}-\mathbf{v}\right)\cdot\nabla f\,\delta\left(f\right)\right]\right.\\&\left.-\overline{\nabla}\cdot\left[\mathbf{P}\,\nabla f\,\delta\left(f\right)\right]-\overline{\nabla}\cdot\left[\rho\,\mathbf{u}\otimes\left(\mathbf{u}-\mathbf{v}\right)\nabla f\,\delta\left(f\right)\right]\right\}\end{aligned}\tag{C.26}$$

The application of the standard Green function technique summarized in Appendix A.2 allows to turn the Eq. (C.26) into the following integral form

$$-\int_{\Re^3}\int_0^\infty \check{G}\,\nabla\cdot(\mathbf{T}\nabla H)\;dt\mathrm{d}V-\int_{\Re^3}\int_0^\infty \check{G}\,\nabla H\cdot(\nabla\cdot\mathbf{T})\;dt\mathrm{d}V=p'_K-p'_{FWHE_l}\tag{C.27}$$

Where, $\tilde{p}'_K$ is the acoustic pressure associates with the integral terms contained inside the first curly brackets which corresponds to the linear solution (i.e. obtained neglecting the quadrupole contribution) of the Hybrid Lighthill-FWHE, see Eq. (3.8). Similarly, the integral solution of elements contained in second curly brackets provide the linear solution of the FWHE, namely $(FWHE_l)$, see Eq. (3.5).

Moreover, the application of the standard Green function technique (see Appendix A.2 for theoretical details) allows to turn the Eq. (C.25) into the following integral form

$$\begin{aligned} &-\int_{\Re^3}\int_0^\infty \check{G}\,\nabla\cdot\nabla\cdot\{H\mathbf{T}\}\;dt\,\mathrm{d}V = -\int_{\Re^3}\int_0^\infty \check{G}\,\nabla\cdot(\mathbf{T}\nabla H)\;dt\,\mathrm{d}V \\ &-\int_{\Re^3}\int_0^\infty \check{G}\,\nabla H\cdot(\nabla\cdot\mathbf{T})\;dt\,\mathrm{d}V - \int_{\Re^3}\int_0^\infty \check{G}\,H\nabla\cdot\nabla(\mathbf{T})\,dt\,\mathrm{d}V \end{aligned} \tag{C.28}$$

recalling that

$$p'_\chi(\mathbf{x},t) = -\int_{\Re^3}\int_0^\infty \check{G}\,\nabla\cdot\nabla\cdot\{H\,\mathbf{T}\}\;dt\,\mathrm{d}V \tag{C.29}$$

combining Eq. (C.28) with Eq. (C.27) the following form of the quadrupole source term of the FWHE is obtained

$$p'_\chi(\mathbf{x},t) = {p'}_K(\mathbf{x},t) - {p'}_{FWHE}(\mathbf{x},t) - \int_{\Re^3}\int_0^\infty H\,\nabla\cdot\nabla\cdot\mathbf{T}\,\check{G}\,dt\,\mathrm{d}V \tag{C.30}$$

In Eq. (C.30), ${p'}_K(\mathbf{x},t)$ and ${p'}_{FWHE}(\mathbf{x},t)$ represent the linear solution (i.e. without the field contribution) of the H-FWHE and FWHE.

Appendix D

Appendix D

D.1 XNAVIS Finite Volume Code

The governing equations for the unsteady motion of an incompressible viscous fluid are briefly recalled in this section. The equations are written in an inertial frame of reference; as some blocks on the total grid move to follow possible moving boundaries, the general form of the governing equations are written with respect to a moving control volume. The continuity and momentum equation in non–dimensional integral form (with respect to a reference velocity $\mathbf{u}_\infty$ and a reference length L) are

$$\begin{aligned} \oint_{S(\mathcal{V})} \mathbf{u}\cdot\mathbf{n}\ \mathrm{d}S &= 0 \\ \frac{\partial}{\partial t}\int_{\mathcal{V}} \mathbf{u}\ \mathrm{d}v + \oint_{S(\mathcal{V})} (\mathcal{F}_c - \mathcal{F}_d)\cdot\mathbf{n}\ \mathrm{d}S &= 0 \end{aligned} \tag{D.1}$$

$\mathcal{V}$ being a control volume, $S(\mathcal{V})$ its boundary, and $\mathbf{n}$ the outward unit normal. In equation (D.1), $\mathbf{u}$ is the flow velocity vector whereas $\mathcal{F}_c$ and $\mathcal{F}_d$ represent convective (inviscid and pressure components) and diffusive fluxes, respectively:

$$\begin{aligned} \mathcal{F}_c &= p\mathbf{I} + (\mathbf{u}-\mathbf{v})\,\mathbf{u} \\ \mathcal{F}_d &= \left(\frac{1}{Re} + \nu_t\right)\left[\nabla\mathbf{u} + (\nabla grad\mathbf{u})^{\mathrm{T}}\right] \end{aligned} \tag{D.2}$$

where $\mathbf{v}$ is the local velocity of the control volume boundary, $Re = U_\infty L/\nu$ the Reynolds number, ν the kinematic viscosity, whereas ν_t denotes the non–dimensional turbulent viscosity. In the following equations, u_i indicates the i–th Cartesian component of the velocity vector (the Cartesian components of the velocity will be also denoted with u, v, and w); p is a variable related to the pressure P and the acceleration of gravity g (parallel to the vertical axis z, downward oriented) by $p = P + z/Fr^2$, $Fr = U_\infty/\sqrt{gL}$ being the Froude number.

The problem in Eq. D.1 is closed by enforcing appropriate conditions at physical and computational boundaries. On solid walls, the relative velocity is set to zero (whereas no condition on the pressure is required); at the (fictitious) inflow boundary, velocity is set to the undisturbed flow value, and the pressure is extrapolated from inside; on the contrary, the pressure is set to zero at the outflow, whereas velocity is extrapolated from inner points.

At the free surface, whose location is one of the unknowns of the problem, the dynamic boundary condition requires continuity of stresses across the surface; if the presence of the air is neglected, the dynamic boundary conditions read []

$$\begin{aligned} p &= \tau_{ij} n_i n_j + \frac{z}{Fr^2} + \frac{\kappa}{We^2} \\ \tau_{ij} n_i t^1_j &= 0 \\ \tau_{ij} n_i t^2_j &= 0 \end{aligned} \tag{D.3}$$

where τ_{ij} is the stress tensor, κ is the average curvature, $We = \sqrt{\rho U_\infty^2 L/\sigma}$ is the Weber number (σ being the surface tension coefficient), whereas $\mathbf{n}$, $\mathbf{t^1}$ and $\mathbf{t^2}$ are the surface normal and two tangential unit vectors, respectively. The actual position of the free surface $F(x,y,z,t) = 0$ is computed by enforcing the kinematic condition

$$\frac{\mathrm{D}\, F(x,y,z,t)}{\mathrm{D}\, t} = 0 \tag{D.4}$$

Initial conditions have to be specified respectively for the velocity field and the free surface configuration; specifically we set

$$\begin{aligned} u_i(x,y,z,0) &= \bar{u}_i(x,y,z) \\ F(x,y,z,0) &= \bar{F}(x,y,z) \end{aligned} \tag{D.5}$$

NUMERICAL MODEL

Spatial discretization

For the numerical solution of the equations (D.1), the fluid domain D is partitioned into N_l structured blocks D^l, each subdivided into $N_i \times N_j \times N_k$ disjoint hexahedrons D^l_{ijk}. In the numerical scheme adopted here, the blocks are not necessarily disjoint, they can be partially overlapped, as it will be explained in the following sections. Conservation laws are then applied to each finite volume:

$$\begin{aligned} &\sum_{s=1}^{6} \int_{\mathcal{S}_s} \mathbf{U} \cdot \mathbf{n} \, \mathrm{d}S = 0 \\ &\frac{\partial}{\partial t} \int_{\mathcal{V}_{ijk}} \mathbf{U} \, \mathrm{d}V + \sum_{s=1}^{6} \int_{\mathcal{S}_s} (\mathcal{F}_c - \mathcal{F}_d) \cdot \mathbf{n} \, \mathrm{d}S = 0 \end{aligned} \tag{D.6}$$

where $\mathcal{S}_s$ is the s-th face of the finite volume D_{ijk}, whose measure is $\mathcal{V}_{ijk}$.

In order to obtain second order accuracy in space, convective and viscous fluxes in the momentum equations, as well as surface integral of the velocity in the continuity equation,

have to be computed by means of trapezoidal rule:

$$\begin{aligned}
\int_{\mathcal{S}_s} \mathbf{U}\cdot\mathbf{n}dS &= \left. u_l n_l \right|_0 A_s + O(\Delta^2 A_s) \\
\int_{\mathcal{S}_s} \mathcal{F}_c\cdot\mathbf{n}dS &= \left. \mathbf{F}_s^c \right|_0 A_s + O(\Delta^2 A_s) \\
\int_{\mathcal{S}_s} \mathcal{F}_d\cdot\mathbf{n}dS &= \left. \mathbf{F}_s^d \right|_0 A_s + O(\Delta^2 A_s)
\end{aligned} \tag{D.7}$$

where the subscript 0 means that the quantities are computed at the face center, A_s is the measure of $\mathcal{S}_s$, Δ is the diameter of $\mathcal{S}_s$ and:

$$\begin{aligned}
\mathbf{F}_s^c &= \begin{pmatrix} u_1(u_l - v_l)n_l + pn_1 \\ u_2(u_l - v_l)n_l + pn_2 \\ u_3(u_l - v_l)n_l + pn_3 \end{pmatrix} \\
\mathbf{F}_s^d &= \begin{pmatrix} \tau_{1l}n_l \\ \tau_{2l}n_l \\ \tau_{3l}n_l \end{pmatrix}
\end{aligned} \tag{D.8}$$

where v_l, $l = 1,2,3$ are the components of the velocity of the control volume. The stress tensor at the cell interface is computed as:

$$\tau_{lm}|_{i+\frac{1}{2},j,k} = \nu_{i+\frac{1}{2},j,k}\left(\frac{\partial u_m}{\partial x_l} + \frac{\partial u_l}{\partial x_m}\right)_{i+\frac{1}{2},j,k} \tag{D.9}$$

The derivatives of the velocity vector are obtained by means of a finite volume approximation:

$$\left.\frac{\partial u_m}{\partial x_l}\right|_{i+\frac{1}{2},j,k} = \frac{1}{V_{i+\frac{1}{2},j,k}}\int_{\Sigma_{i+\frac{1}{2},j,k}} u_m n_l dS + O(\Delta^2) \tag{D.10}$$

where the integral is extended to the volume $V_{i+\frac{1}{2},j,k}$ (whose boundary is $\Sigma_{i+\frac{1}{2},j,k}$) that includes the cell face $S_{i+\frac{1}{2},j,k}$ and is overlapped to half the cell (i,j,k) and half the cell $(i+1,j,k)$. In equation (D.9), $\nu_{i+\frac{1}{2},j,k}$ denotes the sum of the kinematic and turbulent viscosity at the cell face.

The computation of the convective fluxes $\mathbf{F}_s^c$ and the surface integral of the velocity in the continuity equation requires the evaluation of pressure and velocity at the face center. To this aim, a second order ENO-type scheme has been adopted [71]. These schemes were originally developed for compressible fluid flows, on the basis of the hyperbolic nature of the inviscid part of the Navier-Stokes equations. The extension to incompressible flows is possible when working in pseudo-compressible formulation.

The building block of this kind of algorithms is the Godunov's scheme (1959), in which the flux vector at cell interface is computed as the solution of a Riemann problem, whose right and left states are given by the values of the numerical solution at two neighboring cell centers. For example, at the cell face $i+\frac{1}{2},j,k$:

$$\mathbf{F}^c_{i+\frac{1}{2},j,k} = \mathbf{F}^c(\mathbf{q}_l,\mathbf{q}_r) = \mathbf{F}^c(\mathbf{q}_{i,j,k},\mathbf{q}_{i+1,j,k}) \tag{D.11}$$

$\mathbf{q}$ being the vector of the state variables, which, for pseudo–compressible flows, take the form: $\mathbf{q} = (p, u_1, u_2, u_3)^T$. This scheme yields oscillation-free discrete solutions, also when the exact solutions are discontinuous. However it can be shown that the resulting scheme is only first order accurate. Higher order accurate (up to any finite order) oscillation free solutions can be obtained by modifying the evaluation of the right and left states of the Riemann problem as explained in [71]. In the particular case of second order accuracy, it can be shown that left and right states have to be evaluated as:

$$\begin{aligned} \mathbf{q}_l &= \mathbf{q}_{i,j,k} + \frac{1}{2}\text{minmod}(\Delta_{i-1/2}, \Delta_{i+1/2}) \\ \mathbf{q}_r &= \mathbf{q}_{i+1,j,k} - \frac{1}{2}\text{minmod}(\Delta_{i+1/2}, \Delta_{i+3/2}) \end{aligned} \tag{D.12}$$

where $\Delta_{i+1/2} = \mathbf{q}_{i+1,j,k} - \mathbf{q}_{i,j,k}$ and minmod is a function that is applied to each vector component:

$$\begin{aligned} &\text{minmod}(x, y) = \\ &= \begin{cases} 0 & \text{if} \quad xy \leq 0 \\ \text{sign}(x)\min(|x|, |y|) & \text{if} \quad xy > 0 \end{cases} \end{aligned} \tag{D.13}$$

It is easy to prove that:

$$\begin{aligned} \mathbf{q}_l &= \mathbf{q}_{i,j,k} + \frac{1}{2}\text{minmod}(\Delta_{i-1/2}, \Delta_{i+1/2}) \\ &= \mathbf{q}_{i,j,k} + \frac{1}{2}\left.\frac{\partial \mathbf{q}}{\partial x}\right|_{i,j,k} \Delta x + O(\Delta x^2) \\ &= \mathbf{q}_{i+1/2,j,k} + O(\Delta x^2) \end{aligned} \tag{D.14}$$

and:

$$\begin{aligned} \mathbf{q}_r &= \mathbf{q}_{i+1,j,k} - \frac{1}{2}\text{minmod}(\Delta_{i+1/2}, \Delta_{i+3/2}) \\ &= \mathbf{q}_{i+1,j,k} - \frac{1}{2}\left.\frac{\partial \mathbf{q}}{\partial x}\right|_{i+1,j,k} \Delta x + O(\Delta x^2) \\ &= \mathbf{q}_{i+1/2,j,k} + O(\Delta x^2) \end{aligned} \tag{D.15}$$

and therefore, the Riemann flux being a Lipschitz continuous function of its arguments:

$$\mathbf{F}^c(\mathbf{q}_l, \mathbf{q}_r) = \mathbf{F}^c(\mathbf{q}_{i+1/2,j,k}) + O(\Delta x^2) \tag{D.16}$$

The evaluation of the convective flux vector requires the solution of a Riemann problem at each cell interface. In order to simplify the algorithm, a second order accurate solution was used in place of the exact one, which must be computed iteratively, given the nonlinearity of the problem; details of the algorithm can be found in [72].

Temporal integration

The semi-discrete system of equations can be rewritten in vector form as:

$$\Lambda \left.\frac{\partial \mathcal{V}\mathbf{q}}{\partial t}\right|_{ijk} + \mathcal{R}_{ijk} = \mathbf{0} \tag{D.17}$$

where $\Lambda = \text{diag}\,(0,1,1,1)$ and:

$$\mathbf{q} = \frac{1}{\mathcal{V}_{ijk}} \int_{\mathcal{V}_{ijk}} (p/\beta, u, v, w)^T \, \mathrm{d}V \tag{D.18}$$

being the volume average of the unknowns. Moreover, in the previous equation $\mathcal{R}_{ijk}$ represents flux balance on the current cell; β is the pseudo compressibility factor (for more details about artificial compressibility method, see [43]).

In order to have a fully implicit scheme and to obtain a divergence free velocity field, a dual (or pseudo) time–derivative (see [42] for more details) is introduced in the discrete system of equations

$$\left.\frac{\partial \mathcal{V}\mathbf{q}}{\partial \tau}\right|_{ijk} + \Lambda \left.\frac{\partial \mathcal{V}\mathbf{q}}{\partial t}\right|_{ijk} + \mathcal{R}_{ijk} = \mathbf{0} \tag{D.19}$$

and the solution is iterated to steady state with respect to the pseudo time τ, for each physical time step.

The time derivative in the previous equation is approximated by means of a second order accurate three–points backward finite difference approximation formula, whereas the integration with respect to the pseudo time is carried out by means of an implicit Euler scheme, i.e.

$$\begin{aligned} &\frac{(\mathcal{V}\mathbf{q})^{m+1}_{ijk} - (\mathcal{V}\mathbf{q})^{m}_{ijk}}{\Delta\tau} + \\ &\Lambda \frac{3\,(\mathcal{V}\mathbf{q})^{m+1}_{ijk} - 4\,(\mathcal{V}\mathbf{q})^{n}_{ijk} + (\mathcal{V}\mathbf{q})^{n-1}_{ijk}}{2\Delta t} + \mathcal{R}^{m+1}_{ijk} = \mathbf{0} \end{aligned} \tag{D.20}$$

where the superscripts n and m denote the real and dual time levels, $\Delta\tau$ is the pseudo time step and Δt is the physical time step. The previous equation is then solved with respect to $\mathbf{q}^{m+1}_{ijk}$ as in the Beam and Warming's scheme (1978), i.e. the equation is rewritten in "delta" form

$$\begin{aligned} &\left(\mathcal{I} + \frac{3\Delta\tau}{2\Delta t}\Lambda\right) \delta(\mathcal{V}\mathbf{q})^{m}_{ijk} + \Delta\tau \frac{\partial \mathcal{R}_{ijk}}{\partial(\mathcal{V}\mathbf{q})} \left(\delta(\mathcal{V}\mathbf{q})^{m}_{ijk}\right) = \\ &-\Delta\tau \left[\Lambda \frac{3\,(\mathcal{V}\mathbf{q})^{m}_{ijk} - 4\,(\mathcal{V}\mathbf{q})^{n}_{ijk} + (\mathcal{V}\mathbf{q})^{n-1}_{ijk}}{2\Delta t} + \mathcal{R}^{m}_{ijk}\right] \end{aligned} \tag{D.21}$$

$\mathcal{I}$ being the identity matrix and $\delta(\mathcal{V}\mathbf{q})^{m}_{ijk} = (\mathcal{V}\mathbf{q})^{m+1}_{ijk} - (\mathcal{V}\mathbf{q})^{m}_{ijk}$. The operator in the left hand side of the previous equation is solved by an approximate factorization technique. The resulting scheme is unconditionally stable to the linear analysis. Local dual time step $\Delta\tau_{ijk}$ and a multi-grid technique [73, 74] have been used in order to improve the convergence rate of the sub–iteration algorithm.

Turbulence model

Although the above equations are in principle able to carry out a Direct Numerical Simulation (DNS), applications of engineering interest are computationally too demanding for available resources. Therefore the effect of turbulence phenomena are *modeled* through numerical techniques based on the turbulent viscosity.
Specifically, to evaluate it different approaches are available:
i) Reynolds Averaged Navier Stokes Equations (RANSE) with one–equation Spalart and Alamaras [48] closure model
ii) Large Eddy Simulation (LES) with Smagorisky [49] closure model
These models are based respectively on the time average and spatial filtering of the Navier–Stokes equations whose give rise to additional terms that must be modeled to close the problem. For the both the averaged equation are closed by modeling $(-\overline{\rho u_i' u_j'})$ where bar indicates a averaging process such that $\bar{u} = u_i - u_i'$ in which $\bar{u_i}$ and u_i' represent the mean and disturbance velocity, respectively. For the RANS model the mean value is intended respect to the time whereas for the LES as spatial filtering technique (Favre filter).
Moreover, a suitable combination of both model (RANS/LES) namely Detached Eddy Simulation (DES) allows through a transition criteria able to swap between the Spalart-Alamaras (RANS) in the boundary layer and the Smagorisky (LES) in the flow field [50]. In the following the models are briefly outlined.

Reynolds-averaged Navier-Stokes Equation model

For the sake of completeness the model by [48] is recalled here. The model is based on the eddy viscosity concept, i.e. on the assumption that the Reynolds stress tensor $(-\overline{\rho u_i' u_j'})$ is related to the mean strain rate through an apparent turbulent viscosity (eddy viscosity) ν_t:

$$-\overline{u_i' u_j'} = \nu_t \left(\frac{\partial \bar{u}_i}{\partial x_j} + \frac{\partial \bar{u}_j}{\partial x_i} \right) \tag{D.22}$$

ν_t is computed by means of an intermediate variable $\tilde{\nu}$ and the relation:

$$\nu_t = \tilde{\nu} f_{v1}(\chi); \quad \chi = \frac{\tilde{\nu}}{\nu}; \quad f_{v1}(\chi) = \frac{\chi^3}{\chi^3 + C_{v1}^3} \tag{D.23}$$

The variable $\tilde{\nu}$ is computed from the solution of a partial differential equation that reads

$$\begin{aligned} \frac{D\tilde{\nu}}{Dt} &= c_{b1}\left[1 - f_{t2}\right]\tilde{S}\tilde{\nu} \\ &- \left[c_{w1} f_w - \frac{c_{b1}}{k^2} f_{t2}\right]\left[\frac{\tilde{\nu}}{d}\right]^2 \\ &+ f_{t1}\Delta U \\ &+ \frac{1}{\sigma}\left[\nabla \cdot ((\nu + \tilde{\nu})\nabla\tilde{\nu}) + c_{b2}(\nabla\tilde{\nu})^2\right], \end{aligned} \tag{D.24}$$

where $\tilde{S} = S + [\tilde{\nu}/(k^2 d^2)] f_{v2}$, S is the magnitude of the vorticity vector, d the distance from the wall, $f_{t1}, f_{t2}, f_w, f_{v2}$ are functions that depends only on χ and the distance from the

wall; finally, the c-s and k are constants. The first two terms in the right hand side represent production and destruction of $\tilde{\nu}$, respectively; the third one is the so-called "trip" term, that allows to specify the laminar-turbulent transition point location (in the results shown in the next section, this term was always turned off); the last part is a dissipation term, that contains also a non conservative portion $c_{b2}(\nabla\tilde{\nu})^2$ which is responsible, together with the non-linear part of the diffusion term $\nabla\cdot(\tilde{\nu}\nabla\tilde{\nu})$, for the advection of a turbulent front into non-turbulent regions.

LES, Smagorinsky–Lilly model

Akin to the RANS model it is based on the eddy viscosity concept, i.e. on the following assumption

$$-\overline{u_i'u_j'} = \nu_t\left(\frac{\partial\bar{u}_i}{\partial x_j}+\frac{\partial\bar{u}_j}{\partial x_i}\right) \tag{D.25}$$

The first Subgrid Scale Modeling (SGS) was developed by Smagorinsky–Lilly [75], and used in the first LES simulation by [49]. It models the eddy viscosity as:

$$\nu_t = (\mathcal{C}_s\Delta_g)^2\sqrt{2\bar{S}_{ij}\bar{S}_{ij}} = (\mathcal{C}_s\Delta_g)^2\,|\bar{\mathbf{S}}| \tag{D.26}$$

Where

$$S_{ij} = \frac{1}{2}\left(\frac{\partial\bar{u}_i}{\partial x_j}+\frac{\partial\bar{u}_j}{\partial x_i}\right) \tag{D.27}$$

and Δ_g is the grid size and $\mathcal{C}_s$ is a constant.

Detached Eddy Simulation

In order to switch to an LES (Large Eddy Simulation) far from rigid boundaries (where a RANS simulation is retained to overcome the difficulties encountered with the use of LES in near–wall regions) [50], a new distance function $\tilde{d}$ is used, defined by:

$$\tilde{d} = min\,(d, C_{DES}\Delta) \tag{D.28}$$

C_{DES} being another constant and Δ the larger cell size along the three coordinate lines.

Free surface simulation

The presence of the free surface is simulated by mean of a single-phase level-set approach developed in [44], which is briefly recalled here.

In level set approaches (see for example [76] and [77]), a smooth function $\phi(x,y,z,t)$, whose zero level coincides for $t=0$ with the free surface, is defined in the whole physical domain (i.e. in both liquid and air phases); the kinematic boundary condition (D.4) is extended to all the points in the domain, yielding a transport equation for the level set function:

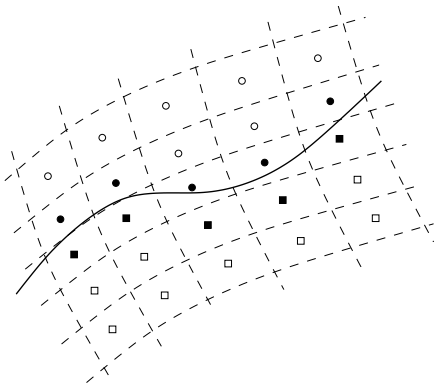

FIGURE D.1: Computational domain. Squares: nodes in the liquid phase; circles: nodes in the gas phase. Full symbols: nodes where the kinematic condition (D.33) is enforced.

$$\begin{aligned} &\frac{\partial \phi(x,y,z,t)}{\partial t} + (\vec{u} - \vec{v}) \cdot \nabla \phi(x,y,z,t) = 0 \\ &\phi(x,y,z,0) = d(x,y,z) \end{aligned} \tag{D.29}$$

$\vec{u}$ being the velocity of the underlying flow, $\vec{v}$ the grid velocity and $d(x,y,z)$ the signed distance from the free surface at $t = 0$. The zero level of the function $\phi(x,y,z,t)$ represents the free surface location for $t > 0$; moreover, initializing $\phi(x,y,z,t)$ as the signed distance from the surface of discontinuity, the sign of the level set function remains unchanged at material points. In classical two–phase level set approaches, the density and the molecular viscosity of the fluid are then assumed to depend on the sign of the level set function; to avoid numerical difficulties related to sharp discontinuities, density and viscosity have a smooth transition around the zero level $\phi(x,y,z,t)$ [77].

In order to maintain the thickness of the interface constant in time and avoid mass loss [77], level set function has to remain a distance function for $t > 0$. In the so–called *re–initialization* step, the level set function $\phi(x,y,z,t)$ is replaced, at each time step, by a new function $\tilde{\phi}(x,y,z,t)$ with the same zero level, but again representing the distance from the interface; the function $\tilde{\phi}(x,y,z,t)$ is computed at each physical time step as the asymptotic (steady state) solution, with respect to the pseudo–time τ, of the equation:

$$\frac{\partial \tilde{\phi}}{\partial \tau} + sign(\phi)(|\nabla \tilde{\phi}| - 1) = 0 \tag{D.30}$$

where $sign$ is the sign function [78].

In the single–phase algorithm adopted here, only the liquid phase of the fluid is computed; the computational domain is formally decomposed in (see figure (D.1)):

- grid points close to the surface of discontinuity (full circles and full squares in figure (D.1)): the level set function is computed by means of the evolution equation (D.29); velocity and pressure in the liquid region (full squares) are computed by means of the Navier Stokes and continuity equations (D.1); pressure is evaluated by using the dynamic boundary condition and the velocity is extrapolated at the points in the air phase

(full circles);

- grid points in the liquid phase region (empty squares in figure (D.1)): the solution is computed by the numerical solution of the governing equations (D.1), and the level set function is enforced to be a distance function by means of equation (D.30);
- grid points in the *"air"* region (empty circles in figure (D.1)): the level set function is computed from equation (D.30) in order to get a distance function, and an extension velocity is computed as done by Adalsteinsson and Sethian [79].

It has to be noted that, in the single–phase formulation, the solution outside the water region is not required; however, the extension of the velocity field outside the water region ensures second order accuracy also close to the interface.

It was found convenient, when computing free surface flows around complex geometries with curvilinear grids, to split the level set function as:

$$\phi(x,y,z,t) = \varphi(x,y,z,t) + z \tag{D.31}$$

where the function $\varphi(x,y,z,t)$ is the solution (from equation (D.29)) of:

$$\frac{\partial \varphi}{\partial t} + \vec{u} \cdot \nabla \varphi + w = 0 \tag{D.32}$$

By doing so, it is easier to assign the boundary condition for the level set function at inflow, that reduces to $\varphi(x,y,z,t) = 0$.

An ENO technique (similar to the one used for the bulk flow) is used to discretize equation (D.32); to this end, the equation is first rewritten in terms of curvilinear coordinates:

$$\frac{\partial \varphi}{\partial t} + U^m \frac{\partial \varphi}{\partial \xi_m} + w = 0 \tag{D.33}$$

$U^m = (u_i - v_i)\dfrac{\partial \xi_m}{\partial x_i}$ being the contra–variant components of the velocity vector. The derivatives of the function $\varphi(x,y,z,t)$ at cell center are approximated by a second order finite difference formula; considering, for instance, the (i,j,k)–cell center, for the coordinate line ξ_1 it reads:

$$\frac{\partial \varphi}{\partial \xi_1} = \varphi_{i+\frac{1}{2},j,k} - \varphi_{i-\frac{1}{2},j,k} \tag{D.34}$$

The interface values $\varphi_{i+\frac{1}{2},j,k}$ is computed as:

$$\varphi_{i+\frac{1}{2},j,k} = \varphi_{i,j,k} + \frac{\text{minmod}(\,\Delta\varphi|_{i+\frac{1}{2}}\,,\,\Delta\varphi|_{i-\frac{1}{2}})}{2} \tag{D.35}$$

if $U^1_{i,j,k} \geq 0$, or:

$$\varphi_{i+\frac{1}{2},j,k} = \varphi_{i+1,j,k} - \frac{\text{minmod}(\,\Delta\varphi|_{i+\frac{3}{2}}\,,\,\Delta\varphi|_{i+\frac{1}{2}})}{2} \tag{D.36}$$

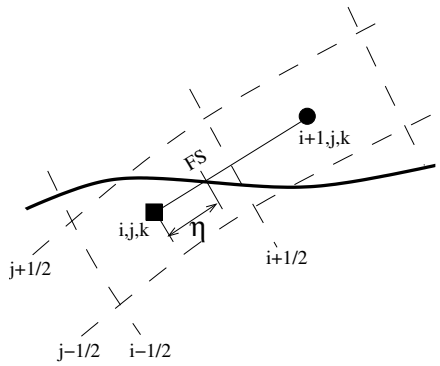

FIGURE D.2: Free surface detection and extrapolation of pressure.

if $U^1_{i,j,k} \leq 0$, and similarly for $\varphi_{i-\frac{1}{2},j,k}$. It has been proved by [71] that this procedure yields a second order approximation to (D.29).

As for the bulk flow, the time discretization of the level-set function is fully implicit and the time derivative is discretized by a three point backward formula. The dual-time stepping technique was used to solve the resulting system of non linear equation, which are solved simultaneously with the Navier-Stokes equations.

For the nodes in the water region which are not close to the surface of discontinuity (empty squares in figure (D.1)), the level set function is enforced to be a distance from the interface when the sub–iteration converges. To this aim, the constrain $|\nabla\phi| = 1$ is enforced by means of an iterative (with respect to the pseudo-time τ) marching ENO scheme with second order accuracy, where the above condition is rewritten as an evolution equation for the level set function $\phi(x,y,z,t)$:

$$\frac{\partial \phi}{\partial \tau} + sign(\phi)\left[\frac{\nabla\phi}{|\nabla\phi|}\cdot\nabla\phi - 1\right] = 0 \tag{D.37}$$

Then, by using the definition (D.31), the previous equation is rewritten in term of $\varphi(x,y,z,t)$ as:

$$\frac{\partial \varphi}{\partial \tau} + \vec{w}\cdot\nabla\varphi + b = 0 \tag{D.38}$$

where:

$$\begin{aligned} \vec{w} &= sign(\phi)\frac{\nabla\phi}{|\nabla\phi|} \\ b &= sign(\phi)\left[\frac{\phi_z}{|\nabla\phi|} - 1\right] \end{aligned} \tag{D.39}$$

This equation is solved with respect to $\varphi(x,y,z,t)$ with a scheme analogous to the one used to solve the kinematic equation (D.32) at the points adjacent to the free surface, with characteristic speed $\vec{w}$. The same equation is used to update the level set function values in the air phase. It can be seen, that, when the sub–iteration converges, it provides a function $\phi(x,y,z,t)$ that satisfies equation (D.29) on the surface $\phi(x,y,z,t) = 0$ and it is a distance function at any other points. Note that $\phi(x,y,z,t)$ is a distance function also at points close to the free surface (full symbols in figure (D.1)) because of equation (D.45) (see later). Once the function $\varphi(x,y,z,t)$ is known throughout the whole domain, the free surface is located

by the surface $\phi(x,y,z,t) = \varphi(x,y,z,t) + z = 0$. The intersection of this surface with the underlying grid line is computed as follows (see figure D.2). Consider, for instance, the coordinate line ξ_1; when in two adjacent points (i,j,k) and $(i+1,j,k)$ the condition

$$\phi_{i,j,k}\,\phi_{i+1,j,k} \leq 0 \tag{D.40}$$

holds, it means that the free surface cuts the segment $\mathbf{P}_{i,j,k} - \mathbf{P}_{i+1,j,k}$ at some point $\mathbf{P}_{FS}$ ($\mathbf{P}_{i,j,k}$ is the position vector that locates the i,j,k point). Then, the portion of the segment below the free surface is:

$$\eta = \frac{|\mathbf{P}_{FS} - \mathbf{P}_{i,j,k}|}{|\mathbf{P}_{i+1,j,k} - \mathbf{P}_{i,j,k}|} = \frac{|\phi_{i,j,k}|}{|\phi_{i+1,j,k} - \phi_{i,j,k}|} \tag{D.41}$$

if $\phi_{i,j,k} < 0$, the level set function having been defined as the distance from the interface. A similar relation holds for $\phi_{i+1,j,k} < 0$, with i and $i+1$ interchanged.

The computation of the residuals for the RANS equations at those points whose neighboring cells are not all into the water region need some attention. In fact, in these cases the numerical convective and viscous fluxes at interfaces that separate two cells, of which one is in the air region (as the interface $\left(i+\frac{1}{2},j,k\right)$ in figure (D.2)), must be evaluated; in these points the proper information to compute the correct flux are needed to retain second order accuracy. To circumvent this difficulty, the following procedure is applied. The pressure at $\left(i+\frac{1}{2},j,k\right)$ is extrapolated as:

$$p_{i+\frac{1}{2},j,k} = p_{i-\frac{1}{2},j,k} + \frac{1}{\frac{1}{2}+\eta}\left(p_{FS} - p_{i-\frac{1}{2},j,k}\right) \tag{D.42}$$

with

$$p_{i-\frac{1}{2},j,k} = \frac{p_{i,j,k} + p_{i-1,j,k}}{2} \tag{D.43}$$

where p_{FS} is computed from the dynamic boundary condition (D.3).

Once the pressure is known, the normal velocity at $(i+\frac{1}{2},j,k)$ is computed by solving the Riemann problem:

$$\left(p_{i+\frac{1}{2},j,k} - p_w\right) + \lambda\left(u_n|_{i+\frac{1}{2},j,k} - u_n|_w\right) = 0 \tag{D.44}$$

being $\lambda = \hat{u}_n + \sqrt{\hat{u}_n^2 + \beta}$ and where p_w and $u_n|_w$ represent the known state on the water side, computed as in (D.12). The tangential velocity is simply extrapolated along the normal to the free surface, given by $\nabla\phi/|\nabla\phi|$, as in the following equation (D.45). The remaining dynamic boundary conditions for the tangential stresses in (D.3) are explicitly enforced when computing the viscous fluxes at the cell interface $\left(i+\frac{1}{2},j,k\right)$.

Outside the water region, extension velocities are computed as:

$$\nabla\phi\cdot\nabla u_i = 0 \qquad\qquad i = 1,2,3 \tag{D.45}$$

which guarantees that $\phi(x,y,z,t)$ evolves as a distance function also at the points adjacent to the free surface (full circles in figure (D.1); see, for the proof, [79]). Since this relation has to be satisfied only when the sub-iteration converge, the previous relation is substituted by an

evolution equation for the velocity components u_i:

$$\frac{\partial u_i}{\partial \tau} + \nabla\phi \cdot \nabla u_i = 0 \tag{D.46}$$

which is solved by a second order ENO scheme analogous to the one used to solve the kinematic equation (D.32) and equation (D.38), characteristic speed being $\nabla\phi$. Note that the values of the velocity, pressure and turbulent viscosity in the air phase are useless when steady state is attained, and therefore they do not affect the formal accuracy of the numerical scheme. Nevertheless, their estimation is of great importance during the iterative procedure at those points that change their physical state from air to water, for which an initial estimate is needed.

Spatial discretization - Overlapping grids

In this section the basic elements of the overlapping grid discretization (or "chimera" method) for both fixed grids and its extension to moving grids will be briefly recalled. For more details and examples of applications the reader is referred to [51, 52, 80].

The introduction of chimera capabilities in the RANS code is given through a modification of both the boundary conditions and internal point treatment for those zones where overlapping appears. In particular, besides the natural type (i.e. wall, symmetry, inflow, outflow, ...), a new type of boundary conditions, the "chimera" type, is added for those boundaries where the solution must be interpolated from other blocks. For this cell, the first step is to find a "donor" cell, i.e. a cell that contain the face center for which an interpolation is needed. In order to retain the best possible approximation, if a boundary cell fall within more that one donor cell, the smallest one is picked as basis for interpolation. Once the donor is identified, then a convex set of eight donor cell centers is searched, and a tri-linear interpolation is used to transfer the solution from one block to the boundary of the one under analysis.

As to internal points, we look at first for possible overlapping for each cell centers. If this overlapping is found, the cell is marked as a "hole" only if the donor cell is "smaller" than the one we are considering. As for boundary cell centers, is more that one possible donors is found, the smallest is chosen as donor. Differently form standard chimera approaches, however, the cell marked as holes are not removed from the computation but the interpolated solution is enforced by adding a forcing term to the Navier-Stokes equations, in a "body-force" fashion:

$$\mathbf{q}^{n+1}_{\text{chimera}} = \mathbf{q}^{n}_{\text{chimera}} - \Delta t \left[\mathcal{R}^n + \frac{k}{\delta} \left(\mathbf{q}^{n}_{\text{chimera}} - \mathbf{q}^{n}_{\text{interp}} \right) \right] \tag{D.47}$$

In the previous equation $\mathbf{q}$ is the vector of the dependent variables, $\mathcal{R}$ is the vector of the residuals, $k = \mathcal{O}(10)$ is a parameter chosen through numerical tests, and δ is the minimum between the cell diameter and the physical time step. This approach is particularly useful when using multigrid and approximate factorization, as it allows to maintain a structured data set.

For the point that fall within a rigid body, the forcing term in the equation is analogous to the previous one, but the velocity in the forcing term is equal to the local velocity of the body.

When dealing with moving grids, of course the grid topology must be re-computed at each time step. In order to speed-up the algorithm, we can exploit the information we have form the previous time step to search donor cells and holes. In particular, for each face center on a chimera boundary, we start the search of the possible donor from the knowledge of the previous ones. For the "holes", the first check is made to verify if the cell is still overlapped by a cell of the same block. When these initial approximations fails to yield a new donor set, the general search procedure is re-started.

D.2 The Differential Aerodynamic Problem for the Velocity Potential

For an inviscid, non–conducting, shock–free, initially isentropic and initially irrotational (initially at rest and in thermodynamic equilibrium) flow, the velocity field may be described by means of a velocity potential function $\phi(\mathbf{x}, t)$ such that $\mathbf{u} = \nabla\phi$.
Similarly to the pressure disturbance, the velocity potential is governed by the following non–homogeneous wave equation [40]

$$-\Box^2\phi = \sigma \tag{D.48}$$

where $\sigma = \left[(c^2 - c_0^2)\nabla^2\phi + 2\mathbf{u}\cdot\dot{\mathbf{u}} + \mathbf{u}\cdot\frac{\nabla u^2}{2}\right]/c^2$ denotes all the non–linear terms.
The problem is completed by the boundary conditions. In the air frame of reference, the boundary condition at infinity is given by $\phi = 0$ (fluid at rest). Then, the surface $\mathcal{S}$ of the body is assumed to impermeable; hence $(\mathbf{u} - \mathbf{v})\cdot\mathbf{n} = 0$ yields $\frac{\partial\phi}{\partial n} = \mathbf{v}\cdot\mathbf{n}$, where $\mathbf{v}$ is the velocity of the points of the surface. In addition for lifting flows the issue of the wake has to be addressed. A detailed analysis is given in Ref. [40] and Ref. [81]. Here, it is sufficient to note that an inviscid isentropic initially–irrotational flow remains irrotational at all times except for those points that come in contact with the surface of the body, because Kelvin's theorem is not applicable in this case. These points form a surface on which the flow is not necessarily potential. This surface, called the wake, is a surface of discontinuity for the potential. From the application of the conservation of mass and linear momentum across a surface of discontinuity, it results that the fluid does not penetrate it (the wake is a material surface) and hence $\Delta(\frac{\partial\phi}{\partial n}) = 0$, and in addition the pressure is continuous across it. Furthermore, the Bernoulli theorem yields that the potential jump across the wake, $\Delta\phi$, remains constant following a wake point and equal to the value it had when it left the trailing edge.
Following the same procedure used in the previous section to extend to the whole space the

potential governing equation, here the domain function $E(\mathbf{x},t)$ defined as

$$E(\mathbf{x},t) = \begin{cases} 1 & \text{if} \quad \mathbf{x} \in \Re^3 \setminus \mathcal{V} \\ 0 & \text{if} \quad \mathbf{x} \in \mathcal{V} \end{cases} \tag{D.49}$$

is introduced, and the extended function $\hat{\phi}(\mathbf{x},t) = E(\mathbf{x},t)\,\phi(\mathbf{x},t)$ is defined. Then using the mathematical relations

$$\nabla^2 [E\phi] = E\nabla^2\phi + \nabla E \cdot \nabla\phi + \nabla \cdot (\phi \nabla E) \tag{D.50}$$

and

$$\frac{\partial^2 \hat{\phi}}{\partial t^2} = (\phi \dot{E})^{\cdot} + \ddot{\phi} E + \dot{\phi}\dot{E} \tag{D.51}$$

the equation governing the velocity potential is recast in the following form

$$-\Box^2 \hat{\phi} \;=\; E\,\sigma + \nabla E \cdot \nabla\phi + \nabla \cdot (\phi \nabla E) - \frac{1}{c_0^2}\left[\dot{\phi}\dot{E} + (\phi\dot{E})^{\cdot}\right] \tag{D.52}$$

that is valid $\forall \mathbf{x} \in \Re^3$.
Observing that $E(\mathbf{x},t) = H[f(\mathbf{x},t)]$ and recalling Eq. (A.13), Eq. (D.52) may be written as

$$\begin{aligned} -\Box^2 \hat{\phi} \;&=\; \sigma\, H(f) + \nabla\phi \cdot \mathbf{n}\,\delta(f) + \nabla \cdot [\phi\,\mathbf{n}\,\delta(f)] + \\ &-\; \frac{1}{c_0^2}\left\{\dot{\phi}\dot{H}(f) + \left[\phi\dot{H}(f)\right]^{\cdot}\right\} \quad \forall \mathbf{x} \in \Re^3 \end{aligned} \tag{D.53}$$

Accounting that $\dot{H}(f) = -\mathbf{v} \cdot \nabla H = -\mathbf{v} \cdot \mathbf{n}\,\delta(f)$ one obtains

$$\begin{aligned} -\Box^2 \hat{\phi} \;&=\; \sigma\, H(f) + \nabla\phi \cdot \mathbf{n}\,\delta(f) + \nabla \cdot [\phi\,\mathbf{n}\,\delta(f)] + \\ &-\; \frac{1}{c_0^2}\left\{-\dot{\phi}\,\mathbf{v} \cdot \mathbf{n}\,\delta(f) + \left[-\phi\,\mathbf{v} \cdot \mathbf{n}\,\delta(f)\right]^{\cdot}\right\} \quad \forall \mathbf{x} \in \Re^3 \end{aligned} \tag{D.54}$$

Bibliography

[1] M. J. Lighthill. “On sound generated aerodynamically. I. General theory”. In: *Proceedings of the Royal Society A.* 211 (1107) (1952), pp. 564–587.

[2] J.E. Ffowcs Williams and D. L. Hawkings. “Sound Generation by Turbulence and Surfaces in Arbitrary Motion”. In: *Philosophical Transactions of the Royal Society A.* 264 (1151) (1969), pp. 321–342.

[3] F. Farassat. “Theory of Noise Generation From Moving Bodies With an Application to Helicopter Rotors”. In: *NASA Technical Report R-451* (1975).

[4] F. Farassat. “Linear acoustic formulas for calculation of rotating blade noise”. In: *AIAA Journal* 19(9) (1981), pp. 1122–1130.

[5] Hanno Heller et al. In: Aeroacoustics Conferences. 0. American Institute of Aeronautics and Astronautics, 1993. Chap. HELINOISE - The European Community rotor acoustics research program. DOI: 10.2514/6.1993-4358. URL: https://doi.org/10.2514/6.1993-4358.

[6] *RHINO Reduction of Helicopter Interior Noise*. https://cordis.europa.eu/project/rcn/5529_en.html. From 1993-01-01 to 1995-12-31.

[7] *HELISHAPE Rotorcraft Aerodynamics and Aeroacoustics*. https://cordis.europa.eu/project/rcn/5881_en.html. From 1993-09-01 to 1996-12-31.

[8] *SNAAP Study of Noise and Aerodynamics of Advanced Propellers*. https://cordis.europa.eu/project/rcn/5577/factsheet/en. From 1993-01-01 to 1996-06-31.

[9] *EROS Development of a Common European Euler Code for Helicopter Rotors*. https://cordis.europa.eu/project/rcn/31964_en.html. From 1996-04-01 to 1999-03-31.

[10] *HELIFLOW Improved experimental and theoretical tools for helicopter aeromechanic and aeroacoustic interactions*. https://cordis.europa.eu/publication/rcn/1874_en.html. 1996-09-01 to 2001-04-30.

[11] *ROSAA Integration of advanced aerodynamics in comprehensive rotorcraft analysis*. https://cordis.europa.eu/project/rcn/43556_en.html. From 1998-03-01 to 2000-05-31.

[12] *APIAN Advanced propulsion integration aerodynamics and noise*. https://cordis.europa.eu/project/rcn/32571/factsheet/en. From 1996-06-01 to 2001-01-31.

[13] Danielle J. Moreau J. Doolan and Laura A. Brooks. “WIND TURBINE NOISE MECHANISMS AND SOME CONCEPTS FOR ITS CONTROL”. In: *Acoustics Australia* 40 (Apr. 2012).

[14] Sandro Ianniello. “The Ffowcs Williams-Hawkings equation for hydroacoustic analysis of rotating blades. Part?1.?The rotpole”. In: 797 (2016), pp. 345–388. ISSN: 0022-1120. DOI: 10.1017/jfm.2016.263. URL: https://www.cambridge.org/core/article/ffowcs-williamshawkings-equation-for-hydroacoustic-analysis-of-rotating-blades-part-1-the-rotpole/9580ECACCC7F9F05739AFA35AD240096.

[15] *SILENV Report Summary Ships oriented innovative solutions to reduce noise and vibrations*. https://cordis.europa.eu/result/rcn/56502_en.html. From 1998-03-01 to 2000-05-31.

[16] *STREAMLINE Strategic Research For Innovative Marine Propulsion Concepts*. https://cordis.europa.eu/project/rcn/94118_en.html. From 2010-03-01 to 2014-02-28.

[17] “28th ITTC, Final Report and Recommendations of the Specialist Committee on Hydrodynamic Noise”. In: *Proc. of the 28th Tank Conference* (2017). Volume II WUXI, China, September 17-22, pp. 491–509.

[18] P. di Francescantonio. “A NEW BOUNDARY INTEGRAL FORMULATION FOR THE PREDICTION OF SOUND RADIATION”. In: *Journal of Sound and Vibration* 202.4 (1997), pp. 491 –509. ISSN: 0022-460X. DOI: https://doi.org/10.1006/jsvi.1996.0843. URL: http://www.sciencedirect.com/science/article/pii/S0022460X96908433.

[19] S. Mendez, M. Shoeybi, and S.Lele ans P. Moin. “On the use of the Ffowcs Williams-Hawkings equation to predict far-field jet noise from large-eddy simulations.” In: *International Journal of Aeroacoustics* 12.4 (2013), pp. 1–20. DOI: https://doi.org/10.1260/1475-472X.12.1-2.1.

[20] P. Kellett, O. Turan, and A. Incecik. “A study of numerical ship underwater noise prediction”. In: *Ocean Engineering* 66 (2013), pp. 113–120. DOI: 10.1016/j.oceaneng.2013.04.006.

[21] Zane Nitzkorski and Krishnan Mahesh. *A dynamic end cap technique for sound computation using the Ffowcs Williams and Hawkings equations*. Vol. 26. Physics of Fluids. 2014, p. 115101.

[22] S. Ianniello, R. Muscari, and A. Di Mascio. “Ship Underwater Noise Assessment by the Acoustic Analogy. Part I: Nonlinear Analysis of a Marine Propeller in a Uniform Flow”. In: *Journal of Marine Science and Technology* 18(4) (2013), pp. 547–570.

[23] C. Testa and L. Greco. “Prediction of submarine scattered noise by the acoustic analogy”. In: *Journal of Sound and Vibration* 426 (2018), pp. 186–218. ISSN: 0022-460X. DOI: https://doi.org/10.1016/j.jsv.2018.04.011. URL: http://www.sciencedirect.com/science/article/pii/S0022460X18302360.

[24] Claudio Testa et al. In: Aeroacoustics Conferences. 0. American Institute of Aeronautics and Astronautics, 2007. Chap. Sound Scattered by Helicopter Fuselage in Descent Flight Conditions. DOI: 10.2514/6.2007-3497. URL: https://doi.org/10.2514/6.2007-3497.

[25] W. Johnson. *Helicopter Theory*. Dover Books on Aeronautical Engineering. Dover Publications, 2012. ISBN: 9780486131825. URL: https://books.google.it/books?id=FiEapaNgjLcC.

[26] "27th ITTC, Final Report and Recommendations of the Specialist Committee on Hydrodynamic Noise". In: *Proc. of the 27th Tank Conference* (2014). Volume II Copenhagen Danemark, pp. 640–679.

[27] W.K Blake. "Propeller cavitation noise: the problems of scaling and prediction". In: *International symposium on cavitation and multi-phase flow noise* (1986). Anaheim, California, USA.

[28] C.E. Brennen. "Cavitation and bubble dynamics". In: *Oxford University Press* (1995).

[29] M. Strasberg. "Propeller cavitation noise after 35 years of study". In: *ASME symposium on Noise and Fluids Engineering* (1977).

[30] Renzo Tonin. "Sources of wind turbine noise and sound propagation". In: *Acoustics Australia* 40.5 (2012), pp. 20–27.

[31] Zane Nitzkorski and Krishnan Mahesh. "A dynamic end cap technique for sound computation using the Ffowcs Williams and Hawkings equations". In: *PHYSICS OF FLUIDS* 12.4 (2013), pp. 1–20. DOI: https://doi.org/10.1260/1475-472X.12.1-2.1.

[32] S. Ianniello and E. De Bernardis. "Farassat's Formulations in Marine Propeller Hydroacoustics". In: *International Journal of aeroacoustics* 14 (2014), pp. 87–103.

[33] Y. Chen and Z. Liu. "Ship propeller broadband noise prediction using the LES and CAA". In: *2016 IEEE/OES China Ocean Acoustics (COA)*. 2016, pp. 1–4.

[34] M. Cansin Özden et al. "Underwater radiated noise prediction for a submarine propeller in different flow conditions". In: *Ocean Engineering* 126 (2016), pp. 488–500. ISSN: 0029-8018. URL: http://www.sciencedirect.com/science/article/pii/S0029801816301913.

[35] Luca GRECO et al. "Marine propellers performance and flow-field prediction by a free-wake panel method". In: *Journal of Hydrodynamics, Ser. B* 26.5 (2014), pp. 780–795. ISSN: 1001-6058. URL: http://www.sciencedirect.com/science/article/pii/S1001605814600871.

[36] A.P. Dowling and J.E. Ffocws Williams. "Sound and Sources of Sound". In: *435–437* 135 (1983), Journal of Fluid Mechanics.

[37] M. Gennaretti, L. Luceri, and L. Morino. "A Unified Boundary Integral Methodology for Aerodynamics and Aeroacoustics of Rotors". In: *461–489* 200,4 (1997), Journal of Sound and Vibration.

[38] Luigi Morino and Massimo Gennaretti. *Toward an Integration of Aerodynamics and Aeroacoustics of Rotors*. 1992.

[39] L. Morino, L.T. Chen, and E. Suciu. "Steady and Oscillatory Subsonic and Supersonic Aerodynamics Around Complex Configurations". In: *AIAA Journal* 13 (1975), pp. 368–374.

[40] L. Morino and M. Gennaretti. "Boundary Integral Equation Methods for Aerodynamics". In: *Computational Nonlinear Mechanics in Aerospace Engineering* 146 (1992). Ed. by S.N. Atluri Progress in Aeronautics & Astronautics. AIAA, Washington, DC, pp. 279–320.

[41] Claudio Testa. "Acoustic Formulations for Aeronautical and Naval Rotorcraft Noise Prediction Based on the Ffowcs Williams and Hawkings Equation". PhD dissertation. Roma Tre University, 2009-01-19.

[42] CHARLES MERKLE. In: Fluid Dynamics and Co-located Conferences. 0. American Institute of Aeronautics and Astronautics, 1987. Chap. Time-accurate unsteady incompressible flow algorithms based on artificial compressibility. DOI: 10.2514/6.1987-1137. URL: https://doi.org/10.2514/6.1987-1137.

[43] Alexandre Joel Chorin. "A Numerical Method for Solving Incompressible Viscous Flow Problems". In: *Journal of Computational Physics* 135.2 (1997), pp. 118–125. ISSN: 0021-9991. URL: http://www.sciencedirect.com/science/article/pii/S0021999197957168.

[44] A. Di Mascio, R. Broglia, and R. Muscari. "On the application of the single-phase level set method to naval hydrodynamic flows". In: *Computers & Fluids* 36.5 (2007), pp. 868–886. ISSN: 0045-7930. URL: http://www.sciencedirect.com/science/article/pii/S0045793006000910.

[45] A. Di Mascio, Riccardo BROGLIA, and Roberto MUSCARI. "Prediction of hydrodynamic coefficients of ship hulls by high-order Godunov-type methods". In: 14.1 (2009), pp. 19–29. ISSN: 09484280. URL: https://ci.nii.ac.jp/naid/10025362566/en/.

[46] Richard M. Beam and R. F. Warming. "An Implicit Factored Scheme for the Compressible Navier-Stokes Equations". In: *AIAA Journal* 16.4 (1978), pp. 393–402. ISSN: 0001-1452. DOI: 10.2514/3.60901. URL: https://doi.org/10.2514/3.60901.

[47] B. FAVINI, R. BROGLIA, and A. DI MASCIO. "MULTIGRID ACCELERATION OF SECOND-ORDER ENO SCHEMES FROM LOW SUBSONIC TO HIGH SUPERSONIC FLOWS". In: *International Journal for Numerical Methods in Fluids* 23.6 (30 September 1996), pp. 589–606. ISSN: 0271-2091. DOI: 10.1002/(SICI)1097-0363(19960930)23:6<589::AID-FLD444>3.0.CO;2-#. URL: https://doi.org/10.1002/(SICI)1097-0363(19960930)23:6<589::AID-FLD444>3.0.CO;2-#.

[48] P.R. Spalart and S.R. Allmaras. "A One-Equation Turbulence Model for Aerodynamic Flows". In: *Aerospace Sciences and Exibit* (Mar. 1993). AIAA 30th Reno NV USA.

[49] Deardorff J. "A numerical study of three-dimensional turbulent channel flow at large Reynolds numbers". In: *Journal of Fluid Mechanics* 41(2) (1970), pp. 453–480.

[50] Philippe R. Spalart. "Detached-Eddy Simulation". In: *Annual Review of Fluid Mechanics* 41 (Jan. 2009), pp. 181–202.

[51] R. MUSCARI. "Simulation of the flow around complex hull geometries by an overlapping grid approach". In: (2005). URL: https://ci.nii.ac.jp/naid/10029739110/en/.

[52] R. Muscari, Riccardo Broglia, and Andrea Di Mascio. *An overlapping grids approach for moving bodies problems*. Proceedings of the International Offshore and Polar Engineering Conference. 2006, pp. 243–248.

[53] Daniel T. Kennedy and Robert A. Van Gorder. "Motion of open vortex-current filaments under the Biot-Savart model". In: 836 (2018), pp. 532–559. ISSN: 0022-1120. DOI: 10.1017/jfm.2017.826. URL: https://www.cambridge.org/core/article/motion-of-open-vortexcurrent-filaments-under-the-biotsavart-model/16D4EABDFC33533819E0471F2F48FECC.

[54] M. J. Lighthill. "On sound generated aerodynamically. II. Turbulence as a source of sound". In: *Proceedings of the Royal Society A.* 222 (1148) (1954), pp. 1–32.

[55] F. Farassat. "Discontinuities in Aerodynamics and Aeroacoustics: the Concept and Applications of Generalized Derivatives". In: *Journal of Sound and Vibration* 55 (2) (1977), pp. 165–193.

[56] F. Farassat. "Introduction to Generalized Functions With Applications in Aerodynamics and Aeroacoustics". In: *NASA Technical Paper 3428* 55 (2) (Apr. 1996).

[57] M.S. Howe. *Theory of Vortex Sound*. CAMBRIDGE TEXTS IN APPLIED MATHEMATICS, 2002.

[58] *AQUO-SONIC Supression Of Underwater Noise Induced by Cavitation*. http://www.aquo.eu/SONIC.htm. From 1 October 2012 3 years duration.

[59] F. Farassat and G. P. Succi. "A review of propeller discrete frequency noise prediction technology with emphasis on two current methods for time domain calculations". In: *Journal of Sound and Vibration* 71(3) (1980), pp. 399–419.

[60] L. V. Lopes et al. "Identification of Spurious Signals from Permeable Ffowcs Williams and Hawkings Surfaces". In: *AHS 73 rd Annual Forum* 210 (2017). Fort Worth, Texas, USA, May 9-11, 2017. URL: https://ntrs.nasa.gov/search.jsp?R=20170005478 2017-11-29T16:31:55+00:00Z.

[61] F. Farassat and M.K. Myers. "Extension of Kirchhoff's Formula to Radiation From Moving Surfaces". In: *Journal of Sound and Vibration* 123 (3) (1988), pp. 451–460.

[62] F. FARASSAT. “ACOUSTIC RADIATION FROM ROTATING BLADES–THE KIRCHHOFF METHOD IN AEROACOUSTICS”. In: *Journal of Sound and Vibration* 239.4 (2001), pp. 785–800. ISSN: 0022-460X. URL: http://www.sciencedirect.com/science/article/pii/S0022460X00932218.

[63] F. FARASSAT. In: Aeroacoustics Conferences. 0. American Institute of Aeronautics and Astronautics, 1987. Chap. Quadrupole source in prediction of the noise of rotating blades - A new source description. DOI: 10.2514/6.1987-2675. URL: https://doi.org/10.2514/6.1987-2675.

[64] S. Zaghi, R. Muscari, and A. Di Mascio. “Assessment of blockage effects in wind tunnel testing of wind turbines”. In: *Journal of Wind Engineering and Industrial Aerodynamics* 154 (2016), pp. 1–9. ISSN: 0167-6105. URL: http://www.sciencedirect.com/science/article/pii/S0167610516301799.

[65] Michael Shur, Philippe Spalart, and Michael Strelets. *Noise prediction for increasingly complex jets. Part I: Methods and tests*. Vol. 4. International Journal of Aeroacoustics. 2005, pp. 213–246.

[66] Jinhee Jeong and Fazle Hussain. “On the identification of a vortex”. In: 285 (1995), pp. 69–94. ISSN: 0022-1120. DOI: 10.1017/S0022112095000462. URL: https://www.cambridge.org/core/article/on-the-identification-of-a-vortex/D26006DDB95FB28DA80E28A581182DF1.

[67] Roberto Muscari, Andrea Di Mascio, and Roberto Verzicco. “Modeling of vortex dynamics in the wake of a marine propeller”. In: *Computers & Fluids* 73 (2013), pp. 65–79. ISSN: 0045-7930. URL: http://www.sciencedirect.com/science/article/pii/S0045793012004549.

[68] T. J. Poinsot and S. K. Lelef. “Boundary conditions for direct simulations of compressible viscous flows”. In: *Journal of Computational Physics* 101.1 (1992), pp. 104–129. ISSN: 0021-9991. URL: http://www.sciencedirect.com/science/article/pii/0021999192900462.

[69] A. Di Mascio, R. Muscari, and G. Dubbioso. “On the wake dynamics of a propeller operating in drift”. In: 754 (2014), pp. 263–307. ISSN: 0022-1120. DOI: 10.1017/jfm.2014.390. URL: https://www.cambridge.org/core/article/on-the-wake-dynamics-of-a-propeller-operating-in-drift/13749E0B22BBE5956745D35537B31FE0.

[70] Taha Sochi. *Principles of Differential Geometry*. Department of Physics and Astronomy University College London Gower Street London, 2016.

[71] Ami Harten et al. “Uniformly High Order Accurate Essentially Non-oscillatory Schemes, III”. In: *Journal of Computational Physics* 131.1 (1997), pp. 3–47. ISSN: 0021-9991. URL: http://www.sciencedirect.com/science/article/pii/S0021999196956326.

[72] A. Di Mascio, R. Broglia, and B. Favini. "Godunov Methods: Theory and Applications". In: ed. by E. F. Toro. Boston, MA: Springer US, 2001. Chap. A Second Order Godunov-Type Scheme for Naval Hydrodynamics, pp. 253–261.

[73] A. Brandt and O. Livne. *Multigrid Techniques*. Society for Industrial and Applied Mathematics, 2011, p. 222. ISBN: 978-1-61197-074-6. DOI: 10.1137/1.9781611970753. URL: https://doi.org/10.1137/1.9781611970753.

[74] B. Favini, R. Broglia, and A. Di Mascio. "Multigrid Acceleration of Second-Order Eno Schemes from Low Subsonic to High Supersonic Flows". In: *INT J NUMER METHOD FLUID* 23 (1997), pp. 589–606. DOI: 0.1002/(SICI)1097-0363(19960930)23:63.3.CO;2-R.

[75] Smagorinsky J. "General Circulation Experiments with the Primitive Equations". In: *Monthly Weather Review* 91(3) (Mar. 1963), pp. 99–164.

[76] Stanley Osher and James A. Sethian. "Fronts propagating with curvature-dependent speed: Algorithms based on Hamilton-Jacobi formulations". In: *Journal of Computational Physics* 79.1 (1988), pp. 12–49. ISSN: 0021-9991. URL: http://www.sciencedirect.com/science/article/pii/0021999188900022.

[77] Mark Sussman, Peter Smereka, and Stanley Osher. "A Level Set Approach for Computing Solutions to Incompressible Two-Phase Flow". In: *Journal of Computational Physics* 114.1 (1994), pp. 146–159. ISSN: 0021-9991. URL: http://www.sciencedirect.com/science/article/pii/S0021999184711557.

[78] E. Rouy and A. Tourin. "A Viscosity Solutions Approach to Shape-From-Shading". In: *SIAM Journal on Numerical Analysis* 29.3 (1992), pp. 867–884. ISSN: 0036-1429. DOI: 10.1137/0729053. URL: https://doi.org/10.1137/0729053.

[79] D. Adalsteinsson and J. A. Sethian. "The Fast Construction of Extension Velocities in Level Set Methods". In: *Journal of Computational Physics* 148.1 (1999), pp. 2–22. ISSN: 0021-9991. URL: http://www.sciencedirect.com/science/article/pii/S0021999198960909.

[80] Riccardo Broglia, Andrea Di Mascio, and Roberto Muscari. "Numerical Study of Confined Water Effects On Self-propelled Submarine In Steady Manoeuvres". In: *International Journal of Offshore and Polar Engineering* 17.02 (2007), p. 8. ISSN: 1053-5381. URL: https://doi.org/.

[81] Morino L. and Tseng K. *A General Theory of Unsteady Compressible Potential Flows With Applications to Airplanes and Rotors*. P.K.BANERJEE and L. Morino, Development in Boundary Element Method vol.6 : Non Linear Problems of Fluid Dynamics, Elsevier Applied Sciences Publishers, Barking, UK. 1990.